DISSERTATION

submitted to the

Combined Faculty of Natural Sciences and Mathematics

of the

Ruperto-Carola-University of Heidelberg, Germany

for the degree of

Doctor of Natural Sciences

put forward by

JONAS KEMMER

born in Oberwesel, Germany

Oral examination: 16 February 2022

Earth-sized planets orbiting M-dwarf stars:

Detection and mass measurement with

CARMENES and TESS

Referees: Prof. Dr. Andreas Quirrenbach
                Prof. Dr. Joachim Wambsganß

Jonas Kemmer

Earth-sized planets orbiting M-dwarf stars: Detection and mass measurement with CARMENES and TESS

Reviewers: Prof. Dr. Andreas Quirrenbach and Prof. Dr. Joachim Wambsganß

Supervisors: Prof. Dr. Andreas Quirrenbach, PD Dr. Sabine Reffert and Dr. Markus Feldt

Ruperto-Carola-University of Heidelberg, Germany

Extrasolar Planet Research Group

Landessternwarte, Zentrum für Astronomie der Universität Heidelberg

Königstuhl 12

69117 and Heidelberg

Zusammenfassung

Der technische Fortschritt der letzten Jahrzehnte erlaubt es uns immer kleinere Planeten immer genauer zu untersuchen. Besonders spannend ist die Charakterisierung erdgroßer Planeten, da wir daraus auch wichtige Erkenntnisse zur Entstehung und Entwicklung unserer eigenen Erde gewinnen können. Ideal für die Suche nach erdgroßen Planeten sind M-Zwerg Sterne. Aufgrund ihrer im Verhältnis zu den Planeten geringen stellaren Massen und kleinen Radien, sind die mit der Radialgeschwindigkeits- und Transitmethode messbaren planetaren Signale bei diesen besonders stark ausgeprägt. In meiner Dissertation beschäftige ich mich mit dem CARMENES Spektrographen, der zu genau diesem Zweck konstruiert wurde. Den ersten Teil bildet ein Fehlerbudget für den visuellen Kanal des Spektrographen, in welchem ich untersuche, wie sich die Unsicherheit der gemessenen Radialgeschwindigkeiten (RVs) zusammensetzt, und wo die technischen Grenzen des Instruments liegen. Im zweiten Teil der Arbeit präsentiere ich die Entdeckung von zwei erdgroßen Planeten mithilfe von CARMENES Beobachtungen. Die beiden kurz-periodischen Planeten GJ 3473 b und GJ 3929 b umkreisen M-Zwerg Sterne und wurden zunächst vom Himmelsdurchmusterungssatelliten TESS als Transitplanetenkanditaten identifiziert. Unsere nachfolgenden Beobachtungen mit der RV-Methode bestätigten ihre planetare Natur und offenbarten im Falle von GJ 3473 zusätzlich einen nicht sternbedeckenden, gemäßigt-warmen Planeten mit sub-Neptun Masse, GJ 3473 c. Eine gemeinsame Modellierung der Transit- und RV-Daten ermöglichte es die genauen Massen und Radien der beiden Transitplaneten zu bestimmen. Die daraus ermittelten Dichten stimmen für beide Planeten am ehesten mit einer $MgSiO_3$ dominierten Zusammensetzung überein. Aufgrund ihrer kurzen Umlaufzeiten und daher hohen Gleichgewichtstemperatur eignen sich beide Planeten zudem besonders gut für die zukünftige Untersuchung ihrer Atmosphären mittels Transitspektroskopie.

Abstract

The technical progress of the last decades has enabled us to study ever smaller planets with increasing precision. The characterisation of Earth-sized planets is particularly exciting, since they can provide important insights into the formation and development of our own Earth. M-dwarf stars are especially suited to search for Earth-sized planets with the radial velocity (RV) and transit method, because the planetary signals are more pronounced for these stars due to their larger planet-to-star mass and radius ratios. In my dissertation, I deal with the CARMENES spectrograph, which was constructed exactly for this purpose. The first part is an error budget for the visual channel of the spectrograph, in which I investigate what comprises the uncertainty of the measured RVs and what the technical limits of the instrument are. In the second part of the thesis, I present the discovery of two Earth-sized planets using CARMENES observations. The two short-period, Earth-sized planets GJ 3473 b and GJ 3929 b orbit M-dwarf stars and were initially identified as transiting planet candidates by the TESS survey satellite. Our follow-up observations using the RV method confirmed their planetary nature and revealed in the case of GJ 3473 another non-transiting, temperate planet with sub-Neptune mass, GJ 3473 c. Joint modelling of the transit and RV data made it possible to determine precise masses and radii for the two transiting planets. The densities determined from this are most consistent with a $MgSiO_3$ composition for both planets. Due to their short orbital periods and therefore high equilibrium temperatures, both are particularly well suited for future atmospheric characterisation using transit spectroscopy.

Preface / Vorwort

Es gibt nur wenige Momente in meinem Leben, die mich so geprägt haben, wie dieser eine Abend im Oktober 2007. Wir waren damals auf einer Klassenfahrt und mein Freund Nils hatte ein neues Hobby: Sterne-Gucken. Er fand das so toll, dass er seine Begeisterung mit möglichst vielen in seinem Umfeld teilen wollte. So kam es, dass wir in einer leicht nebligen Nacht am Ostseestrand mit einem Feldstecher in der Hand standen und Nils meinte: "Guck! Da! Du gehst von diesem hellen Stern die zwei etwas dunkleren Sterne nach oben. Und oben drüber ist ein nebliger Fleck. Das ist unsere Nachbargalaxie, die Andromeda." Unter dunklem Hunsrück-Himmel aufgewachsen, fand ich es schon immer toll den Sternenhimmel anzuschauen, aber ich hatte mich vorher noch nie tiefer damit beschäftigt. Was Nils mir da erzählte, von großen Sternhaufen (natürlich haben wir auch die Plejaden in dieser Nacht geschaut) und noch viel größeren Galaxien, das begeisterte mich sofort. Umso mehr, da das alles in meinem Garten darauf wartete entdeckt zu werden. Wenn er mir erzählte, dass das Licht, dass ich von der hinteren Kante der Andromeda sehe, fast hunderttausend Jahre älter ist als das der vorderen, dann klang das für mich wie Science-Fiction, und doch konnte ich es mit meinen eigenen Augen sehen (na ja, zumindest mit einem Auge, da ich eine meiner Kontaktlinsen verloren hatte – aber das ist eine andere Geschichte).

Auf jeden Fall war es so um mich geschehen und nach einigen gemeinsamen Beobachtungsnächten mit Nils bekam ich mein erstes eigenes Teleskop. Einen 6-Zoll Newton, für den mir mein Vater nach der Art von John Dobson eine eigene Rockerbox gebaut hatte. Aber auch darüber hinaus haben mich meine Eltern bei meinem neuentdeckten Interesse für die Astronomie unterstützt. Meine Neugierde auf die Wissenschaft hinter meinen Beobachtungen wurde zum Beispiel durch ein Abonnement der Zeitschrift Sterne & Weltraum weiter entfacht. Und so kam es auch, dass ich mich im Jahr 2010 für das in der Oberstufe vorgeschriebene Berufspraktikum an verschiedene astronomischen Instituten wendete. Bei Prof. Dr. Chini durfte ich dann den Wissenschaftler*innen vom Astronomischen Institut der Ruhr-Universität in Bochum bei ihrer täglichen Arbeit über die Schulter schauen und besuchte zum ersten Mal eine Vorlesung zum Thema Extrasolare Planeten. Das Thema hatte mich gleich gefesselt und ich schrieb infolgedessen meine Facharbeit im Fach Physik über die "Entdeckungsmethoden zum Nachweis von Exoplaneten". Wahrscheinlich wurde mir dabei klar: Ich möchte Wissenschaftler werden und mehr über diese fremden Welten lernen. Vor allem aber möchte ich auch selbst irgendwann einen neuen Planeten entdecken.

Meinen Weg nach Heidelberg habe ich dank meiner damaligen (genauso Astronomie-begeisterten) Freundin, und heutigen Verlobten, Isabel gefunden, die dort ein Jahr vorher mit ihrem Biologiestudium begonnen hatte. Im Studium konzentrierte ich mich dann ganz auf die Astronomie und durfte in meiner Bachelorarbeit auch zum ersten Mal zum Thema Exoplaneten forschen. Was mich bis heute besonders fasziniert, ist die rasante Entwicklung dieses Forschungsfeldes. Ich habe nachgeschaut, in der Einleitung zu meiner Facharbeit im Jahr 2010 schrieb ich von ungefähr 450 bekannten Exoplaneten. Als ich 2015 meine Bachelorarbeit verfasst habe, waren es dann schon über 1900 Planeten, und drei Jahre später zum Zeitpunkt des Abschlusses meiner Masterarbeit über 3800. Heute kennen wir über 4500 bekannte Planeten außerhalb unseres Sonnensystems und mein Traum ist in Erfüllung gegangen, denn bei ein paar davon gehöre ich zu den Entdecker*innen.

Ich möchte allen, die mich auf meinem Weg hierhin begleitet haben, Danke sagen. Vor allem meinen Eltern, die mich von Beginn an bedingungslos unterstützt haben, und denen ich diese Arbeit widme, und Isabel, ohne deren Rückhalt ich niemals so weit gekommen wäre, sowie natürlich Nils für den Anstoß.

And at this point I would like to switch to English and also say thank you to all the great people that I met during my studies at the university. First of all, I would like to thank my supervisor, Prof. Dr. Andreas Quirrenbach who always supported me with his advice and dedication. I greatly appreciate how he taught me to do the "detectives work" that is needed to fully understand a scientific problem. The working atmosphere that he, together with PD. Sabine Reffert, created in the exoplanet group of the Landessternwarte, has largely contributed to my success and ensured that I felt very comfortable during my time at the Königstuhl. Since Sabine is also my second supervisor, I would also like to thank Sabine for her always valuable feedback to my work. Especially thanks to her ability not to just accept things as they are, but to always ask the right questions. The third supervisor of my thesis was Dr. Markus Feldt, who already supervised me during my Master Thesis at the MPIA. I want to thank him again for the opportunity that he gave me back then and now also for being an unbiased and independent "supervisory body" to keep me on track for the thesis.

Of course, a big thank you also to Prof. Dr. Joachim Wambsganß for being the second referee of my thesis, as well as his inspiring lecture on exoplanets in the winter semester of 2015/16. Furthermore, I would like to thank Prof. Björn Malte Schäfer, who is going to be the fourth examiner of the final oral examination.

This brings me to all my great colleagues at the Landessternwarte, or generally on top of the Königstuhl. Because of the pandemic, we spent much less time together than I would have expected, but still I owe you a lot. Stephan, thank you so much for all the hours of discussion, which significantly shaped my understanding of science. Adrian,

thank you so much for all your knowledge and skills that you shared with me. Without your help, especially at the beginning, I would not have come this far. Diana, thank you so much for all your advice and also for pushing me to always do my best.

Of course, I would also like to thank all my other colleagues from our group, the Nord-Institut, the CARMENES consortium and any other office mates that I had over all the years: special thanks to Florian, Ingo, Paz, and Emily for the great atmosphere in our building; Katja Stock for our great time studying together; José A. Caballero for his editing skills; Trifon Trifonov, Martin Schlecker, Martin Kürster, Silvia Sabotta, Sepideh Sadegi, Nestor Espinoza, Enric Pallé, Rafael Luque and many more for their feedback on my work during our meetings.

Contents

Introduction 1

> *Sherlock Holmes and Dr. Watson were going camping.*
> *They pitched their tent under the stars and went to sleep.*
> *Sometime in the middle of the night Holmes woke*
> *Watson up and said: "Watson, look up at the stars, and*
> *tell me what you see."*
> *Watson replied: "I see millions and millions of stars."*
> *Holmes said: "and what do you deduce from that?"*
> *Watson replied: "Well, if there are millions of stars, and*
> *if even a few of those have planets, it's quite likely there*
> *are some planets like Earth out there. And if there are a*
> *few planets like Earth out there, there might also be life."*
> *And Holmes said: "Watson, you idiot, it means that*
> *somebody stole our tent."*

> — **Unknown author**

1.1 Planets around M dwarfs

The detection of exoplanets is flourishing, bringing the number of known planets outside our Solar System to an impressive 4500[1] and counting. In-depth characterisation of the planetary systems and the determination of precise planetary parameters are key to better understand their nature and compare them to those that we are familiar with.

1.1.1 Host stars

How well we can understand planets is, however, limited and dependent on our knowledge of their host stars. Therefore, we will first have a look at M-type dwarf stars (abbreviated M dwarfs hereafter) as exoplanet hosts, before we dive into the planets themselves.

Within our CARMENES project (see section 1.5; Quirrenbach et al., 2014, 2016, 2018, 2020), we build upon a series of studies that are exploring the properties of our target stars (Alonso-Floriano et al., 2015; Cortés-Contreras et al., 2017; Jeffers et al.,

---

[1]On 6 October 2021, 4525 confirmed planets were listed on the NASA exoplanet archive

2018; Passegger et al., 2018, 2019, 2020a; Díez Alonso et al., 2019; Shulyak et al., 2019; Schweitzer et al., 2019; Cifuentes et al., 2020). Based on this series and other complementary literature, I will in the following summarise the properties of M dwarfs that are relevant in the context of the search for planets with the radial velocity (RV) and transit method (introduced in section 1.2 and section 1.3).

Fundamental properties

M dwarfs are much smaller and less massive than the Sun. Theoretical models fitted to the high-resolution spectra from CARMENES yield typical effective temperatures of $\sim2300\,\mathrm{K}$ for the late-type M9.5 V stars up to $\sim3900\,\mathrm{K}$ for the early-type M0.0 V stars (Passegger et al., 2018, 2019, 2020a). The luminosities, as derived from the integrated spectral energy distribution of multi-passband photometry, are significantly smaller than the Solar luminosity, ranging from $\sim2.4 \times 10^{-4}\,\mathrm{L_\odot}$ for M.9.5 V stars, and increasing to $\sim585 \times 10^{-4}\,\mathrm{L_\odot}$ for M0.0 V stars (Cifuentes et al., 2020). By combining the luminosity with the effective temperature and applying the Stefan-Boltzman law, one can consequently calculate their radii (Schweitzer et al., 2019), which are in the range of $\sim0.01\,\mathrm{R_\odot}$ to $0.6\,\mathrm{R_\odot}$ (Cifuentes et al., 2020). The masses of M dwarfs can be derived on the other hand in a number of ways. For our target stars, Schweitzer et al. (2019) obtained an empirical mass-radius relation from eclipsing binaries that yields masses between $\sim0.08\,\mathrm{M_\odot}$ for the late-type M9.5 V stars up to $\sim0.6\,\mathrm{M_\odot}$ for the early-type M0.0 V dwarfs (Cifuentes et al., 2020).

Due to their low luminosities and temperatures, the so-called habitable zone (HZ) is much closer to M dwarfs compared to other stars. A full discussion on what actually defines the HZ, and if planets around M dwarfs can be habitable at all, is out of scope for this thesis (see Shields et al., 2016, for a review on the topic). Generally, the HZ is nowadays considered as the circumstellar region in which life as we now it from Earth is possible. More precisely, this means that liquid water could exist on a terrestrial planet with an Earth-like atmosphere (e.g., Kasting et al., 1993; Kopparapu et al., 2013, 2014). Following the models of Kopparapu et al. (2013, 2014), the HZ for M dwarfs can therefore be as close as $\sim0.02\,\mathrm{au}$ for the very late-types and reaches out to about $\sim0.3\,\mathrm{au}$ for the early-types. Concurrently, the short periods following from such small orbits in combination with the small stellar masses and radii make it easier to detect planets around M dwarfs (see also subsection 1.2.1 and subsection 1.3.1) and promotes them as prime targets for the detection and characterisation of potentially habitable low-mass planets.

Following the predictions from the initial mass function of our galaxy, M dwarfs are overall very abundant. Indeed, photometric surveys show that they are the most common stars in our solar neighbourhood (e.g., Chabrier, 2003; Henry et al., 2006; Bochanski

et al., 2010; Winters et al., 2015). They therefore provide a large sample of visually bright stars, that can be studied from Earth.

Implications for planet search

Unfortunately, M dwarfs also have disadvantages with regard to the search for planets.

First, their low temperature shifts the peak of their black body radiation to the red and infrared (IR) wavelength regime. This leads to a dilemma: not only loose common spectrographs, which are operating at optical wavelengths, the bulk of the emitted flux from late M-type dwarfs, but also is the radial velocity content at IR wavelengths heavily impaired by telluric water absorption lines (e.g., Reiners & Basri, 2010; Figueira et al., 2016; Artigau et al., 2018; Reiners et al., 2018a; Reiners & Zechmeister, 2020; Bauer et al., 2020). The sweet spot for observations of most M dwarfs is consequently in the wavelength range of $700\,\mathrm{nm}$ to $900\,\mathrm{nm}$ (Reiners & Zechmeister, 2020). This presents particular demands for high-resolution spectroscopy in this wavelength regime (see also chapter 2).

Second, in contrast to the spectra of higher mass stars, which are dominated by atomic absorption lines, the low atmospheric temperatures of M dwarfs enable the formation of molecules that produce numerous, often blended, absorption features (e.g., Tinney & Reid, 1998; Reiners et al., 2018a). The predominant lines are thereby the TiO and VO bands, which span a large fraction of the visual (VIS) wavelength ranges. In consequence this impairs for example the determination of the stellar parameters due to a poorly defined continuum (e.g., Passegger et al., 2016, 2018, 2020a,b; Marfil et al., 2021). Further, the blended lines pose a challenge in determining the RVs using the classical cross-correlation function (CCF) method (Lafarga et al., 2020; Marfil et al., 2021, and subsection 1.2.3).

Above all, stellar activity represents the biggest challenge, which is why I want to dedicate a separate section to this topic.

Stellar activity

Stellar activity can create astrophysical noise that obscures planetary signals. This includes stellar oscillations, the granulation of the stellar surface and above all stellar magnetic activity features as well as long term magnetic cycles.

M dwarfs hold large convective layers and become even fully convective for stars of types M4.0 or later (e.g., Mullan & MacDonald, 2001; Stahler & Palla, 2004; Baraffe et al., 2015; Winters et al., 2021). For Sun-like stars, convection is linked to the existence of strong magnetic fields due to the dynamo effect (Charbonneau, 2020, and references therein). The details on how those mechanisms can be rendered to fully, or almost fully, convective stars are however still under debate. Nonetheless, measurements from

coronal X-ray emission and chromospheric Hα emission show high levels of magnetic activity for M dwarfs (e.g., Reiners & Basri, 2007; Reiners et al., 2010; Shulyak et al., 2019, and references therein). The level of magnetic activity strongly correlates to their rotational velocity. Younger, and therefore faster rotating, M dwarfs are generally more active (Delfosse et al., 1998; Gizis et al., 2002; Morin et al., 2010; Wright et al., 2011; Reiners et al., 2012; Newton et al., 2017; Jeffers et al., 2018).

Jeffers et al. (2018) used the chromospheric Hα emission to further investigate the correlation between the mass and the level of magnetic activity for a large sample of M-dwarf stars from which the CARMENES target stars originated. They found an increasing fraction of Hα active stars starting from $25\,\%$ for early-type to $50\,\%$ for mid-type and $76\,\%$ for the late-type M dwarfs. A subsample of extremely active stars however resides at the border to the fully convective stars (M3.5–M4.5).

In the first place, this magnetic activity manifests as inhomogeneities in the stellar photosphere in the form of dark spots, bright plagues and flares (e.g., Schrijver & Zwaan, 2000). Measurements of the spot sizes show that they can cover more than $10\,\%$ of the stellar surface (e.g., Strassmeier, 2009; Baroch et al., 2020, and references therein). Since the spots evolve and move with the rotation of the star, one consequence are measurable variations in the stellar brightness over time. For example, Newton et al. (2016) investigated more than 300 nearby, mid-to-late M dwarfs and found semi-amplitudes of the variations of about $0.5\,\%$ to $1\,\%$.

Additionally, the magnetically active regions lead to distortions of the stellar spectral line profiles and therefore affect the determination of the RVs (Hatzes, 1996). Thereby, cool spots and flares have in general the largest impact (e.g., Desort et al., 2007; Barnes et al., 2011, 2015; Lafarga et al., 2020). Interestingly, Lafarga et al. (2021) showed that the amount of RV scatter due to activity, the so-called stellar jitter, follows exactly the opposite trend compared to the magnetic activity measured from chromospheric Hα emission by Jeffers et al. (2018). They found that in many cases, stars from the CARMENES sample with low RV scatter turned out to be low-mass stars. This was interpreted by Lafarga et al. (2021) as evidence for the existence of different forms of activity between late- and early-type M dwarfs (i.e., between partially and fully convective stars). Overall, the majority of the stars in their sample shows jitter below $10\,\mathrm{m\,s^{-1}}$, though the most active stars can reach values above $100\,\mathrm{m\,s^{-1}}$.

This stellar jitter is, however, often not random. Magnetically active regions in combination with the rotation of the stars can lead to periodic RV or brightness modulations. As they rotate in and out of the observers view, the changes in the stellar flux and the spectral line profiles will evolve with the stellar rotation period and thus create quasi-periodic signals (Boisse et al., 2011; Haywood et al., 2014; Rajpaul et al., 2015).

On one side, this allows to photometrically determine the rotation period of M dwarfs (e.g., Kron, 1947; Radick et al., 1987; Hartman et al., 2011). Thereby, the rotation

periods measured for M dwarfs range from the fraction of a day, for the often very young and less massive fast rotators, to more than a hundred days for old and more massive stars. A large part of the stars, however, has rotation periods on the order of a few tens of days (Newton et al., 2016; Suárez Mascareño et al., 2016; Díez Alonso et al., 2019).

On the other side, the quasi-periodic variations in the RV measurements present a significant challenge. Their periods and amplitudes often resemble those of planetary signals, which can make it difficult to distinguish real planetary signals from false positives (e.g., Queloz et al., 2001; Boisse et al., 2011; Rajpaul et al., 2016). In addition, they can interfere with the planetary signals, which can make a thorough modelling of the data necessary in order to determine the most precise planetary parameters (e.g., Haywood et al., 2014; Rajpaul et al., 2015; Stock et al., 2020a,b, and references therein).

To disentangle planetary signals from activity, the temporal behaviour of different activity indicators can be investigated. However, the total number of known indicators is very large, and I would like to refer to Schöfer et al. (2019) or Lafarga et al. (2021) for a discussion of the tracers that were investigated using CARMENES. For the scope of this thesis I just want to summarise the indicators that are the best tracers for the stellar rotation period. There are for example the indicators that depict the influence of the activity on the whole stellar spectrum, like the bisector inverse slope (BIS, Queloz et al. 2001) of the CCF, or the chromatic index (CRX, Zechmeister et al. 2018). Thereby, BIS is the difference between the average velocity of the top and the bottom region of the CCF and CRX describes the slope of the change in the measured RV over the different wavelength orders of the instrument. Further, there are indicators based on the profile or strength of individual activity sensitive lines, like the pseudo-equivalent width (pEW$'$, Schöfer et al. 2019) of the chromospheric Hα line and the Ca II IRT, or the photospheric TiO band indices (Schöfer et al., 2019).

1.1.2 The diversity of planets orbiting M dwarfs

Of the more than 4500 confirmed exoplanets, less than $10\,\%$ are known to orbit M dwarfs[2]. One of the reasons is that the early surveys focused more often on Sun-like stars. However, for the reasons mentioned before, this has changed somewhat in recent years. In Figure 1.1, I show the distribution of known M-dwarf planets in the mass-period and radius-period space, which I will take as an opportunity to talk more about the different types of planets that have been discovered so far.

Even though there is a number of giant planets detected around M dwarfs, like for example GJ 436 b (e.g., Butler et al., 2004; Gillon et al., 2007; Lanotte et al., 2014; Trifonov et al., 2018) or GJ 3512 b (Morales et al., 2019), their overall abundance

---

[2]On 6 October 2021, 4525 confirmed planets were listed on the NASA exoplanet archive — 355 were either specified to orbit M dwarfs or have given temperatures between $2300\,\mathrm{K}$ and $4000\,\mathrm{K}$.
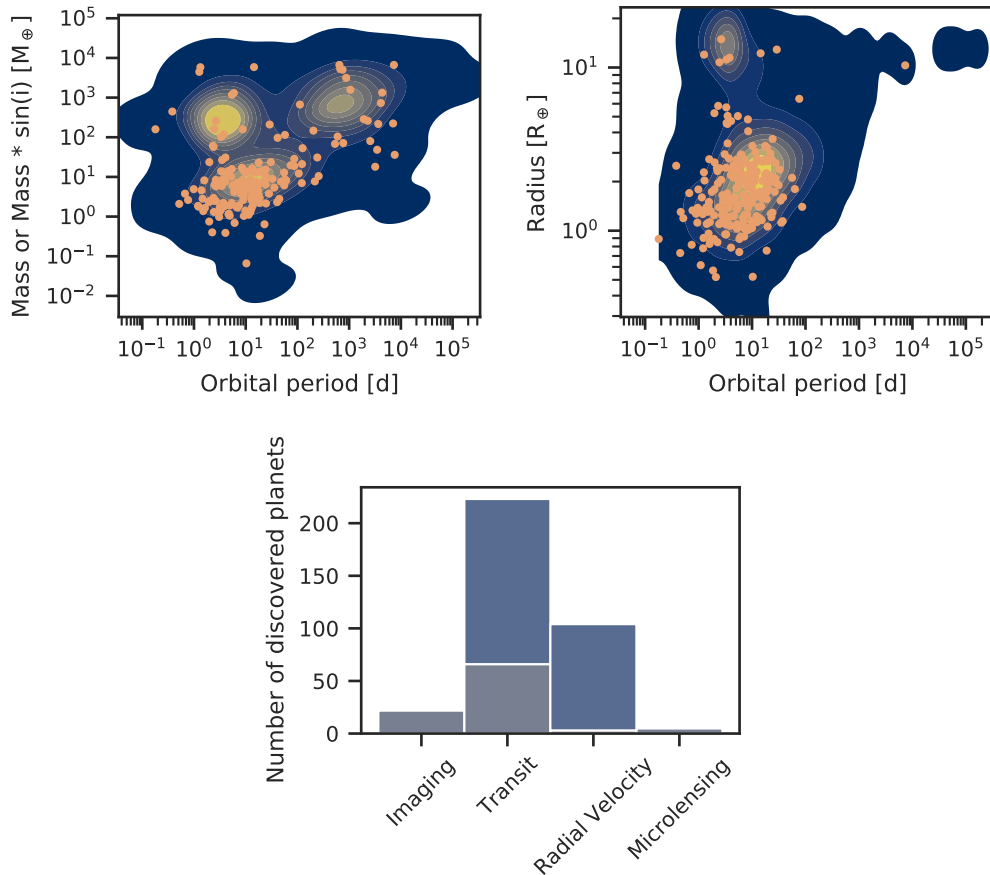
Fig. 1.1.: Properties of the detected M-dwarf planets. *Top panels:* Mass-period (*left*) and radius-period (*right*) distribution of the confirmed exoplanets. The orange dots show the planets around M dwarfs, while the overall distribution of the known planets is depicted by the background shading for comparison. *Bottom panel:* Histogram of the number of detected planets around M dwarfs by their discovery method. A single detection by eclipse timing variations (RR Cae b, Qian et al., 2012) is not included in the histogram. The grey colour denotes the number of planets with mass measurements, which means for transiting planets masses from RVs or transit timing variations (TTVs), or masses for RV planets that where subsequently to the discovery observed to be transiting. Data taken from the planetary systems table of the NASA exoplanet archive (https://exoplanetarchive.ipac.caltech.edu) on 6 October 2021.

is very low. A first analysis of the CARMENES survey by Sabotta et al. (2021) yields an occurrence rate of 0.06 ± 0.04 planets per star for planets with $100\,\mathrm{M_\oplus}$ to $1000\,\mathrm{M_\oplus}$ ($P < 1000\,\mathrm{d}$) compared to 1.32 ± 0.33 planets per star for masses between $1\,\mathrm{M_\oplus}$ and $10\,\mathrm{M_\oplus}$ ($P < 100\,\mathrm{d}$). The majority of M-dwarf planets are therefore of intermediate masses and radii and belong to the class of the sub-Neptunes: the so-called super-Earths and mini-Neptunes (Bonfils et al., 2013; Gaidos et al., 2016; Hsu et al., 2020, and also Figure 1.1).

Interestingly, there are no known planets of those types present in our Solar System. We therefore depend on the characterisation of exoplanets to learn more about their structures and composition. Thereby, their basic nature can be rather diverse. There is for example the hot, rapidly evaporating mini-Neptune GJ 3470 b (e.g., Bonfils et al., 2012; Ehrenreich et al., 2014; Palle et al., 2020), in contrast to the temperate mini-Neptune K2-18 b with a thick H/He atmosphere, in which water vapour was detected (e.g., Montet et al., 2015; Cloutier et al., 2017; Sarkis et al., 2018; Benneke et al., 2019). On the other hand, there are dense and presumably rocky super-Earths, like LHS 1440 b (Dittmann et al., 2017; Lillo-Box et al., 2020) or GJ 357 b (Luque et al., 2019; Jenkins et al., 2019).

To the lower end, the current detection limits constrain the mass and radius distribution (see also section 1.2, section 1.3). Thereby, the smallest known planets reach down to Earth-like rocky planets, as for example the Trappist 1 system (e.g., Gillon et al., 2016, 2017; Luger et al., 2017), or YZ Ceti (Astudillo-Defru et al., 2017b; Robertson, 2018; Stock et al., 2020a). The planet that holds the record for the lowest mass is L 98-59 b, an $M = 0.40\,\mathrm{M_\oplus}$ mass and $R = 0.85\,\mathrm{R_\oplus}$ radius planet that was recently characterised by Demangeon et al. (2021).

1.1.3 Close-in rocky planets

The focus of this thesis is on close-in rocky planets. In the following, I will therefore go into more detail about this particular type of planet. Because we have only recently come to better understand the nature of sub-Neptune planets, the described concepts mostly originate from the universal view of this planetary class, independently of the stellar host mass.

The gap in the radius distribution

At a first glance, the distribution of the Earth-like, super-Earth, and mini-Neptune planets in Figure 1.1 seems rather homogeneous. However, as outlined above, there are huge differences in their basic nature.

Although sub-Neptunian planets were initially believed to be some kind of large Earth-like rocky exoplanets, and thus referred to as super-Earths (Bean et al., 2021), early density assessments gave reason to doubt this as a general assumption (e.g., Barnes et al.,
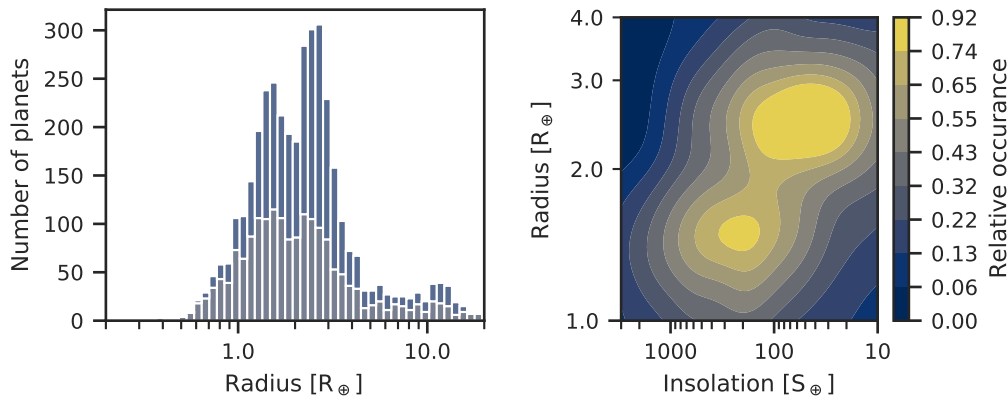
Fig. 1.2.: Radius distribution of the *Kepler* planets. *Left:* Histogram of the planets with radius smaller than $20\,R_\oplus$. Unconfirmed planet candidates are marked in grey. *Right:* Kernel density estimation of the planetary radius as a function of the incident stellar irradiation. Data taken from Berger et al. (2020).

2009; Rogers, 2015). The fact, that there are indeed two distinct groups of planet types was first evident from the refined radius distribution of the *Kepler* (Borucki et al., 2010) exoplanets. The planet's radii show a bimodal distribution with a lack of planets between $1.5\,R_\oplus$ to $2.0\,R_\oplus$ (see Figure 1.2, or for example Fulton et al., 2017; Fulton & Petigura, 2018; Berger et al., 2018, 2020; van Eylen et al., 2018). Follow-up observations of the planets on both side of this "radius valley", or "radius gap", confirms that it marks the transition from the dense super-Earth to the low-density mini-Neptunes (Jontof-Hutter, 2019; Bean et al., 2021, and references therein). Thereby, the actual position of the valley is a function of the orbital periods of the planets, or rather the incident stellar flux (see right panel Figure 1.2, or for example Fulton et al., 2017; van Eylen et al., 2018). This is reinforced by the fact that the position of the gap also varies with the stellar mass, as it moves closer to the star for later spectral types (Cloutier & Menou, 2020; van Eylen et al., 2021). In the subsections below, I will outline the implications of those dependencies and what is currently known about the nature of the sup-Neptune planets.

Are highly irradiated rocky planets stripped cores?

Even though they present a distinct population, current findings suggest that the origin of the close-in, rocky planets is closely linked to the mini-Neptunes.

The bulk densities measured for super-Earths imply that they have a rocky composition, while the low densities of mini-Neptunes are inconsistent with bare rock but suggest a large fraction of volatiles in their envelopes (Jontof-Hutter, 2019; Bean et al., 2021, and references therein).

A currently popular hypothesis suggest that mini-Neptunes are composed of rocky cores holding large H/He atmospheres, which usually make up a few percent of the total mass

(Jontof-Hutter, 2019; Bean et al., 2021, and references therein). Under this assumption, the radius valley and the rocky super-Earth planets originate from atmospheric mass loss of mini-Neptunes. Thereby, the period dependency of the position of the radius valley translates to a dependency on the stellar irradiation incident on the planet (also known as "insolation"). Higher irradiated planets are more prone to losing their atmospheres from heating of the upper layers and thus hydrodynamic outflows similar to a Parker wind (Parker, 1955; Bean et al., 2021, and references therein). There are currently two models discussed in this context that correctly describe the observed gap: First, the photoevaporation model, where high-energy extreme ultraviolet photons from the star are heating the atmosphere (e.g. Owen & Wu, 2013; Lopez & Fortney, 2013; Estrela et al., 2020). Secondly, the core-powered mass-loss model, where IR emission from the planet itself together with the bolometric flux from the star is providing the energy to the atmosphere (e.g. Ginzburg et al., 2018; Gupta & Schlichting, 2019). In reality, as is often the case, both may play a role. However, it is not yet clear, which process is the primary component for the mass loss (Bean et al., 2021). The minute discriminatory features predicted by theoretical models, like different core-mass functions, are still out of reach for the current instruments (Gupta & Schlichting, 2021; Rogers et al., 2021).

Common for both models is that the bare cores should generally have a dry composition to explain the gap, which contradicts the accretion of water outside the snowline as commonly predicted by planet formation models (e.g., Bitsch et al., 2019). Furthermore, a number of recently discovered planets is starting to populate the radius valley (e.g., Bluhm et al., 2020; Stefánsson et al., 2020; Lillo-Box et al., 2020; Cloutier et al., 2021b). The density derived from the mass and radius of those planets indicates that indeed some sub-Neptune planets may contain a large fraction of water as predicted by classical planet formation models (Sotin et al., 2007; Zeng et al., 2019; Haldemann et al., 2020). Therefore, a mixture of planets with large fractions of water and thin H/He atmospheres would also be conceivable to explain the mini-Neptunes. For example, the core-powered mass-loss model is compatible with proportions of up to $20\,\%$ water (Gupta & Schlichting, 2019). Further, Venturini et al. (2020a,b) presented a self-consistent model for planet evolution and photoevaporation that yields pure rocky planets with typical masses below $5\,\mathrm{M_\oplus}$ on the one hand, and water planets with, if at all, thin H/He atmospheres on the other. However, they also emphasize the importance of combining the various possible scenarios into a single framework and thus reconciling the theoretical models with the observations.

Following this, one should also not ignore the fact that the generally accepted theories for the origin of the rocky planets in our Solar System require the formation of bare rocky planets that never possessed H/He atmospheres (e.g., Lopez & Rice, 2018, and references therein). Observational evidence for example show that the Earth has formed after the dissipation of the proto-solar nebula and thus never accreted a large gaseous atmosphere.

Consequently, while the concept of stripped cores may describe the population of highly irradiated planets very well, there are likely multiple pathways that lead to the formation of rocky planets (e.g., Lopez & Rice, 2018, and references therein). The in-depth characterisation of Earth-sized planets is therefore important to better understand their formation and evolution, and thus also the history of our own Earth.

Formation of close-in sub-Neptunes

I described in the previous section how atmospheric mass loss of mini-Neptunes can form rocky super-Earth planets. However, one question remains: how do those actually form so close-in to their host stars? Currently, there are two favoured core accretion models to answer this. The main difference between the models is when and where the bulk of the material is accreted to form the planets (Bean et al., 2021). In the migration model, large planetary cores form preferentially outside the snow line and move inwards due to exchange of angular momentum with the gas in the disk. In the drift model, the building blocks of the planets, the pebbles, themselves undergo this migration (e.g., Johansen & Lambrechts, 2017, and references therein). While the accreted gaseous envelopes are similar, the two models predict different compositions for the rocky cores that can be observationally tested. The cores that formed further out, as supposed by the migration model, are expected to have larger water contents than the cores that formed from dry pebbles that previously crossed the water ice line as in the drift model (e.g., Bitsch et al., 2019; Izidoro et al., 2019).

Both models have in common, that some mechanism is needed to prevent the cores of the mini-Neptunes from undergoing runaway gas accretion and becoming giant planets. Currently, several solutions are proposed. Much attention is for example given to a rapid dissipation of the disk due to photoevaporation that effectively stops the accretion before runaway growth (e.g., Ginzburg et al., 2016; Owen & Wu, 2016; Ogihara et al., 2020), or giant impacts of the growing planets that remove the primordial envelopes and allow only the accretion of thin atmospheres before the disk is cleared (Inamdar & Schlichting, 2015; Dawson et al., 2016, and references therein). One piece of the puzzle constitute in this case the observed super-Earth. If they are in fact the stripped cores of mini-Neptunes, then the maximum mass that we observe for them is a proxy for the core mass limit of mini-Neptunes after which runaway gas accretion is taking place (Dai et al., 2019).

Composition

Combining the radii from transit measurements with masses from RVs or transit timing variations (TTVs) yields the bulk density of a planet. As mentioned earlier, density measurements of super-Earths suggest that they are rather devoid of volatiles, however, what do we actually know about their interior composition? The best proxy for the

interior of rocky planets is logically our own Earth. Most popular today are the empirical two-layer mass-radius relations derived from Earth's seismic model by Zeng et al. (2016, 2019) that can be compared to the bulk density measurements of exoplanets.

On this basis, Dai et al. (2019) performed a homogeneous analysis of 11 super-Earth on ultra-short-period (USP) orbits that is of particular interest. The high temperatures of those planets rule out the presence of any substantial atmospheres and therefore the degeneracy of the radius with the volatile content (a usual shortcoming of the mass-radius relation). Their main result is, that most of the planets are consistent with only a low scatter around an Earth-like composition of 35% iron and 65% silicate rock, which hints to a universal composition of those.

However, the outliers in the Dai et al. sample are also very interesting. K2-141b (Malavolta et al., 2018; Barragán et al., 2018) and K2-229b (Santerne et al., 2018) show a high fraction of iron, similar to Mercury in our own Solar System. It may thus be concluded that the aforementioned giant collisions in fact play a role in the formation of super-Earth planets. Contrary, 55 Cnc e (e.g., McArthur et al., 2004; Winn et al., 2011; Bourrier et al., 2018), has a density that is lower than can be explained by bare rock. This hints at a significant amount of water on the planet, which would be consistent with the migration scenario as described before (e.g., Dorn et al., 2017). Although, it could be possible, that the popular two-layer model does not hold universally to super-Earth. A complete core-less class of planets, rich of Ca and Al minerals, can explain the properties of 55 Cnc e equally well (Dorn et al., 2019).

Additional constraints on the volatile content of the super-Earths actually come from the radius valley that we observe. Planets with higher core mass are able to hold larger atmospheres without loosing them due to evaporation. Though, a higher content of volatiles would increase the planetary radius for a constant mass. The position of the valley is therefore a proxy for the density of the lowest mass cores, that are not getting stripped (Bean et al., 2021). In this way, Owen & Wu (2017) excluded water-rich cores and moreover also showed that an overall Earth-like composition fits the observed radius distribution well.

Atmospheres

Further progress in the characterisation of super-Earth is anticipated from atmospheric investigations. The comparison of measured atmospheres with theoretical models can for example help to break the degeneracies with the volatile content (e.g., Miller-Ricci et al., 2009). Currently, the most used techniques are the transmission and emission spectroscopy, which are suitable to observe the atmospheres of transiting exoplanets (Madhusudhan, 2019, and references therein). In transmission spectroscopy, the changes of the planetary radius at different wavelengths during the primary eclipse serve as a

proxy for the opacity of the planets' atmosphere with respect to the stellar light. For thermal emission spectroscopy, the light emitted from the planetary disk is measured by the changes of the stellar brightness the during secondary eclipse (see section 1.3 for a distinction of the primary and secondary eclipses).

Even the obvious prototypes, Mercury, Venus, Earth and Mars, already show the variety of atmospheres that are possible for rocky planets. Therefore, I want to point out only the characteristics that are implied by the formation scenarios of rocky planets as described above. In the first place, we would expect no prominent spectral features for bare rocky planets without any substantial atmospheres. And indeed, the transmission spectra of close-in, and likely rocky, planets that have been investigated so far are essentially "flat" (e.g., de Wit et al., 2016, 2018; Diamond-Lowe et al., 2018, 2020). However, while this rules out large cloudless H/He atmospheres, such featureless spectra can be also a consequence of absorbing aerosol layers or clouds at high atmospheric altitudes. Therefore, they do not exclude the presence of significant atmospheres with a high mean molecurlar weight. (Bean et al., 2021).

A prime candidate for such an atmosphere is the already mentioned USP 55 Cnc e, since its bulk density suggests a volatile rich atmosphere even though its high insolation rules out the presence of any primordial H/He. However, a detection of an HCN containing atmosphere by Tsiaras et al. (2016) remains controversial (Bean et al., 2021, and references therein).

Another interesting Earth-sized planet, which is claimed to possess an atmosphere, is GJ 1132 b (Morley et al., 2017). Recently, Swain et al. (2021) reported the detection of an atmosphere for GJ 1132 b based on IR features of HCN and CH_4 in a transmission spectrum. As the origin of this atmosphere, Swain et al. (2021) proposed outgassing of primordial hydrogen from the mantle that was initially dissolved in the magma ocean during the formation (e.g., Lustig-Yaeger et al., 2019a; Kite & Barnett, 2020, and references therein). However, similar analyses by Mugnai et al. (2021) and Libby-Roberts et al. (2021) were not able to confirm those spectral features and thus also disproved this discovery. This makes GJ 1132 b another rocky planet where only a flat transmission spectrum could be detected. Future observations maybe can tell whether if possesses a cloudy H/He atmosphere or a heavily enriched secondary atmosphere (Mugnai et al., 2021; Libby-Roberts et al., 2021). GJ 1132 b therefore remains an exciting target for observations with the upcoming generation of instruments.

1.2 The radial velocity method

The detection of planets using the RV method plays a central role in this thesis. With this section I aim to provide some background to the method and with respect to the error budget in chapter 2 highlight some technical aspects that are important in this context.

1.2.1 Basic idea

Newton's third law of action and reaction tells us, that if a planet orbits its host star, the star also needs to orbit the planet — or to be more precise, both orbit their common centre of mass (the barycentre). The component of the stellar motion along our line of sight, the radial velocity (RV), can thereby be measured from the Doppler shift of the stellar spectral lines (relativistic effects can be neglected in this context):

$$\frac{\Delta\lambda}{\lambda} = \pm\frac{v_{\rm r}}{c},$$ (1.1)

where: λ = wavelength

       $\Delta\lambda$ = wavelength shift

       $v_{\rm r}$ = radial velocity

       c = speed of light.

By this means, recurring changes of the stellar RV, can thus indirectly infer the presence of a planetary companion. The period, P, of those follows from equating the exerted centripetal force about the barycentre with the gravitational force between the star and planet, which corresponds to Kepler's third law fitted to the total mass of the system:

$$P^2 = 4\pi^2 \frac{(a_\star + a_{\rm p})^3}{G(M_\star + M_{\rm p})}$$ (1.2)

where: P = orbital period

       G = gravitational constant

       $a_\star$ = stellar semi-major axis

       $a_{\rm p}$ = planet semi-major axis

       $M_\star$ = stellar mass

       $M_{\rm p}$ = planetary mass.

Taking into account the inclination with respect to the reference plane (see Figure 1.3), the RV corresponds in its turning points to the orbital velocity of the star. The RV semi-amplitude, K, of a circular orbit can therefore be written as $K \equiv \frac{2\pi}{P}a_\star \sin i$. Together
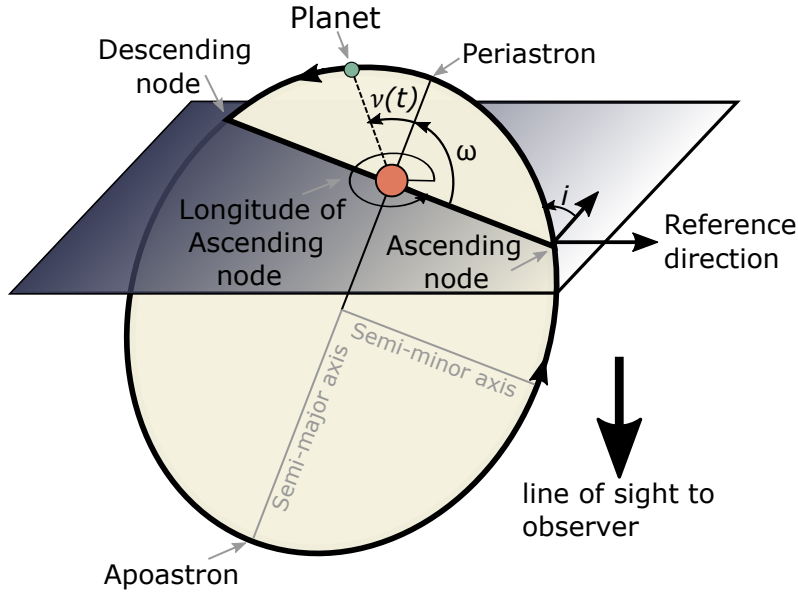
Fig. 1.3.: Projection of a Keplerian orbit into three dimensions. The position of the planet is described by the true anomaly, $\nu(t)$, which is the angle between the direction of the periastron and the connecting line to the barycentre. After Perryman (2011).

with the expression for the centre of mass from the star $a_\star = \frac{(a_\star + a_p)M_p}{M_\star + M_p}$ this can be used to bring Equation 1.2 into the form:

$$f = \frac{M_p^3 \sin i^3}{(M_\star + M_p)^2} = \frac{K^3 P}{2\pi G},$$ (1.3)

which is the so-called mass function for circular orbits (e.g. Perryman, 2011; Wright, 2018). In the case of Keplerian orbits, the expression on the right-hand side expands by the factor $(1 - e^2)^{3/2}$, which considers the eccentricity of the planetary orbit.

For practical purposes, we can formulate the mass function in more common units:

$$\left(\frac{K}{\mathrm{m\,s^{-1}}}\right) \approx 0.6395 \left(\frac{P}{\mathrm{days}}\right)^{-1/3} * \frac{(M_p/M_\oplus) \sin i}{\left((M_\star/M_\odot) + 3 \times 10^{-6}(M_p/M_\oplus)\right)^{2/3}} * \frac{1}{\sqrt{1 - e^2}}$$ (1.4)

Essentially, RV measurements tell us the mass ratio between the two orbiting bodies ($K \propto M_p/M_\star^{2/3}$). Consequently, it is apparent that the RV method is biased towards higher planetary masses for a given stellar mass, since they produce higher RV variations and, likewise, observing lower mass stars enables to detect lower mass planets. Additionally, the amplitude scales with $P^{-1/3}$, which favours the detection of close-in planets. Ideal targets are therefore close-in, high-mass planets orbiting low-mass stars.

1.2.2 Observables and derived parameters

The period and the RV semi-amplitude are the two obvious observables, yet, the shape of the RV contains more information on the Keplerian orbit of the planet. Though it must be kept in mind, that the RV curve actually only gives information on the tangential plane of the orbit. Hence, besides the two already identified observables, there are three more orbital parameters that can be determined.

First, there is the aforementioned eccentricity, which, together with the argument of periastron and semi-major axis, defines the shape and size of the orbit. For zero eccentricity, the resulting RV curve is purely sinusoidal, but adapts a more saw-tooth like shape with increasing eccentric orbits. For such eccentric Keplerian orbits, the argument of periastron, ω (see Figure 1.3) is reflected by the skewness of the RV curve. It specifies the angle between the periastron and the ascending node, i.e., the node where the planet moves through the reference plane and away from the observer. Further, it defines the periastron time, which is the reference time for which the planet passes the periastron (see Figure 1.3). The periastron time comprises the phase information and anchors the orbit in time. For circular orbits, the periastron is undefined. In this case, one chooses conventions like $\omega = 0°$ or $180°$ to specify to which point in the orbit the periastron time refers.

From the two-dimensional projection follows also a major drawback of the RV method: the longitude of the ascending node and inclination of the system remain unknown, so that the actual orientation of the system on the celestial plane cannot be determined. The unknown inclination is thereby a particular obstacle because it is degenerate with the mass of the planet in the mass function ($K \propto M \sin i$, Equation 1.3). RVs alone therefore only allow to determine a minimum planetary mass.

To do so, the stellar mass is an additionally needed input for Equation 1.4. For M dwarfs, it is usually indirectly derived from theoretical or empirical models like the mass-radius relation used for the CARMENES survey (Schweitzer et al., 2019), but in rare cases the orbital dynamics of binary stars can yield precise direct measurements (e.g. Andersen, 1991; Quirrenbach, 2001; Torres et al., 2010). With known stellar mass, the orbital semi-major axis of the orbit can be further calculated using Kepler's third law (Equation 1.2). From the distance to the host star follow then the planetary insolation, S, and equilibrium temperature, T_{eq}, given the temperature or luminosity of the star (e.g. Perryman, 2011).

1.2.3 Practical application

Retrieving RV measurements

As mentioned above, the RV method aims at measuring the Doppler shift of absorption lines in the stellar spectrum caused by motion of the star around the common barycentre. Commonly used nowadays are cross-dispersed Échelle spectrographs for this purpose because of their high resolution and, at the same time, large wavelength range (e.g. Baranne et al., 1996; Mayor et al., 2003; Pepe et al., 2010; Quirrenbach et al., 2014; Seifahrt et al., 2018; Kotani et al., 2018).

Typical resolutions, $R = \lambda/\Delta\lambda$, of spectrographs providing RVs that are precise enough for the detection of exoplanets are about $50\,000$ to $200\,000$. This means that even for the highest resolving instruments, a single resolution element, $\Delta\lambda$, comprises more than $1\,\mathrm{km\,s^{-1}}$ in velocity space. In contrast, following Equation 1.4, the RV signal of a typical super-Earth orbiting a mid M dwarf ($M_\mathrm{p} = 3\,\mathrm{M_\oplus}$, $P = 15\,\mathrm{d}$, $M_\star = 0.3\,\mathrm{M_\odot}$) is less than $2\,\mathrm{m\,s^{-1}}$. Such a precision can therefore only be achieved by observing numerous spectral lines at once in a spectral range that is as wide as possible. Two widely used approaches to measure the Doppler shift are either the cross-correlation with binary masks, short CCF, (Queloz, 1995; Pepe et al., 2002; Lafarga et al., 2020) or least-square fitting of stellar spectrum templates (Anglada-Escudé & Butler, 2012; Astudillo-Defru et al., 2015; Zechmeister et al., 2018). Before that, however, a careful calibration of the spectra themselves is necessary – where the wavelength calibration is one of the crucial steps.

The gas cell technique was a breakthrough in providing a stable reference frame for the observed spectrum (Campbell & Walker, 1979; Marcy & Butler, 1992)[3]. Thereby, an absorbing gas is put into the light path before the spectrograph. The resulting additionally imprinted absorption lines will undergo the same instrumental distortions and shifts as the observed science spectrum. Consequently, they can be used as a fixed reference for the changes of the stellar lines over time. Disadvantages are however the unequal sampling of the reference lines and the inevitable affects on the measured spectrum, like a $20\,\%$ to $30\,\%$ loss of light (Perryman, 2011).

The simultaneous reference technique circumvented the light loss by simply using two independent inputs that are imaged separately on the detector (Baranne et al., 1979, 1996). Emission spectra of hollow-cathode lamps (HCLs) were used in the beginning for this purpose, however, they also suffer from an unequal sampling.

An essential step towards a higher precision was therefore the development of laser frequency combs (LFC, e.g., Murphy et al., 2007; Li et al., 2008; Steinmetz et al., 2008; Wilken et al., 2012) and Fabry-Pérot (FP) interferometers (e.g., Wildi et al., 2010; Reiners

---

[3]While I acknowledge the important contribution of the manuscript by Marcy & Butler (1992) to the field of searching for exoplanets with the RV method, I also acknowledge the harm that G. W. Marcy has done to the scientific community and take a firm stand against sexual harassment or discrimination.

et al., 2014; Bauer et al., 2015; Schwab et al., 2015) for the use as a calibration source. Both provide a dense grid of equally distributed and bright reference lines that are stable to a very high precision, but come with different strengths and weaknesses. FPs are easy to operate and cheap to obtain, however the absolute wavelengths of the lines are unknown, which makes it necessary to calibrate them against an external source (usually HCLs). The frequencies of the LFC lines on the other hand are known to a very high precision and do not need external calibration. However, LFCs are expensive and only operate at a narrower wavelength range (Fischer et al., 2016). The uncertainty that can be reached for both techniques is below $10\,\mathrm{cm\,s^{-1}}$ and therefore well suited for the use with the current generation of spectrographs (Schwab et al., 2015).

How the total error of an RV instrument is composed, will be shown in chapter 2 for the CARMENES visual spectropgraph arm (CARMENES-VIS). In general, the precision of the current state-of-the-art spectrographs is about $0.5\,\mathrm{m\,s^{-1}}$ to $1\,\mathrm{m\,s^{-1}}$ in the VIS, for example ESPRESSO (Pepe et al., 2014, 2021); HARPS (Mayor et al., 2003); or the CARMENES-VIS, and about $0.7\,\mathrm{m\,s^{-1}}$ to $4\,\mathrm{m\,s^{-1}}$ in the IR, for example MAROON-X (Seifahrt et al., 2016, 2018); IRD (Tamura et al., 2012; Kotani et al., 2018); or the CARMENES near-infrared (NIR) spectropgraph arm (CARMENES-NIR).

Interpreting RV measurements

Before the RV measurements that are "coming out of the spectrograph" are suitable for the search of exoplanets, some further corrections are still necessary. First, one must bear in mind that the Earth itself is not a perfect rest frame, but imposes its own motion onto the measured velocities (Wright & Eastman, 2014). The revolution around the barycentre of the Solar System and the rotation of the Earth can easily add up to velocities on the order of several tens of $\mathrm{km\,s^{-1}}$. On top come the precession, nutation and polar motion of the Earth. Furthermore, for objects that are close and have high proper motion, the shifts in the RV due to the changing projection geometry (secular acceleration) has to be considered. Additionally, even though they only play a minor role for measurements on the order of $\mathrm{m\,s^{-1}}$-RVs, relativistic effects like the gravitational time dilation due to the masses in the Solar System and Shapiro delay are routinely corrected for nowadays (Kanodia & Wright, 2018a). Finally, we are not interested in the absolute velocity of the stars, but rather the changes over time. It is therefore convenient to subtract the median velocity from the RVs, so that they are centred around a mean velocity of zero.

The movement of the Earth also leads to different light travel times, so it makes sense to calibrate the time stamps using a unique reference. The standard nowadays is the barycentric Julian date (BJD), which is anchored to the barycentre of the solar system.

Periodograms, like the widely used generalised Lomb-Scargle periodogram (GLS, Zechmeister & Kürster 2009, 2018), can be used to search for periodic signals in the

RV data (see for example subsection 3.4.4, or subsection 4.4.5). However, one must be careful because significant signals in the periodogram do not necessarily have a planetary origin. For example, as explained in subsubsection 1.1.1, stellar activity can produce quasi-periodic signals that can mimic planetary signals. But there are also signals of non-physical origin appearing in a periodogram. Aliases, caused by the discrete sampling of the data, can be undistinguishable from the true underlying signals (e.g. Dawson & Fabrycky, 2010; VanderPlas, 2018; Stock et al., 2020a, and references therein). Or, uncorrected telluric lines in the spectrum can impose signals onto the spectra with periodicities close to one year or its harmonics. A thorough investigation of the present signals is therefore crucial for the understanding of the data at hand. For example, the activity indicators already mentioned in subsubsection 1.1.1 help to detect stellar signals, or in the case of aliasing the `AliasFinder` (Stock et al., 2020a; Stock & Kemmer, 2020) can be used to figure out the true underlying signal.

After identifying the signals that are present in the data, the modelling of the RVs can be performed (see for example subsection 3.4.4, or subsection 4.4.5). In most cases, a non-dynamic model is sufficient, which means the RVs can be considered as the sum of individual Keplerian signals (e.g. Perryman, 2011; Fulton et al., 2018). Added to this are instrumental offsets and jitter terms to account for the instrumental factors and stellar jitter (subsection 1.1.1). Stellar activity signals caused by spots or magnetic cycles are, however, generally of a quasi periodic nature and can therefore only be approximately modelled by static model components. It has therefore nowadays become standard to model activity by non-deterministic Gaussian processes (GPs) implemented as a red-noise component (Espinoza et al., 2019a; Dan Foreman-Mackey et al., 2021; Günther & Daylan, 2021). Bayesian inference methods, like the Markov chain Monte Carlo (e.g. Metropolis et al., 1953; Hastings, 1970) method or nested sampling (Skilling, 2004, 2006), are usually used to finally perform the fits to the data.

1.3 The transit method

In this section I will provide a basic overview on the transit method. Thereby, the technical background only plays a subordinate role compared to the RV method, since the results presented in this thesis are largely based on preprocessed data provided by members of the TESS Follow-Up Observing Program (TFOP).

1.3.1 Basic idea

If the plane of a planetary orbit and the line-of-sight between the Earth and its host star align, the planet will block out part of the stellar light once in every orbit when it passes in front of the stellar disk. This primary eclipse, or more common transit, is often

followed by an occultation of the planet by the star, the secondary eclipse, when the planet moves behind the stellar disk (Figure 1.4). The analysis of the planetary systems presented in this paper is limited to the transits, which I will therefore discuss in more detail below.

The difference in brightness of the star during the transit is directly related to the ratio between the stellar and planetary radius if we assume that the planets night side is by comparison completely dark (Seager & Mallén-Ornelas, 2003; Winn, 2010):

$$\Delta F = \frac{F_{\text{no transit}} - F_{\text{transit}}}{F_{\text{no transit}}} = \frac{\pi R_\star^2 I_\star - (\pi R_\star^2 I_\star - \pi R_p^2 I_\star)}{\pi R_\star^2 I_\star} = \left(\frac{R_p}{R_\star}\right)^2 \equiv p^2, \qquad (1.5)$$

where: ΔF = stellar flux difference or transit depth

F = stellar flux

$R_\star$ = stellar radius

R_p = planetary radius

$I_\star$ = stellar light intensity

p = planet-to-star radius ratio.

For practical purposes, the transit depth can be given in terms of parts per million (ppm) as:

$$\left(\frac{p^2}{\text{ppm}}\right) \approx 83.86 \left(\frac{R_p}{R_\oplus}\right)^2 \left(\frac{R_\star}{R_\odot}\right)^{-2} \qquad (1.6)$$

Following the description above, the detection of periodically reappearing transit events can indirectly hint at the presence of a planet orbiting a star. Future transit events can be predicted using the transit ephemeris:
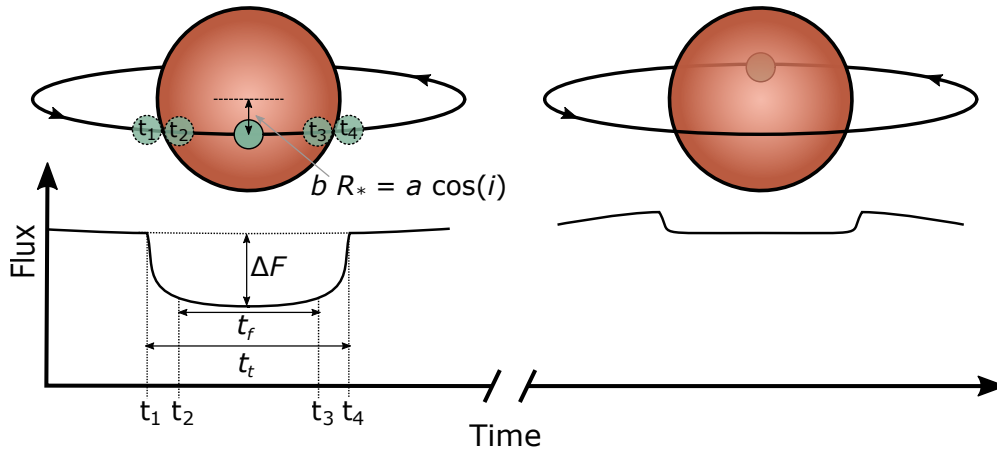
$$t_E = t_0 + E \times P \qquad (1.7)$$

where: t_E = time of transit centre at epoch E

t_0 = time of transit centre at epoch 0

E = Epoch with respect to t_0

P = orbital period.

The conditions for which a planet is actually transiting follow from the geometry of the planetary shadow. For example, for full transits to occur the inclination must hold $\cos(i_{\min}) = R_*/a_p$ (Perryman, 2011), which is only a rather narrow window. Under

Fig. 1.4.: Illustration of primary and secondary eclipse light curves. *Left:* Transit, or primary eclipse, of a planet in front of a star. Four time points characterise the light curve: t_1 is the time of first contact of the planet with the stellar disk; t_2 denotes when the planet's disk is fully in front of the star; t_3 is the second contact of the planet with the stellar limb; and finally t_4 is the last contact between the planet and stellar disk. The time between t_1 and t_4 is called the transit time, while the time between t_2 and t_3 denotes the time of full transit. *Right:* If the geometry of the system aligns, a secondary eclipse accompanies the transit during which the star occults the planet. Since the total flux of the system is the sum of the stellar emission and the reflected light from the planet's day side, the secondary eclipse is also visible as a dip in the light curve. After Perryman (2011); Winn (2010).

the assumption of uniformly distributed orbital inclinations, this can be converted to a general transit probability, $Pr(\text{transit})$, (Borucki & Summers, 1984):

$$Pr(\text{transit}) = \frac{R_\star}{a_p} \approx 0.005 \left(\frac{R_\star}{R_\odot} \right) \left(\frac{a_p}{1 \, \text{au}} \right). \tag{1.8}$$

Similar to the RV method, this results in a bias towards planets on closer orbits because the probability to find a planet transiting is higher. According to Equation 1.8, the same is true for planets orbiting larger stars, which is in contrast to the RV method. However, in practise this is counterbalanced by the fact that planets around smaller stars produce larger signals (Equation 1.6) and are therefore easier to detect. Ideal targets for the transit method are therefore large, i.e., commonly gaseous, close-in planets orbiting intermediate-sized stars.

1.3.2 Observables and derived parameters

The period and transit depth are essential observables of the transit method. Further the transits can be characterised by two timescales: the total transit duration, t_t, and the time of full transit, t_f (see Figure 1.4). Thereby, the total transit time, is the time

between the first and last contact of the stellar and planetary disk and the time of full transit is the time for which the planetary disk is fully in front of the stellar disk.

In addition to the planet-to-star radius ratio, which I described in subsection 1.3.1, we can derive two further dimensionless quantities from this: the impact parameter, b (see Figure 1.4), and the scaled planetary semi-major axis, $a_{\mathrm{p}}/R_\star$. A detailed derivation of those would be, however, out of scope for this thesis and I would like to refer to Seager & Mallén-Ornelas (2003) for this instead. The resulting expressions for circular orbits are (Seager & Mallén-Ornelas, 2003):

$$
\begin{aligned}
b &\equiv \frac{a_{\mathrm{p}}}{R_\star} \cos{(i)} \\
&= \left\{ \frac{\left(1 - \sqrt{\Delta F}\right)^2 - \frac{\sin^2(t_f \pi/P)}{\sin^2(t_t \pi/P)} \left(1 + \sqrt{\Delta F}\right)^2}{1 - [\sin^2(t_f \pi/P) \sin^2(t_t \pi/P)]} \right\}^{1/2},
\end{aligned}
\tag{1.9}
$$

and

$$
\frac{a_{\mathrm{p}}}{R_*} = \left\{ \frac{\left(1 + \sqrt{\Delta F}\right)^2 - b^2 \left[1 - \sin^2(t_t \pi/P)\right]}{\sin^2(t_t \pi/P)} \right\}^{1/2}.
\tag{1.10}
$$

Consequently, the combination of those two parameters directly yields the inclination of the planetary orbit:

$$
i = \cos^{-1}\left(b \frac{R_\star}{a_{\mathrm{p}}}\right).
\tag{1.11}
$$

In fact, the eccentricity of the planetary orbit also affects the light curves. Thereby, the change in the acceleration of the planet on its orbit leads to slightly different times for ingress and egress and therefore a skewed light curve (Barnes, 2007). However, the effect is very small and the information content much less compared to RV measurements (Barnes, 2007; Kipping, 2008; van Eylen & Albrecht, 2015).

From the equations above, it can be seen that the stellar radius is a necessary additional input to derive physical parameters from the measured quantities. In the most cases it is nowadays determined from the Stefan-Boltzman law (see subsection 1.1.1), but can also for example be determined with high precision from asteroseismic observations (e.g., Kjeldsen et al., 2009; Chaplin et al., 2014; Yu et al., 2018, and references therein). If the stellar radius is known, one can thus derive the planetary radius, the planetary semi-major axis and the inclination of the orbit from transit observations. Further, analogous to the RV method, follow the planetary insolation and equilibrium temperature from the semi-major axis, if the stellar temperature or luminosity is known.

A unique feature of the transit method is that it provides a direct measure of the mean stellar density. Combining Kepler's third law and the planet-to-star radius ratio, one gets (assuming the stellar mass is much larger than the planetary mass):

$$\rho_\star = \frac{M_\star}{4/3\pi R_\star^3} = \frac{3\pi}{GP^2}\left(\frac{a_\mathrm{p}}{R_\star}\right)^3. \tag{1.12}$$

1.3.3 Practical application

Retrieving transit observations

Transit photometry is nowadays generally performed using time series of CCD images from cameras with a large field of view (FOV), which, in contrast to the RV method, allows to observe many stars at the same time. The most easy way to retrieve light curves from those images is the so-called simple aperture photometry (SAP), which determines the flux of each star in the FOV star by the sum within a given —often circular— aperture around it (e.g., Gilliland & Brown, 1988).

However, this flux can be largely affected by instrumental systematics or environmental conditions like changes in the atmospheric transparency. The most popular approach to mitigate this is to compare the flux of the target star to the flux of other stars in the FOV, the so-called differential photometry (Howell, 2006; Winn, 2010). In this way, systematic variations in brightness that affect all stars the same, for example, the aforementioned changes in sky transparency, can be corrected. In the classic form, the target flux is simply divided by the sum of all other comparison star apertures. Though, for example the atmospheric extinction is wavelength dependent, which means that the changes in airmass affect different stellar types to a varying degree. The more flexible way is therefore to assume that the flux of the comparison stars is linearly correlated with the target flux. This linear detrending can be performed independently or simultaneously with the transit fit. It has the big advantage that not only the total flux of the comparison stars can be used but also auxiliary information like for example the airmass, changes in the seeing (tracked by the point spread function (PSF) size) and many more (e.g., Collins et al., 2017). For light curves that are dominated by instrumental systematics, for example, space-based missions like Transiting Exoplanet Survey Satellite (TESS, Ricker et al. see subsection 3.2.1; 2015), decomposition approaches have proven beneficial. Thereby, a set of basis vectors that describes the correlations between the light curves of different targets is used instead of the auxiliary parameters (e.g., Smith et al., 2020).

Typical precisions of transit photometry from ground based surveys, such as Super-WASP (Pollacco et al., 2006) or HATNet (Bakos et al., 2004, 2006, 2013), are on the order of $2000\,\mathrm{ppm}$ to $4000\,\mathrm{ppm}$, since they are limited by residual atmospheric effects. Space-based instruments such as TESS, *Kepler*/K2 (Borucki et al., 2010; Howell et al.,

2014) or CHEOPS (Benz et al., 2021), on the other hand, can achieve precisions of less than $\approx 20\,\text{ppm}$.

Interpreting transit observations

In principle, the light curves that are corrected for systematics as described above are suitable to search for transits. However, there are a few more aspects to consider.

Firstly, analogues to the RV method, the timestamps need to be converted to BJD to allow for accurate transit timing.

Also, besides the instrumental and observational systematics, the light curves can be affected by stellar activity. This includes periodic brightness variations caused by stellar spots and faculae (see subsubsection 1.1.1), but also temporary outbursts caused by flares (e.g., Berdyugina, 2005; Strassmeier, 2009; McQuillan et al., 2014). Further, stellar oscillations lead to periodic short-time variations (e.g., García et al., 2010; Yu et al., 2018, and references therein), though they are undetectably small for M-dwarf stars (Rodríguez-López, 2019).

With regard to long-term observations in search of transits, such activity induced brightness modulations should be corrected so that all potential transits are at the same level and thus easier to detect (e.g., Hippke et al., 2019, and references therein). In addition, if not corrected, a varying baseline can lead to incorrect transit depths when fitting light curves with continuous sampling that contain multiple transit events. Stellar activity can also have acute effects on individual transits. In rare cases the projected path of a transiting planet passes over a star spot, which results in a "dent" in the light curve.

The box-fitting least squares (BLS, Kovács et al. 2002) algorithm is commonly used for the search of transit events in photometric times series because of its universal parameterisation and short computation times. However, the improved computational power that is nowadays available makes it increasingly attractive to use also more sophisticated models like the Transit-Least-Squares (TLS, Hippke & Heller 2019) algorithm, which replaces the simple box shape by actual transit shapes (see for example subsection 3.4.1).

However, a significant signal in the BLS or TLS periodogram does not necessarily mean that it is a planet. In addition to false positives due to low signal-to-noise ratio (S/N), possible grazing transits by stellar companions and near-by eclipsing binaries (NEBs) need to be carefully ruled out (e.g., Bryson et al., 2013, and references therein). A crucial feature is the shape of the transit, as NEBs and grazing transits are generally V-shaped rather than the box-shaped transits. NEBs can further be detected by comparing the depth of even and odd transits, since the light loss differs between the primary and secondary eclipse of the brighter star. However, both requires a high S/N, which cannot always be reached. Often only additional data like RVs or high-resolution imaging can undoubtedly confirm the planetary nature of a transit.

Similar to the RV method, transit modelling generally considers individual instrumental offsets and jitter terms (see also subsection 3.4.3, or subsection 4.4.4). However, there are two more parameters that need to be taken into account. First, the stellar limb-darkening has a great impact on the transit light curve and therefore derived planetary parameters (e.g., Knutson et al., 2007; Csizmadia et al., 2013). The different flux between the stellar limb and the stellar centre thereby leads to varying shapes of the transit ingress and egress, depending on the observed wavelength and stellar type. Two very popular models are the linear and quadratic limb-darkening (e.g., Al-Naimiy, 1978; Kipping, 2013), though, there is a variety of limb-darkening laws present in the literature (e.g., Espinoza & Jordán, 2016). The second parameter that needs to be considered is contamination by other stars that are close to the target star in the FOV, since already a dilution of only a few percent will decrease the derived planetary radius (Southworth, 2010). Constraints on such possible dilution can be derived from additional high-resolution images that resolve any faint nearby, or blended stars.

In general, non-dynamical models are sufficient to model transit light curves. However, in the case of massive planetary companions or tightly packet systems, TTVs can occur between individual transit events due to the gravitational pull between the planets (e.g., Holman & Murray, 2005; Agol et al., 2005). In such cases, the transit centre of each observation or a temporal perturbation parameter can be simply added to the model for each transit to account for, and to derive, the TTVs (Eastman et al., 2019). The dynamical information from the TTVs is complementary to the transits and actually allows to derive the planetary masses (e.g., Lithwick et al., 2012; Hadden & Lithwick, 2014; Grimm et al., 2018), however, a detailed discussion of it would be out of scope for this thesis.

1.4 Combining RV and transit observations

Combining RV and transit observations is very powerful for a number of reasons. Above all, the joint detection of a planet with RVs and transits is probably the best evidence for its planetary nature. This is because, on the one hand, the information about the inclination of the system resolves the degeneracy of the RV mass (Equation 1.3). On the other hand, the mass as determined from the RV can exclude grazing transits by stellar companions or NEBs as the origin of the transits (subsection 1.3.3).

Further, combining the planetary radius, as determined by the transit, with the mass from the RVs yields information about the planetary mean density. From the density of a planet we can learn about its composition and structure, and thus also about its formation and evolutionary history (see for example the discussion on the nature of the super-Earths and mini-Neptunes in subsection 1.1.3). In this context, additional
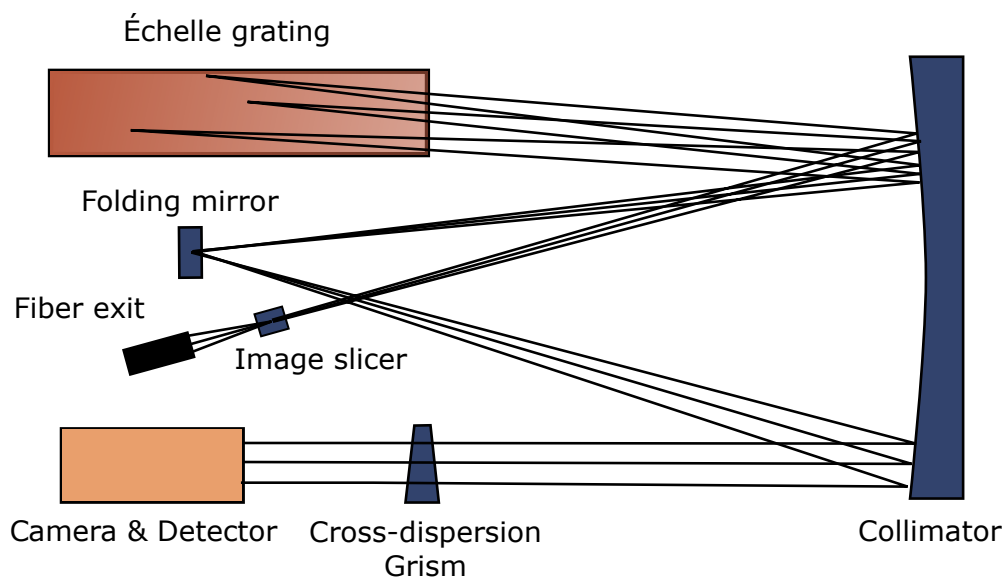
Fig. 1.5.: Schematic design of CARMENES-VIS. The light of the science and the calibration fibers first passes through an image slicer that transforms the image of the fiber output into a pseudo-slit image and thus increases the spectrograph resolution. After the reflection at the collimator, the parallelized light beam reaches the Èchelle grating where it is diffracted and split up into its components. To allow for a more compact instrument design, the diffracted light then hits the collimator again and is directed onto a folding mirror such that another reflection at the collimator produces again a parallel light beam. This parallel beam is passing through a cross-dispersion grism that splits the spectral orders in the direction perpendicular to the grating, such that they are separated on the detector.

planets in the system are also of interest. Due to the different biases, RVs and transits complement each other in their detection capabilities. There might be additional non-transiting planets that can be detected by RVs, or further low-mass transiting planets that are undetectable by RVs.

But there are also very practical reasons. For example, the information from the transits about the exact period and phase of a planet can help to solve alias problems in the RV data (see subsection 3.4.4), or disentangle planetary RV signals from superimposed stellar activity (e.g., Sarkis et al., 2018).

To obtain the most precise planetary parameters, the RV and transit data can be combined in a joint fit with shared parameters for the planetary period, eccentricity, and transit centre (see also subsection 3.4.5 or subsection 4.4.6).

1.5 CARMENES

The acronym CARMENES (Calar Alto high-Resolution search for M dwarfs with Exoearths with Near-infrared and optical Échelle Spectrographs) relates to two elements: a pair of
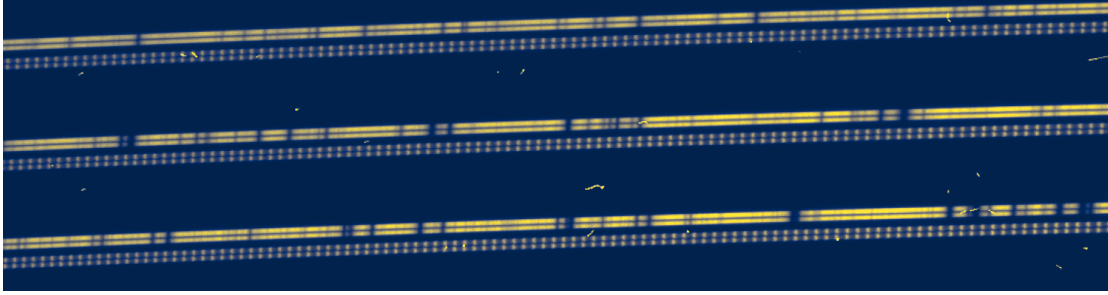
Fig. 1.6.: Zoom-in into a spectrum of GJ 3929 observed with CARMENES. The image shows a cutout from three Èchelle orders, each with the science spectrum on top and the lines from the FP in the bottom. The individual lines are split because of the image slicer.

cross-dispersed Èchelle spectrographs, as well as a survey that is carried out with those (Quirrenbach et al., 2014, 2016, 2018, 2020).

The instrument is mounted in the Cassegrain focus of the $3.5\,\text{m}$ telescope at Calar Alto Observatory in Granada (Spain). It operates in the wavelengths of $0.52\,\mu\text{m}$ to $0.96\,\mu\text{m}$ in the VIS (CARMENES-VIS, $R = 94\,600$) and $0.96\,\mu\text{m}$ to $1.71\,\mu\text{m}$ in the NIR (CARMENES-NIR, $R = 80\,400$). A schematic representation of the design of the CARMENES-VIS, which is also a subject of this work, is shown in Figure 1.5. Two fibers are fed into the spectrograph, one for the science observations and one for the simultaneous calibration using a FP interferometer. The light beam of the fibers is narrowed by an image slicer (see also Figure 1.6), that effectively works like a slit but without the light loss. In combination with the large dispersion of the Èchelle grating, this results in a high resolution of the spectrograph. A cross-dispersion grism in front of the camera provides 41 separated spectral orders that can be used to derive RVs (see Figure 1.6 for a cutout of an M-dwarf spectrum).

The CARMENES survey started with the first light of the instrument in 2016 and ended its guaranteed time observations (GTO) in 2020. It is being continued by a legacy programme since the beginning of 2021. As the name implies, the main goal is to find planets orbiting M dwarfs. So far, 26 planets[4] have been found by the blind search. Particularly noteworthy are, for example, HD 147379 b the first planet discovered by CARMENES (Reiners et al., 2018b), the potentially habitable planets in the Teegarden system (Zechmeister et al., 2019), or the giant planet GJ 3512 b (Morales et al., 2019). Recently, CARMENES has been very successful in the confirmation and characterisation of TESS planet candidates (see Part II of this thesis). Furthermore, as described in subsection 1.1.1, the large databank of M-dwarf spectra resulting from the survey is used to study the stars themselves. In addition, CARMENES is used by the consortium to perform transit spectroscopy of planetary atmospheres (e.g., Nortmann et al., 2018; Yan et al., 2019; Oshagh et al., 2020; Palle et al., 2020).

---

[4]Source: talk by P. Amado at the 15th CARMENES scientific meeting

1.6 This thesis

This thesis is about the discovery and characterisation of terrestrial planets using the RV and transit methods. In doing so, I focussed my research on planets orbiting M-dwarf stars within the framework of the CARMENES project. In the introduction to the field above, I already explained the advantages that M dwarfs offer for the detection of small planets: They are common in the Solar neighbourhood and, due to their comparably small stellar mass and radius, ideal for the detection of small planets. Moreover, their small size makes them suited for the upcoming in-depth characterisation of the planet's atmospheres, from which it is hoped to gain the next major insights into the formation and evolution of exo-Earths. In the exoplanet research community, the combination of all those advantages is often fondly called the "M-dwarf opportunity" (e.g., Plavchan et al., 2015; Charbonneau & Deming, 2007; Charbonneau, 2017). Nevertheless, the study of M-dwarf planets remains a challenge and requires advanced technology and instrumentation.

The work is structured as follows: I described the background of small planets orbiting M dwarfs, as well as the used techniques in the introduction above. In the first part of my thesis, I will present an error budget of the CARMENES-VIS in operation. It complements the error budget that was compiled during the design phase of the instrument and points out where the instrument could be further improved to reach an even higher precision. In the context of this work, it is also an impressive example of the technical demands that have to be met so that we can actually take the "M-dwarf opportunity". In the second part of my thesis, I will introduce our RV follow-up efforts of TESS object of interests (TOIs) with the CARMENES-TESS working group (CARMENES-TESS WG) in order to confirm and characterize planets whose transit signals where first detected by TESS. Particularly, I present the planetary system of GJ 3473 consisting of an inner transiting Earth-sized planet and a non-transiting, outer, sub-Neptunian-mass planet in chapter 3 and the short-period, Earth-sized planet GJ 3929 b in chapter 4. Both transiting planets, GJ 3473 b and GJ 3929 b, make an important contribution to the still small but ever-growing sample of truly Earth-sized planets. In addition, both are particularly well suited in different ways for the atmospheric characterisation with upcoming facilities such as the JWST (Gardner et al., 2006) or the Extremely Large Telescope (ELT, Gilmozzi & Spyromilio 2007). I outline what we could learn from the planets and how they fit into the overall picture of small planets orbiting M dwarfs in the discussion and conclusion in chapter 5.

Part I:

An error budget of CARMENES-VIS in operation

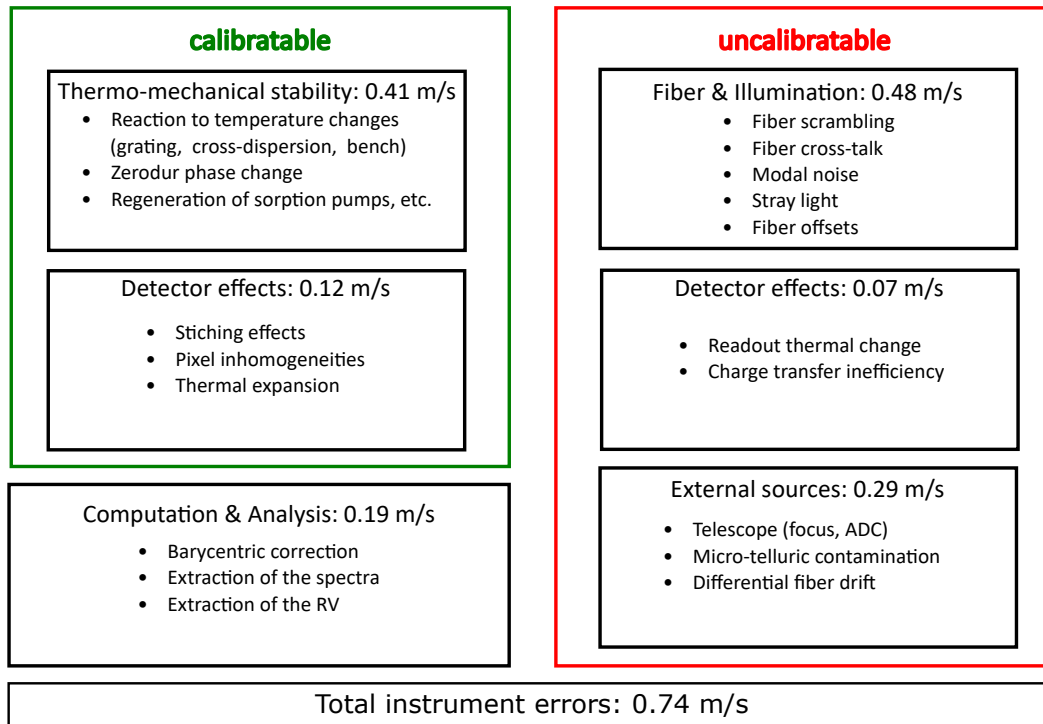# CARMENES-VIS error budget $\quad$ 2

2.1 Introduction

In the era of high-precision spectrographs, detailed error budgets are key to assess the performance of an instrument. Examples for comprehensive error budgets for instruments aiming at sub-$\mathrm{m\,s^{-1}}$ RV precision are for example Podgorski et al. (2014); Halverson et al. (2016); Bechter et al. (2018) and Blackman et al. (2020). The requirements for the CARMENES-VIS were thoroughly investigated in the design phase and summarised in an RV error budget in Ribas et al. (2013, R13 hereafter). The complementary analysis presented here provides a summary of the critical aspects that limit the measurement precision of CARMENES-VIS as identified from the aforementioned error budgets in the recent literature, complemented by information from the commissioning phase and on-sky data. The error budget from Halverson et al. (2016, H16 hereafter) serves as a basis for the investigation and will be completed by terms from the original final design review (FDR) budget of R13.

 In general, the overall uncertainty of an RV measurement can be decomposed into two components (Bechter et al., 2018). First, the photon noise of the measurement, which depends on the target star and the observing conditions. Second, the instrumental systematics on which this work will be focused. The instrument errors themselves again can be separated into two main categories (H16): the ones that can be traced and calibrated by the use of simultaneous measurements of a calibration source and the ones that are uncalibratable. Those uncalibratable terms mostly depend on the intrinsic design and stability of the instrument. In this work, I will further distinguish a third component, which is the analysis of the spectra and the retrieval of the RVs. H16 associates both to the uncalibratable error sources, however, I consider them separately as the used methods are often interchangeable and not specific to the instrument. An overview of the error sources, which were investigated for this thesis, is given in Figure 2.1.

2.2 Calibratable errors

2.2.1 Thermo-mechanical stability

Reaction to temperature changes   The visual channel of CARMENES has no active thermal stabilisation, but follows the room temperature ($\sim 12.5\,°\mathrm{C}$) of the thermal chamber

Fig. 2.1.: Overview of the error terms investigated for the summarised CARMENES error budget.

in which it is located (Quirrenbach et al., 2018). Since the optical bench is thermally shielded and decoupled from the vacuum tank, thermal changes are only transmitted with a long time constant. Thereby, the thermal expansion of the optical bench leads to universal varying optical path lengths and scattering angles in the instrument, which will than translate to RV drifts. Additionally, the thermal expansion of individual sensitive components, like the Échelle grating and the cross-dispersion, affect those drifts. Recently, a forward modelling approach for the CARMENES instrument identified the detector tilt as another critical component (Tala, 2019). The investigation of the instrument performance from Bauer et al. (2020) quotes an overall thermal drift of $2\,\mathrm{m\,s^{-1}\,mK^{-1}}$ related to the temperature measured at the optical bench. This yields individual RV drifts in the order of $2\,\mathrm{m\,s^{-1}}$ to $10\,\mathrm{m\,s^{-1}}$ during the course of one night. To mitigate the effect on the RVs, drift measurements obtained from simultaneous observations of a dense line grid from a FP unit are used in the CARMENES data reduction. The residual error can be estimated from the uncertainties of those drift measurements, which are on the order of $0.4\,\mathrm{m\,s^{-1}}$.

Zerodur phase change   Zerodur is mostly used to build optical components as it undergoes only minor thermal changes. This characteristic comes from its material composition, which is a mixture of glass and ceramic. However, as an ageing phenomenon, there is a phase transition between both, which results in an effective length change of the

material (Bayer-Helms, 1987). This is a very slow process, which corresponds to a drift of approximately $5\,\mathrm{cm\,s^{-1}\,d^{-1}}$ for a typical R4 Échelle mosaic (H16).

Regeneration of sorption pumps, etc. Regular maintenance works can lead to significant offsets in the instrumental drift. For example, the regeneration of the sorption pumps that control the vacuum inside the instrument causes jumps of several hundreds of metres per second (Tala, 2019). Since those tasks are usually performed during the daytime and the jumps are well traced by the daily wavelength calibration, one can expect only a minor impact on the measured RVs. However, the traced instrumental drifts show, that the instrument settles only after a time span of several days (Tala, 2019). It must therefore be assumed that RV measurements, which are taken in this period, could be impaired. Though, this usually only affects individual measurements from the whole RV time series and is therefore negligible for the planet search to first order. Nevertheless, I add an estimated residual error of $5\,\mathrm{cm\,s^{-1}}$ to the error budget.

2.2.2 Detector effects

Stitching effects and pixel inhomogeneities The manufacturing process for larger CCDs leads to regular pixel asymmetries, the so-called stitching errors (Wilken et al., 2010; Bauer et al., 2015; Halverson et al., 2016; Blackman et al., 2020). For CARMENES-VIS, Bauer et al. (2015) showed that such small deviations from an otherwise smooth wavelength solution can result in spurious signals of about $0.5\,\mathrm{m\,s^{-1}}$ amplitude. However, the dense grid of calibration lines from the FP used by CARMENES enables to track and model those asymmetries for the wavelength calibration. The impact on the RVs can therefore be assumed to be very small, and I assume a residual error of $5\,\mathrm{cm\,s^{-1}}$ following Blackman et al. (2020, B20 hereafter).

Thermal expansion Temperature changes of the detector during the exposure cause relative changes of the pixel sizes. The resulting change in radial velocity can be estimated from the thermal expansion of the Silicon absorption layer. The CARMENES-VIS detector cryostat is designed to keep the detector at a temperature of $\sim 160\,\mathrm{K}$, with a thermal stability better than $10\,\mathrm{mK}$ (exemplary checked for August 2020, the temperature log shows a standard deviation of $1.7\,\mathrm{mK}$ and peak to peak variation of $18\,\mathrm{mK}$). Assuming a simple linear thermal expansion and applying an expansion coefficient of about $745.5 \times 10^{-9}\,\mathrm{K^{-1}}$ (Middelmann et al., 2015) to the 4k×4k detector with $15\,\mu\mathrm{m}$ sized pixels, and assuming the $10\,\mathrm{mK}$ temperature fluctuations, results in an expansion of $\sim 0.5\,\mathrm{nm}$ for the whole detector. Given a resolution of $\sim 1.268\,\mathrm{km\,s^{-1}}$ per pixel (Quirrenbach et al., 2018), this corresponds to an approximate velocity change of $\sim 5\,\mathrm{cm\,s^{-1}}$. I therefore conservatively hold an error of $\sim 10\,\mathrm{cm\,s^{-1}}$ for the budget.

2.3 Uncalibratable errors

2.3.1 Fiber and illumination

Fiber scrambling Optical fibers have the advantage that they "scramble" the input image due to the multiple reflections before the light reaches the output. Thus, resulting in an output beam that is to first order independent of the input. The efficiency of the scrambling is measured by the scrambling gain, which is the ratio of the relative displacement of the centre of the input beam at the entrance of the fiber over the relative displacement of the spectral lines at the detector (Stürmer, 2015). For CARMENES, octagonal fibers with a measured effective scrambling gain over 2000 are used (Seifert et al., 2016). Following the definition of the scrambling gain, the RV precision, which can be achieved with these fibers is thus limited by the motion of the input light, i.e., the guiding accuracy of the telescope (B20):

$$\mathrm{RV}_{\mathrm{error}} = \left(\frac{c}{R_{\mathrm{eff}}} \right) \left(\frac{\delta_\theta}{\theta} \right) \left(\frac{1.0}{\mathrm{scrambling\ gain}} \right), \tag{2.1}$$

where: c = speed of light

R = spectrograph resolution

δ_θ = rms of guiding error

θ = projected fiber size.

Using the CARMENES-VIS specifications of $R_{\mathrm{eff}} = 94\,000$, fiber size $= 1.5\,\mathrm{as}$, scrambling gain $= 2000$, and guiding precision of $0.22\,\mathrm{as}$ root mean square (rms) measured by Seifert et al. (2016), the RV error caused by the scrambling gain of the used fibers and the guiding errors is $\Delta \mathrm{RV} = 0.24\,\mathrm{m\,s}^{-1}$.

Fiber cross-talk The large wavelength coverage of CARMENES-VIS allows only a small separation of the individual Échelle orders to be able to fit the whole spectrum on the detector. Hence, there will be a non-negligible pollution between the images of the science and calibration fibers, the so-called fiber cross-talk. The effect is taken into account by our reduction pipeline and mitigated further by lowering the brightness of the FP in the calibration fiber with respect to the science fiber during the observations. The FDR error budget adopts a contribution of $\Delta \mathrm{RV} < 0.2\,\mathrm{m\,s}^{-1}$ by the cross-contamination of the fibers based on simulations. I stick to this value as a conservative estimation.

Modal noise CARMENES uses multi-mode fibers, which means that the light exiting the fibers originates from different propagation modes that can interfere with each other. The resulting speckle pattern is variable and depends on the fiber conditions. As those can vary during the observations (e.g. by temperature variations, pressure
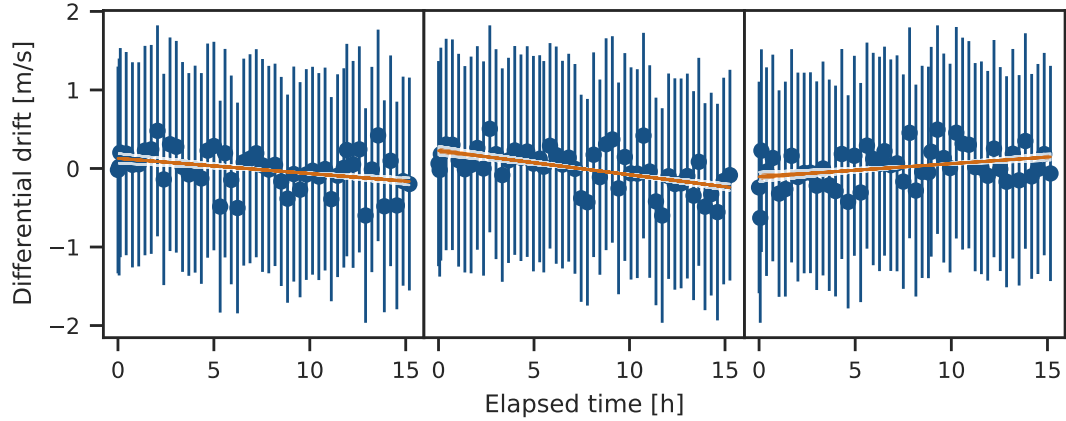
Fig. 2.2.: FP-FP measurement datasets with significant drifts.

changes or vibrations, Bechter et al., 2018), the output centre of the light beam can shift and therefore lead to spurious RV signals. However, the effect can be mitigated by mechanically agitating the fibers in order to deliberately create rapidly changing patterns, which will smooth out during the curse of the observations. The residual error for CARMENES was never tested, but B20 and H16 state effects smaller than $5 \, \mathrm{cm \, s^{-1}}$. For consistency, I stick to the estimated conservative uncertainty of $\Delta \mathrm{RV} < 10 \, \mathrm{cm \, s^{-1}}$ from the FDR error budget.

Stray light   Stray light from the different optical elements that will reach the detector can lead to degraded line profiles and therefore distorted RV measurements (B20). The flat-relative optimal extraction method, which is used by CARMENES, is not able to account for such stray light in the retrieval of the calibrated spectra and therefore makes an effective stray light suppression crucial. Calculations for the total amount of stray light for the CARMENES instrument yield less than $3 \, \%$, which is mostly due the reflection at the Échelle grating (Xu et al., 2012). To effectively mitigate the amount of stray light that reaches the detector, different light stops are implemented in the instrument. Following H16, I estimate a contribution of $5 \, \mathrm{cm \, s^{-1}}$ error for the scattered light.

Fiber offsets   The wavelength calibration of CARMENES is performed on a daily basis to track the thermal changes between the observing nights. As described in subsection 2.2.1, further simultaneous measurements of a calibration fiber are used during the nights to track the drift of the instrument over the course of the observations. However, this requires that both of the fibers show the same behaviour over time. To test this, I obtained the differential drift, which means the difference in measured RV over time between the two fibers from 8 sets of FP-FP measurements. Each test series was taken continuously over a large time span of minimum $6 \, \mathrm{h}$ duration with a cadence of at least 1 observation

per hour. Three of the datasets showed significant, although moderate, correlations between the measured drifts and the elapsed time (see Figure 2.2). The largest drift (middle panel) corresponds to a change of $\sim 0.034\,\mathrm{m\,s^{-1}\,h^{-1}}$ between the two fibers, while the others are much smaller ($< 0.02\,\mathrm{m\,s^{-1}\,h^{-1}}$). I nevertheless adopt this large value as a conservative estimate of the differential drifts that can happen during the night. Together with a median rms RV difference of $0.25\,\mathrm{m\,s^{-1}}$ as measured from the 8 datasets, I sum up the maximum error to $0.35\,\mathrm{m\,s^{-1}}$ for a night with $8\,\mathrm{h}$ of observations.

2.3.2 Detector effects

Readout thermal change   The CCD electronics and amplifiers are a source of heat, which increases during the CCD readout. Those temperature fluctuations lead to thermal hot spots on the surface and hence a warping of the detector, which is not traced by the calibration fiber. Manescau et al. (2010) report changes of the detector surface of $\sim 0.15\,\mathrm{nm\,mK^{-1}}$ for typical large scale CCDs. Assuming the rms temperature variations of $\sim 2\,\mathrm{mK}$ measured at the detector reflect those readout temperature fluctuations yields a velocity error of $\sim 2.5\,\mathrm{cm\,s^{-1}}$. Since this is only a rough estimate, I adopt twice this value, $\Delta \mathrm{RV} \sim 5\,\mathrm{cm\,s^{-1}}$, for the total error budget.

Charge transfer inefficiency (CTI)   The transfer of the pixel charges during the read-out is not perfect. Resulting pixel shifts of electron counts can thus lead to small changes in the line shapes and depths of the retrieved spectra. Thereby, the amount of charge loss is larger for pixels further from the read-out register and affects the RVs stronger for spectra with a low S/N.

The effect of the CTI on the RV as a function of the detector position was investigated by the consortium member F. Bauer by evaluating the measured line positions of the FP as a function of the pixel position (internal communication). As the CARMENES detector is read out from four different corners, the line shift due to distortions by the CTI shows a different trend for the two detector halves (see Figure 2.3). In the middle of the detector a jump of $\sim 5\,\mathrm{m\,s^{-1}}$ in the FP line positions is apparent. However, the measured trends in the line positions for the two detector halves are exactly oppositional and thus cancel out each other fairly good. F. Bauer concluded that for regular science observations no strong effect on the RVs is expected by this.

Additionally, the impact of the CTI on the RVs can be investigated as a function of their S/N. For this I can make use of the large data bank of observations from the CARMENES GTO survey. For all CARMENES GTO observations, I plot the S/N in the reference order (order 36 for CARMENES-VIS) of the observations against the measured RV (corrected for the median RV of each target to account for offsets and drifts of the individual stars) and fit for the slope and offset (see Figure 2.4). No significant change in RV is found for
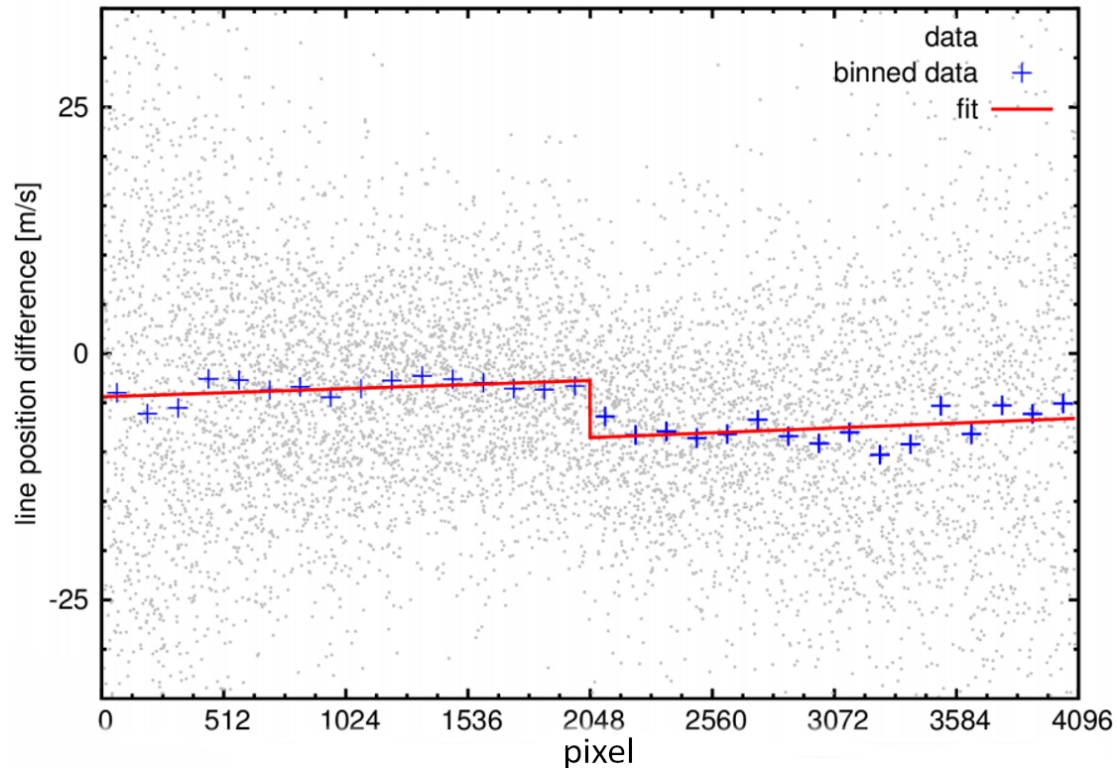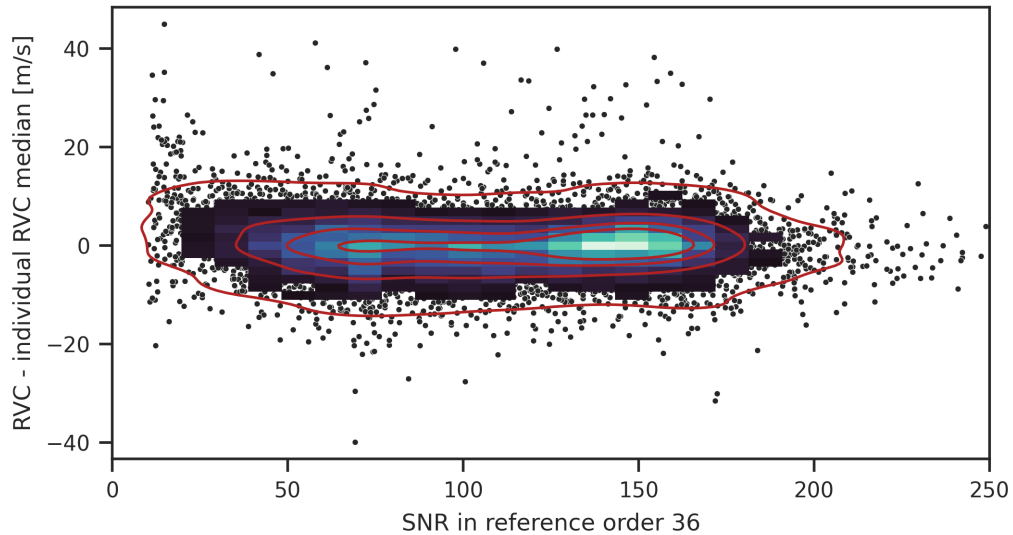
Fig. 2.3.: Investigation of the CTI impact as a function of the detector position (plot by F. Bauer).

the varying S/N of the CARMENES observations. Only for observations with S/N $\lesssim 75$ a possible trend towards higher RV is visible. However, in the standard observing mode this is mitigated by stopping the exposures only when a S/N of ~ 100 is reached (traced by an exposure meter). Only for faint targets, which may exceed the maximum exposure length of $30\,\mathrm{min}$, lower SNRs are expected. The overall effect of the CTI on the RV can therefore be assumed to be small, and I assume a contribution of $5\,\mathrm{cm\,s^{-1}}$ to the error budget following H16.

2.3.3 External sources

Telescope   The telescope optics and mechanics also add to the sources of errors. For example, the impact of guiding errors was discussed in paragraph 2.3.1. Those measured guiding errors also include the vibrations of the telescope due to the "wind shake" (H16). Additionally, deviations in the focus of the instrument lead to achromatic variations in the illumination of the fiber entrance and therefore shifts in the centroid illumination. This is similar to the effect of the atmospheric dispersion, which is mitigated by an atmospheric dispersion corrector. However, the impact on the RV measurements is difficult to assess, and I therefore estimate a conservative contribution of $15\,\mathrm{cm\,s^{-1}}$ to the error budget.

Fig. 2.4.: Investigation of the CTI as a function of S/N.

Micro-telluric contamination   Telluric absorption lines from the Earth's atmosphere that are imprinted on the stellar spectrum can impair the radial velocity measurements. The strength of those lines varies with the air column along the line of sight, as well as the humidity during the observation. Their position changes with respect to the stellar spectrum due to the barycentric motion of the earth. The standard approach for CARMENES measurements, is to mask out the wavelength regimes of known strong telluric lines during the RV retrieval. For the NIR channel, the template division telluric modelling technique has proven to be superior to the simple use of binary masks. However no improvement was found for the CARMENES-VIS spectra (Nagel et al., in prep.). The impact of uncorrected micro-telluric lines, which are present all over the spectra, on the RV measurements is difficult to determine. I therefore follow B20 and assume a contribution of $\sim 25\,\mathrm{cm\,s^{-1}}$ to the radial velocity error based on the results in Cunha et al. (2014).

2.4 Computation and Analysis

Barycentric correction   For the correction of the barycentric Earth radial velocity (BERV), the python package `barycorrpy` (Kanodia & Wright, 2018a,b; Wright & Eastman, 2014) is used. The package allows to calculate the BERV to a sub-$\mathrm{cm\,s^{-1}}$ precision for a given timestamp and pointing direction on the sky. Thanks to the *Gaia* satellite, the positions of the stars in the sky are generally known precise enough, to neglect the BERV error due to the uncertainty of the stellar positions ($\Delta\mathrm{BERV} < 1\,\mathrm{cm\,s^{-1}}$). However, the exposure times for the measurements are not infinitely short and the calculation of the BERV is

therefore not straight forward. The maximum integration time of CARMENES is set to $\Delta t = 30 \, \text{min}$, which yields a maximum change in BERV between the starting point and the end of an exposure of $\sim 50 \, \text{m s}^{-1}$. Precise knowledge of the effective time of an observation is therefore crucial (Wright & Eastman, 2014). In CARMENES, the incoming flux over time is logged with an exposure meter, which is used to calculate a photon weighted exposure midpoint (EMP) to a precision of about three seconds, which yields an uncertainty of $\sim 9 \, \text{cm s}^{-1}$ for the BERV. It is important to note, that the EMP calculated BERV neglects non-linearity of the BERV with time, which is why the authors of the `barycorrpy` package also provide the option to calculate a weighted BERV using the information from an exposure meter.

I used the CARMENES observations from one of the standard stars in the sample to exemplary estimate the difference between those two methods and found a difference in the calculated BERV values of $6 \, \text{cm s}^{-1}$ rms. For CARMENES, which is working in the metre-per-second precision regime, this is tolerable with respect to much higher computational cost, but should be considered for calculating the RVs from spectrographs of the next generation. The overall error of the barycentric correction is therefore estimated to be $\sim 11 \, \text{cm s}^{-1}$.

Reduction pipeline   The performance of the reduction pipeline strongly correlates with the quality of the raw data that are considered. The key aspects are the extraction of the spectra, the wavelength calibration and the computation of the RVs. A detailed examination of those would be far beyond the scope of this thesis, however, the methods used for the CARMENES pipeline were subject to different publications that show their individual practicability. In the following paragraphs I will shortly summarise them.

The extraction of the CARMENES spectra by the `caracal` (Caballero et al., 2016a) pipeline is based on the flat-relative optimal extraction (Zechmeister et al., 2014). In this method, as the name implies, a high S/N master-flat image serves as a reference for the extraction profile, thus eliminating the need for subsequent flat-fielding of the retrieved spectra. The main two limitations of the method are: first, the flux of tilted PSFs is not properly preserved because the method is only one dimensional; second, stray light, or ghost features from nearby contaminating sources, are not taken into account, because the reference spectrum is taken from a flat lamp. A possible improvement would be therefore to switch from the one dimensional extraction to a two-dimensional PSF.

The FP interferometers available for calibrating the CARMENES spectra as described in subsection 1.2.3 are stable to a precision of $10 \, \text{cm}$ per night (Schäfer et al., 2018). Using the spectra of Th-Ne, U-Ar and U-Ne HCL lamps as a reference, a precise wavelength solution is obtained with them on a daily basis following the method of Bauer et al. (2015). In their study they found the difference between the FP wavelength solution and the solution using a LFC to be less than $10 \, \text{m s}^{-1}$ rms. Considering the size of a

resolution element of CARMENES-VIS and the multitude of lines that are considered in the calculation of the RVs, this difference is negligible.

The RVs are retrieved using `serval` (Zechmeister et al., 2018). It is based on the forward modelling technique and uses least-squares fitting of stellar spectrum templates, which are created by coadding all available spectra of the respective target stars. This method is especially suited for retrieving the RVs from cold, absorption line rich stars like the M dwarfs observed by CARMENES. In a comparison to the HARPS data reduction software (DRS) pipeline (Lovis & Pepe, 2007), `serval` is proven to perform superior in terms of resulting RV scatter for a large sample of observations (Trifonov et al., 2020). However, a systematic estimation of the precision of the determined RVs is lacking (as is in general the case for the publicly available RV retrieval codes).

As mentioned in the beginning, it is not straight forward to assess the overall error caused by the analysis of the data as the results depend on the targets, the individual observing conditions and the data quality. I therefore hold an estimated ΔRV of $\sim 15\,\mathrm{cm\,s^{-1}}$ for the calibration and RV computation based on H16.

2.5 Discussion

2.5.1 Comparison to the FDR error budget

Since a qualitative error budget for CARMENES was already prepared during the design phase of the instrument, a comparison between both should be the first logical step.

I list the thermo-mechanical stability of the instrument to be $0.41\,\mathrm{m\,s^{-1}}$, which corresponds to the opto-mechanical stability in the FDR budget. The anticipated uncertainty of $< 0.3\,\mathrm{m\,s^{-1}}$ from the FDR is therefore not achieved. The reason for this is, that the dominating source that I found, the uncertainty in the drift estimation, ΔRV $\sim 0.4\,\mathrm{m\,s^{-1}}$, was not evaluated by R13.

The detector effects, that I determined ($0.12\,\mathrm{m\,s^{-1}}$ calibratable; $0.07\,\mathrm{m\,s^{-1}}$ uncalibratable) comply with the with requirement to be less than $0.2\,\mathrm{m\,s^{-1}}$.

Even though the anticipated guiding accuracy of $0.12\,\mathrm{as}$ rms is not met (see paragraph 2.3.1), the high scrambling factor of the used octagonal fibers keeps the error smaller than the requirement of $0.3\,\mathrm{m\,s^{-1}}$. The estimated impact of the fiber cross-talk and modal noise were adopted from the FDR budget, while the additional term that accounts for stray light in the instrument is negligible. I additionally investigated the expected scatter caused by offsets between the science and the calibration fiber. From sets of continuous FP-FP measurements, I determine a non-negligible drift between the two fibers and a jitter, which contributes $0.35\,\mathrm{m\,s^{-1}}$ to the error budget. This differential drift of the two fibers is actually one of the largest contributors to the overall uncertainty and was not taken into account in the original FDR.

I assume a similar influence from the contamination by micro-tellurics, however those are only estimated values. A. Kaminski[1] is currently investigating the affect of micro-tellurics on the derived CARMENES RVs and will further quantify this value.

The original considers FDR a long-term RV drift due to the ageing of the calibration lamps. However, the given reference of Rupprecht et al. (2004) is misleading as it described the short-term stability of HARPS using Th-Ar-lamps for a simultaneous calibration. Long-term RV drifts due to the ageing of the used calibration lamps still have to be investigated and were not taken into account for this error budget. Anyway, the most obvious solution is to regularly renew or replace the calibration lamps.

I split the RV computation and analysis of the data into two terms: the barycentric correction, and reduction pipeline (i.e., the extraction of the spectra and the extraction of the RV). In the FDR budget an uncertainty less than $0.1\,\mathrm{m\,s^{-1}}$ was specified for the barycentric correction. My analysis showed that this goal is narrowly missed due to small inconsistencies in the handling of the data ($\sim 0.11\,\mathrm{m\,s^{-1}}$). The FDR error budget only partially covered the impact of the reduction pipeline in form of the uncertainty of the wavelength solution (aim $< 0.1\,\mathrm{m\,s^{-1}}$). However, both, the absolute actual uncertainty of the reduction pipeline and the wavelength solution, are only guessed values, which means drawing reliable conclusions from a comparison is not feasible.

In summary, it can be said that there is no significant discrepancy between the specifications of the original FDR error budget and the one compiled here. Nevertheless, one of the largest contributors, the differential drift of the two fibers, was not taken into account originally. Furthermore, some initially estimated values could be replaced by actual measurements or updated expectations based on current findings. This was, however, not possible for all terms from the original FDR, which means that there is also a large overlap between both.

2.5.2 Potentially underestimated terms

The total error as deduced from the investigated terms yields an instrumental RV uncertainty of $\sim 0.74\,\mathrm{m\,s^{-1}}$, which slightly exceeds the requirements from the RV error budget of the FDR ($\Delta\mathrm{RV} < 0.6\,\mathrm{m\,s^{-1}}$) but is still smaller by a factor of 1.6 than the actual determined performance of $1.2\,\mathrm{m\,s^{-1}}$ (Bauer et al., 2020).

The large difference between the predicted and the actual measured instrument performance should therefore be further evaluated. The reason for the huge discrepancy could be, that I am missing crucial terms, or that some of my determined errors are massively underestimated, or both. This applies in particular for the terms that are only based on theoretical assumptions or that were never reviewed after the instrument was build. In Table 2.1, I give an overview of the different terms used in the budget and

---

[1]Member of the CARMENES consortium and Postdoc at the Landessternwarte Königstuhl in Heidelberg.

Tab. 2.1.: Origin of the determined error contributions and how I rank their reliability and impact.

Error term	Origin	Reliability	Impact
Thermo-mechanical stability			
Reaction to temperature changes	indirect measurement	uncertain	high
Zerodur phase change	adopted value	realistic	low
Regeneration of sorption pumps	estimate	uncertain	low
Detector effects			
Stitching effects	adopted value	realistic	low
Pixel inhomogeneities	adopted value	realistic	low
Thermal expansion	rough calculation	realistic	low
Readout thermal change	rough calculation	uncertain	moderate
Charge transfer inefficiency	adopted value	realistic	low
Fiber & Illumination			
Fiber scrampling	rough calculation	realistic	high
Fiber cross-talk	adopted value	realistic	moderate
Modal noise	adopted value	uncertain	moderate
Stray light	adopted value	uncertain	low
Fiber offsets	rough measurement	uncertain	high
External sources			
Telescope focus	adopted value	realistic	moderate
Micro-telluric contamination	adopted value	uncertain	high
Computation & Analysis			
Barycentric correction	calculated	realistic	moderate
Extraction of the spectra	adopted value	uncertain	moderate
Extraction of the RV	adopted value	realistic	moderate

how they were determined. The most critical terms in the error budget are the ones for which the determined values are rather uncertain, while the potential impact is high. In particular, the thermal response of the instrument and the differential drift of the fibers are of interest. Both are related to the thermal stability of the instrument, which is already identified as a determining factor for improving the instrument performance (Amado et al., 2020).

The differential fiber drift was not taken into account in the original FDR error budget, although it is one of the main contributors in this evaluation. It is therefore particularly important to search for its origin and possible mitigation strategies. A simple approach would be to take additional FP-FP measurements in between the observations to get benchmarks for a linear drift correction for each night. This was already proposed by A. Kaminski and is currently under debate in the consortium. The main drawback is thereby the large overhead of additional FP-FP measurements in the tight observing schedule.

Another factor, which has a presumably high impact but is only moderately constrained, is the contribution of the micro-telluric contamination, which is currently also investigated by A. Kaminski. However, while their impact on the current error budget is high, they cannot be responsible for the discrepancy between the error budget and the measured precision, as the value from Bauer et al. (2020) does not consider on-sky observations. The authors determined the instrument performance based on the point-to-point scatter between the nightly calibrations, corrected for the instrumental drift. This means however, that the extraction of the spectra and RVs is explicitly part of the error estimate. While the impact of the Barycentric correction and the extraction of the RV are realistically estimated in my error budget, the uncertainty of the extraction of the spectra is an assumption that was adopted from H16. Besides the improvement of the thermal stability of the instrument, it should be therefore investigated, if the extraction of the CARMENES spectra meets the requirements. Furthermore, the calibration should be excluded as the cause of the large measured instrumental jitter.

Part II:

Follow-up of TESS planet candidates with CARMENES

The CARMENES-TESS
working group

In contrast to the deep, which means on average $K_p > 12\,\text{mag}$, survey of *Kepler* (Borucki et al., 2010; Borucki, 2016), the TESS satellite was built to perform an all-sky survey of bright and nearby stars in order to find planets that are amenable for a precise characterisation using ground-based facilities (Ricker et al., 2015). Thereby, RV follow-up was explicitly intended by the mission concept. As described in subsection 1.1.1, many of those near and bright stars are actually M dwarfs, offering a great synergy between the goals of the TESS mission and the CARMENES survey (see section 1.5). In 2018, the CARMENES consortium therefore decided to devote part of its GTO to the follow-up of TESS planet candidates.

The goal of the CARMENES-TESS WG is to provide an independent confirmation of the TESS planet candidates and to measure their masses using the RV method. Further, combining transit observations with RVs from CARMENES allows for a full planet characterisation as explained in section 1.4.

As described in subsection 1.2.1, M dwarfs are particularly suitable for observing small planets with the RV method. This promoted the CARMENES-TESS WG as an important collaborator to fulfil the TESS level one science requirement, which is to measure the masses of 50 transiting planets with radii smaller than $4\,\text{R}_\oplus$. Many of them will be prime targets for atmospheric characterisation with future instruments such as the JWST or the ELT (Kempton et al., 2018).

The CARMENES-TESS WG is organised as follows. First, a group regularly checks the TOIs issued by the TFOP for candidates around M dwarfs that could be observed with CARMENES. These candidates are discussed and prioritised in meetings with the whole working group regarding their expected scientific output with respect to the required observation time. When the group decides on a target and a false-positive scenario can be excluded by the TFOP working group, the observations are triggered. As soon as the first spectra are available, the CARMENES work package for stellar parameters determines the properties of the host star as described in subsection 1.1.1. Those are a crucial input for precise planetary parameters, since many of the candidate's hosts were never subject to a detailed investigation. For some stars, long term photometric monitoring is arranged by the CARMENES photometry work package in order to determine the stellar rotation period. The obtained RV measurements are regularly analysed by members

of the CARMENES-TESS WG, and it is checked whether the planet candidate can be confirmed. When sufficient data is available, the target is assigned to a person who begins the analysis and usually ultimately leads the publication. For the publication, additional resources of the TFOP are typically used. These can include high-resolution imaging to determine possible contamination of the light curves, as well as follow-up transit observations from ground-based instruments, or RV follow-up, if provided.

In the following, I present the discovery of two planetary systems by the CARMENES-TESS WG around the stars GJ 3473 and GJ 3929, for which I took over the leadership. Besides those two, I also participated in the analysis of other discoveries published by the CARMENES-TESS WG. The complete record can be found at the end of the thesis in the list of my publications.

Discovery of a hot, transiting, Earth-sized planet and a second temperate, non-transiting planet around the M4 dwarf GJ 3473 (TOI-488)

3

Details of authorship: *The text of this chapter was published in Kemmer et al. (2020). I carried out the analysis and the interpretation of the results, as well as prepared the manuscript. Individual shorter text passages, for example parts of the instrument descriptions, were contributed by co-authors. Further, I incorporated suggestions and corrections by the co-authors and the reviewer during the publication process. The text was fitted to the format and nomenclature of the thesis, which included changes in the figure's format and appearance, as well as the occurrence of used acronyms.*

3.1 Introduction

The detection of transiting planets with the RV method enables us to derive a comprehensive characterisation of their properties. In particular, it permits the measurement of a dynamical planetary mass and, hence, a measurement of the planetary mean density when combined with the planetary radius derived from the transit light curve. From comparisons with theoretical models, the density of a planet provides information about its composition and structure and, therefore, it plays a key role in understanding planet formation and evolution (e.g., Southworth, 2010; Rogers, 2015; Fulton et al., 2017; Bitsch et al., 2019; Zeng et al., 2019). Furthermore, additional non-transiting planets in the system can be detected with the RV method. Such multi-planetary systems hold valuable information because the dynamical interaction between the planets can have a significant influence on their formation and evolution, as well as, shaping the currently observed architecture of the system (e.g., Lissauer, 2007; Zhu et al., 2012; Anglada-Escudé et al., 2013; Mills & Mazeh, 2017; Morales et al., 2019).

A significant fraction of the over 3000 transiting exoplanets known today[1] were discovered by the *Kepler* satellite (Borucki et al., 2010; Borucki, 2016). However, *Kepler*'s focus on faint stars ($K_p{>}12\,\text{mag}$) impeded detailed follow-up studies of those planets using ground-based facilities. In contrast, the TESS is now filling in this gap. To date, TESS has already found more than 50 confirmed transiting planets, and many more candidates, orbiting bright, nearby stars ($G \sim 6$–$13\,\text{mag}$, $d \sim 10$–$340\,\text{pc}$). One of its level-one science requirements is to measure the masses for 50 transiting planets with radii smaller than $4\,\text{R}_\oplus$ by RV follow-up observations[2]. What is particularly interesting in this regime are planets that are orbiting M-dwarf stars. The relative transit depth, and thus the detection probability of rocky planets around M dwarfs, is much higher compared to larger stars of earlier spectral types. Still, despite M dwarfs being the most common stars in our Galaxy (e.g., Chabrier, 2003; Henry et al., 2006) and the fact that small planets are more abundant around later type stars (Howard et al., 2012; Bonfils et al., 2013; Mulders et al., 2015; Dressing & Charbonneau, 2015; Gaidos et al., 2016; Hardegree-Ullman et al., 2019), only a few precise dynamical masses of such planets have currently been determined. Prior to the TESS mission, only 12 planets with radii smaller than $R_p = 2\,\text{R}_\oplus$ and dynamical mass measurements to a precision better than $30\,\%$ were known to orbit stars with temperatures $T_\text{eff} < 4000\,\text{K}$. Thanks to the intensive RV follow-up of TESS planet candidates this number already increased by 7 new planets (see Table A.1 for the full list). The brightness of these cool TESS host stars, combined with their small size, makes many of them ideal targets for atmospheric characterisation by transmission or thermal emission spectroscopy with upcoming space-borne or ground-based instruments (Kempton et al., 2018; Batalha et al., 2018).

Here we report the discovery of a planetary system around the intermediate M dwarf GJ 3473. The inner, Earth-sized planet was first detected as a transiting planet candidate by TESS. Our extensive RV monitoring campaign, using CARMENES, IRD, and HARPS, confirms its planetary nature and reveals a second, more massive, non-transiting planet on a wider orbit. This paper is structured as follows: section 3.2 describes the data used in this study. In section 3.3, the properties of the host star are presented. The analysis of the data is set out in section 3.4 and the results are discussed in section 3.5. Finally, we give our conclusions in section 3.6.

---

[1]On 26 August 2020, 3189 transiting exoplanets were listed by exoplanetarchive.ipac.caltech.edu/
[2]https://heasarc.gsfc.nasa.gov/docs/tess/primary-science.html, visited on 28 June 2020

Chapter 3 Discovery of a hot, transiting, Earth-sized planet and a second temperate, non-transiting planet around the M4 dwarf GJ 3473 (TOI-488)

3.2 Data

3.2.1 TESS

GJ 3473 (TIC 452866790) was observed by TESS with a two-minute cadence in Sector 7 (Camera #1, CCD #3) between 7 January and 2 February 2019 and is listed to have a transiting planet candidate on the TESS releases website (TOI–488.01). Due to its proximity to the ecliptic plane, it will not be observed again by TESS during its primary mission, but will be revisited in Sector 34 of the TESS extended mission in the third year[3]. The time series had a gap between $BJD = 2458503.04$ and $BJD = 2458504.71$ because of the data downlink and telescope re-pointing (see Figure 3.2). The light curves produced by the Science Processing Operations Center (SPOC, Jenkins et al. 2016) are available on the Mikulski Archive for Space Telescopes[4]. For our analysis, we used the systematics-corrected simple aperture photometry (PDCSAP) light curve (Smith et al., 2012; Stumpe et al., 2012, 2014). A plot of the target pixel file and the aperture mask that is used for the SAP, generated with `tpfplotter` (Aller et al., 2020), is shown in Figure 3.1. The TESS data have a median internal uncertainty of $2.35\,\mathrm{ppt}$ (parts per thousand) and rms of $2.2\,\mathrm{ppt}$ around the mean. See Luque et al. (2019), Dreizler et al. (2020), Nowak et al. (2020), and Bluhm et al. (2020) for further details on the applied methodology.

3.2.2 High-resolution spectroscopy

High-resolution follow-up spectroscopy of the TESS planet candidates is arranged by the TESS follow-up programme (TFOP) "Precise Radial Velocities" SG4 subgroup[5]. The goal is to achieve a full validation of the candidates and to ultimately provide their mass measurement.

CARMENES. As part of the CARMENES guaranteed time observation programme to search for exoplanets around M dwarfs (Reiners et al., 2018a), we observed GJ 3473 with CARMENES. CARMENES is a high-resolution spectrograph at the $3.5\,\mathrm{m}$ Calar Alto telescope that consists of two cross-dispersed Échelle channels operating in the spectral ranges of $0.52\,\mu\mathrm{m}$ to $0.96\,\mu\mathrm{m}$ in the visible light (VIS, $R = 94\,600$) and $0.96\,\mu\mathrm{m}$ to $1.71\,\mu\mathrm{m}$ in the near infrared (NIR, $R = 80\,400$), respectively. The observations began at the end of March 2019, just after the announcement of the transiting planet candidate, and ended in January 2020. In this period, we collected 67 pairs of VIS and NIR spectra with

---

[3] https://heasarc.gsfc.nasa.gov/cgi-bin/tess/webtess/wtv.py?Entry=452866790, visited on 28 April 2020
[4] https://mast.stsci.edu
[5] https://tess.mit.edu/followup/
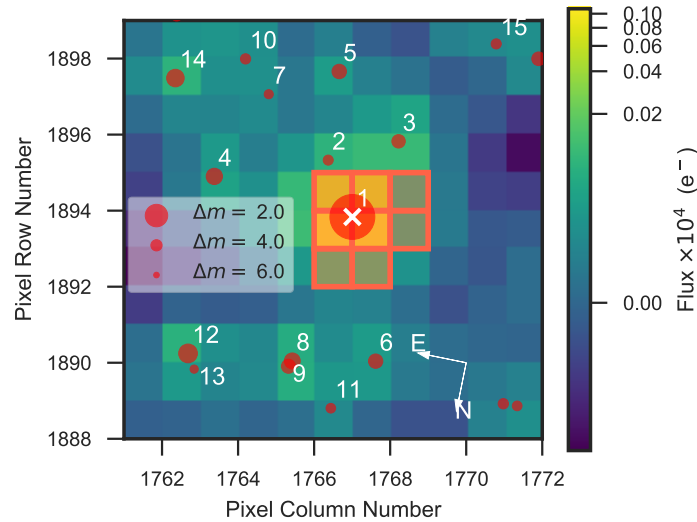
Fig. 3.1.: TESS target pixel file of GJ 3473. The planet-host star is marked by a white cross and the pixels of the aperture mask used for the retrieval of the light curve are highlighted with orange borders. Sources listed in the Gaia DR2 catalogue (Gaia Collaboration et al., 2018) are indicated by red circles (size proportional to their brightness difference with GJ 3473). Source #3 is LP 544–12, the common proper motion companion to GJ 3473.

exposure times of about $30\,\mathrm{min}$ each. Within the standard CARMENES data flow, the spectra are calibrated using `caracal`, while the RVs are calculated using `serval`. The RVs are corrected for barycentric motion, secular perspective acceleration, as well as instrumental drift. To reconstruct small systematic radial-velocity variations, so called nightly zero-point offsets, we use the measured RVs of all other stars with only small intrinsic RV variations from the respective observing nights (see Trifonov et al., 2018; Tal-Or et al., 2019; Trifonov et al., 2020, for details). Spectra without simultaneous FP drift measurements or a S/N lower than 10 are excluded during the process, which results in a total of 64 RV measurements in the VIS and 66 in the NIR. The RVs show a median internal uncertainty of $2.1\,\mathrm{m\,s^{-1}}$ and a weighted rms (wrms) of $3.8\,\mathrm{m\,s^{-1}}$ in the VIS and $11.7\,\mathrm{m\,s^{-1}}$ and $15.6\,\mathrm{m\,s^{-1}}$ in the NIR, respectively. The high scatter in the NIR channel corresponds to our expectation from the photon-noise limit considering the median measured S/N of ~ 63 for the NIR observations (see Bauer et al., 2020, for a detailed analysis of the performance of CARMENES). Due to the low RV amplitude of the transiting planet candidate ($K \approx 2.2\,\mathrm{m\,s^{-1}}$), we therefore used only the VIS data for this study.

IRD. In the course of the Subaru IRD TESS Intensive Follow-up Project (proposal S19A-069I), we observed GJ 3473 with the InfraRed Doppler spectrograph (IRD, Tamura et al., 2012; Kotani et al., 2018), a near-infrared, adaptive optics (AO) corrected, high-

resolution spectrograph ($0.97\,\mu$m to $1.75\,\mu$m, $R \approx 70\,000$) installed on the Subaru 8.2 m telescope. The integration time was set to 300 s to 600 s so that the extracted one-dimensional spectra have S/N ratios of 50–70 per pixel at 1000 nm. A total of 56 frames were acquired for GJ 3473 by IRD on 12 different nights between April 2019 and December 2019, all of which had simultaneous reference spectra from a LFC. The reduction of the raw data was performed with the IRAF Échelle package (Tody, 1993), including the wavelength calibration using Th-Ar HCLs. For the RV analyses, wavelengths were re-calibrated more precisely based on the laser frequency comb spectra. RVs were measured using the forward modelling technique described by Hirano et al. (2020), in which the time-variable telluric absorptions and the instantaneous instrumental profile of the spectrograph were modelled and taken into account in the RV fits. The IRD RVs show a median internal uncertainty of $4.1\,\mathrm{m\,s^{-1}}$ and a wrms of $8.0\,\mathrm{m\,s^{-1}}$.

HARPS. GJ 3473 was also observed by the High Accuracy Radial velocity Planet Searcher (HARPS, Mayor et al., 2003) as part of the ESO programme 1102.C-0339(A). The spectrograph, installed at the European Southern Observatory La Silla 3.6 m telescope, covers the spectral range from $0.378\,\mu$m to $0.691\,\mu$m and has a resolution of $R = 110\,000$. The 32 observations presented here were taken between May 2019 and March 2020. Their exposure times ranged between 30 min and 40 min. We use the reduced spectra from the HARPS DRS (Lovis & Pepe, 2007) and compute their RVs following Astudillo-Defru et al. (2017c), which resulted in a lower rms scatter compared to the RVs retrieved with the serval pipeline. They are calibrated for the barycentric motion, secular perspective acceleration, and instrumental drift. For the HARPS RVs we obtain a median internal uncertainty of $3.4\,\mathrm{m\,s^{-1}}$ and a wrms of $4.8\,\mathrm{m\,s^{-1}}$.

3.2.3 Ground-based transit follow-up

The TFOP subgroup SG1 provides seeing-limited photometry follow-up observations of the TESS planet candidates in order to supplement the available photometry and to provide improved ephemerides for the targets. An overview of the observations, the instruments and the filters used is given in Table 3.1.

LCOGT. We used four transit observations of GJ 3473 from the Las Cumbres Observatory global telescope network (LCOGT, Brown et al. 2013). The observations were taken with the SINISTRO CCDs at the 1 m telescopes of the LCOGT, which have a pixel scale of $0\rlap{.}''389\,\mathrm{pix}^{-1}$ and a FOV of $26' \times 26'$ each. The first transit was observed from the McDonald Observatory (McD) on 19 March 2019 in the z_s filter, two transits were observed from the Cerro Tololo Interamerican Observatory (CTIO) on 21 and 27 February 2020 in i_p filter and one transit in z_s filter on 13 March 2020 from South African Astronomical

Tab. 3.1.: Summary of the ground-based transit follow-up observations.

Telescope	Date	Transit[a]	Filter	t_{exp} [s]	Duration[b] [min]	N_{obs}	Aperture [pix]	rms [ppt]
LCOGT McD	2019-03-19	58	z_s	100	234	110	18	1.25
MuSCAT2	2019-12-21	290	i	30	237	675	32	1.75
MuSCAT2	2019-12-21	290	z_s	20	237	457	32	1.65
MuSCAT2	2020-01-02	300	r	18	254	823	32	2.45
MuSCAT2	2020-01-02	300	i	18	254	845	32	2.12
MuSCAT2	2020-01-02	300	z_s	18	254	845	32	1.60
MuSCAT	2020-01-18	313	r	20	202	553	24	1.85
MuSCAT	2020-01-18	313	z_s	20	202	551	26	1.11
LCOGT CTIO	2020-02-21	341	i_p	60	224	145	20	1.56
LCOGT CTIO	2020-02-27	346	i_p	60	229	145	19	1.58
LCOGT SAAO	2020-03-13	359	z_s	100	230	101	16	1.10

[a] Transit number after the first transit observed by TESS.
[b] Time-span of the observation.

Observatory (SAAO). We calibrated the images with the standard LCOGT `Banzai` pipeline (McCully et al., 2018a,b) and extracted the light curves using `AstroImageJ` (Collins et al., 2017).

MuSCAT. GJ 3473 was observed on 18 January 2020 by the Multi-color Simultaneous Camera for studying Atmospheres of Transiting planets (MuSCAT, Narita et al. 2015) mounted at the $1.88\,\mathrm{m}$ telescope at the Okayama Astro-Complex on Mt. Chikurinji, Japan. MuSCAT is a multi-colour instrument that performs imaging in the g, r and z_s-filter bands at the same time. Each camera has a FOV of $6\farcm1 \times 6\farcm1$ with a pixel scale of $0\farcs358\,\mathrm{pix}^{-1}$. Due to a large scatter in the g band, we only use the r and z_s light curves here. The individual images are corrected for dark current and flat fields, and the light curves are generated using a custom pipeline that is described in Fukui et al. (2011).

MuSCAT2. We made use of two transit observations from MuSCAT2 (Narita et al., 2019). The instrument is mounted at the $1.52\,\mathrm{m}$ Telescopio Carlos Sánchez at the Observatorio del Teide, Spain. MuSCAT2 operates simultaneously in the g, r, i, and z_s passbands and has a FOV of $7\farcm4 \times 7\farcm4$ at $0\farcs44\,\mathrm{pix}^{-1}$ resolution. One transit was observed on 21 December 2019, from which we use the observations in the i and z_s bands. The other transit was observed on 2 January 2020, from which we use the observations in the r, i and z_s bands. Both transits were observed defocussed to optimise the quality of the photometry. The transit signal had too low S/N in the g band to be useful in the fitting,

and the r band observations were affected by systematics on the night of 21 December. The photometry was produced using a dedicated MuSCAT2 photometry pipeline (see Parviainen et al., 2019, for details), and the detrended light curves were created by a fit that aims to simultaneously choose the best target and comparison star apertures, model the systematics using a linear term, and include the transit using PyTransit (Parviainen, 2015).

USAFA. We used the brand-new, recently commissioned $1\,\mathrm{m}$ USAFA Telescope, which is an optically-fast $f/6$ Ritchey-Chrétien telescope with a wide field of view $0°9^2$ and an STA1600 CCD installed on the outskirts of Colorado Springs. We observed GJ 3473 on 04 March 2020. The USAFA data did not firmly detect the transit on target, but ruled out nearby eclipsing binaries in all other stars within the apertures of TESS, LCOGT, and MuSCAT2 (Fig. 3.1).

3.2.4 Photometric monitoring

We used long-term photometric monitoring of GJ 3473 to search for periodic signals associated with the rotation period of the star.

TJO. We observed GJ 3473 with the $80\,\mathrm{cm}$ Joan Oró telescope (TJO, Colomé et al. 2010) at Observatori Astronòmic del Montsec, Spain. The star was monitored between 31 January and 8 May 2020 for a total of 32 nights. Our observations were performed in the Johnson R filter by using the main imaging camera LAIA, which has a 4k $\times$ 4k back illuminated CCD with a pixel scale of $0''\!.4\,\mathrm{pix}^{-1}$ and a FOV of $30'$. We calibrated each image for bias and dark current as well as applied flat field images using the ICAT (Colome & Ribas, 2006) pipeline. Differential photometry was extracted with AstroImageJ using the aperture size and set of comparison stars that minimised the rms of the photometry. Low S/N data due to high airmass or bad weather were removed. The data were binned to one measurement per hour. The median internal uncertainty is $2.7\,\mathrm{ppt}$, while the rms is $9.4\,\mathrm{ppt}$ around the mean. For the estimation of the stellar rotation period with a Gaussian process, we binned these data to one data point per night. This reduces short term variations caused by jitter and yields a median internal uncertainty of $2.9\,\mathrm{ppt}$ and a rms of $7.4\,\mathrm{ppt}$ around the mean.

MEarth. The all-sky transit survey MEarth consists of 16 robotic $40\,\mathrm{cm}$ telescopes with a FOV of $26'$ located at two observatories in the southern and northern hemisphere (Berta et al., 2012). We use archival photometric monitoring data from the MEarth-North project DR8[6] covering the time span from 2008 to 2010 and 2011 to 2018. In total, we

---

[6]https://www.cfa.harvard.edu/MEarth/DR8/

retrieved 6220 observations of GJ 3473 from the archive. They were observed with telescopes 1 and 4 in the broad RG715 filter. For the photometric analysis of the host star, we use the individual nightly binned time series, which shows a median internal uncertainty of $2.6\,\mathrm{ppt}$ and a rms of $8.7\,\mathrm{ppt}$ around the mean.

3.2.5 High-resolution imaging

As part of the standard process for validating transiting exoplanets and to assess the possible contamination of bound or unbound companions on the derived planetary radii (Ciardi et al., 2015), high-resolution images of GJ 3473 were taken within the TFOP "High Resolution Imaging" SG3 subgroup.

Gemini/NIRI. Nine images of GJ 3473 in the Brγ narrow filter ($\lambda_0 = 2.1686; \Delta\lambda = 0.0295\,\mu\mathrm{m}$) were taken with the NIRI instrument mounted at the $8.1\,\mathrm{m}$ Gemini North telescope (Hodapp et al., 2003) on 22 March 2019 as part of the Gemini programme GN-2019A-LP-101. The science frames had an exposure time of $3.5\,\mathrm{s}$ each and were dithered in a grid pattern with $\sim 100\,\mathrm{pix}$ spacing ($\sim 2\overset{''}{.}2$). A sky background image was created by median combining the dithered images. The basic reduction included bad pixel interpolation, flatfield correction, sky background subtraction, and alignment and co-adding of the images.

Keck/NIRC2. The Keck Observatory observations were made with the NIRC2 instrument on the $10\,\mathrm{m}$ Keck II telescope behind the natural guide star AO system (Service et al., 2016, and references therein). The observations were taken on 25 March 2019 in the standard three-point dither pattern that is used with NIRC2 to avoid the left lower quadrant of the detector, which is typically noisier than the other three quadrants. The dither pattern step size was $3''$ and was repeated four times. The observations were also obtained in the narrow-band Brγ filter ($\lambda_0 = 2.1686; \Delta\lambda = 0.0326\,\mu\mathrm{m}$) with an integration time of $20\,\mathrm{s}$ with one coadd per frame for a total of $300\,\mathrm{s}$ on target. The camera was in the narrow-angle mode with a full field of view of $\sim 10''$ and a pixel scale of $0\overset{''}{.}099\,442\,\mathrm{pix}^{-1}$.

3.3 Properties of GJ 3473

The star GJ 3473 (G 50–16, Karmn J08023+033) was included in the TESS Input Catalogue as TIC 452866790 and was declared a TESS object of interest (TOI-488) after the transiting planet candidate was found. A summary of the stellar parameters is given in Table 3.2. The star was classified as an M4.0 V star by Hawley et al. (1996), but it was never subject to an in-depth analysis of its properties (e.g., Newton et al.,

Tab. 3.2.: Stellar parameters of GJ 3473

Parameter	Value	Ref.
Name and identifiers		
Name	GJ 3473	Gli91
Alt. name	G 50–16	Gic59
Karmn	J08023+033	Cab16
TIC	452866790	Stas19
TOI	488	TESS releases
Coordinates and spectral type		
α (J2000)	08 02 22.88	*Gaia* DR2
δ (J2000)	+03 20 19.7	*Gaia* DR2
Sp. type	M4.0 V	Haw96
G [mag]	12.4650 ± 0.0003	*Gaia* DR2
T [mag]	11.1972 ± 0.0073	Stas19
J [mag]	9.627 ± 0.023	2MASS
Parallax and kinematics		
$\mu_\alpha \cos\delta$ [mas yr^{-1}]	-403.17 ± 0.09	*Gaia* DR2
μ_δ [mas yr^{-1}]	-381.01 ± 0.05	*Gaia* DR2
π [mas]	36.52 ± 0.05	*Gaia* DR2
d [pc]	27.39 ± 0.04	*Gaia* DR2
γ [km s^{-1}]	-1.101 ± 0.011	This work
U [km s^{-1}]	-3.11 ± 0.05	This work
V [km s^{-1}]	-27.66 ± 0.06	This work
W [km s^{-1}]	-66.44 ± 0.07	This work
Photospheric parameters		
$T_{\rm eff}$ [K]	3347 ± 54	This work
$\log g$ [dex]	4.81 ± 0.06	This work
[Fe/H] [dex]	$+0.11 \pm 0.19$	This work
Physical parameters		
$L_\star$ [$L_\odot$]	0.01500 ± 0.00019	This work
$R_\star$ [$R_\odot$]	0.364 ± 0.012	This work
$M_\star$ [$M_\odot$]	0.360 ± 0.016	This work
Activity parameters		
pEW' (Hα) [Å]	$+0.08 \pm 0.15$	This work
$\log R'_{\rm HK}$ [dex]	-5.62 ± 0.22	This work
$v \sin i$ [km s^{-1}]	< 2	This work
$P_{\rm rot}$ [d]	168.3 ± 4.2	This work

References. Gli91: Gliese & Jahreiß (1991); Gic59: Giclas et al. (1959); Cab16: Caballero et al. (2016a); Stas19: Stassun et al. (2019); *Gaia* DR2: Gaia Collaboration et al. (2018); Haw96: Hawley et al. (1996); 2MASS: Skrutskie et al. (2006).

2014). To determine precise stellar parameters, we used the high-resolution spectra from the CARMENES follow-up observations. Following Passegger et al. (2018, 2019) and applying a measured upper limit of $v \sin i = 2 \, \mathrm{km \, s^{-1}}$, we calculated the effective temperature T_{eff}, $\log g$, and [Fe/H] from a fit to a grid of PHOENIX stellar atmosphere models (Husser et al., 2013) using a χ^2 method. The derived T_{eff} matches the literature spectral type taking into account the uncertainties in both parameters (Alonso-Floriano et al., 2015; Passegger et al., 2018; Cifuentes et al., 2020). Next, we determined the bolometric luminosity, $L_\star$, by integrating the spectral energy distribution in 14 broad passbands from optical B to $W4$ with the *Gaia* DR2 parallax (Gaia Collaboration et al., 2018) as in Cifuentes et al. (2020). The radius, $R_\star$, was subsequently calculated using the Stephan-Boltzmann law. Lastly, the mass, $M_\star$, was derived from the Schweitzer et al. (2019) empirical mass-radius relation derived from eclipsing binaries. The values determined in this way are consistent with the mass and radius determined from isochrones (Morton, 2015). We updated the Galactocentric space velocities UVW according to Cortés-Contreras (2016) by combining the *Gaia* DR2 parameters and the absolute velocity measured from the CCF of the spectra with a weighted binary mask (Lafarga et al., 2020). Using the space velocities and the BANYAN Σ Bayesian classification tool (Gagné et al., 2018), we found no indication that GJ 3473 is a member of any nearby young stellar association. Instead, it is most probably a field star located in the Galactic thin disk.

GJ 3473 is listed in the Washington Double Star catalogue (Mason et al., 2001) as the primary of the binary system LDS 5160 (Luyten Double Star), with a date of first satisfactory observation in 1949. The secondary, at an angular separation of $49\rlap{.}''29 \pm 0\rlap{.}''09$ to the southeast of GJ 3473 ($\theta = 222\rlap{.}°8 \pm 14\rlap{.}°1$), is LP 544–12 (GJ 3474, source #3 in Figure 3.1), a $J = 12.2$ mag M6 V star that shares the proper motion and parallax values of our planet-host star, but with a third of its mass (Luyten, 1979; Reid et al., 1995; Newton et al., 2017). At the distance of GJ 3473, the angular separation between the two stars translates into a projected physical separation of 1349.9 ± 3.1 au.

3.4 Analysis and results

3.4.1 Transit search within the TESS light curve

A transiting planet candidate around GJ 3473 was announced on 14 March 2020 via the TESS releases website[7]. The candidate passed all tests from the SPOC Data Validation Report (Twicken et al., 2018; Jenkins, 2002; Li et al., 2019) and it is listed on the Exoplanet Follow-up Observing Program[8] webpage as having a period of $1.1981 \, \mathrm{d}$ and a

---

[7] https://tess.mit.edu/toi-releases
[8] https://exofop.ipac.caltech.edu/tess/target.php?id=452866790
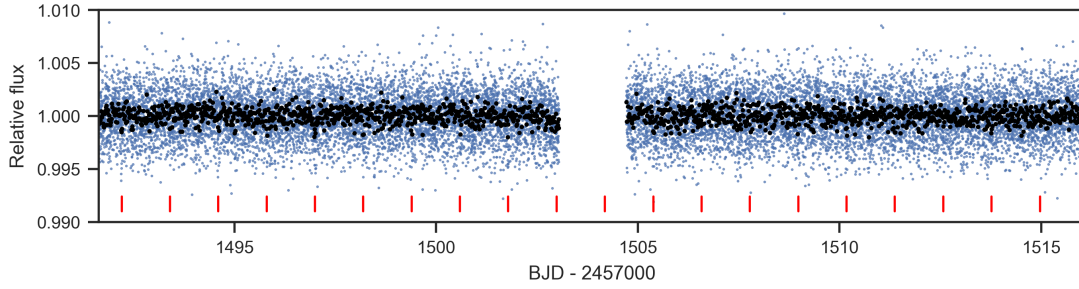
Fig. 3.2.: TESS systematic-corrected PDCSAP light curve. The blue dots are the measurements and the black dots are the data binned to $20\,\mathrm{min}$. The transit times are marked by red ticks.
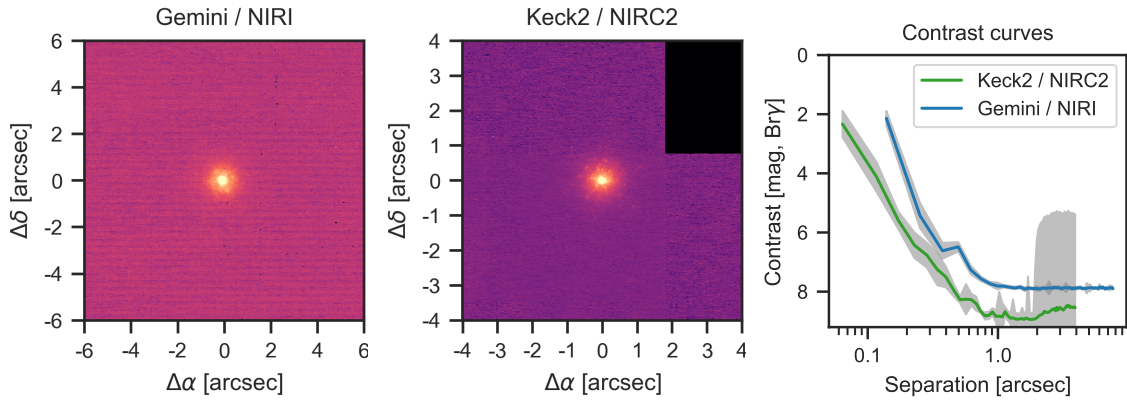
Fig. 3.3.: AO images and contrast curves of the Keck II and Gemini North observations of GJ 3473. The grey shaded regions in the contrast curves are the uncertainty, which apparently rises dramatically for NIRC2 because of a dead quadrant.

transit depth of $1.051\,\mathrm{ppt}$. We performed an independent transit search on the PDCSAP light curve using the Transit-Least-Squares (TLS, Hippke & Heller 2019)[9] method. We consider a signal to be significant if it reaches a signal detection efficiency (SDE; Alcock et al., 2000; Pope et al., 2016) of at least SDE ≥ 8. The TLS shows a highly significant transit signal ($P \approx 1.1979\,\mathrm{d}$) with an SDE of ~ 18.4 and a transit depth of $1.071\,\mathrm{ppt}$. After pre-whitening of the photometric data by fitting for this signal, a TLS of the residuals shows no remaining significant signals with SDE ≥ 8.

3.4.2 Adaptive-optics imaging and limits of photometric contamination

As part of our standard process for validating transiting exoplanets and to assess the possible contamination of bound or unbound companions on the derived planetary radii (Ciardi et al., 2015), we investigated the deep AO images from NIRC2 at Keck II and

---

[9] https://github.com/hippke/tls

NIRI at Gemini North shown in Figure 3.3. Both images were taken in Brγ narrow filters. No companions are visible to a separation of $7''.5$. The contrast curves are obtained by injecting fake sources of different brightness at different separations from the star and determining the radial 5σ detection limit. The NIRC2 observations are sensitive up to a contrast of $\Delta m = 8.3\,\mathrm{mag}$ at a separation of $0''.5$ to the star, but only span the region of the inner $3''$ to $4''$. The area further out up to $6''.0$ is covered by the NIRI image, which reaches a contrast level of $\Delta m = 7.9\,\mathrm{mag}$. We therefore conclude, based on a combination of the contrast curves, a visual inspection of the AO images in Figure 3.3, and the Baraffe et al. (2003) COND models for an approximate solar age, that GJ 3473 does not have a high-mass brown dwarf or more massive companion at 13–160 au. Furthermore, using additional 2MASS imaging and *Gaia* DR2 astro-photometry, we ruled out the presence of stellar companions of any mass at separations beyond 160 au up to a few thousands au (excluding the known companion LP 544–12). Another indicator for binarity is the re-normalised a posteriori mean error of unit weight (RUWE), which quantifies the goodness-of-fit of the astrometric solution in the *Gaia* DR2 (Arenou et al., 2018; Lindegren et al., 2018). At approximate separations between 1.3 au and 13 au, any hypothetical stellar companion would cause GJ 3473 to have a *Gaia* RUWE value larger than 1.41 (its actual value is 1.06; Cifuentes et al., 2020, and references therein) and an asymmetric point spread function in the NIRC2 and NIRI images. At separations closer than 1.3 au, we would see a double-peaked CCF or a long-term trend in the CARMENES RV data. We cannot exclude, however, the presence of substellar objects of a few Jupiter masses at wide separations (with orbital periods much longer than the RV coverage) or unfavourably aligned objects at close separations.

Additionally, we assessed the photometric contamination of the TESS light curves using Eq. 6 in Espinoza et al. (2019a). From the AO images, we obtained upper limits from $5\,\mathrm{mag}$ to $8\,\mathrm{mag}$ in contrast for the inner area from $0''.15$ to $7''.5$, which correspond to contamination below than $1\,\%$. For the nearby *Gaia* sources apparent in Figure 3.1, we make use of the fact that the TESS and *Gaia* G_{RP}-band filter are very similar. We find that for the brightest nearby source (# 3 in Figure 3.1), which is its binary companion LP 544–12, the dilution factor would be 0.96. However, given the separation of $48''.9$ to GJ 3473, this is negligible and, thus, we assume for our modelling that there are no contaminating sources nearby.

3.4.3 Transit-only modelling

In order to refine the orbital period of the transiting planet candidate that was determined from the TLS analysis and to evaluate whether the individual follow-up observations show adequate transit detections, we first investigated the photometric observations separately from the RV measurements.

For all modelling tasks in this work, we used `juliet` (Espinoza et al., 2019a)[10], a fitting tool that uses nested sampling to efficiently evaluate the parameter space of a given prior volume and to allow for model comparison based on Bayesian evidences. Here, `juliet` combines publicly available packages for RVs and transits, namely, `radvel` (Fulton et al., 2018)[11] and `batman` (Kreidberg, 2015)[12]. It allows us to choose among a range of different nested sampling algorithms for the fitting. We opted for `dynesty` (Speagle, 2020)[13] because of its simple usage with regard to multi-processing. Additionally, `juliet` provides the implementation of GPs in the models using either `george` (Ambikasaran et al., 2015)[14] or `celerite` (Foreman-Mackey et al., 2017)[15].

As a first step, we modelled all of the 15 available ground based follow-up observations of transit events obtained by the TFOP SG1[16] separately with the TESS light curve while fitting for the transit centre of each transit (see Eastman et al., 2019, and the documentation of `juliet` for details of the implementation). In doing so, we re-parametrised the scaled semi-major axis to the stellar density, ρ_*. In this manner we can make use of the derived stellar parameters to obtain a density estimation as a fit prior. Furthermore, we implement the parameter transformation suggested by Espinoza (2018) and fit for the parameters, r_1 and r_2, instead of the planet-to-star radius ratio, p, and the impact parameter, b. A quadratic limb-darkening model is used for the TESS data (Espinoza & Jordán, 2015), which is parametrised by the q_1 and q_2 parameters (Kipping, 2013), while a linear model is used for the ground-based follow-up observations. We used a linear term to detrend the LCOGT and MuSCAT light curves with airmass, while the MuSCAT2 light curves were pre-detrended (see subsection 3.2.3). Based on the results from subsection 3.4.2, we fix the dilution factor to one for all instruments, but consider free individual instrumental offsets. Also instrumental jitter terms are taken into account and added in quadrature to the nominal instrumental errorbar.

By carrying out this pre-analysis we were able to disregard observations that show no, or only marginal transits, or seem to be only apparent transits with transit centres far from a linear ephemeris. The final dataset, which is presented in section 3.2 and which we use for the analysis in this work, includes 7 transit events with 11 observations of firm transit detections (cf. Table 3.1).

In the next step, we combined these observations and fit for a common period and time of transit centre that serve as a basis for the joint analysis. In doing so, we determine $P = 1.1980034^{+0.0000022}_{-0.0000023}$ d and $t_0 = 2458492.20410^{+0.00052}_{-0.00050}$.

---

[10]https://juliet.readthedocs.io/en/latest/
[11]https://radvel.readthedocs.io/en/latest
[12]https://www.cfa.harvard.edu/~lkreidberg/batman/
[13]https://github.com/joshspeagle/dynesty
[14]https://george.readthedocs.io/en/latest/
[15]https://celerite.readthedocs.io/en/stable
[16]As of 13 March 2020
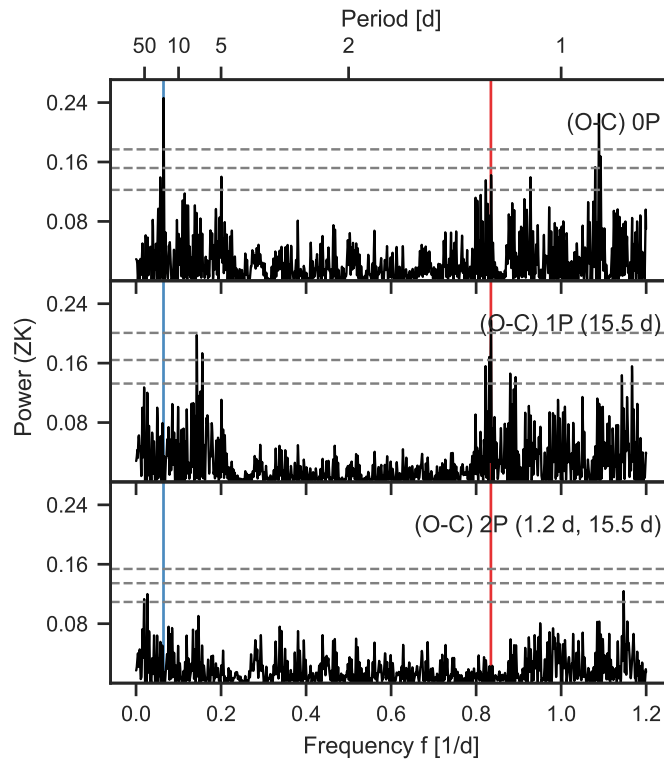
Fig. 3.4.: GLS periodograms of the RV measurements. Vertical lines mark the transiting planet (b, solid red) and the new RV planet (c, solid blue). The horizontal dashed grey lines show the false alarm probability (FAP) of 10%, 1% and 0.1% determined from $10\,000$ random realisations of the measurements.

3.4.4 RV-only modelling

We approach the analysis of the RVs with a signal search in the data, proceeding as if we do not know of the transiting planet a priori. In Figure 3.4 the GLS of the residuals from different fits of increasing complexity to the combined RVs from CARMENES, IRD, and HARPS are shown. We normalised the periodograms using the parametrisation of Zechmeister & Kürster (2009, ZK). For all fits, we used Gaussian distributed priors for the signal of the transiting planet candidate based on the results from subsection 3.4.3 and a narrow uniform range around the peak of the second signal. Instrumental offsets and jitter are treated separately for each dataset. For comparison we list the Bayesian evidences of the fits in Table 3.4.

The first panel in Figure 3.4 shows the periodogram of the residuals after fitting a flat model that only includes offsets and instrumental jitter to the CARMENES, IRD, and HARPS measurements. The strongest signal apparent in the RV data is a period at $15.5\,\mathrm{d}$. After subtracting this periodicity with a circular Keplerian fit, the residual periodogram shows a significant signal (FAP $< 1\%$), coincident with the period of the

transiting planet at $P \approx 1.198\,\mathrm{d}$ (see the middle panel of Figure 3.4). The FAP for a signal to occur especially at this frequency can be evaluated using the method by Baluev (2008) and the power of the signal in a Lomb-Scargle periodogram. By this means, we find a spectral FAP $\approx 0.003\,\%$. We verify this using a bootstrap method of 1×10^6 random realisations over a decreasing frequency range centred on the period in question, which yields FAP $\approx 0.002\,\%$. This is in agreement with the Baluev method and we therefore assume a FAP of $0.002\,\%$ to $0.003\,\%$ for the signal to occur at the expected period. Furthermore, the phase of this signal matches the phase of the planet candidate from TESS and we thus report a highly significant detection of the transiting planet candidate in the RV. The two other signals of significant power at periods of $6.41\,\mathrm{d}$ and $7.00\,\mathrm{d}$ are aliases of the former signal of the transiting planet due to the approximately daily sampling. This is reflected by the fact that they disappear when the $15.5\,\mathrm{d}$ signal is fitted together with the period of the transiting planet at $P \approx 1.198\,\mathrm{d}$ (see the bottom panel of Figure 3.4). Given that RV data provide more information on the eccentricity of an orbit, we performed an analogous analysis using eccentric orbits. We find that the difference between a circular and eccentric orbit is indistinguishable ($\Delta \ln \mathcal{Z} = -0.45$) and, therefore, we use the results for the simpler circular model fits. The residuals of this fit comprising two circular Keplerian signals do not show any further periodicities with FAPs above our significance criterion of $1\,\%$.

3.4.5 Joint modelling

For the final retrieval of the most precise parameters we perform a joint fit of the TESS observations, the ground-based transit follow-ups, and the combined RV data. The model includes two circular planets: firstly, the transiting planet that is detected in the photometry and RV data; secondly, a non-transiting planet that is only apparent in the RV data. The model of the joint fit comprises 58 free parameters, which turns the fit into a high-dimensional problem. A fit with uninformed priors would therefore be very costly. Hence, we make use of the findings from the photometry-only analysis in subsection 3.4.3 and the RV-only analysis in subsection 3.4.4 – that is, we implement Gaussian distributed priors for the planetary parameters, as, for example, in Brahm et al. (2019); Espinoza et al. (2019b); Kossakowski et al. (2019); Luque et al. (2019) or Bluhm et al. (2020). Since we use uninformed priors for the planetary parameters for the transit and RV-only fits, nested sampling warrants an efficient exploration of the possible parameter space fitting the individual datasets. Planetary parameters specific to a given data type, such as the planetary semi-amplitude in RV data or planet-to-star radius (and others) in transit data, would not change significantly in a joint fit as they are independent from the other data to first order. Generally, this also holds true for the shared parameters since they are mostly driven by either one or the other method. Likewise, using the posterior results

Tab. 3.3.: Posterior parameters of the joint fit of the transit and RV data.

Parameter	Posterior[a]	Units
Stellar parameters		
$\rho_\star$	$10.93^{+0.66}_{-0.69}$	$\mathrm{g\,cm^{-3}}$
Planetary parameters		
P_b	$1.1980035^{+0.0000018}_{-0.0000019}$	d
$t_{0,b}$	$2458492.20408^{+0.00043}_{-0.00042}$	d
$r_{1,b}$	$0.557^{+0.044}_{-0.049}$	...
$r_{2,b}$	$0.03184^{+0.00069}_{-0.00067}$	...
K_b	$2.21^{+0.35}_{-0.35}$	$\mathrm{m\,s^{-1}}$
$\sqrt{e_b}\sin\omega_b$	0 (fixed)	...
$\sqrt{e_b}\cos\omega_b$	0 (fixed)	...
P_c	$15.509^{+0.033}_{-0.033}$	d
$t_{0,c}$	$2458575.62^{+0.42}_{-0.43}$	d
K_c	$3.75^{+0.45}_{-0.42}$	$\mathrm{m\,s^{-1}}$
$\sqrt{e_c}\sin\omega_c$	0 (fixed)	...
$\sqrt{e_c}\cos\omega_c$	0 (fixed)	...

[a] Error bars denote the 68% posterior credibility intervals. The posteriors of the instrumental parameters are continued in Table A.4.

from the transit-only and RV-only fits as a prior knowledge for the joint fit is therefore justified given that the chosen prior volume for the joint fit does not restrict the posterior volume from the individual fits. Following this, the width of the priors that we choose for the planetary parameters of the joint fit are three times the standard deviation of the posterior results from the individual best fits. It limits the computational cost, but still allows the nested sampling algorithm to freely explore the parameter space since the Gaussian distribution has no strict borders. In the end, the posterior distribution of our joint fit is much narrower than that of the input priors, which shows that the input priors were conservatively chosen to map the relevant parameter space and did not reject crucial possible solutions. Descriptions and justifications of the adopted instrumental parameters and priors can be found in the respective subsections subsection 3.4.3 and subsection 3.4.4. A summary of the used priors is given in Table A.2.

In Figure 3.6 and Figure 3.5, we show the final models of the joint fit based on the posterior of the sampling. The median posteriors of the planetary parameters are shown

in Table 3.3 and the full list of the posteriors of the instrumental parameters is given in Table A.4.
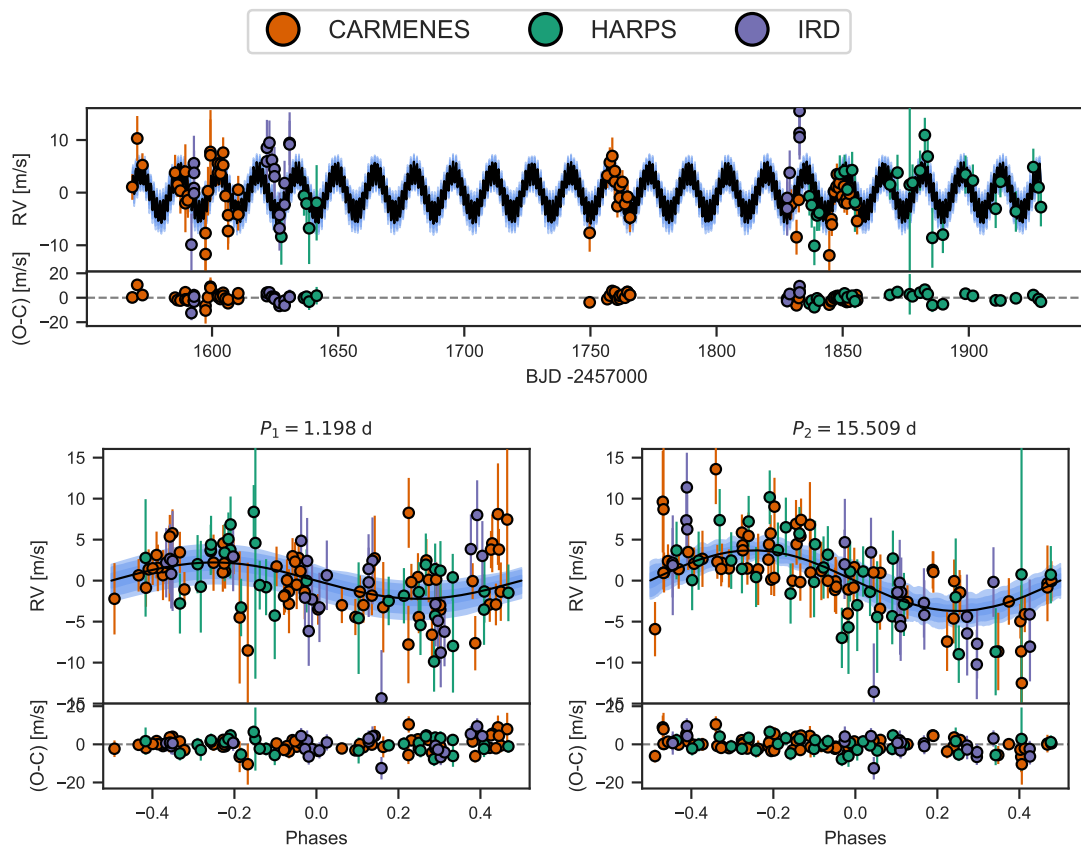
Fig. 3.5.: Results from the joint fit for the RV data of CARMENES, IRD, and HARPS. The top part of each panel shows the measurements as coloured circles – error bars include the instrumental jitters added in quadrature – and the median of the best-fit `juliet` model as the black curve. The grey shaded areas mark the $68\,\%$, $95\,\%$ and $99\,\%$ credibility intervals. To avoid overcrowding of the figure, we binned the IRD data, which were taken with a high cadence, to chunks of $30\,\mathrm{min}$ each. In the lower part, the residuals after the model is subtracted (O-C) are shown. *Top panel:* RVs over time. *Bottom panels:* RVs phase-folded to the periods of the transiting planet (*left*) and the new RV planet (*right*).
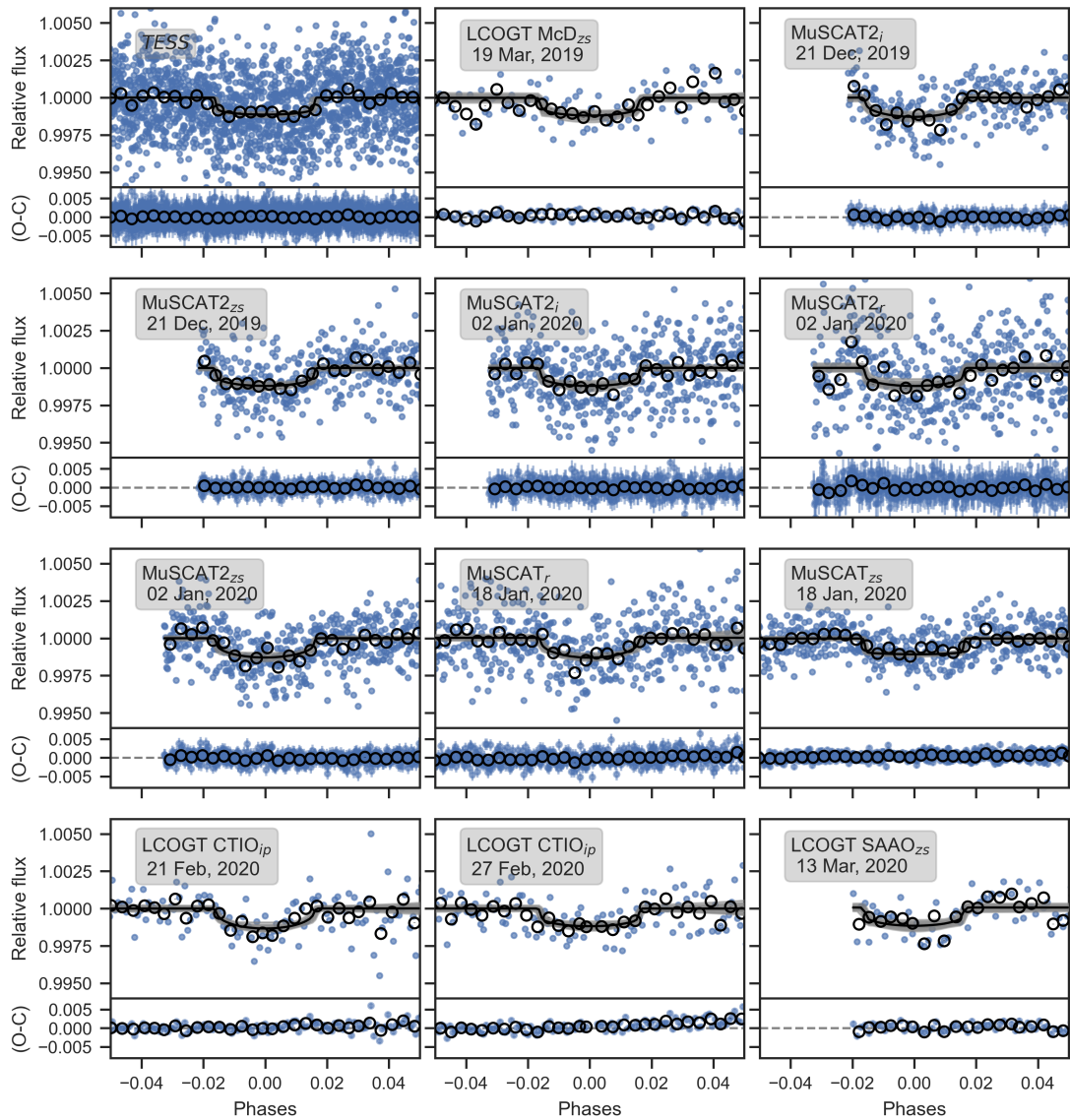
Fig. 3.6.: Results from the joint fit for the transit observations. In the top part of each panel, the black curve presents the best-fit `juliet` model together with the 68%, 95% and 99% credibility intervals displayed by the grey shaded regions. The observations of the respective instruments are phase-folded to the period of the transiting planet. For the fit, the individual data points (blue) are used, but the binned data are also shown for clarity (white circles). Error bars of the individual measurements with the instrumental jitter terms added in quadrature are only displayed in the bottom part of the panels, which show the residuals after subtracting the model (O-C). The names of the instruments and the dates of the observations are denoted in the grey boxes in the upper left corner of each panel.

3.4.6 Stellar activity

We investigated a set of activity indicators derived from the CARMENES spectra to search for signals of stellar activity that would interfere with the transiting planet candidate or provide information on the origin of the second periodicity that is visible in the RV data (see subsection 3.4.4). In Figure 3.7, the GLS periodograms of 13 selected activity indicators, as well as our applied nightly zero-point offsets, are shown. The CRX and the differential line width (dLW) are products of the `serval` reduction pipeline (Zechmeister et al., 2018). From the CCF (see section 3.3), the full-width at half-maximum, the contrast, and the bisector span are determined (Lafarga et al., 2020). The pEW′ after subtraction of an inactive template spectrum of the chromospheric Hα, Ca II IRT (a, b and c), He I $\lambda 10\,833$ Å and He I D$_3$ lines, and the photospheric TiO $\lambda 7050$ Å and TiO $\lambda 8430$ Å indices are calculated following Schöfer et al. (2019).

A measured median pEW′ of the Hα line of $+0.08 \pm 0.15$ Å indicates that GJ 3473 is a rather inactive star (Jeffers et al., 2018). We find a significant, although moderate, correlation between RV and the CRX and Na I D activity indices, however the GLS periodograms from the extensive set of activity indicators do not show any power at the frequencies of the transiting planet candidate or the 15.5 d signal. The dLW, CCF contrast, TiO $\lambda 7050$ Å and He I $\lambda 10\,833$ Å show a forest of signals with $1\% < \text{FAP} < 10\%$ in the range of approximately 30 d to 100 d. This is consistent with a lower limit of the stellar rotation period to be longer than ~ 9 d as determined from $v \sin i < 2\,\text{km s}^{-1}$, however there is no common periodicity or conclusive pattern, which would hint at the rotation period of the star. The most significant signal, which is apparent in the He I $\lambda 10\,833$ Å indicator, has a period of around 100 d. From the HARPS spectra we derive $\log R'_{\text{HK}} = -5.62 \pm 0.22$, which is equivalent to a stellar rotation period of 109 ± 37 d following the R'_{HK} vs. P_{rot} relationship of Astudillo-Defru et al. (2017a). We also investigated GLS periodograms of the HARPS activity indicators derived by the DRS pipeline, but we do not find any significant periodicity and, therefore, we do not present them here.

3.4.7 Photometric stellar rotational period

We combined the R-band TJO data collected between January and May 2020 and the RG715-band MEarth data taken between 2008 and 2018 to determine a stellar rotation period. A marginalised likelihood periodogram (MLP, Feng et al. 2017) analysis of the combined data, where we fit for jitter and offsets between the datasets, indicated a preliminary periodicity of 160 d. The MLP uses sinusoidal functions to model possible significant signals. However, stellar activity tends to be quasi-periodic and can also deviate significantly from a simple sinusoidal. Thus, we used a GP to fit the photometry in a second approach.
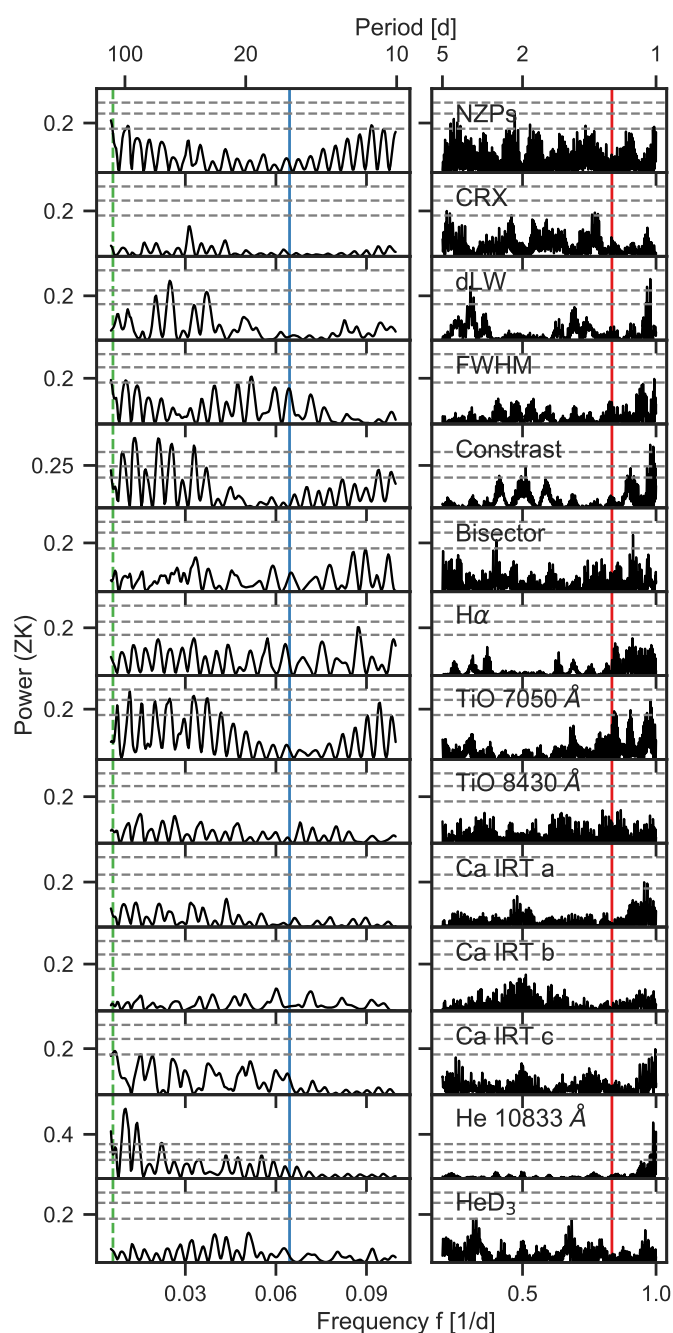
Fig. 3.7.: GLS periodograms of a number of activity indicators based on spectroscopic data obtained by CARMENES, split into two frequency ranges. The vertical lines mark the frequencies of the transiting planet candidate (red solid), the $15.5\,\mathrm{d}$ periodicity visible in the RV (blue solid; see subsection 3.4.4), and the determined photometric rotation period (dashed green; see subsection 3.4.7). The horizontal grey lines show the FAP of $10\,\%$, $1\,\%$ and $0.1\,\%$ determined from $10\,000$ random realisations of the measurements.
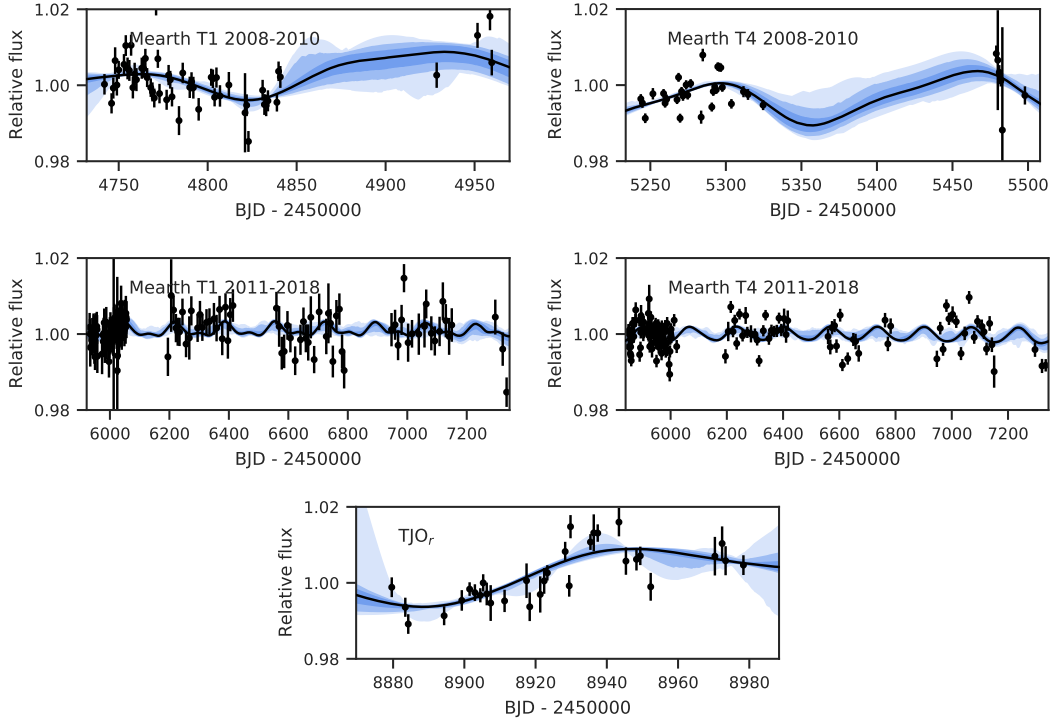
Fig. 3.8.: Gaussian process fits to the photometric monitoring data of GJ 3473. From top to bottom: MEarth T1 2008-2010, MEarth T4 2008-2010, MEarth T1 2011-2018, MEarth T4 2011-2018, and TJO. The black line shows the median GP model extracted for each instrument and the blue shades denote the $68\,\%$, $95\,\%$ and $99\,\%$ confidence intervals.

We used `juliet` and select the quasi-periodic kernel by `george` for the modelling of the photometric data:

$$k_{i,j}(\tau) = \sigma_{GP}^2 \exp\left(-\alpha\tau^2 - \Gamma\sin^2\left(\pi\tau/P_{\mathrm{rot}}\right)\right), \tag{3.1}$$

where σ_{GP} is the amplitude of the GP component given in ppt (or $\mathrm{m\,s^{-1}}$ when applied to RV data), Γ is the amplitude of GP sine-squared component, α is the inverse length-scale of the GP exponential component given in $\mathrm{d^{-2}}$, P_{rot} is the period of the GP quasi-periodic component given in days, and $\tau = |t_i - t_j|$ is the temporal distance between two measurements. To perform a blind search for quasi-periodic signals with the GP model, we put in uninformed priors for σ_{GP}, Γ_i, and α, but take a uniform range from $2\,\mathrm{d}$ to $200\,\mathrm{d}$ for P_{rot}.

In doing so, the data of each instrument are averaged into nightly bins because of the large dataset and the computationally expensive log-likelihood evaluation of the used kernel. A daily sampling of the photometry is reasonable since we are searching for signals with periods of at least multiple days (see subsection 3.4.6). Furthermore, binning reduces short-term variations due to jitter and decreases the uncertainties of the
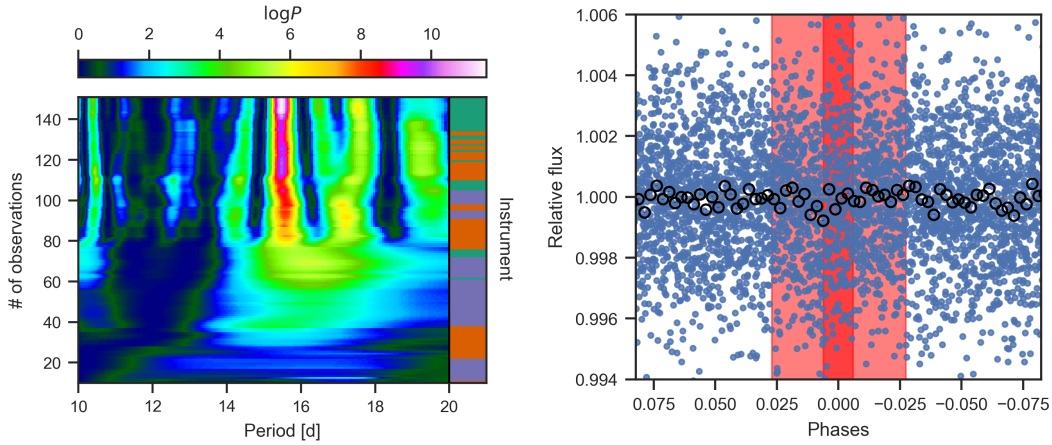
Fig. 3.9.: Investigation of the $15.5\,\mathrm{d}$ signal *Left:* Stacked BGLS periodogram of the residuals after fitting for the transiting planet. The colourbar on the right side indicates the instrument of the corresponding data point (orange: CARMENES, purple: IRD, green: HARPS). *Right*: TESS light curve phase-folded to the period and time of transit centre of GJ 3473 c as determined from the RVs. The saturated red shaded region indicates the expected transit, while the light red shaded region denotes the $68\,\%$ credibility interval of the time of transit centre.

data points. For the GP model, we consider that each dataset can have different solutions for the amplitude parameters, σ_{GP} and Γ. This accounts for the possibility that the stellar activity depends on wavelength and might impact each instrument differently. However, the timescale parameters, such as the rotational period, P_{rot}, and the exponential decay of the signal α, for example, due to spot-life time, should not depend on the instrument. For the latter two parameters, we therefore allow only for global solutions of the GP model. We also model the flux offset between the photometric datasets, as well as an extra jitter component, which is added in quadrature to the diagonal of the resulting covariance matrix. Our GP fit, using unconstrained priors (Table A.3), results in only one specific region within the prior volume that has a high density of posterior samples with high likelihood. We show the nightly binned photometric data and the GP fit with its uncertainties in Fig 3.8.

From the posterior solutions we derive a photometric rotation period, $P_{\mathrm{rot,phot}} = 168.3^{+4.2}_{-3.1}\,\mathrm{d}$ for GJ 3473, which is consistent with the result from the MLP analysis and, within 2σ, with the expected period from $\log R'_{\mathrm{HK}}$. Both estimates show that GJ 3473 is a slow rotator, which should not exhibit strong signals related to activity. This is also in agreement with the spectroscopic activity indicators, which do not exhibit a predominant periodicity and no Hα activity.

Tab. 3.4.: Bayesian log-evidences for the different models used to fit the RVs.

Model	Periods[a] [d]	$\ln \mathcal{Z}$	$\Delta \ln \mathcal{Z}$
0 Planets	...	-474.6 ± 0.2	0
1 Planet	1.20	-468.1 ± 0.2	6.5
1 Planet	15.5	-456.7 ± 0.3	17.9
1 Planet + GP	1.20	-444.9 ± 0.3	29.7
2 Planets	15.5, 1.20	-442.7 ± 0.3	31.9

[a] Rounded to three digits.

3.4.8 Investigation of the $15.5\,\mathrm{d}$ signal

The $15.5\,\mathrm{d}$ signal seems to be unrelated to stellar activity or the stellar rotation period. Following Figure 3.5, the signal looks stable for the entire period of observations and shows no significant deviations from a circular Keplerian motion. However, we thoroughly examined the signal in order to assess its nature and to test whether we can attribute it unambiguously to a planetary origin.

We used `juliet` to perform a model comparison based on the Bayesian evidence of different models, applied to the RV data only, in order to check whether the $15.5\,\mathrm{d}$ signal is indeed best fit with a Keplerian model. The log-evidences of the results are shown in Table 3.4. As outlined by Trotta (2008), we consider a difference of $\Delta \ln \mathcal{Z} > 2$ as weak evidence that one of the models is preferred over the others and $\Delta \ln \mathcal{Z} > 5$ that a model is significantly favoured. We use Gaussian distributed priors based on the posterior solutions from subsection 3.4.3 to account for the transiting planet candidate, and uniform priors for instrumental offsets and jitter. However, we adopted two approaches to include the $15.5\,\mathrm{d}$ signal in the modelling: on the one hand, a simple two-planet model is fitted to the data and on the other hand, we implement a quasi-periodic GP (see Equation 3.1 in subsection 3.4.7) to test the possibility that the second signal does not have a Keplerian nature and is only of a quasi-periodic origin, for example due to stellar activity. We find a difference of ($\Delta \ln \mathcal{Z} = 2.2$) in favour of the two-planet model compared to the model including a quasi-periodic component for the $15.5\,\mathrm{d}$ signal. This offers only a weak evidence, confirming, nonetheless, that the signal is legitimately fitted by a Keplerian model.

Another way to test the coherence of a signal for a given dataset is the use of the so-called stacked Bayesian generalised Lomb-Scargle periodogram (Mortier et al., 2015). The diagram in the left panel of Figure 3.9 shows the probability of the $15.5\,\mathrm{d}$ signal normalised to the minimum of the considered frequency range (Mortier & Collier Cameron, 2017) for an increasing number of observations. The period of the signal is uncertain

when only a few observations are included, but starting with more than 80 observations, a signal of consistently rising probability is detected at the period in question. This indicates that the signal is stable in phase and amplitude over the whole observational period of a $360\,\mathrm{d}$ time baseline, as is likely for a planetary signal. A colour-coded bar on the right side of the diagram specifies which of the instruments the considered data points originate from. As there are no variations of the signal caused by chunks of data from one specific instrument, we can also conclude that the signal is consistent between the different instruments.

Even though there are no obvious signs of more than one transiting planet in the TESS light curve (see subsection 3.4.1), we searched for transits of the $15.5\,\mathrm{d}$ signal based on its parameters derived from the RV observations. Since the period of the planet is larger than half of the time span of the TESS data, which comprise only one sector, a potential transit is likely to occur only once in the data. The right panel in Figure 3.9 shows the TESS data phase-folded to the expected time of transit centre. No obvious transit signals are visible. However, to quantify whether in fact there is no transit signal, we ran two more `juliet` fits on the TESS data using Gaussian distributed priors based on the posterior of the planetary parameters in Table 3.3. The model considering only the transiting planet is favoured by $\Delta \ln \mathcal{Z} \approx 3.6$ over the model that treats the second periodicity as a transiting planet. Thus, we conclude that no significant transiting signal is associated with the $15.5\,\mathrm{d}$ periodicity.

3.5 Discussion

3.5.1 GJ 3473 b

Our derived mass and radius confirm the planetary nature of the transiting planet candidate detected by TESS. GJ 3473 b has a mass of $1.86^{+0.30}_{-0.30}\,\mathrm{M_\oplus}$ and a radius of $1.264^{+0.050}_{-0.049}\,\mathrm{R_\oplus}$, which correspond to a density of $5.03^{+1.07}_{-0.93}\,\mathrm{g\,cm^{-3}}$ and, thus, fits in the regime of Earth-sized planets with a density consistent with a composition dominated by $MgSiO_3$ (see Figure 3.10). A summary of the derived physical parameters of the planet can be found in Table 3.5.

With an insolation flux of $59.4 \pm 5.0\,\mathrm{S_\oplus}$, GJ 3473 b is one of the hottest transiting Earth-mass planets with a dynamical mass measurement that has been detected so far (see Figure 3.11). Its equilibrium temperature corresponds to $773 \pm 16\,\mathrm{K}$, assuming a zero Bond albedo. If the planet had an atmosphere, thermochemical equilibrium calculations predict water and methane to be the dominant opacity sources in the near/mid infrared (NIR/mid-infrared) of the transmission spectrum of GJ 3473 b, assuming a

Tab. 3.5.: Derived planetary parameters of GJ 3473 b and c based on the posteriors of the joint fit.

Parameter	Posterior[a]		Units
	GJ 3473 b	GJ 3473 c	
Derived transit parameters			
$p = R_{\mathrm{p}}/R_{\star}$	$0.03184^{+0.00069}_{-0.00067}$	$\ldots$	$\ldots$
$b = (a/R_{\star})\cos i_{\mathrm{p}}$	$0.336^{+0.066}_{-0.074}$	$\ldots$	$\ldots$
$a/R_{\star}$	$9.39^{+0.19}_{-0.21}$	$\ldots$	$\ldots$
i_p	$87.95^{+0.47}_{-0.45}$	$\ldots$	deg
$u_{1,TESS}$	$0.26^{+0.28}_{-0.18}$	$\ldots$	$\ldots$
$u_{2,TESS}$	$0.10^{+0.28}_{-0.22}$	$\ldots$	$\ldots$
t_T	$0.950^{+0.015}_{-0.014}$	$\ldots$	h
Derived physical parameters[b]			
M_{p}	$1.86^{+0.30}_{-0.30}$	$\geq 7.41^{+0.91}_{-0.86}$	$M_{\oplus}$
R_{p}	$1.264^{+0.050}_{-0.049}$	$\ldots$	$R_{\oplus}$
ρ_{p}	$5.03^{+1.07}_{-0.93}$	$\ldots$	$\mathrm{g\,cm^{-3}}$
g_{p}	$11.4^{+2.1}_{-2.0}$	$\ldots$	$\mathrm{m\,s^{-2}}$
a_{p}	$0.01589^{+0.00062}_{-0.00062}$	$0.0876^{+0.0035}_{-0.0034}$	au
T_{eq}[c]	773^{+16}_{-15}	$329.1^{+6.6}_{-6.4}$	K
S	$59.4^{+5.0}_{-4.5}$	$1.95^{+0.17}_{-0.15}$	$S_{\oplus}$
ESM[d]	6.8 ± 0.3	$\ldots$	$\ldots$

[a] Error bars denote the 68% posterior credibility intervals.
[b] We sample from a normal distribution for the stellar mass, stellar radius and stellar luminosity that is based on the results from section 3.3.
[c] Assuming a zero Bond albedo.
[d] Emission spectroscopy metric (Kempton et al., 2018).

cloud-free solar-abundance scenario[17] (e.g., Madhusudhan, 2012; Mollière et al., 2015; Molaverdikhani et al., 2019a); see the red line in Figure 3.12. In this scenario, the main transmission spectral features in the optical are expected to be alkali (Na and K), although their expected strength depends on a number of parameters such as the planetary atmospheric metallicity. The emission spectrum is heavily muted by water and methane absorption, causing very low relative flux at wavelengths shorter than $\sim 3\,\mu$m; see the blue line in Figure 3.12. The dominant spectral features of a cloudy atmosphere

---

[17]Explanatory note at the time of writing the thesis: meanwhile I consider the scenario of a Hydrogen dominated atmosphere as unlikely. For a discussion of it see the discussion and conclusions in chapter 5
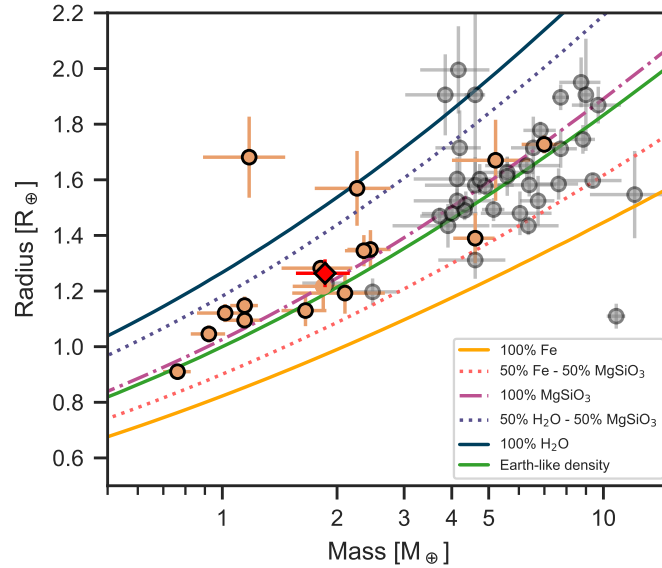
Fig. 3.10.: Mass-radius diagram for small well characterised planets ($R < 2\,\mathrm{R}_\oplus$, $\Delta M < 30\,\%$) based on the TEPcat catalogue (Southworth, 2011, visited on 14 April 2020). Planets orbiting stars with temperature $T_{\mathrm{eff}} < 4000\,\mathrm{K}$ are displayed in orange colour, while the rest is displayed as grey circles. GJ 3473 b is marked with a red diamond. For comparison, theoretical mass-radius relations from Zeng et al. (2016, 2019) are overlayed.

in the optical and NIR are expected to be similar to those of a cloud-free atmosphere, although with lower amplitudes and less pronounced methane features (Molaverdikhani et al., 2020).

In addition, disequilibrium processes could change the composition and thermal structure of the planetary atmosphere. Depending on the exact temperature structure and methane abundance profile, vertical mixing could lead to methane quenching (e.g., Molaverdikhani et al., 2019b). Hydrocarbon haze (soot) production could act as a carbon-sink in the atmosphere, which might cause a reduced carbon-to-oxygen (C/O) ratio (e.g., Molaverdikhani et al., 2019b; Gao et al., 2020). While haze opacities tend to obscure the optical to NIR wavelength range, a reduced C/O ratio could result in an enhancement of CO_2 production. This causes a prominent feature at around $4.5\,\mu\mathrm{m}$ (see e.g., Kawashima & Ikoma, 2019; Nowak et al., 2020). Atmospheres with higher metallicities are likely to lead to more prominent CO_2 features (see e.g., Heng & Lyons, 2016; Molaverdikhani et al., 2019b; Nowak et al., 2020; Schlecker et al., 2020). Hence, this spectral feature appears to be a key feature to retrieve planetary atmosphere metallicities, which, in turn, helps us to understand the formation history of the planet and the stellar system.

The amplitudes of the transmission spectral features of GJ 3473 b are estimated to be around $10\,\mathrm{ppm}$ to $40\,\mathrm{ppm}$ for the discussed model. This poses a challenge for future observations of this planet through transmission spectroscopy. However, the relatively
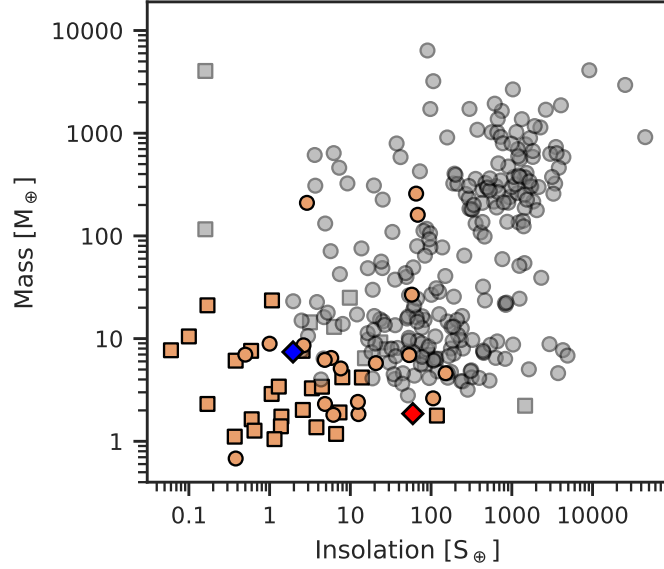
Fig. 3.11.: Mass-insolation diagram for small RV planets based on the planetary systems composite data table of the `exoplanetarchive.ipac.caltech.edu/` (visited on 28 August 2020). Planets orbiting stars with temperature $T_{\mathrm{eff}} < 4000\,\mathrm{K}$ are displayed in orange colour, while the rest is plotted as grey circles. Planets with a dynamical mass measurement are shown as circles and planets with only a minimum mass ($M \sin i$) measurement with boxes. GJ 3473 b and c are marked with red and blue diamonds.

high temperature of this planet causes the emission spectral features at wavelengths longer than $\sim 3\,\mu\mathrm{m}$ to vary from tens of ppm in NIR to hundreds ppm in MIR wavelengths up to $4\,\mu\mathrm{m}$. We calculate the emission spectroscopy metric (ESM), based on Kempton et al. (2018) to be 6.8 ± 0.3, which is close to what Kempton et al. (2018) classify as high-quality atmospheric characterisation targets (ESM > 7.5).

3.5.2 GJ 3473 c

Our RV modelling shows evidence for a second planet in the system. Its derived period is likely not linked to the stellar rotation period of $168\,\mathrm{d}$ as determined in subsection 3.4.7. Furthermore, the analysis of a comprehensive set of activity indicators exhibits no signs of stellar activity at the period in question. The analysis of the pEW′ of the Hα line and the $\log R'_{\mathrm{HK}}$ index describes GJ 3473 as a rather inactive star, which would contradict the relatively high RV amplitude of $\sim 3.8\,\mathrm{m\,s^{-1}}$ if the signal was attributed to activity (cf. subsection 3.4.6). Furthermore, the signal is coherent for at least one year of observations and invariant with respect to the different instruments (see subsection 3.4.8).

We therefore conclude that the $15.5\,\mathrm{d}$ signal in the RVs is caused by a second planet in the system, GJ 3473 c. The planet has a lower mass limit of $7.41^{+0.91}_{-0.86}\,\mathrm{M_\oplus}$. Further physical parameters derived for this planet are shown in Table 3.5. No transit signals
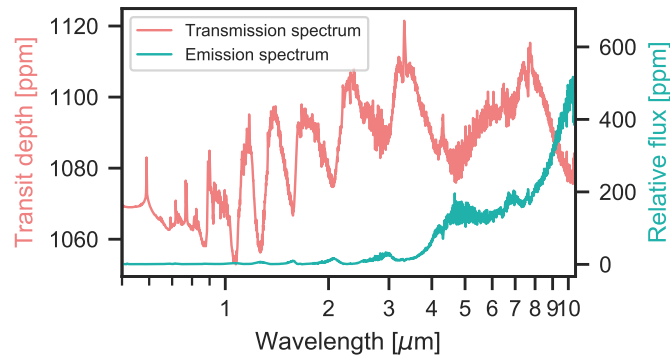
Fig. 3.12.: Representative synthetic cloud free transmission and emission spectrum of GJ 3473 b.

of GJ 3473 c are found within the TESS data. An estimate of its bulk composition from theoretical models is not feasible because the derived mass places the planet just in the regime of the radius dichotomy between super-Earths and mini-Neptunes (e.g., Owen & Wu, 2013; Jin et al., 2014; Fulton et al., 2017; Zeng et al., 2017; Cloutier & Menou, 2020). However, the non-detection of transits is not unexpected when an orbit co-planar to GJ 3473 b ($i = 87.95 \pm 0.47°$) is assumed. The minimum inclination for at least grazing transits at a separation of $0.0876 \pm 0.0035\,\mathrm{au}$ from the host star would be $i > 89.47°$ considering a planet at the empirical upper radius limit for mini-Neptunes. At a distance of $8.66^{+0.13}_{-0.13} \times 10^{-2}\,\mathrm{au}$ from the host star, GJ 3473 c receives $1.98^{+0.17}_{-0.15}$ times the stellar flux compared to Earth, which places it outside the inner boundary of the optimistic habitable zone, $1.49\,\mathrm{S}_\oplus > \mathrm{S} > 0.22\,\mathrm{S}_\oplus$, as defined by Kopparapu et al. (2014). The planet therefore is a temperate super-Earth or mini-Neptune such as GJ 887 c (Jeffers et al., 2020), GJ 686 b (Lalitha et al., 2019; Affer et al., 2019), GJ 685 b (Pinamonti et al., 2019) or GJ 581 c (Udry et al., 2007) (see Figure 3.11).

3.5.3 Comparison to synthetic planet populations

We compare the planetary system of GJ 3473 with a synthetic M-dwarf planet population from a core accretion model of planet formation (Burn et al., 2021)[18] to assess the frequency of such a configuration. There, planets like GJ 3473 b are relatively abundant and often accompanied by multiple other planets in the system. More than $10\,\%$ of their synthetic systems contain systems with a combination of planets similar to GJ 3473 b and c with respect to their masses and periods. The systems with an architecture closest to GJ 3473 suggest a low bulk density for the outer planet, which can currently not be tested observationally. Another theoretical prediction from the core accretion paradigm is a

---

[18]Explanatory note at the time of writing the thesis: at the time the manuscript was published, the Burn et al. (2021) manuscript was still in preparation. The correct reference to the article was added for the thesis.
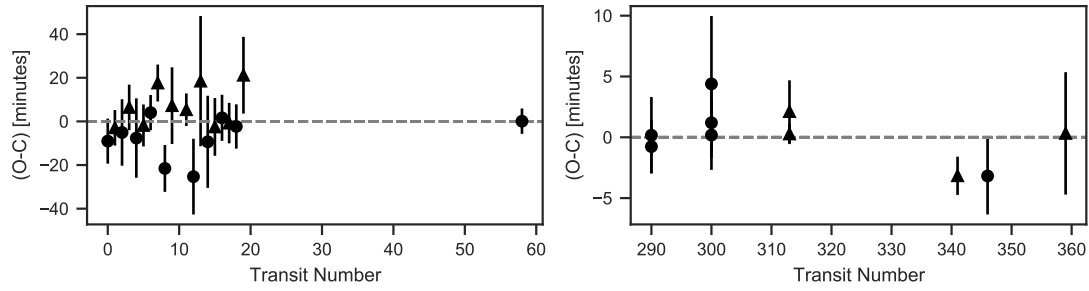
Fig. 3.13.: TTVs measured for the transits of GJ 3473 b based on the results from the joint fit. Even transits are depicted as circles and odd transits as triangles. The observations corresponding to the transit numbers can be found in Table 3.1.

higher frequency of distant companions for volatile-poor inner planets such as GJ 3473 b (Schlecker et al., 2020). While the current results do not demonstrate any clear evidence for planets beyond GJ 3473 c, further long-term monitoring is needed to probe the outer system.

3.5.4 Search for transit timing variations

The period ratio of the two planets ($P_b \approx 1.20\,\mathrm{d}$, $P_c \approx 15.5\,\mathrm{d}$) does not suggest the presence of strong TTVs for the transiting planet. However, we used `juliet` to perform a fit that only explores possible TTVs in the system. For this, we re-ran the joint fit but fixed all parameters to the results in Table 3.3 and Table A.4 and added a TTV parameter for each transit (Gaussian distributed prior with 0 mean and a standard deviation of $0.03\,\mathrm{d}$, see the documentation of `juliet` for details). Although the results in Figure 3.13 indicate TTVs up to $\sim 20\,\mathrm{min}$, the error bars are rather large. The main reason for this is the small transit depth of GJ 3473 b compared to the scatter of the data points (see Figure 3.6). A GLS analysis of the TTVs reveals no significant periodicity that would indicate the presence of another massive planet in the system.

3.6 Conclusions

Here we report the discovery of a planetary system around the M4.0 V dwarf GJ 3473 based on an extensive set of RV measurements from CARMENES, IRD, and HARPS, as well as space-based TESS photometry and photometric transit follow-up observations from LCOGT, MuSCAT, and MuSCAT2, and high-resolution images from Keck/NIRC2 and Gemini/NIRI. We confirm the planetary nature of GJ 3473 b (TOI-488.01) and present its detailed characterisation from a simultaneous fit of the RV and transit data. The short-period planet has a mass of $M_b = 1.86 \pm 0.30\,\mathrm{M_\oplus}$ and a radius of $R_b =$

$1.264 \pm 0.050\,\mathrm{R}_{\oplus}$, which yields a density that is consistent with a rocky composition. The planet complements the sample of small planets with mass and radius measurements better than $30\,\%$ and contributes to the TESS mission's primary goal to measure the masses of 50 planets with radii smaller than $4\,\mathrm{R}_{\oplus}$. Its proximity to the host star makes GJ 3473 b attractive for thermal emission spectroscopy. Synthetic cloud-free emission spectra predict amplitudes of the transmission spectral features up to 100s ppm in the MIR.

The RV data show evidence for an additional, non-transiting planet in the system. GJ 3473 c has a minimum mass of $M_c \sin i = 7.41 \pm 0.91\,\mathrm{M}_{\oplus}$ and an orbital period of $P_c = 15.509 \pm 0.033\,\mathrm{d}$, which places it just outside the inner boundary of the habitable zone.

The planetary system of GJ 3473 is another multi-planet system discovered around an M dwarf with planets in the range of Earth-like masses to super-Earths and mini-Neptunes. A comparison with synthetic planet populations shows that systems similar to GJ 3473 may be relatively abundant and often host multiple planets. We therefore encourage further long-time monitoring of the system to find additional planets.

Discovery and mass measurement of the hot, transiting, Earth-sized planet GJ 3929 b

<div style="text-align: right">**4**</div>

Details of authorship: *The text of this chapter was submitted to Astronomy & Astrophysics on the 12 November 2021. I carried out the analysis and the interpretation of the results as well as prepared the manuscript. Individual shorter text passages, for example parts of the instrument descriptions, were contributed by co-authors. Further, I incorporated suggestions and corrections by the co-authors before the submission. The text was fitted to the format and nomenclature of the thesis, which included changes in the figure's format and appearance, as well as the occurrence of used acronyms.*

4.1 Introduction

The TESS satellite has led to the discovery and characterisation of a multitude of small exoplanets. This growth was facilitated by the intensive spectroscopic follow-up in order to measure RV of the TOIs (Guerrero et al., 2021) and, thus, confirm their planetary nature by measuring their masses. (e.g. Cloutier et al., 2019; Günther et al., 2019; Luque et al., 2019; Astudillo-Defru et al., 2020; Dreizler et al., 2020; Kemmer et al., 2020; Nowak et al., 2020; Stefánsson et al., 2020; Soto et al., 2021; Bluhm et al., 2020, 2021). These discoveries provide valuable data in the ongoing debate as to the origins of super-Earths and mini-Neptunes.

The so-called "radius gap", first observationally shown by Fulton et al. (2017), divides the transiting sub-Neptunian planets into two different populations. Complementary mass measurements for planets on both sides of the gap confirmed their differing nature: dense and presumably rocky super-Earths with smaller radii and puffy enveloped mini-Neptunes with larger radii (e.g., Rogers, 2015; Jontof-Hutter, 2019; Bean et al., 2021, and references therein). However, it is not clear which formation mechanisms lead to these distinct planet types.

For example, rocky super-Earths could be created by photo-evaporation (Owen & Wu, 2013, 2017) or core-powered mass loss (Ginzburg et al., 2018; Gupta & Schlichting,

2019) of mini-Neptunes with hydrogen dominated atmospheres. The upper radius and mass limit of the rocky planets and its dependency on the planet's period, or rather instellation, are often seen as evidence for this theory (e.g., van Eylen et al., 2018, 2021; Bean et al., 2021, and references therein). On the other hand, the growing number of planets residing in the gap pose a challenge to this, since their high instellation usually excludes substantial H/He atmospheres (e.g., Ment et al., 2019; Dai et al., 2019; Bluhm et al., 2020). A possible explanation would be the existence of "water planets", which were predicted by classical planet formation models (e.g., Bitsch et al., 2019). In fact, self-consistent planet formation models like the ones by Venturini et al. (2020a,b) predict a bimodal distribution, with purely rocky planets on one side and water-enriched planets on the other. Probing the atmospheres of mini-Neptunes will break the density degeneracy between H/He atmospheres and water-planets and provide more insight (Rogers & Seager, 2010; Lopez & Fortney, 2014; Zeng et al., 2019). But also the position of the radius gap, anchored by the distribution of planets on both sides is a probe for the underlying principles and an important input for theoretical models that aim to describe the formation and evolution of those planets (Bean et al., 2021, and references therein).

Considered on their own, the planets below the radius gap are also interesting. For example, the increasing statistical sample of the smallest planets will tell us if super-Earths are different from planets with masses and radii similar to Earth, or if the underlying formation mechanisms are the same. Related to this is the question of how abundant atmospheres with high mean molecular weight similar to the ones that we observe in the Solar System actually are. Particularly suited to answer those questions are the planets orbiting M-dwarf stars, as these will be the first ones where the atmospheric characterisation of exo-Earths will be possible and provide unique insight in their structure and composition (e.g. Rauer et al., 2011; Barstow & Irwin, 2016; Morley et al., 2017; Kempton et al., 2018).

In this study, we present the discovery of a hot Earth-sized planet orbiting the M3.5 V-dwarf star GJ 3929. Based on transit signals observed by TESS, we performed an intensive RV follow-up campaign with CARMENES to confirm its planetary origin. The characterisation of the planet was supported by photometric follow-up from SAINT-EX and LCOGT that helped to refine the transit parameters. Furthermore, we report the detection of a non-transiting, sub-Neptunian-mass planet candidate with a wider orbit, which is evident in the RV data.

Our paper is organised as follows: in section 4.2 we present the used data and in section 4.3 we describe the stellar properties of GJ 3929. The analysis of the data is performed in section 4.4 and our findings are discussed in section 4.5. Finally, section 4.6 gives a summary of our results.
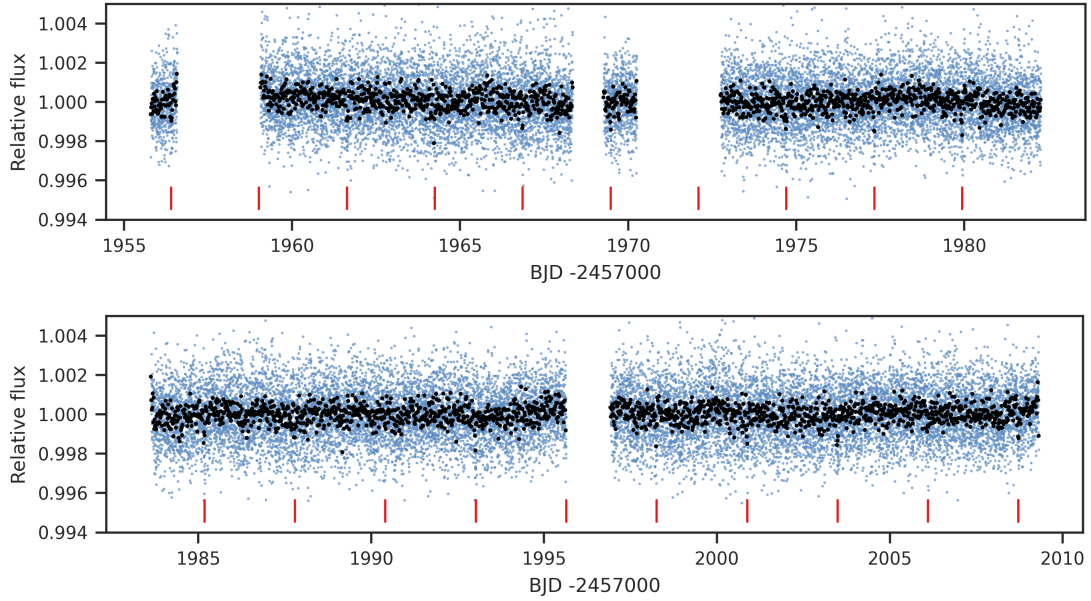
Fig. 4.1.: TESS PDCSAP light curves for sector 24 (*top*) and sector 25 (*bottom*). The blue points are the measurements and the black dots are $20\,\mathrm{min}$ bins. The transit times of GJ 3929 b are indicated by red ticks.

4.2 Data

4.2.1 High-resolution spectroscopy

CARMENES. We took 78 observations of GJ 3929 between July 2020 and July 2021 with CARMENES[1] (Quirrenbach et al., 2014) in the course of the guaranteed time observation and legacy programme. The dual-channel spectrograph covers the spectral ranges of $0.52\,\mu\mathrm{m}$ to $0.96\,\mu\mathrm{m}$ in the visible light (VIS, $R = 94\,600$) and $0.96\,\mu\mathrm{m}$ to $1.71\,\mu\mathrm{m}$ in the near infrared (NIR, $R = 80\,400$). For the data reduction and extraction of the RVs, we used `caracal` and `serval`, following our standard approach (see chapter 3). After discarding spectra with low S/N or missing drift correction, we retrieved 73 RVs in the VIS with a median internal uncertainty of $1.9\,\mathrm{m\,s^{-1}}$ and a wrms of $4.0\,\mathrm{m\,s^{-1}}$ and 72 RVs in the NIR with a median internal uncertainty of $7.3\,\mathrm{m\,s^{-1}}$ and wrms $9.1\,\mathrm{m\,s^{-1}}$ in the NIR, respectively. Due to the large scatter of the NIR data and the small expected amplitude of the transiting planet candidate, we only considered the VIS data in our analysis (Bauer et al., 2020).

Tab. 4.1.: Summary of transit observations.

Telescope	Date	Filter	t_{exp} [s]	Airmass[a]	Duration[b] [min]	N_{obs}	Aperture [pix]	10-min rms [ppt]	Detrending
TESS S24	2020-04-16 to 2020-05-12	T	120	...	38 138	14 650	16	0.64	PDC
TESS S25	2020-05-14 to 2020-06-08	T	120	...	36 967	17 246	17	0.63	PDC
SAINT-EX	2021-03-20	$I + z$[c]	10	1.64→1.0→1.05	334	638	11	2.19	PCA
LCOGT McD	2021-04-10	z'_s	40	1.54→1.02	183	158	19	0.95	$totc, width$[d]
LCOGT CTIO	2021-04-10	z'_s	40	2.89→2.40→2.84	203	175	19	1.31	$totc, width$[d]
LCOGT Haleakalā Observatory (HAL)	2020-04-15	g'	180	1.10→1.03→1.14	203	101	20	1.17	$totc, bjd$[d]
LCOGT Haleakalā Observatory (HAL)	2020-04-15	r'	38	1.10→1.03→1.14	206	286	20	0.71	$totc, bjd$[d]
LCOGT Haleakalā Observatory (HAL)	2020-04-15	i'	25	1.10→1.03→1.14	205	403	20	0.68	sky, bjd[d]
LCOGT Haleakalā Observatory (HAL)	2020-04-15	z'_s	21	1.10→1.03→1.14	207	510	20	0.62	$width, bjd$[d]

[a] The arrows indicate how the airmass has changed over the observation.
[b] Time-span of the observation.
[c] Combined range
[d] Simultaneous to the fits. Explanation of detrending parameters: $totc \equiv$ comparison ensemble counts; $width \equiv$ FWHM of target; $bjd \equiv$ BJD timestamp of observation; $sky \equiv$ sky background brightness.

4.2.2 Transit photometry

For our analysis, we combined the TESS observations with ground based follow-up transit photometry obtained by the TESS follow-up observing programme subgroup one. The parameters of the used transit observations are summarised in Table 4.1. In the following, we provide an overview of the instruments and applied data reduction.

TESS. We retrieved TESS observations for GJ 3929 (TOI 2013) from the Mikulski Archive for Space Telescopes[2] for the two sectors 24 and 25 (see Figure 4.1). In sector 24 (camera #1, CCD #1), one transit event was not observed because of the interruption during the data downlink between $BJD = 2458968.35$ and $BJD = 2458969.27$. In sector 25 (Camera #1, CCD #2), the measurements were stopped for data download between $BJD = 2458995.63$ and $BJD = 2458996.91$, which led to one only partially observed transit. We used the PDCSAP light curves provided by the SPOC, which are based on SAP light curves but further corrected for instrument characteristics. The aperture masks used for retrieving the SAP light curves are shown in Figure 4.2. To reduce the computational cost of the analysis, we used the extracted transit events only. In doing so, the baseline for each transit was set to ± 3 h with respect to the expected times of transit centre.

SAINT-EX. The first follow-up transit photometry for GJ 3929 was taken with the SAINT-EX[3] telescope located at the Observatorio Astronómico Nacional, in the Sierra de San Pedro Mártir in Baja California, Mexico. SAINT-EX consists of an Andor iKon-L camera mounted to an 1 m f/8 Ritchey-Chrétien telescope with a pixel scale of $0''.34\,\mathrm{pix}^{-1}$, which corresponds to a FOV of $12' \times 12'$ (Demory et al., 2020). The reduction of the data was performed using the instrument's custom pipeline `prince` that performs the standard

---

[1]Calar Alto high-Resolution search for M dwarfs with Exoearths with Near-infrared and visible Echelle Spectrographs, http://carmenes.caha.es.
[2]https://mast.stsci.edu.
[3]Searching and characterising transiting exoplanets.
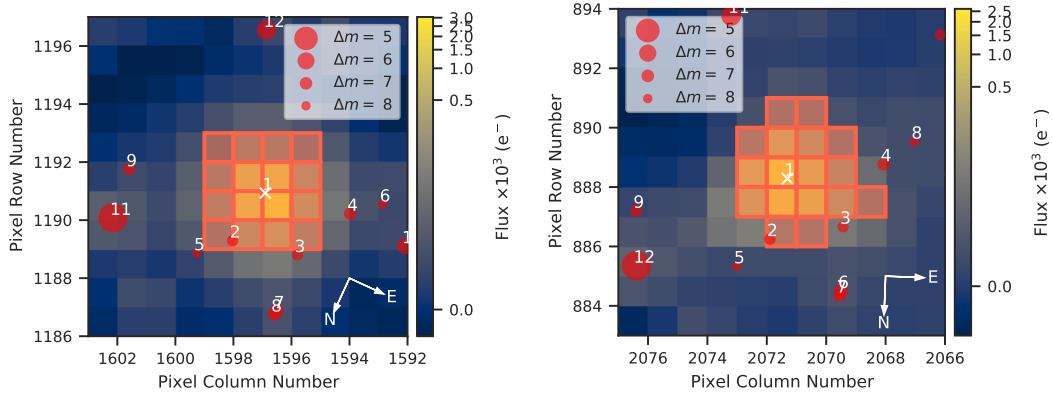
Fig. 4.2.: TESS TPFs of GJ 3929. *Top:* TESS sector 24, *bottom:* TESS sector 25. The position of GJ 3929 is denoted by a white cross and the aperture mask used to create the PDCSAP light curves is shown as the pixels with orange borders. For comparison, nearby sources from the *Gaia* DR2 catalogue (Gaia Collaboration et al., 2018), up to a difference of $\Delta m = 8\,\mathrm{mag}$ in brightness compared to GJ 3929, are plotted by red circles. Figure created using `tpfplotter` (Aller et al., 2020).

image reduction steps including bias, dark, and flat-field correction and provides light curves obtained from differential photometry (Demory et al., 2020). The light curve used for our analysis was further corrected for systematics using a principle component analysis method based on the light curves of all suitable stars in the FOV except for the target star (Wells et al., 2021).

LCOGT. Two transit events were observed with instruments from the LCOGT. The first one was observed contemporaneously by the SINISTRO CCDs at the $1\,\mathrm{m}$ telescopes of the McD and CTIO. Both instruments have a pixel scale of $0\overset{''}{.}389\,\mathrm{pix}^{-1}$ and a FOV of $26' \times 26'$. However, the higher airmass at LCOGT CTIO (see Table 4.1), led to worse seeing (estimated point spread function size $5\overset{''}{.}34\,\mathrm{pix}^{-1}$ vs. $3\overset{''}{.}97\,\mathrm{pix}^{-1}$) and, therefore, larger scatter of the measurements. The second transit event was observed by the recently commissioned MuSCAT3[4] camera (Narita et al., 2020) mounted to the $2\,\mathrm{m}$ Faulkes Telescope North at Haleakalā Observatory (HAL). MuSCAT3 operates simultaneously in the four passbands g', r', i', and z'_s and has a pixel scale of $0\overset{''}{.}27\,\mathrm{pix}^{-1}$ corresponding to a FOV of $9\overset{'}{.}1 \times 9\overset{'}{.}1$. All LCOGT observations were calibrated by the standard LCOGT `Banzai` pipeline, and photometric data were extracted using `AstroImageJ`.

4.2.3 Long-term photometry

In addition to the photometric transit observations, we used long-term photometry to determine the stellar rotation period.

---

[4]Multicolor Simultaneous Camera for studying Atmospheres of Transiting exoplanets 3.

HATNet. The photometric variability of GJ 3929 was previously investigated by Hartman et al. (2011) using data from the HATNet telescope network (Bakos et al., 2004, 2006). HATNet comprises a network of six cameras attached to $11\,\mathrm{cm}$ telescopes located in Arizona and Hawai'i. The cameras have a FOV of $8°2 \times 8°2$ and a pixel scale of $14''\,\mathrm{pix}^{-1}$. We retrieved the observations covering a time span of $200\,\mathrm{d}$ between December 2004 and July 2005 from the NASA Exoplanet Archive[5]. The data were taken by the telescopes #9 and #11 in the Cousins I_c filter at the Fred Lawrence Whipple Observatory in Arizona. Originally the data were taken with a cadence of $5.5\,\mathrm{min}$, but for our search for long-periodic signals we used the nightly binned values. In this way, we obtain a mean uncertainty of $1.24\,\mathrm{ppt}$ and rms of $2.19\,\mathrm{ppt}$.

ASAS-SN. We obtained more than $5\,\mathrm{yr}$ of archival data from ASAS-SN (Shappee et al., 2014; Kochanek et al., 2017), which were taken between April 2013 and September 2018. ASAS-SN currently consists of 24 cameras mounted to $14\,\mathrm{cm}$ Nikon telephoto lenses at six different sites around the globe. Each unit has a FOV of $4°5 \times 4°5$ with a pixel scale of $8''0\,\mathrm{pix}^{-1}$. The observations of GJ 3929 were obtained in the V band with the second camera in Hawai'i and have a mean uncertainty of $4.82\,\mathrm{ppt}$ and rms of $6.68\,\mathrm{ppt}$.

TJO. We observed GJ 3929 from April to October 2021 with the $0.8\,\mathrm{m}$ TJO telescope at the Montsec Observatory in Lleida, Spain. We obtained a total of 593 images with an exposure time of $60\,\mathrm{s}$ using the Johnson R filter of the LAIA imager, a 4k × 4k CCD with a field of view of $30'$ and a scale of $0''4\,\mathrm{pix}^{-1}$. The images were calibrated with darks, bias, and flat fields with the `icat` pipeline of the TJO (Colome & Ribas, 2006). The differential photometry was extracted with `AstroImageJ` using the aperture size that minimised the rms of the resulting relative fluxes, and a selection of the ten brightest comparison stars in the field that did not show variability. Then, we used our own pipelines to remove outliers and measurements affected by poor observing conditions or presenting a low signal-to-noise ratio. For our analysis we binned the data nightly, which resulted in a total of 54 measurements with a mean uncertainty of $1.90\,\mathrm{ppt}$ and rms of $6.22\,\mathrm{ppt}$.

4.2.4 High-resolution imaging

AstraLux. We observed GJ 3929 with the high-spatial resolution camera AstraLux (Hormuth et al., 2008), located at the $2.2\,\mathrm{m}$ telescope of the Calar Alto Observatory (Almería, Spain). The observations were carried out on 7 August 2020 at 1.1 airmasses and under moderate weather conditions with a mean seeing of $1''1$. In total, we obtained $93\,700$ frames in the Sloan Digital Sky Survey z' filter (SDSS z) with $10\,\mathrm{ms}$ exposure times and windowed to a FOV of $6'' \times 6''$. We used the instrument pipeline to

---

[5] https://exoplanetarchive.ipac.caltech.edu/docs/datasethelp/ETSS_HATNet.html.

select the $10\,\%$ frames with the highest Strehl ratio (Strehl, 1902) and to combine them into a final high-spatial resolution image. Based on this final image, a sensitivity curve was computed by using our own developed `astrasens`[6] package (Lillo-Box et al., 2012, 2014).

4.3 Properties of GJ 3929

The star GJ 3929 (G 180-18, Karmn J15583+354) is located at a distance of only $15.830 \pm 0.006\,\mathrm{pc}$ and shows a high proper motion (Schneider et al., 2016; Gaia Collaboration et al., 2018). Lépine et al. (2013) classified the star as an M3.5 V red dwarf. We calculated homogeneous stellar parameters from the CARMENES high-resolution spectra using our standard method: the luminosity, $L_\star = 0.011\,55 \pm 0.000\,11\,\mathrm{L_\odot}$, is determined as in Cifuentes et al. (2020). Following Passegger et al. (2019), and assuming $v \sin i = 2\,\mathrm{km\,s^{-1}}$, we derived the effective temperature, $T_\mathrm{eff} = 3369 \pm 51\,\mathrm{K}$, surface gravity $\log g = 4.84 \pm 0.04\,\mathrm{dex}$, and metallicity $[\mathrm{Fe/H}] = 0.00 \pm 0.16\,\mathrm{dex}$ using the VIS spectra. Finally, we computed the stellar radius, $R_\star = 0.315 \pm 0.010\,\mathrm{R_\odot}$ using the Stefan-Boltzman law and consequentially the mass, $M_\star = 0.309 \pm 0.014\,\mathrm{R_\odot}$ from the empirical mass-radius relation for M dwarfs of Schweitzer et al. (2019). Additionally, we computed Galactocentric space velocities UVW as in Cortés-Contreras et al. (2017).

From the analysis of the Hα pEW$'$ we found that GJ 3929 is an Hα-inactive star and is consistent with the previous results of Schöfer et al. (2019) and Jeffers et al. (2018). In addition, we investigated if there are any correlations between the measured CARMENES RV values and all of the activity indices using the Pearson's r coefficient where a value of > 0.7 or < -0.7 indicates strong correlation or anti-correlation as previously described by Jeffers et al. (2020). We found no strong or even moderate correlations between the measured CARMENES RVs and the acticity indicies, confirming that GJ 3929 is a magnetically inactive star. In subsection 4.4.7, we present a combined analysis of CARMENES activity indicators and photometry from HATNet, ASAS-SN, and TJO, from which we determine a stellar rotation period of $122 \pm 13\,\mathrm{d}$.

GJ 3929 has no known stellar companions. From the high-resolution imaging presented in subsection 4.4.2, we can rule out companions up to contrasts of $\Delta m = 4\,\mathrm{mag}$ down to a separation of $0''\!.2$ and $\Delta m = 5.5\,\mathrm{mag}$ for separations of $0''\!.4$ to $2''$. Additionally, *Gaia* provides a RUWE of 1.19, which is below the critical value of 1.41 that would hint to a close companion. Besides, we complemented the multiplicity analysis with a wide common-proper-motion companion search with *Gaia* EDR3 data up to a projected physical separation of 10^5 au (over 10 arcmin in angular separation); no wide companions with similar parallax and proper motion were found. Further, the astrometric excess-

---

[6]https://github.com/jlillo/astrasens.

Tab. 4.2.: Stellar parameters of GJ 3929.

Parameter	Value	Ref.
Name and identifiers		
Name	GJ 3929	Gli91
Alternative name	G 180–18	Gic59
Karmn	J15583+354	Cab16
TIC	188589164	Stas19
TOI	2013	Gue21
Gaia EDR3	1372215976327300480	*Gaia* EDR3
Coordinates and spectraltype		
α (epoch 2016.0)	15 58 18.80	*Gaia* EDR3
δ (epoch 2016.0)	+35 24 24.3	*Gaia* EDR3
Spectral type	M3.5 V	Lép13
G [mag]	11.5066 ± 0.0028	*Gaia* EDR3
T [mag]	10.2705 ± 0.0074	Stas19
J [mag]	8.694 ± 0.024	2MASS
Parallax and kinematics		
$\mu_\alpha \cos\delta$ [mas yr^{-1}]	-143.06 ± 0.02	*Gaia* EDR3
μ_δ [mas yr^{-1}]	318.12 ± 0.03	*Gaia* EDR3
π [mas]	63.173 ± 0.020	*Gaia* EDR3
d [pc]	15.830 ± 0.006	*Gaia* EDR3
γ [km s^{-1}]	$+9.54 \pm 0.01$	Jeff18
U [km s^{-1}]	-21.05 ± 0.04	This work
V [km s^{-1}]	$+10.85 \pm 0.06$	This work
W [km s^{-1}]	$+14.66 \pm 0.08$	This work
RUWE	1.19	*Gaia* EDR3
Photospheric parameters		
T_{eff} [K]	3369 ± 51	This work
$\log g$ [dex]	4.84 ± 0.04	This work
[Fe/H] [dex]	$+0.00 \pm 0.16$	This work
Physical parameters		
$L_\star$ [$L_\odot$]	0.01155 ± 0.00011	Cif20
$R_\star$ [$R_\odot$]	0.315 ± 0.010	This work
$M_\star$ [$M_\odot$]	0.309 ± 0.014	This work
Activity parameters		
pEW$'$ (Hα) [Å]	-0.029 ± 0.031	This work
$v \sin i$ [km s^{-1}]	< 2	This work
P_{rot} [d]	122 ± 13	This work

References. Gli91: Gliese & Jahreiß (1991); Gic59: Giclas et al. (1959); Cab16: Caballero et al. (2016b); Stas19: Stassun et al. (2019); Gue21: Guerrero et al. (2021); *Gaia* EDR3: Gaia Collaboration et al. (2021); Lép13: Lépine et al. (2013); 2MASS: Skrutskie et al. (2006); Jeff18: Jeffers et al. (2018); Cif20: Cifuentes et al. (2020).
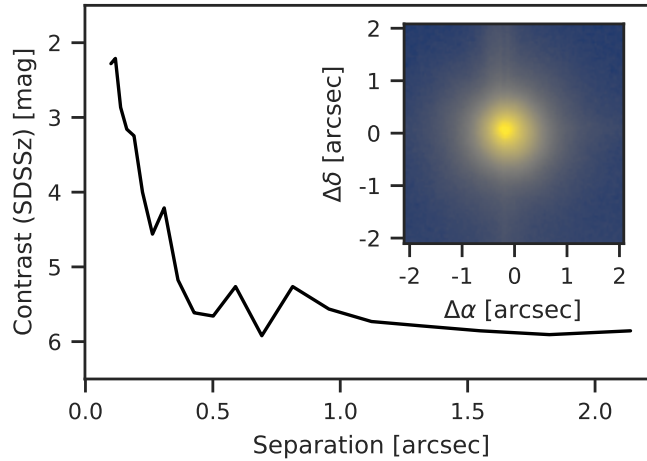
Fig. 4.3.: Contrast curve of the AstraLux high-resolution image. The image used to create the contrast curve is shown in the inset.

noise is $0.22\,\mathrm{mas}$, which is consistent with the jitter of other sources with comparable G magnitudes between $11\,\mathrm{mag}$ and $13\,\mathrm{mag}$. Our RV analysis in subsection 4.4.5 also shows no signals that would indicate any massive companions. A summary of the compiled stellar parameters and their sources is provided in Table 4.2.

4.4 Analysis and results

4.4.1 Transit detection by the SPOC

The SPOC investigated the PDCSAP flux time series for sector 24 with the Transiting Planet Search (Jenkins et al., 2002, 2010, 2020) module using an adaptive, wavelet-based matched filter, which detected transit events with a period of $\sim$2.6 d and generated a "threshold crossing event". The data were fitted with an initial limb-darkened transit model (Li et al., 2019) and subjected to a suite of diagnostic tests to help elucidate the nature of the signal (Twicken et al., 2018). The transit signal passed all the tests in the Data Validation module, and was promoted from "threshold crossing event" to TOI status by the TESS Science Office on 19 June 2020 after reviewing the Data Validation reports (Guerrero et al., 2021). Subsequent joint analyses of sectors 24 and 25 indicated that the transit source is located within $2''\!.8 \pm 6''\!.6$ of GJ 3929. The multiple transiting planet search failed to identify any additional transiting planet signatures.

4.4.2 Limits of photometric contamination

As seen in Figure 4.2, there are no *Gaia* sources down to a brightness difference of $\Delta G \approx 7\,\mathrm{mag}$ within the apertures used for creating the SAP light curves. The SPOC estimated a contamination in the photometric aperture of about $0.4\,\%$ for both sectors, based on the crowding and the location of the target star on the CCD using the pixel response functions reconstructed from data collected during commissioning and early science operations. Nevertheless, we obtained additional lucky imaging observations to rule out contamination of the light curves by bound or unbound companions at sub-arcsecond separations (subsection 4.2.4). The AstraLux image of GJ 3929 and the contrast curve created from it are shown in Figure 4.3. We find no evidence of additional sources within this FOV and within the computed sensitivity limit. This allows us to set an upper limit to the contamination in the light curve of around $0.4\,\%$ down to $0\rlap{.}''4$ and $2.5\,\%$ down to $0\rlap{.}''2$.

Analogous to Lillo-Box et al. (2014), we further used the contrast curve to estimate the probability of contamination from blended sources in the TESS aperture based on the TRILEGAL[7] Galactic model (v1.6, Girardi et al., 2012). The transiting planet candidate around GJ 3929 produces a signal that could be mimicked by blended eclipsing binaries with magnitude contrasts up to $\Delta m_{\mathrm{b,max}} \approx 7.3\,\mathrm{mag}$ in the SDSSz passband. Translating this contrast results in a low probability of $0.1\,\%$ for an undetected source, and an even lower probability of such a source being an appropriate eclipsing binary. Given these numbers, we assumed that the transit signal is not due to a blended binary star and that the probability of a contaminating source is nearly zero.

4.4.3 Modelling technique

We used `juliet`[8] for the analysis and modelling of the transit and RV data. Thereby, we follow our method as detailed for example by Luque et al. (2019), Kemmer et al. (2020), or Stock et al. (2020a). Because of the variety of instruments used and the large dataset, it would not be reasonable to perform the model selection on the combined RV and transit data. Therefore, in the following we first present transit-only and RV-only analyses to determine the individually best fitting models, which were later combined into a joint fit to retrieve the most precise parameters for the system.

---

[7]http://stev.oapd.inaf.it/cgi-bin/trilegal.
[8]https://juliet.readthedocs.io/en/latest/.

4.4.4 Transit-only modelling

In the first step of the modelling, we combined the TESS light curves with the SAINT-EX and LCOGT follow-up transits to obtain a very precise updated ephemeris of the transiting planet candidate, which was later used as prior information for the RV-only modelling.

Planet parameters. Based on the analysis of the TESS light curves by the SPOC pipeline (Li et al., 2019), the transiting planet candidate has a period of $P = 2.616\,277 \pm 0.000\,113\,\text{d}$. We used this information to set a uniform prior between $2\,\text{d}$ and $3\,\text{d}$ for our analysis. The time-of-transit centre was chosen accordingly to be uniform between BJD $2\,459\,319.0\,\text{d}$ and $2\,459\,322.0\,\text{d}$, which comprises the last follow-up transit event that we observed, namely the LCO-HAL transit. Following our usual approach (e.g. Luque et al., 2019; Kemmer et al., 2020; Bluhm et al., 2021), we fitted for the stellar density, ρ_*, instead of the scaled planetary semi-major axis, a/R_*. In doing so, we used a normally distributed prior centred on the density calculated from the parameters in Table 4.2, for which we assigned a width of three times the propagated uncertainty. Further, we implemented the re-parameterised fit variables r_1 and r_2, which replace the planet-to-star radius ratio, p, and the impact parameter, b, and allow for a uniform sampling between zero and one (Espinoza, 2018). Since the information content regarding the eccentricity is rather small for the light curves (Barnes, 2007; Kipping, 2008; van Eylen & Albrecht, 2015), we assumed it to be zero for the transit-only modelling. Constraints on the eccentricity were later investigated using the RV data (see subsection 4.4.5).

Instrument parameters. The analysis of the high-resolution images (subsection 4.4.2) did not indicate any contaminating sources within the apertures that were used to generate the light curves. Therefore, the dilution factor was fixed to one for all instruments. Following Espinoza & Jordán (2015), we used a quadratic limb-darkening law for the space-based TESS light curves, parameterised by q_1 and q_2 as in Kipping (2013). The parameters were shared between the two sectors. For all the other ground-based follow-up observations, we assumed a linear limb darkening with coefficient q. The offsets between the instruments, $mflux$, were assumed to be normally distributed around 0 with a standard deviation of 0.1, whereas the additional scatter that was added in quadrature to the nominal uncertainty values was log-uniformly distributed between $0\,\text{ppm}$ and $5000\,\text{ppm}$. The light curves from the LCOGT were detrended simultaneously with the fits, whereas, following a preliminary analysis, detrending of the SAINT-EX light curve did not bring any improvement, which is why we refrained from doing so in the analysis. See Table 4.1 for an overview of the used detrending parameters of the individual light curves. In doing so, we determined a refined period of $P = 2.616\,270\,9(47)\,\text{d}$ and $t_0 = 2\,459\,320.057\,81(33)\,\text{d}$ from the fit.
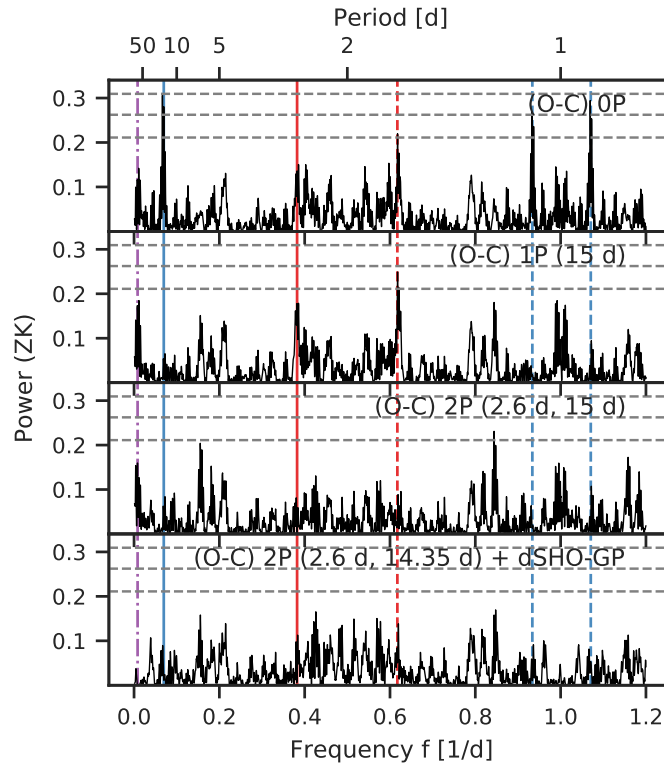
Fig. 4.4.: GLS periodogram analysis of the RVs. The period, $P = 2.62\,\text{d}$, and one-day alias, $P = 1.62\,\text{d}$, of the transiting planet are marked by the red solid and dashed lines, while the ~ 15-day periodicity and its daily aliases are marked by blue solid and dashed lines, respectively. Additionally, even though insignificant in the periodogram, the stellar rotation period of $P = 122\,\text{d}$ (subsection 4.4.7) is indicated by the purple dot-dashed line. We normalised the power using the parameterisation of Zechmeister & Kürster (2009) and the 10, 1, and $0.1\,\%$ FAPs denoted by the horizontal grey dashed lines are calculated using the analytic expression.

In order to search for additional transit signals in the data, we applied the model from this fit to the entire TESS dataset (i.e. uncropped) and ran a TLS periodogram on the residuals. The periodogram did not show any further significant signals.

4.4.5 RV-only modelling

Periodogram analysis

We used GLS periodograms implemented in the `Exo-Striker` (Trifonov, 2019; Trifonov et al., 2021) to identify prominent signals in the RV data, as illustrated by Figure 4.4. The dominant period is not that of the transiting planet candidate at about $2.6\,\text{d}$, but a signal with periodicity of $P \approx 15\,\text{d}$ and its one-day aliases. Furthermore, aliasing due to the seasonal observability of GJ 3929 ($f_s \approx 1/292\,\text{d}^{-1}$) splits the $\sim$15-day signal up into multiple close peaks by itself. The two prominent peaks are thereby at periods

of $P \approx 14.3\,\mathrm{d}$ and $P \approx 15.0\,\mathrm{d}$ (see also subsubsection 4.4.5). As there are no obvious indications of a transiting signal corresponding to these two periodicities that would help to distinguish the aliases, we used a sinusoidal fit with an uninformative period boundary between $10\,\mathrm{d}$ and $20\,\mathrm{d}$ to subtract the signal, and determined a period of $P = 15.03\,\mathrm{d}$. The residuals of this fit show a peak with about $2\,\%$ FAP at a period of $P \approx 1.62\,\mathrm{d}$. This period corresponds to the one-day alias of the 2.62-day signal seen in the transits, which is itself apparent only as an insignificant signal in the GLS periodogram. The photometric observations presented in the previous section, however, supplied precise information on the period and transit time, and hence phase, of the transiting planet candidate. We therefore simultaneously fitted the $\sim$15-day signal in combination with a sinusoid of $P \approx 2.62\,\mathrm{d}$ whose ephemeris was fixed to the values from subsection 4.4.4. The residuals of this fit do not show any power at the period of $P \approx 1.62\,\mathrm{d}$, which confirms that the peak is indeed correlated in phase with the signal of the transiting planet candidate and, thus, caused by aliasing. Even though never significant, a peak near the stellar rotation period of $122\,\mathrm{d}$ is also visible in the GLS periodograms (see subsection 4.4.7).

Determining the true period underlying the $\sim$15 d GLS peaks

We made use of the `AliasFinder`[9] to identify the true period underlying the GLS peaks of $14.3\,\mathrm{d}$ and $15.0\,\mathrm{d}$, which are aliases of each other caused by the $f_s \approx 1/292\,\mathrm{d}^{-1}$ sampling frequency. The script implements the principle of Dawson & Fabrycky (2010) and allows to visually compare the observed periodogram with synthetic periodograms originating from different possible alias frequencies. In doing so, we excluded the influence of the 2.62-day signal by first removing it from the data with a sine fit, as we did for the periodogram analysis. Figure 4.5 shows the resulting comparison periodograms for the 14.3-day and 15.0-day periods. Each panel shows three sections of the full periodogram: the first panel is the region around $\sim$15 d that highlights the aliasing due to the $\sim$292 d sampling ($f_\mathrm{alias} = |f \pm \frac{1}{292\,\mathrm{d}}|$), and the other two show the aliases of the daily sampling (*middle panel*: $f_\mathrm{alias} = |f - \frac{1}{1\,\mathrm{d}}|$), *right panel*: $f_\mathrm{alias} = |f + \frac{1}{1\,\mathrm{d}}|$)). The idea behind is that the true frequency should be able to explain both patterns well, as they are generated independently by it.

While the phases originating from simulating the 15.0-day period show less deviations from the observed phases than those from the 14.3-day period (see the circles in Figure 4.5), the evaluation of the periodograms implies that $14.3\,\mathrm{d}$ is the period underlying our data. The peaks originating from the 15.0-day period show a shifted distribution when compared to the observed periodogram, which can be seen especially in the daily aliases. There, the envelope of the aliases at $\sim$1.07 d is shifted towards shorter periods and those at $\sim$0.94 d towards longer periods – just as it is expected when the simulated

---

[9] https://github.com/JonasKemmer/AliasFinder.
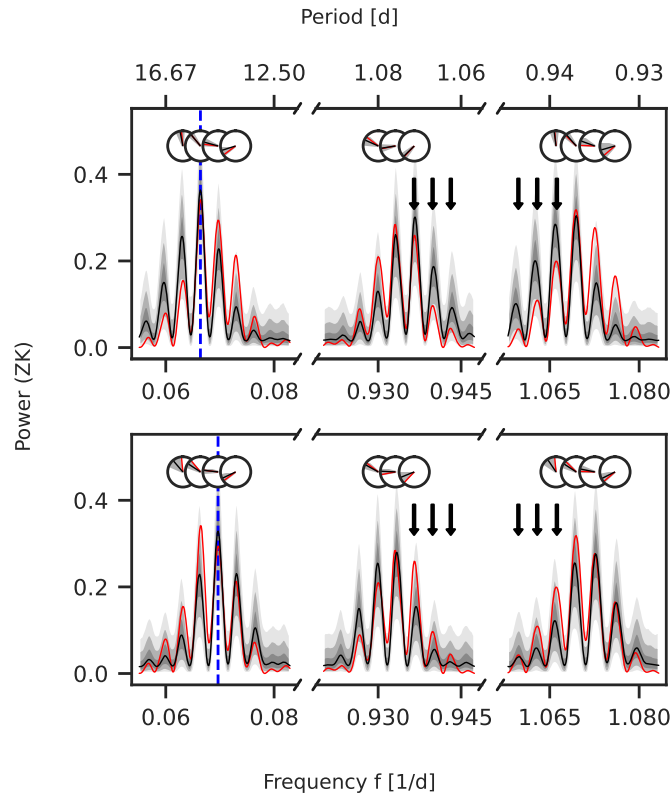
Fig. 4.5.: Alias test for the 14.3-day and 15.0-day periods using `AliasFinder`. We generated 5000 synthetic datasets for each period to produce synthetic periodograms (black lines), which are compared with the periodogram of the observed data (red lines). The simulation for the 15.0-day signal is shown in the top row and the simulation for the 14.3-day signal in the bottom row, each period indicated by a vertical blue dashed line, respectively. Black lines depict the median of the samples for each simulation, and the grey shaded areas are the 50, 90, and $99\,\%$ confidence intervals. Further, the phases of the peaks as determined by the GLS periodogram are displayed in the circles, following the same colour scheme (the grey shades denote the standard deviations of the simulated peaks). The black arrows point out the difference in the periodograms for the daily aliases that allows to identify the best matching period (see the text for the discussion).

period is larger than the underlying one (see the black arrows in Figure 4.5). The distribution of the simulated periodogram originating from the 14.3-day period, on the other hand, follows the observed periodogram. This is also reflected by the rms power of the residuals after subtracting the median GLS model from the observed one, where we found a value of 7.12 for the 14.3-day period and 7.97 for the 15.0-day period. We also got the same result if we generated the periodograms from the posterior samples of the fits, as shown in section B. Therefore, we concluded that the 14.3-day period is the true period of the ~ 15-day signal, and adopted from then on a uniform prior corresponding to the peak width in the periodogram between $13.98\,\mathrm{d}$ and $14.71\,\mathrm{d}$ whenever this signal

Tab. 4.3.: Model comparison for RVs based on Bayesian log-evidence.

Model	$\ln \mathcal{Z}$	$\Delta \ln \mathcal{Z}$
No planet:		
0P	-213.3	-6.0
Two-signal models (without activity modelling):		
2P$_{(2.6\,d,\,14.3\,d)}$	-211.2	-3.9
2P$_{(2.6\,d\text{-ecc},\,14.3\,d)}$	-211.8	-4.5
2P$_{2.6\,d,\,14.3\,d\text{-ecc})}$	-211.2	-3.9
2P$_{(2.6\,d\text{-ecc},\,14.3\,d\text{-ecc})}$	-212.1	-4.8
Three-signal models (with activity modelling):		
2P$_{(2.6\,d,\,14.3\,d)}$ + dSHO-GP$_{(120\,d)}$	$\mathbf{-207.3}$	**0.0**
2P$_{(2.6\,d\text{-ecc},\,14.3\,d)}$ + dSHO-GP$_{(120\,d)}$	-207.7	-0.4
2P$_{(2.6\,d,\,14.3\,d\text{-ecc})}$ + dSHO-GP$_{(120\,d)}$	-208.0	-0.7
2P$_{(2.6\,d\text{-ecc},\,14.3\,d\text{-ecc})}$ + dSHO-GP$_{(120\,d)}$	-208.7	-1.4

was considered in a fit. Using the 14.3-day period for pre-whitening of the periodogram instead of the uninformative prior as done in the paragraph above improved the FAP of the transiting planet candidate's alias in the residual GLS periodogram to $0.8\,\%$.

Significance of the transiting planet candidate in the RVs

In the next step, we derived the FAP for the signal in the RVs to occur exactly at the period of the transiting planet candidate. One problem is the strong aliasing, which has the consequence that the 1.62-day alias of the transit signal has in fact the highest power in the periodogram. For our approach, we used the randomisation method discussed by Hatzes (2019), Luque et al. (2019), Kemmer et al. (2020), or Bluhm et al. (2021), where the FAP is determined for increasingly smaller frequency ranges around the period in question and extrapolated with a third-order polynomial fit to a window size of zero. To account for the aliasing in our case, we considered two windows that comprise the two peaks at 2.62-day and 1.62-day in the periodogram and compared their combined power with the combined power of the respective highest peaks within the two windows. In doing so, we found a FAP of $0.1\,\%$ (Figure B.2) and therefore concluded that we detected a genuine signal of the transiting planet candidate in the RV measurements.

Model comparison

Planet and instrument parameters. The periodogram and alias analysis showed two relevant periodicities in the RV data: the strong signal at $P \approx 14.3\,\mathrm{d}$ and the transiting

planet candidate at $P \approx 2.62\,\text{d}$. As a result, the basis for our model comparison is a "two-signal model". Further, in subsection 4.4.7 we determined the stellar rotation period to be $122\,\text{d}$, which is recognizable as a peak in the periodogram of the RV data (Figure 4.4), but not significantly in terms of FAP. We took this into consideration for the modelling by testing whether an additional GP term that is optimised to mitigate stellar activity signals can improve the fit (referred to as "three-signal models").

Based on the results from Sects. 4.4.2 and 4.4.5, we could assume that the 2.62-day periodicity is indeed due to a true transiting planet. Therefore, we fixed the period and time-of-transit centre for the first model component to the values from the transit-only modelling (subsection 4.4.4). This choice is justified because the precision of the transiting planet candidate's ephemeris as determined from the photometry is much higher than what could be achieved from the RV data. To investigate the eccentricity of the signal, we tested a sinusoid against a Keplerian model for the transiting planet. Thereby, the eccentricity was parameterised by $\mathcal{S}_1 = \sqrt{e}\sin\omega$ and $\mathcal{S}_2 = \sqrt{e}\cos\omega$ with uniform priors between -1 and 1 (Espinoza et al., 2019a). The prior of the RV amplitude of the signal was set uniformly between $0\,\text{m\,s}^{-1}$ and $50\,\text{m\,s}^{-1}$.

For the 14.3-day signal, we tested a sinusoidal or Keplerian model in the same manner. The period prior was set uniformly between $13.98\,\text{d}$ and $14.71\,\text{d}$, following the analysis with `AliasFinder` in subsubsection 4.4.5, and the time-of-transit centre was chosen uniform between the first epoch of the RV data, $2\,459\,061.0\,\text{d}$, and $2\,459\,081.0\,\text{d}$ to avoid a multimodal distribution of the posterior.

We investigated whether the RVs are affected by stellar activity by adding a GP component whose prior on the rotation period, $P_{\text{GP, rv}}$, was set uniformly between $100\,\text{d}$ and $150\,\text{d}$ to cover the period determined from the photometry. Our GP kernel was the sum of two simple harmonic oscillators as described in Kossakowski et al. (2021), hereafter called dSHO-GP ($\equiv$ double simple-harmonic-oscillator). In doing so, the prior on the standard deviation, $\sigma_{\text{GP,rv}}$, of the GP model was specified to be uniform between $0\,\text{m\,s}^{-1}$ and $50\,\text{m\,s}^{-1}$ following the Keplerian models. Further, we used a uniform prior between 0.1 and 1 for the fractional amplitude, $f_{\text{GP,rv}}$, of the second component with respect to the first, and log-uniform priors between 1×10^{-1} and 1×10^4 for the quality factor of the secondary component, $Q_{0,\text{GP,rv}}$, and the difference to the first component, $dQ_{\text{GP,rv}}$, respectively. For the instrumental parameters of CARMENES, we used uniform priors between $-100\,\text{m\,s}^{-1}$ and $100\,\text{m\,s}^{-1}$ for the offset and $0\,\text{m\,s}^{-1}$ to $100\,\text{m\,s}^{-1}$ for the jitter.

Results. In Table 4.3, we show the Bayesian log-evidence for the models that combine the two signals from the periodogram and the stellar activity, as described above. The highest Bayesian log-evidence was found for the model considering sinusoidal components for the 2.62-day and 14.3-day periods in combination with the GP that accounts

for stellar activity. The difference in log-evidence compared to a completely flat model, which means considering only the RV offset and jitter, is $|\Delta \ln \mathcal{Z}| = 6$. Following Trotta (2008), we thus assumed the three-signal model to be significantly better ($|\Delta \ln \mathcal{Z}| > 5$).

In comparison with the two-signal models, the models that account for stellar activity are only moderately to almost significantly favoured ($|\Delta \ln \mathcal{Z}| > 2.5$). The reason for this is probably the low activity amplitude of $\sim 3\,\mathrm{m\,s^{-1}}$ combined with the fact that only roughly three periods were covered by the RV observations (~ 350-day baseline compared to a period of $\sim 120\,\mathrm{d}$). Nonetheless, considering that even small influences from stellar activity can affect the planetary parameters (e.g. Stock et al., 2020b), and that even strong activity signals do not have to be evident in the periodogram (Nava et al., 2020), we proceeded with the models that include the GP.

Of these models, those that consider eccentric orbits for one of the two signals are at best indistinguishable, $|\Delta \ln \mathcal{Z}| < 1$, from the model with the highest log-evidence that considers only circular orbits. It can therefore be assumed that the two signals have a low eccentricity, if any. For such low-eccentricity orbits, however, the value is mainly determined by the large error bars and the phase coverage of our RV measurements (Hara et al., 2019). This ambiguity is reflected in the indistinguishability of the models and the unconstrained posteriors of the eccentricities ($e_{2.6\,\mathrm{d}} = 0.28 \pm 0.23$; $e_{14.3\,\mathrm{d}} = 0.20 \pm 0.20$). For the transiting planet, also considering its short period, it is therefore justified to assume a circular orbit in our further modelling (van Eylen et al., 2019). Since we do not know the nature of the 14.3-day signal, we proceeded with it in the same way in order to be consistent, and chose the model considering two circular signals for the joint fit.

To exclude the possibility that the choice of our model significantly influences the parameters of the transit planet candidate, we compared the fitted semi-amplitudes and the resulting minimum masses for the different models (Figure B.3). Additionally, we also performed a fit corresponding to the **2P$_{(2.6\,\mathrm{d},\,14.3\,\mathrm{d})}$ + dSHO-GP$_{(120\,\mathrm{d})}$** model, but replacing the period prior of the 14.3-day signal with a prior considering the 15.0-day alias. All models agree within the interquartile range and show no significant differences. Yet, choosing the 15.0-day alias instead of the 14.3-day period results in a slightly higher planet mass, as is the case for most of the other models. However, those higher masses are also generally accompanied by larger errors.

4.4.6 Joint modelling

The highest information content is provided by the combination of the transit and RV data, which is why we performed a joint fit to derive precise parameters of the transiting planet. Based on our results from the transit- and RV-only analyses, the model consists of a circular orbit for the transiting planet with $P \approx 2.62\,\mathrm{d}$ fitted to the transit and RV data, in combination with the sinusoidal 14.3-day signal, and the dSHO-GP representing
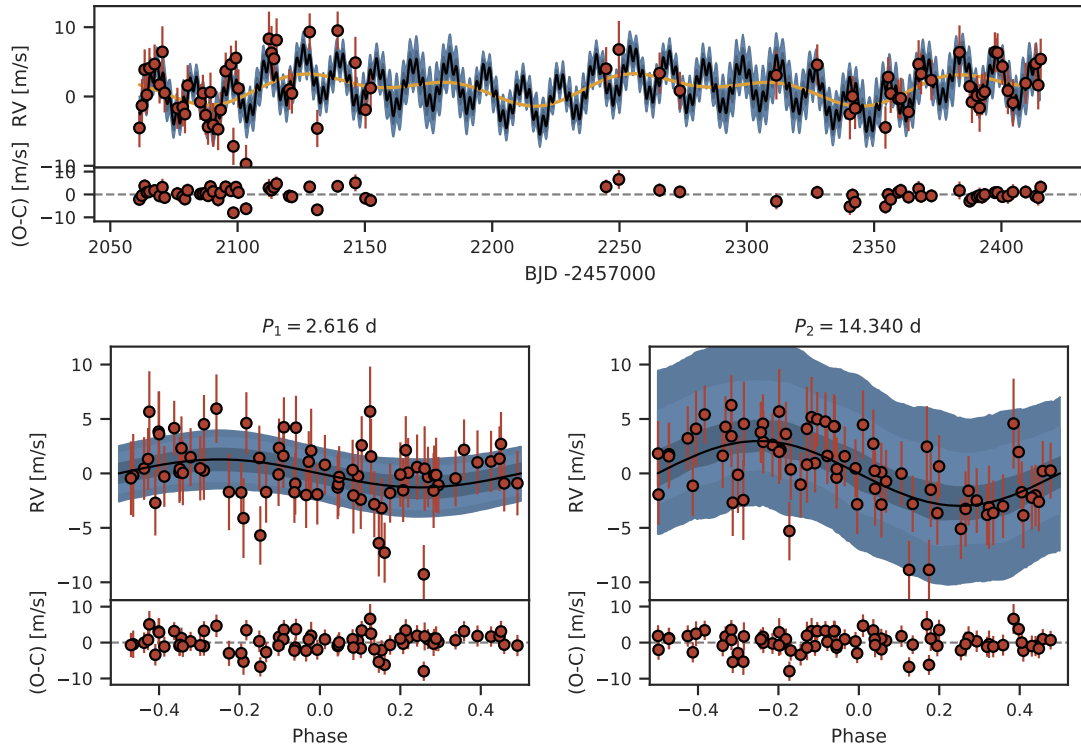
Fig. 4.6.: Results for the CARMENES RV from the joint fit with the transits. The black lines show the median of $10\,000$ samples from the posterior and the blue shaded areas denote the $68\,\%$, $95\,\%$ and $99\,\%$ credibility intervals respectively. The orange line shows the GP model. Error bars of the measurements include the instrumental jitter added in quadrature. The residuals after subtracting the median models are shown in the lower panels of each plot. *Top:* RVs over time. *Bottom:* RVs phase-folded to the periods of the transiting planet (*left*) and the $14.3\,\mathrm{d}$ signal (*right*).

the stellar activity, in the RV data only. The priors used for the fit correspond to the combination of the transit- and RV-only priors as described in Sects. 4.4.4 and 4.4.5, and are summarised in Table B.1.

We present the posterior parameters of the transiting planet, the 14.3-day signal, and the GP in Table 4.4, while the posteriors of the instrumental parameters are shown in Table B.2. Plots of the final models retrieved from the posteriors are shown in Figure 4.6 for the RVs and Figure 4.7 for the transits.

Given the uncertainty of $36\,\%$ in the RV semi-amplitude of the transiting planet candidate, we checked whether our choice of the 14.3-day signal to be the period underlying the $\sim$15-day aliases had a significant effect on the planetary parameters. In section B the results from a joint fit considering the 15.0-day period to be the true period are presented. While the derived RV semi-amplitude for the transiting planet candidate is indeed slightly larger, it is fully consistent with the results presented here. Coincidently, the higher amplitude in combination with the approximately unchanged uncertainties
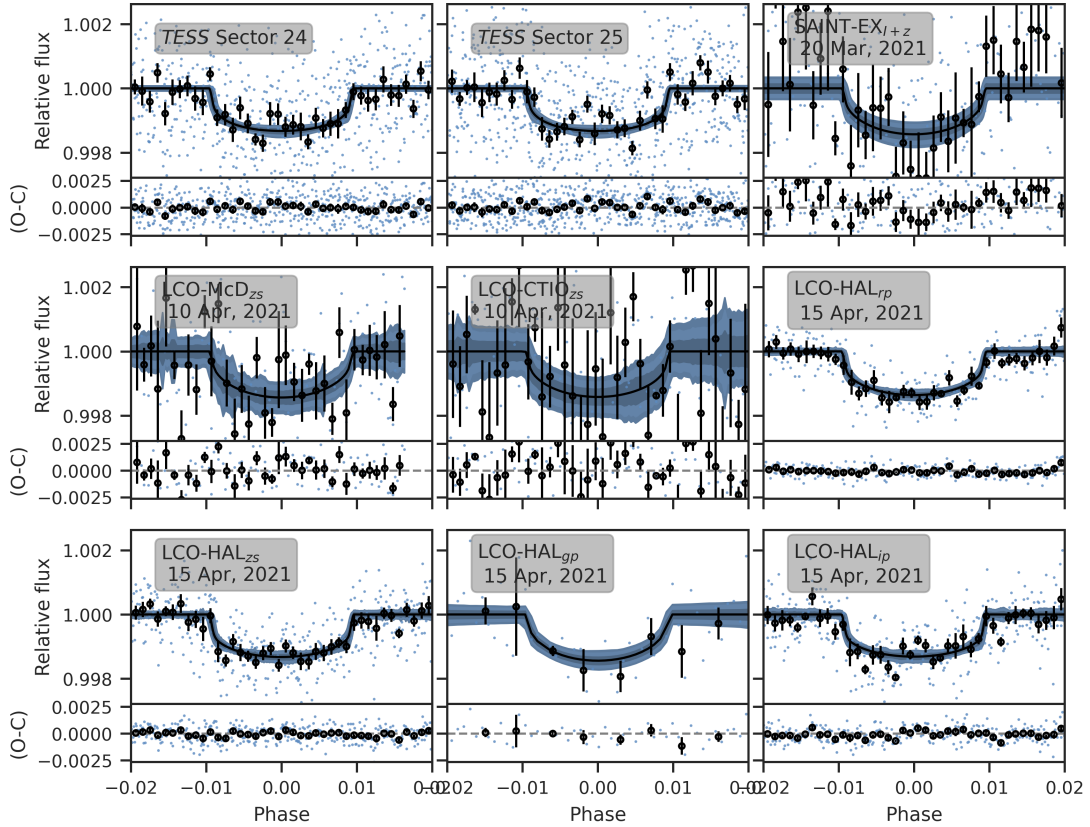
Fig. 4.7.: Results from the joint fit for the transit observations. The black lines represent the median of 10 000 samples from the posterior phase-folded to the period of the transiting planet. Credibility intervals of 68 %, 95 % and 99 % are displayed by the blue shaded areas. The black points show the data binned to 0.001 in phase, and the measurements that were used for the fit are denoted by the blue dots. As for the RVs, the residuals after subtracting the median model are shown in the lower panel of each plot.

resulted in a significant measurement ($\sim 3.3\sigma$). However, following the analysis in subsubsection 4.4.5 and section B, we were confident that $P \approx 14.3\,\mathrm{d}$ is the true period and, therefore, accepted the non-significant amplitude from the corresponding fit.

4.4.7 Stellar rotation period

Activity indicators

The wide wavelength range of CARMENES allows to compute many indicators that are sensitive to stellar activity. A full list of all activity indicators that are routinely derived from the CARMENES spectra can be found in Zechmeister et al. (2018, spectral indices), Schöfer et al. (2019, photospheric and chromospheric indices), and Lafarga et al. (2020, parameters related to the cross-correlation function). For the sake of clarity, we only selected the indicators from the VIS channel that exhibit signals with FAP < 1 % in

Tab. 4.4.: Median posterior parameters of the transiting planet, the ~14.3 d signal, and the GP.

Parameter	Posterior[a]	Units
Stellar density		
$\rho_\star$	$12.39^{+0.97}_{-0.95}$	$\mathrm{g\,cm}^{-3}$
GJ 3929 b		
P_{b}	$2.616\,267^{+4.7\times10^{-6}}_{-4.9\times10^{-6}}$	d
$t_{0,\mathrm{b}}$[b]	$2\,459\,320.057\,42^{+0.000\,38}_{-0.000\,34}$	d
$r_{1,\mathrm{b}}$	$0.514^{+0.060}_{-0.077}$	...
$r_{2,\mathrm{b}}$	$0.032\,66^{+0.000\,70}_{-0.000\,72}$	...
K_{b}	$1.29^{+0.47}_{-0.46}$	$\mathrm{m\,s}^{-1}$
14.3 d signal		
$P_{(14.3\,\mathrm{d})}$	$14.340^{+0.043}_{-0.038}$	d
$t_{0,(14.3\,\mathrm{d})}$[b]	$2\,459\,072.15^{+0.46}_{-0.46}$	d
$K_{(14.3\,\mathrm{d})}$	$3.03^{+0.48}_{-0.47}$	$\mathrm{m\,s}^{-1}$
GP parameters		
$P_{\mathrm{GP,\,rv}}$	$128.5^{+3.2}_{-3.1}$	d
$\sigma_{\mathrm{GP,\,rv}}$	$2.13^{+0.97}_{-0.73}$	$\mathrm{m\,s}^{-1}$
$f_{\mathrm{GP,\,rv}}$	$0.48^{+0.16}_{-0.17}$	...
$Q_{0,\mathrm{GP,\,rv}}$	1110^{+3510}_{-970}	...
$dQ_{\mathrm{GP,\,rv}}$	$1.25^{+5.61}_{-0.95}$	...

[a] Error bars denote the 68% posterior credibility intervals.
[a] Barycentric Julian Date in the Barycentric Dynamical Time standard.

a GLS periodogram and present them in Figure 4.8. None of these signals coincide with the period of the transiting planet candidate or the 14.3-day signal. However, all periodograms show a fairly similar pattern of peaks between $50\,\mathrm{d}$ and $300\,\mathrm{d}$. The cause here is also a strong aliasing due to the seasonal observability of GJ 3929 and the resulting strong sampling frequency of $f_s \approx 1/292\,\mathrm{d}^{-1}$ (see also subsection 4.4.5).

Particularly prominent is the Hα index derived from `serval`, which shows the strongest peak at a period of ~118 d, in combination with its first order aliases at ~82 d and ~212 d. Additionally, there is another significant peak with a ~65-day period, which could be misinterpreted as the second harmonic ($\equiv P/2$) of the 118-day period, but is actually its second order alias. The oppositely signed counterpart of this second order alias produces a significant long-term trend in the data. This is similar to the periodogram of the CRX, which is consistent with either an underlying period of ~126 d that shows aliasing up
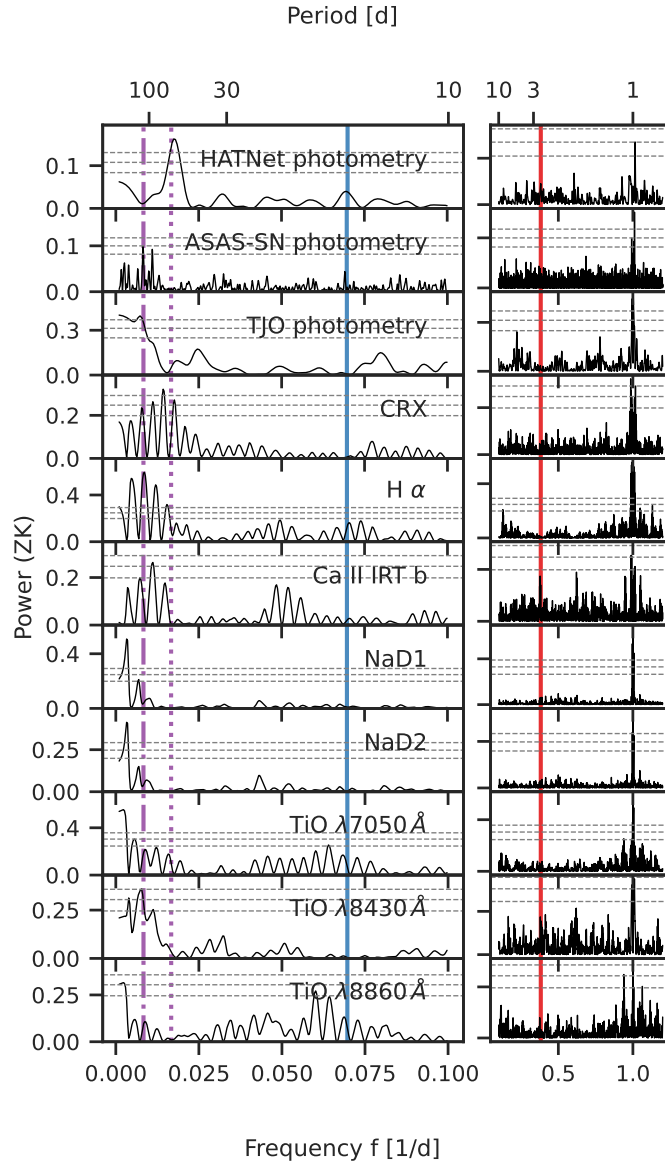
Fig. 4.8.: GLS periodograms of the photometry and activity indicators.The first three panels show the photometry from HATNet, ASAS-SN and TJO and the following panels show the activity indicators derived from CARMENES that show signals with less than 1% FAP. The stellar rotation of $P \approx 122\,\mathrm{d}$, as determined from the photometry, is indicated by the purple dot-dashed line and its second harmonic ($P/2$) by the purple dotted line. As in Figure 4.4, the period of the transiting planet is denoted by the red solid line and the $\sim 15\,\mathrm{d}$ periodicity is marked in blue, respectively. We normalised the power using the parameterisation of Zechmeister & Kürster (2009) and the 10, 1 and 0.1% false alarm probabilities denoted by the horizontal grey dashed lines are calculated using the analytic expression.

to third order, or a $\sim$70-day periodicity producing up to second order aliases. Further, analogous patterns can be found for the Ca II IRT b index as well as the TiO $\lambda8430$Å band.

Long-term photometry

We created GLS periodograms of the HATNet, ASAS-SN, and TJO data (see the first three panels of Figure 4.8). The GLS of the HATNet data shows a highly significant peak at a period of $P \approx 57\,\mathrm{d}$, which is consistent with the rotation period reported by Hartman et al. (2011), who applied a variance period-finder using a harmonic series. However, the detection of the period was flagged as "questionable" by the authors as they did not recognise a clear variability by eye. The ASAS-SN data, on the other hand, show two prominent peaks in the GLS: one at $P \approx 91\,\mathrm{d}$ and an even more significant one at $P \approx 122\,\mathrm{d}$. A look at the window function of the data shows that these two peaks are generated by aliasing due to a sampling frequency of $f_s \approx 1/362\,\mathrm{d}^{-1}$. The $122\,\mathrm{d}$ period is also supported by the TJO data. They show a peak at about $140\,\mathrm{d}$, which is, due to the short baseline, embedded in a plateau for periods larger than $100\,\mathrm{d}$.

The photometry and spectroscopic activity indicators thus share a common periodicity of about $\sim$120 d, which is about twice the period published by Hartman et al. (2011) based on the HATNet data alone. However, it is reasonable that $P \approx 120\,\mathrm{d}$ is the actual rotation period of the star and that HATNet shows the second harmonic.

We therefore proceeded with a combined fit of the HATNet, ASAS-SN, and TJO data using the dSHO-GP model as in Kossakowski et al. (2021) to determine a precise value for it. In doing so, we used normally distributed priors for the instrumental offsets centred around 0 with a standard deviation of 0.1 and log-uniform priors for the instrumental jitter terms between $1\,\mathrm{ppm}$ and $10 \times 10^6\,\mathrm{ppm}$. For the GP hyperparameters we used separate instrument priors for the standard deviation, $\sigma_{\mathrm{GP,phot}}$ (log-uniform between 1×10^{-8} and 1), the quality factor of the secondary oscillation Q_0 and the difference to the quality factor of the primary oscillation $dQ_{\mathrm{GP,phot}}$ (both log-uniform between 0.1 and 1×10^4), and the fractional amplitude, $f_{\mathrm{GP,phot}}$ between both (uniform between 0 and 1). The GP rotation period, $P_{\mathrm{GP,phot}}$, however, was shared between all instruments with a uniform prior between $100\,\mathrm{d}$ and $150\,\mathrm{d}$ to avoid the 91-day alias of the ASAS-SN data and the 57-day second order harmonic of the HATNet data. In this way, we determined a photometric rotation period of $P_{\mathrm{rot}} = 122 \pm 13\,\mathrm{d}$.

Thus, we obtained three different measurements of the stellar rotation period: $128.5 \pm 3.2\,\mathrm{d}$ from the RV measurements (Table 4.4), approximately 118-126 d from the activity indicators and $122 \pm 13\,\mathrm{d}$ from the photometry. All three measurements are consistent with each other. Causes for the differences in the measured periods can be different active latitudes at the times of the measurement, differential rotation, or, in the
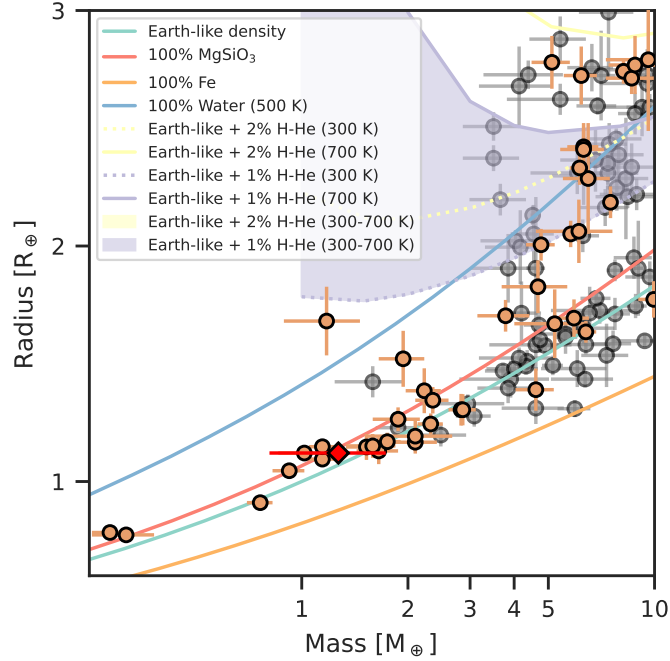
Fig. 4.9.: Mass-radius diagram of well characterised planets with $R < 3\,R_\oplus$ and $M < 10\,M_\oplus$. The plot shows the planets from the TEPcat catalogue (Southworth, 2011, visited on 8 November 2021) with ΔM and $\Delta R < 30\,\%$. Planets with host star temperatures $T_{\mathrm{eff}} < 4000\,K$ are shown in orange colour and planets with hotter hosts in grey. GJ 3929 b is marked with a red diamond. Additionally, theoretical mass-radius relations from Zeng et al. (2019) are shown for reference.

case of the activity indicators, the differences between photospheric and chromospheric indicators. Since photometrically-determined rotation periods are often considered to be the most reliable and the RV measurement has a likely underestimated uncertainty, we adopt the photometric period of $P_{\mathrm{rot}} = 122 \pm 13\,\mathrm{d}$ as the rotation period of GJ 3929, which fittingly comprises all three measurements the best.

4.5 Discussion

4.5.1 GJ 3929 b

Our analysis confirms the planetary nature of the transiting planet GJ 3929 b. Table 4.5 shows the planetary parameters derived from our joint fit. Its mass and radius of $M_{\mathrm{b}} = 1.27 \pm 0.46\,M_\oplus$ and $R_{\mathrm{b}} = 1.121 \pm 0.044\,R_\oplus$, respectively, put it into the regime of small Earth-sized planets. This makes GJ 3929 b comparable to other planets with confirmed masses orbiting M-dwarf stars that were detected by TESS. These include for example (in order of their detection), L 98–59 b (Kostov et al., 2019; Cloutier et al.,

2019; Demangeon et al., 2021), TOI-270 b (Günther et al., 2019), GJ 357 b (Luque et al., 2019; Jenkins et al., 2019), GJ 1252 b (Shporer et al., 2020), GJ 3473 b (Kemmer et al., 2020), LHS-1140 c (Ment et al., 2019; Lillo-Box et al., 2020), LHS 1478 b (Soto et al., 2021), or L231–32 b (van Eylen et al., 2021).

Although the uncertainty in mass allows a wide range of compositions for GJ 3929 b (see Figure 4.9), its small radius places it below the radius gap for M-dwarf planets (Cloutier et al., 2020a; van Eylen et al., 2021) and, hence, makes a rocky composition very likely. The derived mean density of $\rho_{\mathrm{b}} = 4.9 \pm 2.0\,\mathrm{g\,cm^{-3}}$ is compatible with a $MgSiO_3$-dominated composition. GJ 3929 b thus expands the statistical sample of rocky super-Earths needed to further investigate the properties of the radius gap. For example, as a planet orbiting a mid-type M star, it is important for studies of the dependence of the gap on the stellar mass or the incident flux, as in van Eylen et al. (2021).

With an orbital period of $P_{\mathrm{b}} = 2.62\,\mathrm{d}$, GJ 3929 b receives 19.8 ± 1.8 times the solar flux on Earth, which corresponds to an equilibrium temperature of $T_{\mathrm{eq}} = 587 \pm 13\,\mathrm{K}$ (assuming zero Bond albedo). In combination with the host star brightness ($J = 8.694\,\mathrm{mag}$), this results in a transmission spectroscopy metric (TSM) of 22.8 ± 13.1. GJ 3929 b is thus above the threshold of $\mathrm{TSM} > 10$ determined by Kempton et al. (2018) and belongs to the sample of small terrestrial planets that are especially attractive for atmospheric follow-up observations with the upcoming JWST (Gardner et al., 2006).

Although unlikely given the Earth-like radius and consequently location below the radius gap, the uncertainty in the determined density does not completely exclude the presence of a significant atmosphere. An atmosphere with a high mean molecular weight would be difficult to probe, however, as it has been shown for other comparable small M-dwarf planets (e.g., Luque et al., 2019; Bower et al., 2019; Nowak et al., 2020), the dominant species of carbon dioxide and water are expected to produce absorption features that are observable with instruments such as the JWST or the ELT (Gilmozzi & Spyromilio, 2007).

Systematic in-depth atmospheric characterisation of rocky planets like GJ 3929 b is expected to provide answers to questions such as the abundance and composition of retained primordial atmospheres or secondary atmospheres formed by outgassing.

4.5.2 Planet candidate GJ 3929 [c]

The strongest signal in the CARMENES RV data is not related to the transiting planet or the stellar rotation. It has a period of $P_{\mathrm{[c]}} = 14.340 \pm 0.043\,\mathrm{d}$ and an RV semi-amplitude of $K_{\mathrm{[c]}} = 3.03 \pm 0.48\,\mathrm{m\,s^{-1}}$. The strong aliasing caused by the seasonal observability of GJ 3929 unfortunately prevented a meaningful analysis of the stability of the signal. In combination with the FAP of the signal, which is still higher than $0.1\,\%$ in the non-pre-whitened periodogram, we thus introduce it as a planet candidate, namely GJ 3929 [c].

Tab. 4.5.: Derived planet parameters for GJ 3929 b and the planet candidate.

Parameter	Posterior P_b [a]	Posterior $P_{(14.3\,d)}$ [a]	Units
Derived transit parameters			
$p = R_p/R_\star$	$0.032\,66^{+0.0007}_{-0.000\,72}$	$\dots$	$\dots$
$b = (a_p/R_\star)\cos i_p$	$0.271^{+0.089}_{-0.115}$	$\dots$	$\dots$
$a_p/R_\star$	$16.49^{+0.42}_{-0.44}$	$\dots$	$\dots$
i_p	$89.06^{+0.41}_{-0.34}$	$\dots$	deg
Derived physical parameters [b]			
M_p	$1.27^{+0.46}_{-0.46}$	$\dots$	$M_\oplus$
$M_p \sin i$	$1.27^{+0.46}_{-0.46}$	$5.26^{+0.84}_{-0.83}$	$M_\oplus$
R_p	$1.121^{+0.044}_{-0.043}$	$\dots$	$R_\oplus$
ρ_p	$4.9^{+2.0}_{-1.9}$	$\dots$	$\mathrm{g\,cm^{-3}}$
g_p	$9.9^{+3.8}_{-3.6}$	$\dots$	$\mathrm{m\,s^{-2}}$
a_p	$0.0241^{+0.0011}_{-0.0011}$	$0.0781^{+0.0011}_{-0.0012}$	au
$T_{\mathrm{eq,\,p}}$ [c]	$587.0^{+13.0}_{-12.0}$	$326.3^{+7.5}_{-7.5}$	K
S	$19.8^{+1.8}_{-1.6}$	$1.893^{+0.058}_{-0.055}$	$S_\oplus$
ESM [d]	$5.03^{+0.37}_{-0.32}$	$\dots$	$\dots$
TSM [d]	$22.8^{+13.1}_{-6.3}$	$\dots$	$\dots$

[a] Error bars denote the 68% posterior credibility intervals.
[b] Sampled from normal distributions for stellar mass, radius, and luminosity based on the results from section 4.3.
[c] Assuming a zero Bond albedo.
[d] Emission and transmission spectroscopy metrics (Kempton et al., 2018).

The mass derived from the joint fit for this potential planet is $M_{[c]} \geq 5.26 \pm 0.84\,M_\oplus$, which puts it into the regime of the sub-Neptune-mass planets.

In a co-planar orbit such a planet could be transiting, even though only for a very small range ($b_{[c]} = 0.87 \pm 0.35$ assuming the inclination of the inner planet). Full transits should show signals comparably to or larger than those of the less massive inner planet. The fact that we do not detect any other potentially transiting signals in the TESS data after subtracting the 2.62-day planet suggests that there could be shallow grazing transits, if any. But, confirming the detection of such would be complicated by the uncertainty of the ephemeris as determined from the RVs, $t_{\mathrm{transit,\,m}} = 2\,459\,072.15(46)\,\mathrm{d} + m * 14.340(43)\,\mathrm{d}$, which makes it furthermore plausible that some transits could fall just inside the data gaps of TESS. This is important to note, because applying a TLS periodogram to the unbinned HATNet data in the range of $0\,\mathrm{d}$ to $40\,\mathrm{d}$ gives rise to a signal with a SDE of approximately 9.75 (i.e., FAP $< 0.01\,\%$) at a period of $P \approx 14.14\,\mathrm{d}$ (see Figure B.4).

Moreover, even though unexpected, the GLS of the unbinned HATNet data shows, besides the strongest peak at the stellar rotation period, a highly significant peak at $P \approx 14.5\,\mathrm{d}$ and another peak with FAP $< 1\,\%$ at $P \approx 2.63\,\mathrm{d}$. Any attempt in fitting the transiting planet together with or without the planet candidate to the HATNet data, however, brought up questionable results. The reason is likely the rms scatter of $6.7\,\mathrm{ppt}$ of the HATNet data compared to a transit depth of $\sim 1\,\mathrm{ppt}$ to $8\,\mathrm{ppt}$ for the transiting planet and the planet candidate (based on its mass, we would expect it to have a radius smaller than $3\,\mathrm{R}_\oplus$).

4.5.3 Implications for a multi-planet system

Planets such as the candidate GJ 3929 [c] in company to GJ 3929 b are frequently detected (e.g. Sabotta et al., 2021; Cloutier et al., 2021b). Further, combinations of terrestrial planets and sub-Neptunes are also commonly predicted by population synthesis models based on the core accretion paradigm of planet formation (Emsenhuber et al., 2020; Schlecker et al., 2021; Burn et al., 2021). Following the angular momentum deficit stability criterium from Laskar & Petit (2017), the system would be stable for eccentricities of the outer companion candidate up to 0.45.

4.6 Conclusions

The analysis of the TESS transit observations in combination with the RV follow-up from CARMENES and transit follow-up from SAINT-EX and LCOGT confirms the planetary nature of the Earth-sized, short-period, planet GJ 3929 b. Along with the brightness of its M-dwarf host, its high equilibrium temperature makes GJ 3929 b a prime target for atmospheric follow-up with the upcoming generation of facilities, such as JWST, which will provide unique insight into the composition and, thus, formation and evolution of small and rocky planets.

Further, the RV measurements showed evidence for a second sub-Neptunian-mass planet candidate, namely GJ 3929 [c]. Its period is far from the rotation period of the star that we determined from archival photometry and, therefore, likely not linked to stellar activity. Besides, the candidate is promising because we detected a signal in the TLS periodogram of archival photometric HATNet data close to the orbital period determined from the RVs. Yet, additional follow-up is needed to confirm its planetary nature, given that the strong aliasing of the RVs and the time gap with respect to the HATNet data made it difficult to provide an in-depth investigation of the signal.

If the planetary nature of GJ 3929 [c] can indeed be proven, the GJ 3929 system would join the growing number of multi-planetary systems with relatively short periods

around M-dwarf stars. Of particular interest would be whether GJ 3929 [c] is actually a transiting planet and, thus, whether it would be possible to determine its density.

Discussion and Conclusions

> *Remember to look up at the stars and not down at your feet. Try to make sense of what you see and wonder about what makes the universe exist. Be curious. And however difficult life may seem, there is always something you can do and succeed at. It matters that you don't just give up.*

> — **Stephen Hawking**
> theoretical physicist and cosmologist, (1942-2018)

In my thesis, I presented an error budget for the CARMENES-VIS spectrograph in operation, as well as three new planet detections. While the error budget may be symbolical for the limits of the RV method, the planet discoveries show what this means in practical application. GJ 3473 b and GJ 3929 b are both Earth-sized planets for which we obtained a radius and mass measurement. Thus, both contribute to the TESS level one science requirement of measuring the masses for 50 planets with radii smaller than $4\,R_{\oplus}$. Given the increasing frequency of such discoveries, it is fair to say that we have now entered an era in which the discovery and characterisation of Earth-sized planets are no longer the exception but become actually routine. GJ 3473 c is a sub-Neptunian mass planet in the temperate zone. Since it is orbiting GJ 3473 together with GJ 3473 b, it is especially valuable for planet-formation theory and the question of how planets in multi-planetary systems affect each other. Not to be forgotten is also the fact that GJ 3473 is actually part of a binary system with GJ 3474 and thus adds to the still small sample of planets known in binary-star systems.

While I discussed the above-mentioned findings already individually in section 3.5 and section 4.5, I would like to place them jointly a little more in the overall picture in the following.

5.1 The mass-radius diagram for small planets around M dwarfs

The resounding success of the TESS mission becomes apparent in Figure 5.1, where I show a literature compilation of the small planets orbiting M dwarfs known at the time
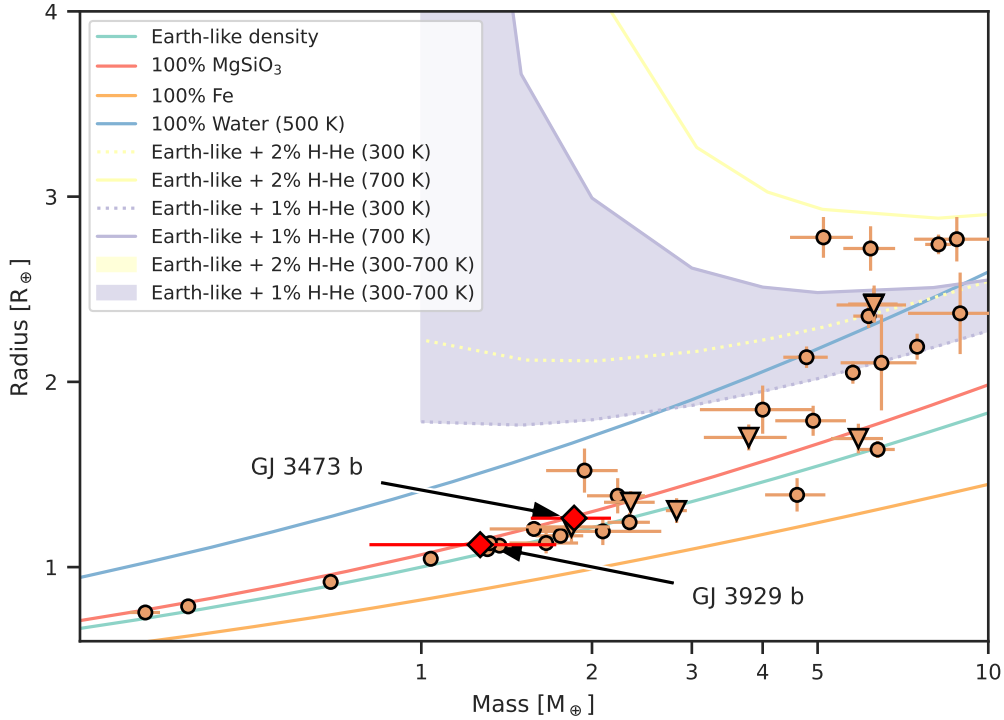
Fig. 5.1.: Mass-radius diagram of small planets orbiting M dwarfs (see Table 5.1 for the underlying sample). The red diamonds mark GJ 3473 b and GJ 3929 b presented in this thesis. Other planets discovered by the CARMENES-TESS WG are denoted by the orange triangles and the planets taken from the literature by orange circles. Theoretical mass-radius relations from Zeng et al. (2019) are overlaid for comparison.

of finalising my thesis as presented in Table 5.1. More than half of the planets shown there were discovered based on TESS transit detections. With seven newly discovered planets (two of them are GJ 3473 b and GJ 3929 b), the CARMENES-TESS WG has a large share in this. The question is, however, what can we learn from these planets? Even though one should be careful when interpreting the observed mass-radius distribution – the observational biases of the transit and RV method are not considered and the sample is not corrected for completeness – I would like to qualitatively evaluate what is shown in Figure 5.1.

Strikingly, almost all planets with masses less than $3\,M_\oplus$ agree best with rocky, Earth-like or super-Earth, planets composed of mainly $MgSiO_3$. The two planets that I presented in this thesis are part of this group. A noticeable exception is L 98-56 d ($M = 1.94\,M_\oplus$, $R = 1.52\,R_\oplus$; Demangeon et al., 2021), which has a lower density and is more compatible with higher volatile contents. On the other hand, the second group, planets with masses higher than $3\,M_\oplus$, can have diverse compositions. Some of them can be classified as rocky super-Earths, like for example TOI-1235 b ($M = 5.9\,M_\oplus$, $R = 1.694\,R_\oplus$; Bluhm et al., 2020) discovered by the CARMENES-TESS WG. The majority however has densities that
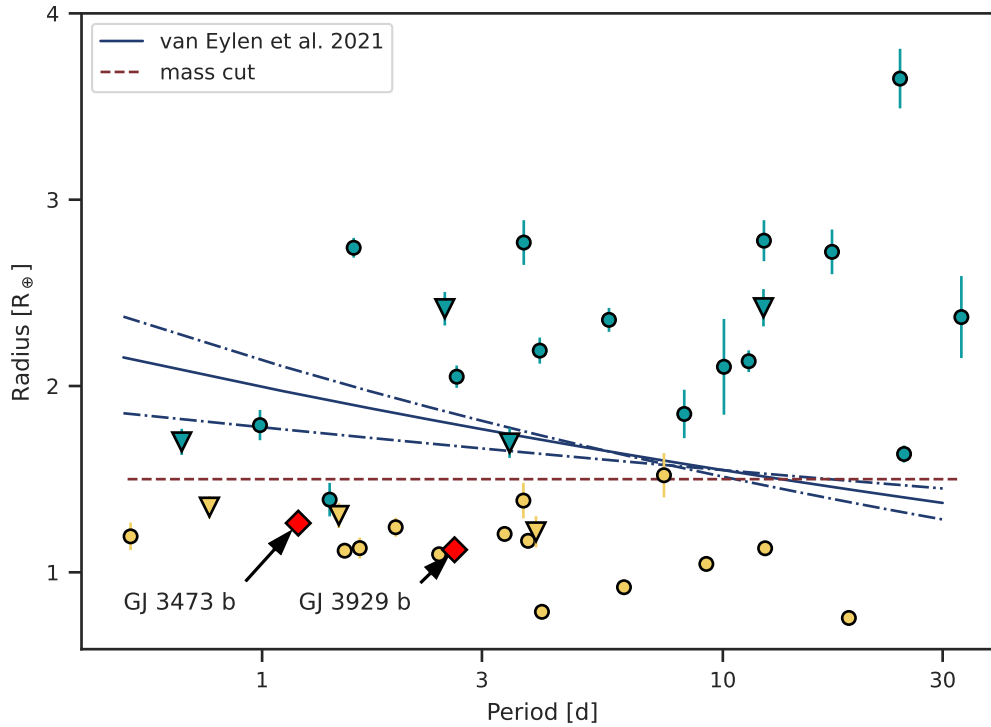
Fig. 5.2.: Period-radius diagram of small planets orbiting M dwarfs (see Table 5.1 for the underlying sample). GJ 3473 b and GJ 3929 b, introduced in this thesis, are denoted by the red diamonds. Yellow and blue colour indicate planets with masses smaller, respectively larger, than $3\,M_\oplus$. The planets discovered by the CARMENES-TESS WG are marked by triangles instead of circles. The blue lines denote the location of the radius valley determined by van Eylen et al. (2021) and the red dotted line is an exemplary cut that divides the two populations discussed for Figure 5.1.

are ambiguous, as described in subsection 1.1.3. They could be planets covered by large amounts of water (blue line), as well as rocky cores enlarged by a few percent H/He in mass (purple and yellow shaded regions). The planets with the largest radii are, however, inconsistent with being water-planets as their density is lower than that of pure water ice and are thus in our picture expected to possess H/He atmospheres. One of these planets is GJ 1214 b ($M = 8.17\,M_\oplus$, $R = 2.742\,R_\oplus$; e.g, Charbonneau et al., 2009; Cloutier et al., 2021a), which was already discovered in 2009 and was even already subject to an atmospheric characterisation. Kreidberg et al. (2014) found that the transmission spectrum that they observed was inconsistent with a high mean molecular weight, which indeed rules out a water dominated atmosphere. However, the spectrum was featureless, which hinted the presence of clouds but also inhibited a more detailed characterisation of its composition.

To investigate whether I can also detect the radius valley for M-dwarf planets, I compare the sample of small M-dwarf planets with the period-radius relation from

van Eylen et al. (2021, vE21 hereafter) in Figure 5.2. They used a machine learning algorithm to determine the position of the radius valley for M-dwarf planets. The study was only recently published and is based on a sample that is similar to the one presented here. Differences result from the fact that I strictly adopt for all planets characterised by CARMENES the corresponding parameters and take into account planets with larger uncertainties in the mass ($\Delta M = 30\,\%$ compared to $\Delta M = 20\,\%$ by vE21).

First, it is noticeable that there are planets that fall right in the centre of the valley determined by vE21. Among them is the just-mentioned, rocky TOI-1235 b. It was also part of the sample considered by vE21, but was actually excluded from their analysis as being an outlier. Further, L 98-59 d, which was not included in vE21 because the precise mass measurement by Demangeon et al. (2021) was published only recently. Other than that, the radius valley determined by vE21 matches the distribution of small planets presented here.

In their study, vE21 compared their determined location of the valley with the one observed for FGK stars and concluded that the slope and lower position of the M-dwarf radius valley is in good agreement with the photoevaporation and core-powered mass loss of rocky cores with pure H/He atmospheres as I described in subsection 1.1.3. However, as apparent from Figure 5.2, I would like to remark that the distribution would also be consistent with a simple mass cut using the two groups that I discussed for the mass-radius diagram (Figure 5.1). For illustration, I have drawn a line at a radius of at $1.5\,R_\oplus$ which is the lower boundary of the radius valley determined by Fulton et al. (2017) and corresponds to a mass of approximately $4.5\,M_\oplus$ assuming an Earth-like density. Such a bimodal mass distribution with pure rocky planets on one side and planets of divers composition on the other is predicted by the formation and evolution model of Venturini et al. (2020a,b) that I mentioned in subsection 1.1.3.

Consequently, the scatter in the radii observed for mini-Neptunes would be mainly caused by varying amounts of water and only slightly altered by the presence of H/He atmospheres that are subject to photoevaporation. However, the typical masses in the Venturini et al. (2020a,b) model are about $3\,M_\oplus$ for pure rocky planets and $10\,M_\oplus$ for mini-Neptunes. This is higher than observed for the two M-dwarf planet populations. It would therefore be relevant to investigate the dependency on the stellar mass for Venturini et al.'s model, as I think that a shift to lower planetary masses with lower stellar host masses is quite conceivable. The outlier from the bimodal distribution, L 168-9 b ($M = 4.6\,M_\oplus$, $R = 1.39\,R_\oplus$, $P = 1.40\,d$; Astudillo-Defru et al., 2020), could be due to its high density an interesting example for planets resulting from collisions that are generally thought to have higher core-mass fractions.

The most important distinctive feature between the two hypotheses of either dry planets with H/He atmospheres or water planets, is the period-radius relation that is predicted by photoevaporation (see also subsection 1.1.3). Although vE21 are able to

reproduce the slope observed in the Kepler sample also for M-dwarf planets, their result seems to be mainly supported by only a few planets from the second mass peak (in Figure 5.2 only two planets with masses higher than $3\,M_\oplus$ are below the radius valley). This is critical insofar as the sample has not been corrected for completeness. I therefore do not see their results as evidence that mini-Neptunes must have dry, rocky, cores and that super-Earths form from atmospheric mass loss. Due to the clear bimodality in the mass, I think that models predicting the existence of water planets to explain the mini-Neptunes should get more attention again. Nevertheless, in order to distinguish between photoevaporation of H/He from dry, rocky, cores and models that include water planets, it will be important to further complete the sample on both sides of the valley and, thus, significantly improving the statistics.

5.2 Rocky exoplanets orbiting M dwarfs

I discussed the overall emerging picture of small planets orbiting M-dwarf stars in the previous section. In the following, I would like to go into more detail for the rocky, Earth-like and super-Earth planets that include GJ 3473 b and GJ 3929 b.

What Dai et al. (2019) have shown for well characterised USP planets in general is also evident for the Earth-like and super-Earth planets orbiting M dwarfs (Figure 5.1): they follow the Zeng et al. (2019) mass-radius relations for Earth-like compositions very closely. Consequently, this indicates a universal composition and thus formation process for those planets as suggested by Dressing et al. (2015). Consequently, independent whether they formed already dry or were subject to atmospheric loss, we can assume that these planets do not have large H/He atmospheres since this would significantly enlarge their radius (Lopez & Fortney, 2014). Still, the measured densities do not exclude (secondary) atmospheres with high mean molecular weight, which for example can form by outgassing of the mantle or volcanism (Morley et al., 2017; Kite & Barnett, 2020).

Yet, as I described in the introduction, undisputed evidence for an atmosphere of a terrestrial planet outside our solar system still has to be found. The scientific community is therefore eagerly awaiting the atmospheric study of exoplanets with the next generation of instruments like the JWST – which besides just arrived at the spaceport in Kourou as I write these lines – or the ELT. Of course one of the most important requirements for this is to find and characterise suitable candidates beforehand. Consequently, the work of Kempton et al. (2018) is currently one of the most cited studies in the TESS community. In there, they presented the already mentioned TSM and ESM, which describe the amenability of a target for JWST based on the expected S/N of the observations. Further, they determined thresholds of TSM > 10 and ESM > 7.5 which classify terrestrial planets

Tab. 5.1.: Small transiting planets with mass measurements orbiting M dwarfs (GJ 3473 b and GJ 3929 b presented in this thesis are not listed). Planets in this list orbit stars with temperatures lower than $4000\,\mathrm{K}$, have a radius smaller than $4\,\mathrm{R}_\oplus$ and a mass uncertainty smaller than $30\,\%$. Discoveries taken from the CARMENES-TESS WG, the NASA Exoplanet Archive and the list of well-studied exoplanets from the TEPCat.

Planet name	Mass [$M_\oplus$]	Radius [$R_\oplus$]	Period [d]	Reference
GJ 1132 b	1.66 ± 0.23	1.130 ± 0.056	1.628 931 ± 0.000 027	Bonfils et al. (2018)
GJ 1214 b	8.17 ± 0.43	2.742 ± 0.053	1.580 404 33 ± 0.000 000 13	Cloutier et al. (2021a)
GJ 1252 b	2.09 ± 0.56	1.193 ± 0.074	0.518 234 9 ± 0.000 006 3	Shporer et al. (2020)
GJ 357 b	1.84 ± 0.31	1.217 ± 0.084	3.930 720 ± 0.000 080	Luque et al. (2019)
GJ 486 b	2.82 ± 0.12	1.305 ± 0.067	1.467 119 ± 0.000 031	Trifonov et al. (2021)
K2-146 b	5.77 ± 0.18	2.05 ± 0.06	2.644 600 ± 0.000 060	Hamann et al. (2019)
K2-146 c	7.49 ± 0.24	2.19 ± 0.07	4.004 98 ± 0.000 11	Hamann et al. (2019)
K2-18 b	8.92 ± 1.70	2.37 ± 0.22	32.939 623 ± 0.000 100	Sarkis et al. (2018)
K2-3 b	6.48 ± 0.99	2.103 ± 0.257	10.054 626 ± 0.000 011	Kosiarek et al. (2019)
Kepler-26 b	5.12 ± 0.65	2.78 ± 0.11	12.2800 ± 0.0030	Jontof-Hutter et al. (2016)
Kepler-26 c	6.20 ± 0.65	2.72 ± 0.12	17.255 90 ± 0.000 60	Jontof-Hutter et al. (2016)
L 168-9 b	4.60 ± 0.56	1.39 ± 0.09	1.401 50 ± 0.000 18	Astudillo-Defru et al. (2020)
L 98-59 c	2.22 ± 0.26	1.385 ± 0.095	3.690 677 7 ± 0.000 002 6	Demangeon et al. (2021)
L 98-59 d	1.94 ± 0.28	1.521 ± 0.119	7.450 724 5 ± 0.000 008 1	Demangeon et al. (2021)
LHS 1140 b	6.38 ± 0.46	1.635 ± 0.046	24.736 94 ± 0.000 41	Lillo-Box et al. (2020)
LHS 1140 c	1.76 ± 0.17	1.169 ± 0.038	3.777 920 ± 0.000 030	Lillo-Box et al. (2020)
LHS 1478 b	2.33 ± 0.20	1.242 ± 0.051	1.949 537 8 ± 0.000 004 1	Soto et al. (2021)
LTT 3780 b	2.34 ± 0.24	1.35 ± 0.06	0.768 448 ± 0.000 055	Nowak et al. (2020)
LTT 3780 c	6.29 ± 0.63	2.42 ± 0.10	12.2519 ± 0.0030	Nowak et al. (2020)
TOI-1201 b	6.28 ± 0.88	2.415 ± 0.090	2.491 986 3 ± 0.000 003 1	Kossakowski et al. (2021)
TOI-1231 b	15.4 ± 3.3	3.65 ± 0.16	24.245 586 ± 0.000 066	Burt et al. (2021)
TOI-1235 b	5.90 ± 0.62	1.694 ± 0.080	3.444 717 ± 0.000 042	Bluhm et al. (2020)
TOI-1634 b	4.91 ± 0.70	1.790 ± 0.081	0.989 343 ± 0.000 015	Cloutier et al. (2021b)
TOI-1685 b	3.78 ± 0.63	1.70 ± 0.07	0.669 140 3 ± 0.000 002 3	Bluhm et al. (2021)
TOI-269 b	8.8 ± 1.4	2.77 ± 0.12	3.697 710 4 ± 0.000 003 7	Cointepas et al. (2021)
TOI-270 b	1.58 ± 0.26	1.206 ± 0.039	3.360 153 8 ± 0.000 004 8	van Eylen et al. (2021)
TOI-270 c	6.15 ± 0.37	2.355 ± 0.064	5.660 573 1 ± 0.000 003 1	van Eylen et al. (2021)
TOI-270 d	4.78 ± 0.43	2.133 ± 0.058	11.379 573 ± 0.000 013	van Eylen et al. (2021)
TOI-776 b	4.0 ± 0.9	1.85 ± 0.13	8.246 610 ± 0.000 050	Luque et al. (2021)
TRAPPIST-1 b	1.374 ± 0.069	1.116 ± 0.014	1.510 826 0 ± 0.000 006 0	Agol et al. (2021)
TRAPPIST-1 c	1.308 ± 0.056	1.097 ± 0.014	2.421 937 ± 0.000 018	Agol et al. (2021)
TRAPPIST-1 d	0.388 ± 0.012	0.788 ± 0.011	4.049 219 ± 0.000 026	Agol et al. (2021)
TRAPPIST-1 e	0.692 ± 0.022	0.920 ± 0.013	6.101 013 ± 0.000 035	Agol et al. (2021)
TRAPPIST-1 f	1.039 ± 0.031	1.045 ± 0.013	9.207 540 ± 0.000 032	Agol et al. (2021)
TRAPPIST-1 g	1.321 ± 0.038	1.129 ± 0.015	12.352 446 ± 0.000 054	Agol et al. (2021)
TRAPPIST-1 h	0.326 ± 0.020	0.755 ± 0.014	18.772 866 ± 0.000 210	Agol et al. (2021)

to be one of the top planets for follow-up that can be expected to be found by the TESS mission.

GJ 3473 b with ESM $= 6.8 \pm 0.3$ and GJ 3929 b with TSM $= 23^{+13}_{-6}$ are thus among the prime targets for the upcoming era of atmospheric characterisation (see also the discussions in section 3.5 and section 4.5). Following the discussion above, we should assume that they possess – if at all – atmospheres with high mean molecular weight. This means the strongest detectable spectral features will be H_2O, CO, CO_2, NO_2, NH_3 or CH_4 (e.g., Morley et al., 2017). Thereby, besides the molecular abundances in the first place, surface gravity and equilibrium temperature of the planets are the major parameters that define their spectra (Madhusudhan, 2019). Since we have determined the latter two in our analysis, observing a spectrum would provide us with detailed knowledge about the composition of the planetary atmosphere. In turn, this would give us in-depth knowledge of the planet's composition and evolution (see for example the discussion on the different water contents predicted by the migration and drift model in the introduction in subsection 1.1.3).

Its hot equilibrium temperature facilitates GJ 3473 b for follow-up using emission spectroscopy. This technique is particularly interesting because it provides information on the day-side temperature of the planet and can even yield valuable information on the temperature pressure profile of the atmosphere (e.g., Kreidberg, 2018; Madhusudhan, 2019, and references therein). Further, as Lustig-Yaeger et al. (2019b) has shown for the TRAPPIST system, emission spectroscopy could be capable to look below cloud decks that would obscure features in transmission spectra. The exemplary synthetic spectra of GJ 3473 b shown in section 3.5 consider a hydrogen dominated atmosphere, which I meanwhile exclude due to the above-mentioned reasons. Nevertheless, comparing it to other planets in the literature can tell us more about what to expect from an atmosphere with a high mean molecular weight. There is for example GJ 1132 b, which is of similar size and slightly lower equilibrium temperature. As described in the introduction, a H/He atmosphere would be inconsistent with its observed flat transmission spectrum (Mugnai et al., 2021; Libby-Roberts et al., 2021). However, due to its high equilibrium temperature, an atmosphere with a high mean molecular weight could be detected with high-confidence using 10 to 20 eclipse observations by JWST according to Morley et al. (2017) and Kempton et al. (2018).

GJ 3929 b, on the other hand, is particularly well suited for transmission spectroscopy. In technical terms, the technique probes the atmosphere at the day-night terminator region (Madhusudhan, 2019). Thereby it allows for much better constraints on the composition compared to emission spectroscopy because of the much more pronounced absorption features in contrast to the more smooth thermal emission (Greene et al., 2016). GJ 3929 b is also not that much different from GJ 1132 b, so that the analysis of the synthetic transmission spectra presented by Morley et al. (2017) can serve as a proxy

for what could be expected from an atmospheric characterisation. For example, they showed that spectral features of a Venus-like atmosphere would be detectable with fewer than 20 transit observations by JWST. Furthermore, they predict that observations with high S/N could even discriminate between bulk densities either more consistent with Earth or Venus. However, a more precise mass determination for GJ 3929 b would be beneficial because the large errors in the mass transfer to uncertainties in the derived atmospheric scale height that is needed to interpret the spectrum (Kreidberg, 2018; Madhusudhan, 2019).

5.3 Towards the characterisation of habitable rocky exoplanets

With a RV semi-amplitude of $1.29\,\mathrm{m\,s^{-1}}$, GJ 3929 b belongs to the planets with the smallest signal detected by CARMENES so far. Unfortunately, as I mentioned in the previous section, the resulting uncertainty in the mass determination of the planet impairs also the accuracy of potential atmospheric investigations.

Following Hatzes (2019), the S/N of a RV detection can be approximated by:

$$\mathrm{S/N} \approx \sqrt{\frac{N}{2}}\,\frac{K}{\sigma_{\mathrm{meas}}} \tag{5.1}$$

where: N = number of observations

K = RV semi-amplitude

σ_{meas} = uncertainty of the measurements

The obvious approach to lower the uncertainty of the measured RV amplitude would thus certainly be to simply take more measurements. Though, as the S/N scales with $\sqrt{N/2}$, in the case of GJ 3929 one would need to more than double the number of observations to reach a precision better than, for example, $25\,\%$. Given the cost of observations, and to be honest also the time pressure set by competitors, this is often not feasible. The second option is thus to lower the uncertainty of the measurements in the first place. In the error budget presented in chapter 2, I discussed the different factors that play a role for the CARMENES-VIS instrument in this regard. For example, the differential drift was a component that was originally not considered, but actually accounts for a large proportion of the total error. This knowledge can not only be used to improve CARMENES' performance in the first place with the coming update, but also to optimise the design of future spectrographs. Nevertheless, the limits of CARMENES-VIS also become clear in the error budget. The S/N of a single observation strongly depends on the photon noise. A logical step would be therefore to increase the number of detected

photons by using longer exposure times. As I have shown in section 2.4, the mandatory correction of the barycentric motion of the Earth, however, sets a limit to this. For GJ 3929 we actually encountered this issue and hit the maximum feasible integration time of $30\,\text{min}$ and consequently only a mean S/N of 70, which is below the anticipated value of 100.

As obvious as it may sound, in our quest towards the in-depth characterisation of habitable, rocky, exoplanets we consequently need larger telescopes with greater collecting powers. It is hence not surprising that the newest generation of spectrographs, like ESPRESSO in the optical or MAROON-X in the IR were built for telescopes of the $8\,\text{m}$-class. Both already demonstrated their astonishing capabilities. With L 98-59 b, ESPRESSO measured the smallest mass of an exoplanet known so far ($M = 0.40 \pm 0.16\,\text{M}_\oplus$, $K = 0.46 \pm 0.20\,\text{m\,s}^{-1}$; Demangeon et al., 2021). MAROON-X contributed significantly to the discovery of GJ 486 b in a collaborative effort together with CARMENES (Trifonov et al., 2021). The RV measurements thereby reached median uncertainties of $0.39\,\text{m\,s}^{-1}$ in MAROON-X's red arm and $0.82\,\text{m\,s}^{-1}$ in the blue.

With a nominal instrumental precision of $10\,\text{cm\,s}^{-1}$ (Pepe et al., 2021), ESPRESSO even finally breaks the barrier to the detection of Earth-like planets in the habitable zone of Sun-like stars. However, stellar activity poses a huge challenge to this. For GJ 3929, the RV signal imposed by the stellar activity was on the order of $2\,\text{m\,s}^{-1}$ and thus similar to the variation measured for the Sun (Haywood et al., 2016). While the actual level of activity depends on the stellar type, its state of activity and other factors, it still becomes clear that detecting truly Earth-like, habitable, planets is only possible with robust methods to handle it. It is therefore not surprising that a lot of energy is currently being put into characterising and further developing the kernels for GP regression (e.g., Gilbertson et al., 2020; Stock, 2021; Perger et al., 2021; Barragán et al., 2021). For this, however, we also need a deeper understanding of active stars in the first place. Just like the more accurate mass and radius determinations made possible by *Gaia* have led to the detection of the radius valley, our understanding of stellar activity will be crucial for the detection and characterisation of truly Earth-like planets in the future. In doing so, even though they might become less competitive regarding the detection of planets compared to flagships like ESPRESSO, instruments on smaller telescopes will still have a vital role as they can provide important auxiliary information about the planet's host stars. With its extensive series of studies on the characterisation of M dwarfs, CARMENES is already building today an important foundation for this.

Beyond that, the knowledge about stellar activity is also relevant for the atmospheric characterisation of planets. As I have written before, rocky planets orbiting M dwarfs will be the first ones for which atmospheric characterisation will be possible. However, Rackham et al. (2018) have shown that the stellar contamination of the transit depth generated by spots and faculae on the stellar surface can exceed the depth of the expected

atmospheric spectral features by a factor of 10. Planets orbiting inactive stars, such as GJ 3473 b are therefore prime targets for the detection of atmospheres with high mean molecular weight in the near future. Even if such planets are not habitable by our understanding (subsubsection 1.1.1), their study will nevertheless give us important insights into the structure and composition of the atmospheres of rocky exoplanets. This knowledge is important in terms of what exactly we need to look for if we search for biosignatures of extraterrestrial life. The fact that there are many pitfalls in doing so has been recently shown in the controversy surrounding the detection of Phosphine in the atmosphere of Venus (e.g.; Greaves et al., 2021; Bains et al., 2021; Snellen et al., 2020; Villanueva et al., 2021; Encrenaz et al., 2020). For unambiguous evidence, the most suited will be the combined observation of many indicators at once. Convenient due to their large signatures in the spectrum are for example O_2, O_3, CH_4, C_2H_6, N_2O, CH_3Cl, CH_3SH, DMS, or DMDS (e.g., Schwieterman et al., 2018, and references therein).

We thus need to meet four conditions to be able to characterise truly habitable Earth-like planets: precise stellar parameters for an accurate planet radius and mass, a deep understanding of stellar activity and its effects on the spectrum, knowledge on the general structure and composition of exo-Earth atmospheres, and above all powerful facilities for the detection. The ambitions of the scientific community in this regard are high. For example, the American Decadal Survey on Astronomy and Astrophysics 2020 (National Academies of Sciences, Engineering & Medicine, 2021) recently recommended the development of a space-based infrared/optical/ultraviolet telescope for high-contrast imaging of habitable exo-Earths as one of the key projects. In combination with advances in the ground-based instrumentation, we will in this way probably soon be able to answer one of the fundamental questions of astronomy: how abundant is life outside our own Earth.

Publications of Jonas Kemmer

First- and second-author publications

Publications presented in this thesis[1].:

- ***Kemmer, J.**; Dreizler, S.; Kossakowski, D.; et al. 2021
  "*Discovery and mass measurement of the hot, transiting, Earth-sized planet GJ 3929 b*",
  A&A, submitted

- ***Kemmer, J.**; Stock, S.; Kossakowski, D.; et al. 2020
  "*Discovery of a hot, transiting, Earth-sized planet and a second temperate, non-transiting planet around the M4 dwarf GJ 3473 (TOI-488)*",
  A&A, 642, A236

Others:

- *Kossakowski, D.; **Kemmer, J.**; Bluhm, P.: et al. 2021
  "*TOI-1201 b: A mini-Neptune transiting a bright and moderately young M dwarf*",
  A&A, forthcoming

- Stock, S.; **Kemmer, J.**; Reffert, S.: et al. 2020
  "*The CARMENES search for exoplanets around M dwarfs. Characterization of the nearby ultra-compact multiplanetary system YZ Ceti*",
  A&A, 636, A119

- Stock, S. & **Kemmer, J.** 2020
  "*AliasFinder: A Python script to search for the true planetary frequency within radial velocity data*",
  Journal of Open Source Software, 5, 1771

- Mancini, L.; **Kemmer, J.**; Southworth, J.; et al. 2016
  "*An optical transmission spectrum of the giant planet WASP-36 b*",
  MNRAS, 459, 1393

---

[1]Publications by the CARMENES-TESS WG are marked with an asterisk

Co-authored publications

- *Espinoza, N.; Pallé, E.; **Kemmer, J.**; et al. 2021
  "*A transiting, temperate mini-Neptune orbiting the M dwarf TOI-1759 unveiled by TESS*",
  ApJ, submitted

- *González-Álvarez, E.; Zapatero Osorio, M. R.; Sanz-Forcada, J.; et al. (incl. **Kemmer, J.**) 2021
  "*A multi-planetary system orbiting the early-M dwarf TOI-1238*",
  A&A, forthcoming

- *Bluhm, P.; Pallé, E.; Molaverdikhani, K.; et al. (incl. **Kemmer, J.**) 2021
  "*An ultra-short-period transiting super-Earth orbiting the M3 dwarf TOI-1685*",
  A&A, 650, A78

- *Soto, M. G. Anglada-Escudé, G.; Dreizler, S; et al. (incl. **Kemmer, J.**) 2021
  "*Mass and density of the transiting hot and rocky super-Earth LHS 1478 b (TOI-1640 b)*",
  A&A, 649, A144

- *Dreizler, S.; Crossfield, I.J.M.; Kossakowski, D.; et al. (incl. **Kemmer, J.**) 2020
  "*The CARMENES search for exoplanets around M dwarfs. LP 714-47 b (TOI 442.01): populating the Neptune desert*",
  A&A, 644, A127

- Stock, S.; Nagel, E.; **Kemmer, J.**; et al. 2020
  "*The CARMENES search for exoplanets around M dwarfs. Three temperate-to-warm super-Earths*",
  A&A, 643, A112

- *Nowak, G.; Luque, R.; Parviainen, H.; et al. (incl. **Kemmer, J.**) 2020
  "*The CARMENES search for exoplanets around M dwarfs. Two planets on opposite sides of the radius gap transiting the nearby M dwarf LTT 3780*",
  A&A, 642, A173

- *Bluhm, P.; Luque, R.; Espinoza, N.; et al. (incl. **Kemmer, J.**) 2020
  "*Precise mass and radius of a transiting super-Earth planet orbiting the M dwarf TOI-1235: a planet in the radius gap?*",
  A&A, 639, A132

- Morales, J. C.; Mustill, A. J.; Ribas, I.; et al. (incl. **Kemmer, J.**) 2019
  "*A giant exoplanet orbiting a very-low-mass star challenges planet formation models*",
  Science, 365, 1441

- *Luque, R.; Pallé, E.; Kossakowski, D.; et al. (incl. **Kemmer, J.**) 2019
  "*Planetary system around the nearby M dwarf GJ 357 including a transiting, hot, Earth-sized planet optimal for atmospheric characterization*",
  A&A, 628, A39

- Zechmeister, M.; Dreizler, S.; Ribas, I.; et al. (incl. **Kemmer, J.**) 2019
  "*The CARMENES search for exoplanets around M dwarfs. Two temperate Earth-mass planet candidates around Teegarden's Star*",
  A&A, 627, A49

- Keppler, M.; Benisty, M.; Müller, A.; et al. (incl. **Kemmer, J.**) 2018
  "*Discovery of a planetary-mass companion within the gap of the transition disk around PDS 70*",
  A&A, 617, A44

Bibliography

Affer, L., Damasso, M., Micela, G., et al. 2019, A&A, 622, A193, doi: 10.1051/0004-6361/201834868

Agol, E., Steffen, J., Sari, R., & Clarkson, W. 2005, MNRAS, 359, 567, doi: 10.1111/j.1365-2966.2005.08922.x

Agol, E., Dorn, C., Grimm, S. L., et al. 2021, PSJ, 2, 1, doi: 10.3847/PSJ/abd022

Al-Naimiy, H. M. 1978, Ap&SS, 53, 181, doi: 10.1007/BF00645913

Alcock, C., Allsman, R., Alves, D. R., et al. 2000, ApJ, 542, 257, doi: 10.1086/309530

Aller, A., Lillo-Box, J., Jones, D., Miranda, L. F., & Barceló Forteza, S. 2020, åp, 635, A128, doi: 10.1051/0004-6361/201937118

Almenara, J. M., Dorn, C., Bonfils, X., & Udry, S. 2018, MNRAS, 478, 460, doi: 10.1093/mnras/sty1050

Alonso-Floriano, F. J., Morales, J. C., Caballero, J. A., et al. 2015, A&A, 577, A128, doi: 10.1051/0004-6361/201525803

Amado, P. J., Becerril, S., & Herranz, J. 2020. https://carmenes.caha.es/int/documents/OFF/CARMENES-AGR019a.pdf

Ambikasaran, S., Foreman-Mackey, D., Greengard, L., Hogg, D. W., & O'Neil, M. 2015, IEEE Transactions on Pattern Analysis and Machine Intelligence, 38, 252, doi: 10.1109/TPAMI.2015.2448083

Andersen, J. 1991, A&A Rev., 3, 91, doi: 10.1007/BF00873538

Anglada-Escudé, G., & Butler, R. P. 2012, ApJS, 200, 15, doi: 10.1088/0067-0049/200/2/15

Anglada-Escudé, G., Tuomi, M., Gerlach, E., et al. 2013, A&A, 556, A126, doi: 10.1051/0004-6361/201321331

Arenou, F., Luri, X., Babusiaux, C., et al. 2018, A&A, 616, A17, doi: 10.1051/0004-6361/201833234

Artigau, É., Malo, L., Doyon, R., et al. 2018, AJ, 155, 198, doi: 10.3847/1538-3881/aab77d

Astropy Collaboration, Robitaille, T. P., Tollerud, E. J., et al. 2013, A&A, 558, A33, doi: 10.1051/0004-6361/201322068

Astropy Collaboration, Price-Whelan, A. M., Sipocz, B. M., et al. 2018, AJ, 156, 123, doi: 10.3847/1538-3881/aabc4f

Astudillo-Defru, N., Delfosse, X., Bonfils, X., et al. 2017a, A&A, 600, A13, doi: 10.1051/0004-6361/201527078

Astudillo-Defru, N., Bonfils, X., Delfosse, X., et al. 2015, A&A, 575, A119, doi: 10.1051/0004-6361/201424253

Astudillo-Defru, N., Bonfils, X., Almenara, J. M., et al. 2017b, A&A, 605, L11, doi: 10.1051/0004-6361/201731581

Astudillo-Defru, N., Forveille, T., Bonfils, X., et al. 2017c, A&A, 602, A88, doi: 10.1051/0004-6361/201630153

Astudillo-Defru, N., Cloutier, R., Wang, S. X., et al. 2020, A&A, 636, A58, doi: 10.1051/0004-6361/201937179

Bains, W., Petkowski, J. J., Seager, S., et al. 2021, Astrobiology, 21, 1277, doi: 10.1089/ast.2020.2352

Bakos, G., Noyes, R. W., Latham, D. W., et al. 2006, in Tenth Anniversary of 51 Peg-b: Status of and prospects for hot Jupiter studies, ed. L. Arnold, F. Bouchy, & C. Moutou, 184–186

Bakos, G. Á., Noyes, R. W., Kovács, G., et al. 2004, PASP, 116, 266, doi: 10.1086/382735

Bakos, G. Á., Csubry, Z., Penev, K., et al. 2013, PASP, 125, 154, doi: 10.1086/669529

Baluev, R. V. 2008, MNRAS, 385, 1279, doi: 10.1111/j.1365-2966.2008.12689.x

Baraffe, I., Chabrier, G., Barman, T. S., Allard, F., & Hauschildt, P. H. 2003, A&A, 402, 701, doi: 10.1051/0004-6361:20030252

Baraffe, I., Homeier, D., Allard, F., & Chabrier, G. 2015, A&A, 577, A42, doi: 10.1051/0004-6361/201425481

Baranne, A., Mayor, M., & Poncet, J. L. 1979, Vistas in Astronomy, 23, 279, doi: 10.1016/0083-6656(79)90016-3

Baranne, A., Queloz, D., Mayor, M., et al. 1996, A&AS, 119, 373

Barnes, J. R., Jeffers, S. V., & Jones, H. R. A. 2011, MNRAS, 412, 1599, doi: 10.1111/j.1365-2966.2010.17979.x

Barnes, J. R., Jeffers, S. V., Jones, H. R. A., et al. 2015, ApJ, 812, 42, doi: 10.1088/0004-637X/812/1/42

Barnes, J. W. 2007, PASP, 119, 986, doi: 10.1086/522039

Barnes, R., Jackson, B., Raymond, S. N., West, A. A., & Greenberg, R. 2009, ApJ, 695, 1006, doi: 10.1088/0004-637X/695/2/1006

Baroch, D., Morales, J. C., Ribas, I., et al. 2020, A&A, 641, A69, doi: 10.1051/0004-6361/202038213

Barragán, O., Aigrain, S., Rajpaul, V. M., & Zicher, N. 2021, MNRAS, doi: 10.1093/mnras/stab2889

Barragán, O., Gandolfi, D., Dai, F., et al. 2018, A&A, 612, A95, doi: 10.1051/0004-6361/201732217

Barrett, P., Hsu, J. C., Hanley, C., et al. 2012, PyFITS: Python FITS Module

Barstow, J. K., & Irwin, P. G. J. 2016, MNRAS, 461, L92, doi: 10.1093/mnrasl/slw109

Batalha, N. E., Lewis, N. K., Line, M. R., Valenti, J., & Stevenson, K. 2018, ApJ, 856, L34, doi: 10.3847/2041-8213/aab896

Bauer, F. F., Zechmeister, M., & Reiners, A. 2015, A&A, 581, A117, doi: 10.1051/0004-6361/201526462

Bauer, F. F., Zechmeister, M., Kaminski, A., et al. 2020, A&A, 640, A50, doi: 10.1051/0004-6361/202038031

Bayer-Helms, F. 1987, Metrologia, 23, 145, doi: 10.1088/0026-1394/23/3/003

Bean, J. L., Raymond, S. N., & Owen, J. E. 2021, Journal of Geophysical Research (Planets), 126, e06639, doi: 10.1029/2020JE006639

Bechter, A. J., Bechter, E. B., Crepp, J. R., King, D., & Crass, J. 2018, in Society of Photo-Optical Instrumentation Engineers (SPIE) Conference Series, Vol. 10702, Ground-based and Airborne Instrumentation for Astronomy VII, ed. C. J. Evans, L. Simard, & H. Takami, 107026T, doi: 10.1117/12.2313658

Benneke, B., Wong, I., Piaulet, C., et al. 2019, ApJ, 887, L14, doi: 10.3847/2041-8213/ab59dc

Benz, W., Broeg, C., Fortier, A., et al. 2021, Experimental Astronomy, 51, 109, doi: 10.1007/s10686-020-09679-4

Berdyugina, S. V. 2005, Living Reviews in Solar Physics, 2, 8, doi: 10.12942/lrsp-2005-8

Berger, T. A., Huber, D., Gaidos, E., & van Saders, J. L. 2018, ApJ, 866, 99, doi: 10.3847/1538-4357/aada83

Berger, T. A., Huber, D., Gaidos, E., van Saders, J. L., & Weiss, L. M. 2020, AJ, 160, 108, doi: 10.3847/1538-3881/aba18a

Berta, Z. K., Irwin, J., Charbonneau, D., Burke, C. J., & Falco, E. E. 2012, AJ, 144, 145, doi: 10.1088/0004-6256/144/5/145

Berta-Thompson, Z. K., Irwin, J., Charbonneau, D., et al. 2015, Nature, 527, 204, doi: 10.1038/nature15762

Bitsch, B., Raymond, S. N., & Izidoro, A. 2019, A&A, 624, A109, doi: 10.1051/0004-6361/201935007

Blackman, R. T., Fischer, D. A., Jurgenson, C. A., et al. 2020, AJ, 159, 238, doi: 10.3847/1538-3881/ab811d

Bluhm, P., Luque, R., Espinoza, N., et al. 2020, A&A, 639, A132, doi: 10.1051/0004-6361/202038160

Bluhm, P., Pallé, E., Molaverdikhani, K., et al. 2021, A&A, 650, A78, doi: 10.1051/0004-6361/202140688

Bochanski, J. J., Hawley, S. L., Covey, K. R., et al. 2010, AJ, 139, 2679, doi: 10.1088/0004-6256/139/6/2679

Boisse, I., Bouchy, F., Hébrard, G., et al. 2011, A&A, 528, A4, doi: 10.1051/0004-6361/201014354

Bonfils, X., Gillon, M., Udry, S., et al. 2012, A&A, 546, A27, doi: 10.1051/0004-6361/201219623

Bonfils, X., Delfosse, X., Udry, S., et al. 2013, A&A, 549, A109, doi: 10.1051/0004-6361/201014704

Bonfils, X., Almenara, J.-M., Cloutier, R., et al. 2018, A&A, 618, A142, doi: 10.1051/0004-6361/201731884

Borucki, W. J. 2016, Reports on Progress in Physics, 79, 036901, doi: 10.1088/0034-4885/79/3/036901

Borucki, W. J., & Summers, A. L. 1984, Icarus, 58, 121, doi: 10.1016/0019-1035(84)90102-7

Borucki, W. J., Koch, D., Basri, G., et al. 2010, Science, 327, 977, doi: 10.1126/science.1185402

Bourrier, V., Dumusque, X., Dorn, C., et al. 2018, A&A, 619, A1, doi: 10.1051/0004-6361/201833154

Bower, D. J., Kitzmann, D., Wolf, A. S., et al. 2019, A&A, 631, A103, doi: 10.1051/0004-6361/201935710

Brahm, R., Espinoza, N., Jordán, A., et al. 2019, AJ, 158, 45, doi: 10.3847/1538-3881/ab279a

Brasseur, C. E., Phillip, C., Fleming, S. W., Mullally, S. E., & White, R. L. 2019, Astrocut: Tools for creating cutouts of TESS images

Brown, T. M., Baliber, N., Bianco, F. B., et al. 2013, Publications of the Astronomical Society of the Pacific, 125, 1031, doi: 10.1086/673168

Bryson, S. T., Jenkins, J. M., Gilliland, R. L., et al. 2013, PASP, 125, 889, doi: 10.1086/671767

Burn, R., Schlecker, M., Mordasini, C., et al. 2021, arXiv e-prints, arXiv:2105.04596

Burt, J. A., Dragomir, D., Mollière, P., et al. 2021, AJ, 162, 87, doi: 10.3847/1538-3881/ac0432

Butler, R. P., Vogt, S. S., Marcy, G. W., et al. 2004, ApJ, 617, 580, doi: 10.1086/425173

Caballero, J. A., Guàrdia, J., Del López Fresno, M., et al. 2016a, in Society of Photo-Optical Instrumentation Engineers (SPIE) Conference Series, Vol. 9910, Observatory Operations: Strategies, Processes, and Systems VI, ed. A. B. Peck, R. L. Seaman, & C. R. Benn, 99100E, doi: 10.1117/12.2233574

Caballero, J. A., Cortés-Contreras, M., Alonso-Floriano, F. J., et al. 2016b, in 19th Cambridge Workshop on Cool Stars, Stellar Systems, and the Sun (CS19), Cambridge Workshop on Cool Stars, Stellar Systems, and the Sun, 148, doi: 10.5281/zenodo.60060

Campbell, B., & Walker, G. A. H. 1979, PASP, 91, 540, doi: 10.1086/130535

Casper da Costa-Luis, Stephen Karl Larroque, Kyle Altendorf, et al. 2021, tqdm: A fast, Extensible Progress Bar for Python and CLI, Zenodo, doi: 10.5281/zenodo.5517697

Chabrier, G. 2003, PASP, 115, 763, doi: 10.1086/376392

Chaplin, W. J., Basu, S., Huber, D., et al. 2014, ApJS, 210, 1, doi: 10.1088/0067-0049/210/1/1

Charbonneau, D. 2017, in LPI Contributions, Vol. 2042, Habitable Worlds 2017: A System Science Workshop, 4132

Charbonneau, D., & Deming, D. 2007, arXiv e-prints, arXiv:0706.1047

Charbonneau, D., Berta, Z. K., Irwin, J., et al. 2009, Nature, 462, 891, doi: 10.1038/nature08679

Charbonneau, P. 2020, Living Reviews in Solar Physics, 17, 4, doi: 10.1007/s41116-020-00025-6

Ciardi, D. R., Beichman, C. A., Horch, E. P., & Howell, S. B. 2015, ApJ, 805, 16, doi: 10.1088/0004-637X/805/1/16

Cifuentes, C., Caballero, J. A., Cortés-Contreras, M., et al. 2020, A&A, 642, A115, doi: 10.1051/0004-6361/202038295

Cloutier, R., Charbonneau, D., Deming, D., Bonfils, X., & Astudillo-Defru, N. 2021a, AJ, 162, 174, doi: 10.3847/1538-3881/ac1584

Cloutier, R., & Menou, K. 2020, AJ, 159, 211, doi: 10.3847/1538-3881/ab8237

Cloutier, R., Astudillo-Defru, N., Doyon, R., et al. 2017, A&A, 608, A35, doi: 10.1051/0004-6361/201731558

Cloutier, R., Astudillo-Defru, N., Bonfils, X., et al. 2019, A&A, 629, A111, doi: 10.1051/0004-6361/201935957

Cloutier, R., Rodriguez, J. E., Irwin, J., et al. 2020a, AJ, 160, 22, doi: 10.3847/1538-3881/ab9534

Cloutier, R., Eastman, J. D., Rodriguez, J. E., et al. 2020b, AJ, 160, 3, doi: 10.3847/1538-3881/ab91c2

Cloutier, R., Charbonneau, D., Stassun, K. G., et al. 2021b, AJ, 162, 79, doi: 10.3847/1538-3881/ac0157

Cointepas, M., Almenara, J. M., Bonfils, X., et al. 2021, A&A, 650, A145, doi: 10.1051/0004-6361/202140328

Collins, K. A., Kielkopf, J. F., Stassun, K. G., & Hessman, F. V. 2017, AJ, 153, 77, doi: 10.3847/1538-3881/153/2/77

Colome, J., & Ribas, I. 2006, IAU Special Session, 6, 11

Colomé, J., Casteels, K., Ribas, I., & Francisco, X. 2010, in Society of Photo-Optical Instrumentation Engineers (SPIE) Conference Series, Vol. 7740, Software and Cyberinfrastructure for Astronomy, ed. N. M. Radziwill & A. Bridger, 77403K, doi: 10.1117/12.857672

Cortés-Contreras, M. 2016, PhD thesis, Universidad Complutense de Madrid

Cortés-Contreras, M., Béjar, V. J. S., Caballero, J. A., et al. 2017, in Highlights on Spanish Astrophysics IX, ed. S. Arribas, A. Alonso-Herrero, F. Figueras, C. Hernández-Monteagudo, A. Sánchez-Lavega, & S. Pérez-Hoyos, 497–498

Csizmadia, S., Pasternacki, T., Dreyer, C., et al. 2013, A&A, 549, A9, doi: 10.1051/0004-6361/201219888

Cunha, D., Santos, N. C., Figueira, P., et al. 2014, A&A, 568, A35, doi: 10.1051/0004-6361/201423723

Dai, F., Masuda, K., Winn, J. N., & Zeng, L. 2019, ApJ, 883, 79, doi: 10.3847/1538-4357/ab3a3b

Dan Foreman-Mackey, Arjun Savel, Rodrigo Luger, et al. 2021, exoplanet-dev/exoplanet: exoplanet v0.4.4, Zenodo, doi: 10.5281/zenodo.4469745

Dawson, R. I., & Fabrycky, D. C. 2010, ApJ, 722, 937, doi: 10.1088/0004-637X/722/1/937

Dawson, R. I., Lee, E. J., & Chiang, E. 2016, ApJ, 822, 54, doi: 10.3847/0004-637X/822/1/54

de Wit, J., Wakeford, H. R., Gillon, M., et al. 2016, Nature, 537, 69, doi: 10.1038/nature18641

de Wit, J., Wakeford, H. R., Lewis, N. K., et al. 2018, Nature Astronomy, 2, 214, doi: 10.1038/s41550-017-0374-z

Delfosse, X., Forveille, T., Perrier, C., & Mayor, M. 1998, A&A, 331, 581

Delrez, L., Gillon, M., Triaud, A. H. M. J., et al. 2018, MNRAS, 475, 3577, doi: 10.1093/mnras/sty051

Demangeon, O. D. S., Zapatero Osorio, M. R., Alibert, Y., et al. 2021, A&A, 653, A41, doi: 10.1051/0004-6361/202140728

Demory, B.-O., Pozuelos, F. J., Gómez Maqueo Chew, Y., et al. 2020, A&A, 642, A49, doi: 10.1051/0004-6361/202038616

Desort, M., Lagrange, A.-M., Galland, F., Udry, S., & Mayor, M. 2007, A&A, 473, 983, doi: 10.1051/0004-6361:20078144

Diamond-Lowe, H., Berta-Thompson, Z., Charbonneau, D., & Kempton, E. M.-R. 2018, AJ, 156, 42, doi: 10.3847/1538-3881/aac6dd

Diamond-Lowe, H., Charbonneau, D., Malik, M., Kempton, E. M.-R., & Beletsky, Y. 2020, AJ, 160, 188, doi: 10.3847/1538-3881/abaf4f

Dittmann, J. A., Irwin, J. M., Charbonneau, D., et al. 2017, Nature, 544, 333, doi: 10.1038/nature22055

Dorn, C., Harrison, J. H. D., Bonsor, A., & Hands, T. O. 2019, MNRAS, 484, 712, doi: 10.1093/mnras/sty3435

Dorn, C., Hinkel, N. R., & Venturini, J. 2017, A&A, 597, A38, doi: 10.1051/0004-6361/201628749

Dreizler, S., Crossfield, I. J. M., Kossakowski, D., Plavchan, P., & et al. 2020, A&A, submitted

Dressing, C. D., & Charbonneau, D. 2015, ApJ, 807, 45, doi: 10.1088/0004-637X/807/1/45

Dressing, C. D., Charbonneau, D., Dumusque, X., et al. 2015, ApJ, 800, 135, doi: 10.1088/0004-637X/800/2/135

Díez Alonso, E., Caballero, J. A., Montes, D., et al. 2019, A&A, 621, A126, doi: 10.1051/0004-6361/201833316

Eastman, J. D., Rodriguez, J. E., Agol, E., et al. 2019, arXiv e-prints, arXiv:1907.09480

Ehrenreich, D., Bonfils, X., Lovis, C., et al. 2014, A&A, 570, A89, doi: 10.1051/0004-6361/201423809

Emsenhuber, A., Mordasini, C., Burn, R., et al. 2020, arXiv e-prints, arXiv:2007.05561

Encrenaz, T., Greathouse, T. K., Marcq, E., et al. 2020, åp, 643, L5, doi: 10.1051/0004-6361/202039559

Espinoza, N. 2018, Research Notes of the American Astronomical Society, 2, 209, doi: 10.3847/2515-5172/aaef38

Espinoza, N., & Jordán, A. 2015, MNRAS, 450, 1879, doi: 10.1093/mnras/stv744

—. 2016, MNRAS, 457, 3573, doi: 10.1093/mnras/stw224

Espinoza, N., Kossakowski, D., & Brahm, R. 2019a, MNRAS, 490, 2262, doi: 10.1093/mnras/stz2688

Espinoza, N., Hartman, J. D., Bakos, G. A., et al. 2019b, AJ, 158, 63, doi: 10.3847/1538-3881/ab26bb

Estrela, R., Swain, M. R., Gupta, A., Sotin, C., & Valio, A. 2020, ApJ, 898, 104, doi: 10.3847/1538-4357/ab9a4d

Feng, F., Tuomi, M., & Jones, H. R. A. 2017, MNRAS, 470, 4794, doi: 10.1093/mnras/stx1126

Figueira, P., Adibekyan, V. Z., Oshagh, M., et al. 2016, A&A, 586, A101, doi: 10.1051/0004-6361/201526900

Fischer, D. A., Anglada-Escude, G., Arriagada, P., et al. 2016, PASP, 128, 066001, doi: 10.1088/1538-3873/128/964/066001

Foreman-Mackey, D. 2018, Research Notes of the American Astronomical Society, 2, 31, doi: 10.3847/2515-5172/aaaf6c

Foreman-Mackey, D., Agol, E., Angus, R., & Ambikasaran, S. 2017, ArXiv

Fukui, A., Narita, N., Tristram, P. J., et al. 2011, PASJ, 63, 287, doi: 10.1093/pasj/63.1.287

Fulton, B. J., & Petigura, E. A. 2018, AJ, 156, 264, doi: 10.3847/1538-3881/aae828

Fulton, B. J., Petigura, E. A., Blunt, S., & Sinukoff, E. 2018, PASP, 130, 044504, doi: 10.1088/1538-3873/aaaaa8

Fulton, B. J., Petigura, E. A., Howard, A. W., et al. 2017, AJ, 154, 109, doi: 10.3847/1538-3881/aa80eb

Gagné, J., Mamajek, E. E., Malo, L., et al. 2018, ApJ, 856, 23, doi: 10.3847/1538-4357/aaae09

Gaia Collaboration, Brown, A. G. A., Vallenari, A., et al. 2018, A&A, 616, A1, doi: 10.1051/0004-6361/201833051

—. 2021, A&A, 649, A1, doi: 10.1051/0004-6361/202039657

Gaidos, E., Mann, A. W., Kraus, A. L., & Ireland, M. 2016, MNRAS, 457, 2877, doi: 10.1093/mnras/stw097

Gao, P., Thorngren, D. P., Lee, G. K. H., et al. 2020, Nature Astronomy, doi: 10.1038/s41550-020-1114-3

García, R. A., Mathur, S., Salabert, D., et al. 2010, Science, 329, 1032, doi: 10.1126/science.1191064

Gardner, J. P., Mather, J. C., Clampin, M., et al. 2006, Space Sci. Rev., 123, 485, doi: 10.1007/s11214-006-8315-7

Giclas, H. L., Slaughter, C. D., & Burnham, R. 1959, Lowell Observatory Bulletin, 4, 136

Gilbertson, C., Ford, E. B., Jones, D. E., & Stenning, D. C. 2020, ApJ, 905, 155, doi: 10.3847/1538-4357/abc627

Gilliland, R. L., & Brown, T. M. 1988, PASP, 100, 754, doi: 10.1086/132232

Gillon, M., Pont, F., Demory, B.-O., et al. 2007, A&A, 472, L13, doi: 10.1051/0004-6361:20077799

Gillon, M., Jehin, E., Lederer, S. M., et al. 2016, Nature, 533, 221, doi: 10.1038/nature17448

Gillon, M., Triaud, Amaury H. M. J., Demory, B.-O., et al. 2017, Nature, 542, 456, doi: 10.1038/nature21360

Gilmozzi, R., & Spyromilio, J. 2007, The Messenger, 127, 11

Ginsburg, A., Sipocz, B. M., Brasseur, C. E., et al. 2019, AJ, 157, 98, doi: 10.3847/1538-3881/aafc33

Ginzburg, S., Schlichting, H. E., & Sari, R. 2016, ApJ, 825, 29, doi: 10.3847/0004-637X/825/1/29

—. 2018, MNRAS, 476, 759, doi: 10.1093/mnras/sty290

Girardi, L., Barbieri, M., Groenewegen, M. A. T., et al. 2012, Astrophysics and Space Science Proceedings, 26, 165, doi: 10.1007/978-3-642-18418-5_17

Gizis, J. E., Reid, I. N., & Hawley, S. L. 2002, AJ, 123, 3356, doi: 10.1086/340465

Gliese, W., & Jahreiß, H. 1991, Preliminary Version of the Third Catalogue of Nearby Stars

Greaves, J. S., Richards, A. M. S., Bains, W., et al. 2021, Nature Astronomy, 5, 655, doi: 10.1038/s41550-020-1174-4

Greene, T. P., Line, M. R., Montero, C., et al. 2016, ApJ, 817, 17, doi: 10.3847/0004-637X/817/1/17

Grimm, S. L., Demory, B.-O., Gillon, M., et al. 2018, A&A, 613, A68, doi: 10.1051/0004-6361/201732233

Guerrero, N. M., Seager, S., Huang, C. X., et al. 2021, ApJS, 254, 39, doi: 10.3847/1538-4365/abefe1

Gupta, A., & Schlichting, H. E. 2019, MNRAS, 487, 24, doi: 10.1093/mnras/stz1230

—. 2021, MNRAS, 504, 4634, doi: 10.1093/mnras/stab1128

Günther, M. N., & Daylan, T. 2021, ApJS, 254, 13, doi: 10.3847/1538-4365/abe70e

Günther, M. N., Pozuelos, F. J., Dittmann, J. A., et al. 2019, Nature Astronomy, 3, 1099, doi: 10.1038/s41550-019-0845-5

Hadden, S., & Lithwick, Y. 2014, ApJ, 787, 80, doi: 10.1088/0004-637X/787/1/80

Haldemann, J., Alibert, Y., Mordasini, C., & Benz, W. 2020, A&A, 643, A105, doi: 10.1051/0004-6361/202038367

Halverson, S., Terrien, R., Mahadevan, S., et al. 2016, in Society of Photo-Optical Instrumentation Engineers (SPIE) Conference Series, Vol. 9908, Ground-based and Airborne Instrumentation for Astronomy VI, ed. C. J. Evans, L. Simard, & H. Takami, 99086P, doi: 10.1117/12.2232761

Hamann, A., Montet, B. T., Fabrycky, D. C., Agol, E., & Kruse, E. 2019, AJ, 158, 133, doi: 10.3847/1538-3881/ab32e3

Hara, N. C., Boué, G., Laskar, J., Delisle, J.-B., & Unger, N. 2019, MNRAS, 489, 738, doi: 10.1093/mnras/stz1849

Hardegree-Ullman, K. K., Cushing, M. C., Muirhead, P. S., & Christiansen, J. L. 2019, AJ, 158, 75, doi: 10.3847/1538-3881/ab21d2

Harris, C. R., Millman, K. J., van der Walt, S. J., et al. 2020, Nature, 585, 357, doi: 10.1038/s41586-020-2649-2

Hartman, J. D., Bakos, G. A., Noyes, R. W., et al. 2011, AJ, 141, 166, doi: 10.1088/0004-6256/141/5/166

Hastings, W. K. 1970, Biometrika, 57, 97, doi: 10.1093/biomet/57.1.97

Hatzes, A. P. 1996, PASP, 108, 839, doi: 10.1086/133805

—. 2019, The Doppler Method for the Detection of Exoplanets, doi: 10.1088/2514-3433/ab46a3

Hawley, S. L., Gizis, J. E., & Reid, I. N. 1996, AJ, 112, 2799, doi: 10.1086/118222

Haywood, R. D., Collier Cameron, A., Queloz, D., et al. 2014, MNRAS, 443, 2517, doi: 10.1093/mnras/stu1320

Haywood, R. D., Collier Cameron, A., Unruh, Y. C., et al. 2016, MNRAS, 457, 3637, doi: 10.1093/mnras/stw187

Heng, K., & Lyons, J. R. 2016, ApJ, 817, 149

Henry, T. J., Jao, W.-C., Subasavage, J. P., et al. 2006, AJ, 132, 2360, doi: 10.1086/508233

Hippke, M., David, T. J., Mulders, G. D., & Heller, R. 2019, AJ, 158, 143, doi: 10.3847/1538-3881/ab3984

Hippke, M., & Heller, R. 2019, A&A, 623, A39, doi: 10.1051/0004-6361/201834672

Hirano, T., Gaidos, E., Winn, J. N., et al. 2020, ApJ, 890, L27, doi: 10.3847/2041-8213/ab74dc

Hodapp, K. W., Jensen, J. B., Irwin, E. M., et al. 2003, PASP, 115, 1388, doi: 10.1086/379669

Holman, M. J., & Murray, N. W. 2005, Science, 307, 1288, doi: 10.1126/science.1107822

Hormuth, F., Brandner, W., Hippler, S., & Henning, T. 2008, Journal of Physics Conference Series, 131, 012051, doi: 10.1088/1742-6596/131/1/012051

Howard, A. W., Marcy, G. W., Bryson, S. T., et al. 2012, ApJS, 201, 15, doi: 10.1088/0067-0049/201/2/15

Howell, S. B. 2006, Handbook of CCD Astronomy, Vol. 5

Howell, S. B., Sobeck, C., Haas, M., et al. 2014, PASP, 126, 398, doi: 10.1086/676406

Hsu, D. C., Ford, E. B., & Terrien, R. 2020, MNRAS, 498, 2249, doi: 10.1093/mnras/staa2391

Hunter, J. D. 2007, Computing in Science & Engineering, 9, 90, doi: 10.1109/MCSE.2007.55

Husser, T.-O., Wende-von Berg, S., Dreizler, S., et al. 2013, A&A, 553, A6, doi: 10.1051/0004-6361/201219058

Inamdar, N. K., & Schlichting, H. E. 2015, MNRAS, 448, 1751, doi: 10.1093/mnras/stv030

Izidoro, A., Bitsch, B., Raymond, S. N., et al. 2019, arXiv e-prints, arXiv:1902.08772

Jeffers, S. V., Schöfer, P., Lamert, A., et al. 2018, A&A, 614, A76, doi: 10.1051/0004-6361/201629599

Jeffers, S. V., Dreizler, S., Barnes, J. R., et al. 2020, Science (New York, N.Y.), 368, 1477, doi: 10.1126/science.aaz0795

Jeffreys, H. 1946, Proceedings of the Royal Society of London Series A, 186, 453, doi: 10.1098/rspa.1946.0056

Jenkins, J. M. 2002, ApJ, 575, 493, doi: 10.1086/341136

Jenkins, J. M., Caldwell, D. A., & Borucki, W. J. 2002, ApJ, 564, 495, doi: 10.1086/324143

Jenkins, J. M., Tenenbaum, P., Seader, S., et al. 2020, Kepler Data Processing Handbook: Transiting Planet Search

Jenkins, J. M., Chandrasekaran, H., McCauliff, S. D., et al. 2010, in Society of Photo-Optical Instrumentation Engineers (SPIE) Conference Series, Vol. 7740, Software and Cyberinfrastructure for Astronomy, ed. N. M. Radziwill & A. Bridger, 77400D, doi: 10.1117/12.856764

Jenkins, J. M., Twicken, J. D., McCauliff, S., et al. 2016, in Society of Photo-Optical Instrumentation Engineers (SPIE) Conference Series, Vol. 9913, Proc. SPIE, 99133E, doi: 10.1117/12.2233418

Jenkins, J. S., Pozuelos, F. J., Tuomi, M., et al. 2019, MNRAS, 490, 5585, doi: 10.1093/mnras/stz2937

Jin, S., Mordasini, C., Parmentier, V., et al. 2014, ApJ, 795, 65, doi: 10.1088/0004-637X/795/1/65

Johansen, A., & Lambrechts, M. 2017, Annual Review of Earth and Planetary Sciences, 45, 359, doi: 10.1146/annurev-earth-063016-020226

Jontof-Hutter, D. 2019, Annual Review of Earth and Planetary Sciences, 47, 141, doi: 10.1146/annurev-earth-053018-060352

Jontof-Hutter, D., Ford, E. B., Rowe, J. F., et al. 2016, ApJ, 820, 39, doi: 10.3847/0004-637X/820/1/39

Kanodia, S., & Wright, J. 2018a, Research Notes of the American Astronomical Society, 2, 4, doi: 10.3847/2515-5172/aaa4b7

Kanodia, S., & Wright, J. T. 2018b, Barycorrpy: Barycentric velocity calculation and leap second management

Kasting, J. F., Whitmire, D. P., & Reynolds, R. T. 1993, Icarus, 101, 108, doi: 10.1006/icar.1993.1010

Kawashima, Y., & Ikoma, M. 2019, ApJ, 877, 109, doi: 10.3847/1538-4357/ab1b1d

Kemmer, J., Stock, S., Kossakowski, D., et al. 2020, åp, 642, A236, doi: 10.1051/0004-6361/202038967

Kempton, E. M.-R., Bean, J. L., Louie, D. R., et al. 2018, PASP, 130, 114401, doi: 10.1088/1538-3873/aadf6f

Kipping, D. M. 2008, MNRAS, 389, 1383, doi: 10.1111/j.1365-2966.2008.13658.x

—. 2013, MNRAS, 435, 2152, doi: 10.1093/mnras/stt1435

Kipping, D. M., Nesvorný, D., Buchhave, L. A., et al. 2014, ApJ, 784, 28, doi: 10.1088/0004-637X/784/1/28

Kite, E. S., & Barnett, M. N. 2020, Proceedings of the National Academy of Science, 117, 18264

Kjeldsen, H., Bedding, T. R., & Christensen-Dalsgaard, J. 2009, in Transiting Planets, ed. F. Pont, D. Sasselov, & M. J. Holman, Vol. 253, 309–317, doi: 10.1017/S1743921308026537

Knutson, H. A., Charbonneau, D., Noyes, R. W., Brown, T. M., & Gilliland, R. L. 2007, ApJ, 655, 564, doi: 10.1086/510111

Kochanek, C. S., Shappee, B. J., Stanek, K. Z., et al. 2017, PASP, 129, 104502, doi: 10.1088/1538-3873/aa80d9

Kopparapu, R. K., Ramirez, R. M., SchottelKotte, J., et al. 2014, ApJ, 787, L29, doi: 10.1088/2041-8205/787/2/L29

Kopparapu, R. K., Ramirez, R., Kasting, J. F., et al. 2013, ApJ, 765, 131, doi: 10.1088/0004-637X/765/2/131

Kosiarek, M. R., Crossfield, I. J. M., Hardegree-Ullman, K. K., et al. 2019, AJ, 157, 97, doi: 10.3847/1538-3881/aaf79c

Kossakowski, D., Espinoza, N., Brahm, R., et al. 2019, MNRAS, 490, 1094, doi: 10.1093/mnras/stz2433

Kossakowski, D., Kemmer, J., Bluhm, P., et al. 2021, arXiv e-prints, arXiv:2109.09346

Kostov, V. B., Schlieder, J. E., Barclay, T., et al. 2019, AJ, 158, 32, doi: 10.3847/1538-3881/ab2459

Kotani, T., Tamura, M., Nishikawa, J., et al. 2018, in Society of Photo-Optical Instrumentation Engineers (SPIE) Conference Series, Vol. 10702, Ground-based and Airborne Instrumentation for Astronomy VII, ed. C. J. Evans, L. Simard, & H. Takami, 1070211, doi: 10.1117/12.2311836

Kovács, G., Zucker, S., & Mazeh, T. 2002, A&A, 391, 369, doi: 10.1051/0004-6361:20020802

Kreidberg, L. 2015, PASP, 127, 1161, doi: 10.1086/683602

—. 2018, in Handbook of Exoplanets, ed. H. J. Deeg & J. A. Belmonte, 100, doi: 10.1007/978-3-319-55333-7

Kreidberg, L., Bean, J. L., Désert, J.-M., et al. 2014, Nature, 505, 69, doi: 10.1038/nature12888

Kron, G. E. 1947, PASP, 59, 261, doi: 10.1086/125964

Lafarga, M., Ribas, I., Lovis, C., et al. 2020, A&A, 636, A36, doi: 10.1051/0004-6361/201937222

Lafarga, M., Ribas, I., Reiners, A., et al. 2021, åp, 652, A28, doi: 10.1051/0004-6361/202140605

Lalitha, S., Baroch, D., Morales, J. C., et al. 2019, A&A, 627, A116, doi: 10.1051/0004-6361/201935534

Lanotte, A. A., Gillon, M., Demory, B.-O., et al. 2014, A&A, 572, A73, doi: 10.1051/0004-6361/201424373

Laskar, J., & Petit, A. C. 2017, A&A, 605, A72, doi: 10.1051/0004-6361/201630022

Li, C.-H., Benedick, A. J., Fendel, P., et al. 2008, Nature, 452, 610, doi: 10.1038/nature06854

Li, J., Tenenbaum, P., Twicken, J. D., et al. 2019, PASP, 131, 024506, doi: 10.1088/1538-3873/aaf44d

Libby-Roberts, J. E., Berta-Thompson, Z. K., Diamond-Lowe, H., et al. 2021, arXiv e-prints, arXiv:2105.10487

Lightkurve Collaboration, Cardoso, J. V. d. M., Hedges, C., et al. 2018, Lightkurve: Kepler and TESS time series analysis in Python

Lillo-Box, J., Barrado, D., & Bouy, H. 2012, A&A, 546, A10, doi: 10.1051/0004-6361/201219631

—. 2014, A&A, 566, A103, doi: 10.1051/0004-6361/201423497

Lillo-Box, J., Figueira, P., Leleu, A., et al. 2020, A&A, 642, A121, doi: 10.1051/0004-6361/202038922

Lindegren, L., Hernández, J., Bombrun, A., et al. 2018, A&A, 616, A2, doi: 10.1051/0004-6361/201832727

Lissauer, J. J. 2007, ApJ, 660, L149, doi: 10.1086/518121

Lithwick, Y., Xie, J., & Wu, Y. 2012, ApJ, 761, 122, doi: 10.1088/0004-637X/761/2/122

Lopez, E. D., & Fortney, J. J. 2013, ApJ, 776, 2, doi: 10.1088/0004-637X/776/1/2

—. 2014, ApJ, 792, 1, doi: 10.1088/0004-637X/792/1/1

Lopez, E. D., & Rice, K. 2018, MNRAS, 479, 5303, doi: 10.1093/mnras/sty1707

Lovis, C., & Pepe, F. 2007, A&A, 468, 1115, doi: 10.1051/0004-6361:20077249

Luger, R., Sestovic, M., Kruse, E., et al. 2017, Nature Astronomy, 1, 0129, doi: 10.1038/s41550-017-0129

Luque, R., Pallé, E., Kossakowski, D., et al. 2019, A&A, 628, A39, doi: 10.1051/0004-6361/201935801

Luque, R., Serrano, L. M., Molaverdikhani, K., et al. 2021, A&A, 645, A41, doi: 10.1051/0004-6361/202039455

Lustig-Yaeger, J., Meadows, V. S., & Lincowski, A. P. 2019a, AJ, 158, 27, doi: 10.3847/1538-3881/ab21e0

—. 2019b, ApJ, 887, L11, doi: 10.3847/2041-8213/ab5965

Luyten, W. J. 1979, New Luyten catalogue of stars with proper motions larger than two tenths of an arcsecond; and first supplement; NLTT. (Minneapolis (1979)); Label 12 = short description; Label 13 = documentation by Warren; Label 14 = catalogue

Lépine, S., Hilton, E. J., Mann, A. W., et al. 2013, AJ, 145, 102, doi: 10.1088/0004-6256/145/4/102

Madhusudhan, N. 2012, ApJ, 758, 36

—. 2019, ARA&A, 57, 617, doi: 10.1146/annurev-astro-081817-051846

Malavolta, L., Mayo, A. W., Louden, T., et al. 2018, AJ, 155, 107, doi: 10.3847/1538-3881/aaa5b5

Manescau, A., Gullieuszik, M., Iwert, O., et al. 2010, in Society of Photo-Optical Instrumentation Engineers (SPIE) Conference Series, Vol. 7739, Modern Technologies in Space- and Ground-based Telescopes and Instrumentation, ed. E. Atad-Ettedgui & D. Lemke, 77394C, doi: 10.1117/12.856829

Mann, A. W., Dupuy, T., Muirhead, P. S., et al. 2017, AJ, 153, 267, doi: 10.3847/1538-3881/aa7140

Marcy, G. W., & Butler, R. P. 1992, PASP, 104, 270, doi: 10.1086/132989

Marfil, E., Tabernero, H. M., Montes, D., et al. 2021, arXiv e-prints, arXiv:2110.07329

Mason, B. D., Wycoff, G. L., Hartkopf, W. I., Douglass, G. G., & Worley, C. E. 2001, AJ, 122, 3466, doi: 10.1086/323920

Mayor, M., Pepe, F., Queloz, D., et al. 2003, The Messenger, 114, 20

McArthur, B. E., Endl, M., Cochran, W. D., et al. 2004, ApJ, 614, L81, doi: 10.1086/425561

McCully, C., Volgenau, N. H., Harbeck, D.-R., et al. 2018a, in Society of Photo-Optical Instrumentation Engineers (SPIE) Conference Series, Vol. 10707, Proc. SPIE, 107070K, doi: 10.1117/12.2314340

McCully, C., Turner, M., Volgenau, N., et al. 2018b, Lcogt/Banzai: Initial Release, Zenodo, doi: 10.5281/zenodo.1257560

McQuillan, A., Mazeh, T., & Aigrain, S. 2014, ApJS, 211, 24, doi: 10.1088/0067-0049/211/2/24

Ment, K., Dittmann, J. A., Astudillo-Defru, N., et al. 2019, AJ, 157, 32, doi: 10.3847/1538-3881/aaf1b1

Metropolis, N., Rosenbluth, A. W., Rosenbluth, M. N., Teller, A. H., & Teller, E. 1953, J. Chem. Phys., 21, 1087, doi: 10.1063/1.1699114

Middelmann, T., Walkov, A., Bartl, G., & Schödel, R. 2015, Phys. Rev. B, 92, 174113, doi: 10.1103/PhysRevB.92.174113

Miller-Ricci, E., Seager, S., & Sasselov, D. 2009, ApJ, 690, 1056, doi: 10.1088/0004-637X/690/2/1056

Mills, S. M., & Mazeh, T. 2017, ApJ, 839, L8, doi: 10.3847/2041-8213/aa67eb

Molaverdikhani, K., Henning, T., & Mollière, P. 2019a, ApJ, 873, 32, doi: 10.3847/1538-4357/aafda8

—. 2019b, ApJ, 883, 194, doi: 10.3847/1538-4357/ab3e30

—. 2020, ApJ, 899, 53, doi: 10.3847/1538-4357/aba52b

Mollière, P., van Boekel, R., Dullemond, C., Henning, T., & Mordasini, C. 2015, ApJ, 813, 47

Montet, B. T., Morton, T. D., Foreman-Mackey, D., et al. 2015, ApJ, 809, 25, doi: 10.1088/0004-637X/809/1/25

Morales, J. C., Mustill, A. J., Ribas, I., et al. 2019, Science, 365, 1441, doi: 10.1126/science.aax3198

Morin, J., Donati, J.-F., Petit, P., et al. 2010, MNRAS, 407, 2269, doi: 10.1111/j.1365-2966.2010.17101.x

Morley, C. V., Kreidberg, L., Rustamkulov, Z., Robinson, T., & Fortney, J. J. 2017, ApJ, 850, 121, doi: 10.3847/1538-4357/aa927b

Mortier, A., & Collier Cameron, A. 2017, A&A, 601, A110, doi: 10.1051/0004-6361/201630201

Mortier, A., Faria, J. P., Correia, C. M., Santerne, A., & Santos, N. C. 2015, A&A, 573, A101, doi: 10.1051/0004-6361/201424908

Morton, T. D. 2015, isochrones: Stellar model grid package

Mugnai, L. V., Modirrousta-Galian, D., Edwards, B., et al. 2021, AJ, 161, 284, doi: 10.3847/1538-3881/abf3c3

Mulders, G. D., Pascucci, I., & Apai, D. 2015, ApJ, 798, 112, doi: 10.1088/0004-637X/798/2/112

Mullan, D. J., & MacDonald, J. 2001, ApJ, 559, 353, doi: 10.1086/322336

Murphy, M. T., Udem, T., Holzwarth, R., et al. 2007, MNRAS, 380, 839, doi: 10.1111/j.1365-2966.2007.12147.x

Nagel, E., Czesla, S., Kaminski, A., et al. in prep.

Narita, N., Fukui, A., Kusakabe, N., et al. 2015, Journal of Astronomical Telescopes, Instruments, and Systems, 1, 045001, doi: 10.1117/1.JATIS.1.4.045001

—. 2019, Journal of Astronomical Telescopes, Instruments, and Systems, 5, 015001, doi: 10.1117/1.JATIS.5.1.015001

Narita, N., Fukui, A., Yamamuro, T., et al. 2020, in Society of Photo-Optical Instrumentation Engineers (SPIE) Conference Series, Vol. 11447, Society of Photo-Optical Instrumentation Engineers (SPIE) Conference Series, 114475K, doi: 10.1117/12.2559947

National Academies of Sciences, Engineering, & Medicine. 2021, Pathways to Discovery in Astronomy and Astrophysics for the 2020s (Washington, DC: The National Academies Press), doi: 10.17226/26141

Nava, C., López-Morales, M., Haywood, R. D., & Giles, H. A. C. 2020, AJ, 159, 23, doi: 10.3847/1538-3881/ab53ec

Newton, E. R., Charbonneau, D., Irwin, J., et al. 2014, AJ, 147, 20, doi: 10.1088/0004-6256/147/1/20

Newton, E. R., Irwin, J., Charbonneau, D., et al. 2017, ApJ, 834, 85, doi: 10.3847/1538-4357/834/1/85

—. 2016, ApJ, 821, 93, doi: 10.3847/0004-637X/821/2/93

Nortmann, L., Pallé, E., Salz, M., et al. 2018, Science, 362, 1388, doi: 10.1126/science.aat5348

Nowak, G., Luque, R., Parviainen, H., et al. 2020, A&A, 642, A173, doi: 10.1051/0004-6361/202037867

Ogihara, M., Kunitomo, M., & Hori, Y. 2020, ApJ, 899, 91, doi: 10.3847/1538-4357/aba75e

Oshagh, M., Bauer, F. F., Lafarga, M., et al. 2020, åp, 643, A64, doi: 10.1051/0004-6361/202039213

Owen, J. E., & Wu, Y. 2013, ApJ, 775, 105, doi: 10.1088/0004-637X/775/2/105

—. 2016, ApJ, 817, 107, doi: 10.3847/0004-637X/817/2/107

—. 2017, ApJ, 847, 29, doi: 10.3847/1538-4357/aa890a

Palle, E., Nortmann, L., Casasayas-Barris, N., et al. 2020, A&A, 638, A61, doi: 10.1051/0004-6361/202037719

Parker, E. N. 1955, ApJ, 122, 293, doi: 10.1086/146087

Parviainen, H. 2015, MNRAS, 450, 3233, doi: 10.1093/mnras/stv894

Parviainen, H., Tingley, B., Deeg, H. J., et al. 2019, A&A, 630, A89, doi: 10.1051/0004-6361/201935709

Passegger, V. M., Wende-von Berg, S., & Reiners, A. 2016, A&A, 587, A19, doi: 10.1051/0004-6361/201322261

Passegger, V. M., Reiners, A., Jeffers, S. V., et al. 2018, A&A, 615, A6, doi: 10.1051/0004-6361/201732312

Passegger, V. M., Schweitzer, A., Shulyak, D., et al. 2019, A&A, 627, A161, doi: 10.1051/0004-6361/201935679

—. 2020a, A&A, 634, C2, doi: 10.1051/0004-6361/201935679e

Passegger, V. M., Bello-GarcOrdieres-Meré, J., Caballero, J. A., et al. 2020b, A&A, 642, A22, doi: 10.1051/0004-6361/202038787

Pedregosa, F., Varoquaux, G., Gramfort, A., et al. 2011, Journal of Machine Learning Research, 12, 2825

Pepe, F., Mayor, M., Galland, F., et al. 2002, A&A, 388, 632, doi: 10.1051/0004-6361:20020433

Pepe, F., Molaro, P., Cristiani, S., et al. 2014, Astronomische Nachrichten, 335, 8

Pepe, F., Cristiani, S., Rebolo, R., et al. 2021, A&A, 645, A96, doi: 10.1051/0004-6361/202038306

Pepe, F. A., Cristiani, S., Rebolo Lopez, R., et al. 2010, in Society of Photo-Optical Instrumentation Engineers (SPIE) Conference Series, Vol. 7735, Ground-based and Airborne Instrumentation for Astronomy III, ed. I. S. McLean, S. K. Ramsay, & H. Takami, 77350F, doi: 10.1117/12.857122

Perger, M., Anglada-Escudé, G., Ribas, I., et al. 2021, åp, 645, A58, doi: 10.1051/0004-6361/202039594

Perryman, M. 2011, The Exoplanet Handbook

Pinamonti, M., Sozzetti, A., Giacobbe, P., et al. 2019, A&A, 625, A126, doi: 10.1051/0004-6361/201834969

Plavchan, P., Latham, D., Gaudi, S., et al. 2015, arXiv e-prints, arXiv:1503.01770

Podgorski, W., Bean, J., Bergner, H., et al. 2014, in Society of Photo-Optical Instrumentation Engineers (SPIE) Conference Series, Vol. 9147, Ground-based and Airborne Instrumentation for Astronomy V, ed. S. K. Ramsay, I. S. McLean, & H. Takami, 91478W, doi: 10.1117/12.2056329

Pollacco, D. L., Skillen, I., Collier Cameron, A., et al. 2006, PASP, 118, 1407, doi: 10.1086/508556

Pope, B. J. S., Parviainen, H., & Aigrain, S. 2016, MNRAS, 461, 3399, doi: 10.1093/mnras/stw1373

Qian, S.-B., Liu, L., Zhu, L.-Y., et al. 2012, MNRAS, 422, L24, doi: 10.1111/j.1745-3933.2012.01228.x

Queloz, D. 1995, in New Developments in Array Technology and Applications, ed. A. G. D. Philip, K. Janes, & A. R. Upgren, Vol. 167, 221

Queloz, D., Henry, G. W., Sivan, J. P., et al. 2001, A&A, 379, 279, doi: 10.1051/0004-6361:20011308

Quirrenbach, A. 2001, in The Formation of Binary Stars, ed. H. Zinnecker & R. Mathieu, Vol. 200, 539

Quirrenbach, A., Amado, P. J., Caballero, J. A., et al. 2014, in Society of Photo-Optical Instrumentation Engineers (SPIE) Conference Series, Vol. 9147, Ground-based and Airborne Instrumentation for Astronomy V, ed. S. K. Ramsay, I. S. McLean, & H. Takami, 91471F, doi: 10.1117/12.2056453

Quirrenbach, A., Amado, P. J., Caballero, J. A., et al. 2016, in Society of Photo-Optical Instrumentation Engineers (SPIE) Conference Series, Vol. 9908, Ground-based and Airborne Instrumentation for Astronomy VI, ed. C. J. Evans, L. Simard, & H. Takami, 990812, doi: 10.1117/12.2231880

Quirrenbach, A., Amado, P. J., Ribas, I., et al. 2018, in Society of Photo-Optical Instrumentation Engineers (SPIE) Conference Series, Vol. 10702, Ground-based and Airborne Instrumentation for Astronomy VII, ed. C. J. Evans, L. Simard, & H. Takami, 107020W, doi: 10.1117/12.2313689

Quirrenbach, A., CARMENES Consortium, Amado, P. J., et al. 2020, in Society of Photo-Optical Instrumentation Engineers (SPIE) Conference Series, Vol. 11447, Society of Photo-Optical Instrumentation Engineers (SPIE) Conference Series, 114473C, doi: 10.1117/12.2561380

Rackham, B. V., Apai, D., & Giampapa, M. S. 2018, ApJ, 853, 122, doi: 10.3847/1538-4357/aaa08c

Radick, R. R., Thompson, D. T., Lockwood, G. W., Duncan, D. K., & Baggett, W. E. 1987, ApJ, 321, 459, doi: 10.1086/165645

Rajpaul, V., Aigrain, S., Osborne, M. A., Reece, S., & Roberts, S. 2015, MNRAS, 452, 2269, doi: 10.1093/mnras/stv1428

Rajpaul, V., Aigrain, S., & Roberts, S. 2016, MNRAS, 456, L6, doi: 10.1093/mnrasl/slv164

Rauer, H., Gebauer, S., Paris, P. V., et al. 2011, A&A, 529, A8, doi: 10.1051/0004-6361/201014368

Reid, I. N., Hawley, S. L., & Gizis, J. E. 1995, AJ, 110, 1838, doi: 10.1086/117655

Reiners, A., Banyal, R. K., & Ulbrich, R. G. 2014, A&A, 569, A77, doi: 10.1051/0004-6361/201424099

Reiners, A., & Basri, G. 2007, ApJ, 656, 1121, doi: 10.1086/510304

—. 2010, ApJ, 710, 924, doi: 10.1088/0004-637X/710/2/924

Reiners, A., Bean, J. L., Huber, K. F., et al. 2010, ApJ, 710, 432, doi: 10.1088/0004-637X/710/1/432

Reiners, A., Joshi, N., & Goldman, B. 2012, AJ, 143, 93, doi: 10.1088/0004-6256/143/4/93

Reiners, A., & Zechmeister, M. 2020, ApJS, 247, 11, doi: 10.3847/1538-4365/ab609f

Reiners, A., Zechmeister, M., Caballero, J. A., et al. 2018a, A&A, 612, A49, doi: 10.1051/0004-6361/201732054

Reiners, A., Ribas, I., Zechmeister, M., et al. 2018b, åp, 609, L5, doi: 10.1051/0004-6361/201732165

Ribas, I., Reiners, A., Seifert, W., et al. 2013. https://carmenes.caha.es/int/documents/FDR/CARMENES-FDR-01C-Science-ErrorBudget.pdf

Ricker, G. R., Winn, J. N., Vanderspek, R., et al. 2015, Journal of Astronomical Telescopes, Instruments, and Systems, 1, 014003, doi: 10.1117/1.JATIS.1.1.014003

Robertson, P. 2018, ApJ, 864, L28, doi: 10.3847/2041-8213/aadc0b

Rodríguez-López, C. 2019, Frontiers in Astronomy and Space Sciences, 6, 76, doi: 10.3389/fspas.2019.00076

Rogers, J. G., Gupta, A., Owen, J. E., & Schlichting, H. E. 2021, MNRAS, 508, 5886, doi: 10.1093/mnras/stab2897

Rogers, L. A. 2015, ApJ, 801, 41, doi: 10.1088/0004-637X/801/1/41

Rogers, L. A., & Seager, S. 2010, ApJ, 712, 974, doi: 10.1088/0004-637X/712/2/974

Rupprecht, G., Pepe, F., Mayor, M., et al. 2004, in Society of Photo-Optical Instrumentation Engineers (SPIE) Conference Series, Vol. 5492, Ground-based Instrumentation for Astronomy, ed. A. F. M. Moorwood & M. Iye, 148–159, doi: 10.1117/12.551267

Sabotta, S., Schlecker, M., Chaturvedi, P., et al. 2021, åp, 653, A114, doi: 10.1051/0004-6361/202140968

Santerne, A., Brugger, B., Armstrong, D. J., et al. 2018, Nature Astronomy, 2, 393, doi: 10.1038/s41550-018-0420-5

Sarkis, P., Henning, T., Kürster, M., et al. 2018, AJ, 155, 257, doi: 10.3847/1538-3881/aac108

Schlecker, M., Mordasini, C., Emsenhuber, A., et al. 2020, arXiv e-prints, arXiv:2007.05563

Schlecker, M., Pham, D., Burn, R., et al. 2021, arXiv e-prints, arXiv:2104.11750

Schneider, A. C., Greco, J., Cushing, M. C., et al. 2016, ApJ, 817, 112, doi: 10.3847/0004-637X/817/2/112

Schrijver, C. J., & Zwaan, C. 2000, Solar and Stellar Magnetic Activity

Schwab, C., Stürmer, J., Gurevich, Y. V., et al. 2015, PASP, 127, 880, doi: 10.1086/682879

Schweitzer, A., Passegger, V. M., Cifuentes, C., et al. 2019, A&A, 625, A68, doi: 10.1051/0004-6361/201834965

Schwieterman, E. W., Kiang, N. Y., Parenteau, M. N., et al. 2018, Astrobiology, 18, 663, doi: 10.1089/ast.2017.1729

Schäfer, S., Guenther, E. W., Reiners, A., et al. 2018, in Society of Photo-Optical Instrumentation Engineers (SPIE) Conference Series, Vol. 10702, Ground-based and Airborne Instrumentation for Astronomy VII, ed. C. J. Evans, L. Simard, & H. Takami, 1070276, doi: 10.1117/12.2315241

Schöfer, P., Jeffers, S. V., Reiners, A., et al. 2019, A&A, 623, A44, doi: 10.1051/0004-6361/201834114

Seager, S., & Mallén-Ornelas, G. 2003, ApJ, 585, 1038, doi: 10.1086/346105

Seifahrt, A., Bean, J. L., Stürmer, J., et al. 2016, in Society of Photo-Optical Instrumentation Engineers (SPIE) Conference Series, Vol. 9908, Ground-based and Airborne Instrumentation for Astronomy VI, ed. C. J. Evans, L. Simard, & H. Takami, 990818, doi: 10.1117/12.2232069

Seifahrt, A., Stürmer, J., Bean, J. L., & Schwab, C. 2018, in Society of Photo-Optical Instrumentation Engineers (SPIE) Conference Series, Vol. 10702, Ground-based and Airborne Instrumentation for Astronomy VII, ed. C. J. Evans, L. Simard, & H. Takami, 107026D, doi: 10.1117/12.2312936

Seifert, W., Xu, W., Stahl, O., et al. 2016, in Proc. SPIE, Society of Photo-Optical Instrumentation Engineers (SPIE) Conference Series, 990865, doi: 10.1117/12.2231582

Service, M., Lu, J. R., Campbell, R., et al. 2016, PASP, 128, 095004, doi: 10.1088/1538-3873/128/967/095004

Shappee, B. J., Prieto, J. L., Grupe, D., et al. 2014, ApJ, 788, 48, doi: 10.1088/0004-637X/788/1/48

Shields, A. L., Ballard, S., & Johnson, J. A. 2016, Phys. Rep., 663, 1, doi: 10.1016/j.physrep.2016.10.003

Shporer, A., Collins, K. A., Astudillo-Defru, N., et al. 2020, ApJ, 890, L7, doi: 10.3847/2041-8213/ab7020

Shulyak, D., Reiners, A., Nagel, E., et al. 2019, A&A, 626, A86, doi: 10.1051/0004-6361/201935315

Skilling, J. 2004, in American Institute of Physics Conference Series, Vol. 735, Bayesian Inference and Maximum Entropy Methods in Science and Engineering: 24th International Workshop on Bayesian

Inference and Maximum Entropy Methods in Science and Engineering, ed. R. Fischer, R. Preuss, & U. von Toussaint, 395–405, doi: 10.1063/1.1835238

Skilling, J. 2006, Bayesian Analysis, 1, 833, doi: 10.1214/06-BA127

Skrutskie, M. F., Cutri, R. M., Stiening, R., et al. 2006, AJ, 131, 1163, doi: 10.1086/498708

Smith, J. C., Stumpe, M. C., van Cleve, J. E., et al. 2012, PASP, 124, 1000, doi: 10.1086/667697

Smith, J. C., Stumpe, M. C., Jenkins, J. M., et al. 2020, Kepler Data Processing Handbook: Presearch Data Conditioning

Snellen, I. A. G., Guzman-Ramirez, L., Hogerheijde, M. R., Hygate, A. P. S., & van der Tak, F. F. S. 2020, åp, 644, L2, doi: 10.1051/0004-6361/202039717

Sotin, C., Grasset, O., & Mocquet, A. 2007, Icarus, 191, 337, doi: 10.1016/j.icarus.2007.04.006

Soto, M. G., Anglada-Escudé, G., Dreizler, S., et al. 2021, A&A, 649, A144, doi: 10.1051/0004-6361/202140618

Southworth, J. 2010, MNRAS, 408, 1689, doi: 10.1111/j.1365-2966.2010.17231.x

—. 2011, MNRAS, 417, 2166, doi: 10.1111/j.1365-2966.2011.19399.x

Speagle, J. S. 2020, MNRAS, 493, 3132, doi: 10.1093/mnras/staa278

Stahler, S. W., & Palla, F. 2004, The Formation of Stars

Stassun, K. G., Oelkers, R. J., Paegert, M., et al. 2019, AJ, 158, 138, doi: 10.3847/1538-3881/ab3467

Stefánsson, G., Kopparapu, R., Lin, A., et al. 2020, AJ, 160, 259, doi: 10.3847/1538-3881/abbe19

Steinmetz, T., Wilken, T., Araujo-Hauck, C., et al. 2008, Science, 321, 1335, doi: 10.1126/science.1161030

Stock, S. 2021, Analysis of high-precision spectroscopic data in search of exoplanet signals close to the stellar noise limit (Heidelberg), doi: 10.11588/heidok.00029962

Stock, S., & Kemmer, J. 2020, The Journal of Open Source Software, 5, 1771, doi: 10.21105/joss.01771

Stock, S., Kemmer, J., Reffert, S., et al. 2020a, A&A, 636, A119, doi: 10.1051/0004-6361/201936732

Stock, S., Nagel, E., Kemmer, J., et al. 2020b, A&A, 643, A112, doi: 10.1051/0004-6361/202038820

Strassmeier, K. G. 2009, A&A Rev., 17, 251, doi: 10.1007/s00159-009-0020-6

Strehl, K. 1902, Astronomische Nachrichten, 158, 89, doi: 10.1002/asna.19021580604

Stumpe, M. C., Smith, J. C., Catanzarite, J. H., et al. 2014, PASP, 126, 100, doi: 10.1086/674989

Stumpe, M. C., Smith, J. C., van Cleve, J. E., et al. 2012, PASP, 124, 985, doi: 10.1086/667698

Stürmer, J. 2015, Technologies for improving the precision of radial velocity measurements with high-resolution, fibre-fed échelle spectrographs, doi: 10.11588/heidok.00018207

Suárez Mascareño, A., Rebolo, R., & González Hernández, J. I. 2016, A&A, 595, A12, doi: 10.1051/0004-6361/201628586

Swain, M. R., Estrela, R., Roudier, G. M., et al. 2021, AJ, 161, 213, doi: 10.3847/1538-3881/abe879

Tal-Or, L., Trifonov, T., Zucker, S., Mazeh, T., & Zechmeister, M. 2019, MNRAS, 484, L8, doi: 10.1093/mnrasl/sly227

Tala, M. 2019, Perspectives of the radial velocity method: Physical modeling of the wavelength solution & exoplanetary detections around giant stars (Heidelberg), doi: 10.11588/heidok.00026834

Tamura, M., Suto, H., Nishikawa, J., et al. 2012, in Society of Photo-Optical Instrumentation Engineers (SPIE) Conference Series, Vol. 8446, Ground-based and Airborne Instrumentation for Astronomy IV, ed. I. S. McLean, S. K. Ramsay, & H. Takami, 84461T, doi: 10.1117/12.925885

The pandas development team. 2020, pandas-dev/pandas: Pandas, Zenodo, doi: 10.5281/zenodo.3509134

Tinney, C. G., & Reid, I. N. 1998, MNRAS, 301, 1031, doi: 10.1046/j.1365-8711.1998.02079.x

Tody, D. 1993, in Astronomical Society of the Pacific Conference Series, Vol. 52, Astronomical Data Analysis Software and Systems II, ed. R. J. Hanisch, R. J. V. Brissenden, & J. Barnes, 173

Torres, G., Andersen, J., & Giménez, A. 2010, A&A Rev., 18, 67, doi: 10.1007/s00159-009-0025-1

Trifonov, T. 2019, The Exo-Striker: Transit and radial velocity interactive fitting tool for orbital analysis and N-body simulations

Trifonov, T., Tal-Or, L., Zechmeister, M., et al. 2020, A&A, 636, A74, doi: 10.1051/0004-6361/201936686

Trifonov, T., Kürster, M., Zechmeister, M., et al. 2018, A&A, 609, A117, doi: 10.1051/0004-6361/201731442

Trifonov, T., Caballero, J. A., Morales, J. C., et al. 2021, Science, 371, 1038, doi: 10.1126/science.abd7645

Trotta, R. 2008, Contemporary Physics, 49, 71, doi: 10.1080/00107510802066753

Tsiaras, A., Rocchetto, M., Waldmann, I. P., et al. 2016, ApJ, 820, 99, doi: 10.3847/0004-637X/820/2/99

Twicken, J. D., Catanzarite, J. H., Clarke, B. D., et al. 2018, PASP, 130, 064502, doi: 10.1088/1538-3873/aab694

Udry, S., Bonfils, X., Delfosse, X., et al. 2007, A&A, 469, L43, doi: 10.1051/0004-6361:20077612

van Eylen, V., Agentoft, C., Lundkvist, M. S., et al. 2018, MNRAS, 479, 4786, doi: 10.1093/mnras/sty1783

van Eylen, V., & Albrecht, S. 2015, ApJ, 808, 126, doi: 10.1088/0004-637X/808/2/126

van Eylen, V., Albrecht, S., Huang, X., et al. 2019, AJ, 157, 61, doi: 10.3847/1538-3881/aaf22f

van Eylen, V., Astudillo-Defru, N., Bonfils, X., et al. 2021, MNRAS, doi: 10.1093/mnras/stab2143

VanderPlas, J. T. 2018, ApJS, 236, 16, doi: 10.3847/1538-4365/aab766

Venturini, J., Guilera, O. M., Haldemann, J., & Ronco, MarMordasini, Christoph. 2020a, A&A, 643, L1, doi: 10.1051/0004-6361/202039141

Venturini, J., Guilera, O. M., & Ronco, MarMordasini, Christoph. 2020b, A&A, 644, A174, doi: 10.1051/0004-6361/202039140

Villanueva, G. L., Cordiner, M., Irwin, P. G. J., et al. 2021, Nature Astronomy, 5, 631, doi: 10.1038/s41550-021-01422-z

Virtanen, P., Gommers, R., Oliphant, T. E., et al. 2020, Nature Methods, 17, 261, doi: 10.1038/s41592-019-0686-2

Waqas Bhatti, Luke G. Bouma, & Joshua Wallace. 2017, Astrobase, Zenodo, doi: 10.5281/zenodo.1185231

Waskom, M. 2021, The Journal of Open Source Software, 6, 3021, doi: 10.21105/joss.03021

Wells, R. D., Rackham, B. V., Schanche, N., et al. 2021, A&A, 653, A97, doi: 10.1051/0004-6361/202141277

Wes McKinney. 2010, in Proceedings of the 9th Python in Science Conference, ed. Stéfan van der Walt & Jarrod Millman, 56–61, doi: 10.25080/Majora-92bf1922-00a

Wildi, F., Pepe, F., Chazelas, B., Lo Curto, G., & Lovis, C. 2010, in Society of Photo-Optical Instrumentation Engineers (SPIE) Conference Series, Vol. 7735, Ground-based and Airborne Instrumentation for Astronomy III, ed. I. S. McLean, S. K. Ramsay, & H. Takami, 77354X, doi: 10.1117/12.857951

Wilken, T., Lovis, C., Manescau, A., et al. 2010, MNRAS, 405, L16, doi: 10.1111/j.1745-3933.2010.00850.x

Wilken, T., Lo Curto, G., Probst, R. A., et al. 2012, Nature, 485, 611, doi: 10.1038/nature11092

Winn, J. N. 2010, in Exoplanets, ed. S. Seager, 55–77

Winn, J. N., Matthews, J. M., Dawson, R. I., et al. 2011, ApJ, 737, L18, doi: 10.1088/2041-8205/737/1/L18

Winters, J. G., Charbonneau, D., Henry, T. J., et al. 2021, AJ, 161, 63, doi: 10.3847/1538-3881/abcc74

Winters, J. G., Henry, T. J., Lurie, J. C., et al. 2015, AJ, 149, 5, doi: 10.1088/0004-6256/149/1/5

Wright, J. T. 2018, in Handbook of Exoplanets, ed. H. J. Deeg & J. A. Belmonte, 4, doi: 10.1007/978-3-319-55333-7_4

Wright, J. T., & Eastman, J. D. 2014, PASP, 126, 838, doi: 10.1086/678541

Wright, N. J., Drake, J. J., Mamajek, E. E., & Henry, G. W. 2011, ApJ, 743, 48, doi: 10.1088/0004-637X/743/1/48

Xu, W., Seifert, W., Stahl, O., et al. 2012. https://carmenes.caha.es/int/documents/oFDR/CARMENES-oFDR-02A-VISChannel-Optics-Design.pdf

Yan, F., Casasayas-Barris, N., Molaverdikhani, K., et al. 2019, åp, 632, A69, doi: 10.1051/0004-6361/201936396

Yu, J., Huber, D., Bedding, T. R., et al. 2018, ApJS, 236, 42, doi: 10.3847/1538-4365/aaaf74

Zechmeister, M., Anglada-Escudé, G., & Reiners, A. 2014, A&A, 561, A59, doi: 10.1051/0004-6361/201322746

Zechmeister, M., & Kürster, M. 2009, A&A, 496, 577, doi: 10.1051/0004-6361:200811296

—. 2018, GLS: Generalized Lomb-Scargle periodogram

Zechmeister, M., Reiners, A., Amado, P. J., et al. 2018, A&A, 609, A12, doi: 10.1051/0004-6361/201731483

Zechmeister, M., Dreizler, S., Ribas, I., et al. 2019, A&A, 627, A49, doi: 10.1051/0004-6361/201935460

Zeng, L., Jacobsen, S. B., & Sasselov, D. D. 2017, Research Notes of the AAS, 1, 32, doi: 10.3847/2515-5172/aa9ed9

Zeng, L., Sasselov, D. D., & Jacobsen, S. B. 2016, ApJ, 819, 127, doi: 10.3847/0004-637X/819/2/127

Zeng, L., Jacobsen, S. B., Sasselov, D. D., et al. 2019, Proceedings of the National Academy of Science, 116, 9723, doi: 10.1073/pnas.1812905116

Zhu, Z., Hartmann, L., Nelson, R. P., & Gammie, C. F. 2012, Research Notes of the AAS, 746, 110, doi: 10.1088/0004-637X/746/1/110

Software

The purpose of this list is to provide a (still incomplete) overview on the software that I used for my thesis and to give proper credit to all the open source software developers without which such a work would not be feasible.

`AliasFinder` Python script to search for the true planetary frequency within radial velocity data (https://github.com/JonasKemmer/AliasFinder; Stock et al., 2020a; Stock & Kemmer, 2020)

`Astrobase` A Python package for analyzing light curves and finding variable stars (https://astrobase.readthedocs.io/en/latest/; Waqas Bhatti et al., 2017)

`AstroImageJ` Image Processing and Photometric Extraction for Ultra-Precise Astronomical Light Curves (https://www.astro.louisville.edu/software/astroimagej/; Collins et al., 2017)

`Astropy` A common core package for Astronomy in Python (https://www.astropy.org; Astropy Collaboration et al., 2013, 2018)

`astroquery` An Astronomical Web-querying Package in Python (https://astroquery.readthedocs.io/en/latest/; Ginsburg et al., 2019)

`BANYAN Σ`/`BANYAN Σ` **Bayesian classification tool** Bayesian Analysis for Nearby Young AssociatioNs Σ (http://www.exoplanetes.umontreal.ca/banyan/; Gagné et al., 2018)

`Banzai` Real-time processing of the imaging data from the network of LCOGT (McCully et al., 2018a,b)

`barycorrpy` package for the calculation of the BERV (https://github.com/shbhuk/barycorrpy; Kanodia & Wright, 2018a,b; Wright & Eastman, 2014)

`batman` BAsic Transit Model cAlculatioN in Python (https://lweb.cfa.harvard.edu/~lkreidberg/batman/; Kreidberg, 2015)

`caracal` CARMENES Reduction And CALibration software, (Caballero et al., 2016a)

`celerite2` Developed version of `celerite` (https://celerite2.readthedocs.io/en/latest/; Foreman-Mackey, 2018)

celerite A scalable method for Gaussian Process regression (https://celerite.readthedocs.io/en/stable/; Foreman-Mackey et al., 2017)

dynesty A dynamic nested sampling package for estimating Bayesian posteriors and evidences (https://dynesty.readthedocs.io/en/latest/; Speagle, 2020)

Exo-Striker Transit and Radial velocity Interactive Fitting tool for Orbital analysis and N-body simulations (https://github.com/3fon3fonov/exostriker; Trifonov, 2019)

george A Python library for Gaussian Process Regression (https://george.readthedocs.io/en/latest/; Ambikasaran et al., 2015)

ICAT/ICAT pipeline A General Purpose Image Reduction and Analysis Tool for Robotic Observatories (Colome & Ribas, 2006)

IRAF Échelle package A IRAF package for the reduction of Échelle spectrograph data (Tody, 1993)

isochrones A python package that provides a simple interface to grids of stellar evolution models (https://isochrones.readthedocs.io/en/latest/; Morton, 2015)

juliet Joint analysis of exoplanetary RVs and transits in Python (https://juliet.readthedocs.io/en/latest/index.html; Espinoza et al., 2019a)

lightkurve A Python package to analyze time series data from *Keppler* and TESS (https://docs.lightkurve.org/; Lightkurve Collaboration et al., 2018)

Matplotlib A comprehensive library for creating static, animated, and interactive visualizations in Python (https://matplotlib.org/; Hunter, 2007)

NumPy The fundamental package for scientific computing with Python (https://numpy.org/; Harris et al., 2020)

pandas An open source data analysis and manipulation tool (https://pandas.pydata.org; The pandas development team, 2020; Wes McKinney, 2010)

prince SAINT-EX custom pipeline for image reduction (Demory et al., 2020)

PyFITS A Python library providing access to FITS files (https://pyfits.readthedocs.io/en/latest/; Barrett et al., 2012)

PyTransit A python package for fast and easy exoplanet transit modelling in PYTHON Curves (https://pytransit.readthedocs.io/en/latest/; Parviainen, 2015)

radvel The Radial Velocity Fitting Toolkit (https://radvel.readthedocs.io/en/latest/; Fulton et al., 2018)

scikit-learn Machine Learning in Python (https://scikit-learn.org/stable/; Pedregosa et al., 2011)

SciPy Fundamental Algorithms for Scientific Computing in Python (https://www.scipy.org/; Virtanen et al., 2020)

seaborn A Python statistical data visualization library (https://seaborn.pydata.org/; Waskom, 2021)

serval SpEctrum Radial Velocity AnaLyser (https://github.com/mzechmeister/serval; Zechmeister et al., 2018)

tesscut A Python package for making astronomical cutouts (https://astrocut.readthedocs.io/en/latest/; Brasseur et al., 2019)

tpfplotter target pixel file plotter (https://github.com/jlillo/tpfplotter; Aller et al., 2020)

tqdm A fast, Extensible Progress Bar for Python and CLI (https://tqdm.github.io/; Casper da Costa-Luis et al., 2021)

Abbreviations and Symbols

Abbreviations

Gaia *Gaia*

Kepler *Kepler* space telescope

AO adaptive optics

ASAS-SN All-Sky Automated Survey for Supernovae

AstraLux Lucky Imager of the Calar Alto Observatory in Spain

BERV barycentric Earth radial velocity

BIS bisector inverse slope

BLS box-fitting least squares

C_2H_6 Ethane

CARMENES Calar Alto high-Resolution search for M dwarfs with Exoearths with Near-infrared and optical Échelle Spectrographs

CARMENES-NIR CARMENES NIR spectropgraph arm

CARMENES-TESS WG CARMENES-TESS working group

CARMENES-VIS CARMENES visual spectropgraph arm

Ca II IRT Calcium II infrared triplet (located at $849.8\,\text{nm}$, $854.2\,\text{nm}$ and $866.2\,\text{nm}$)

CCD charge-coupled devide

CCF cross-correlation function

CH_3Cl Chloromethane

CH_3SH Methanethiol

CH_4 Methane

CO Carbon monoxide

CO$_2$ Carbon dioxide

CRX chromatic index

CTI charge transfer inefficiency

CTIO Cerro Tololo Interamerican Observatory

dLW differential line width

DMDS dimethyl disulfide

DMS dimethyl Sulfide

DRS HARPS data reduction software

dSHO double simple-harmonic-oscillator

ELT Extremely Large Telescope

EMP exposure midpoint

ESM emission spectroscopy metric

ESPRESSO Èchelle SPectrograph for Rocky Exoplanets and Stable Spectroscopic Observations

FAP false alarm probability

FDR final design review

FOV field of view

FP Fabry-Pérot

GLS generalised Lomb-Scargle periodogram

GTO guaranteed time observations

Hα H-alpha (brightest spectral line in the Balmer series at $656.28\,\mathrm{nm}$)

H$_2$O Hydrogen dioxide

H/He Hydrogen/Helium

HAL Haleakalā Observatory

HARPS High Accuracy Radial velocity Planet Searcher

HATNet Hungarian Automated Telescope Network

HCL hollow-cathode lamp

HCN Hydrogen Cyanide

He I Helium I (located at $1083.3\,\text{nm}$)

HZ habitable zone

IR infrared

IRD InfraRed Doppler spectrograph

JWST James Webb Space Telescope

LCOGT Las Cumbres Observatory global telescope network

LFC laser frequency comb

MAROON-X M dwarf Advanced Radial velocity Observer Of Neighboring eXoplanets

McD McDonald Observatory

MEarth M dwarf stars in search of new Earth-like exoplanets

MgSiO$_3$ Bridgmanite

MLP marginalised likelihood periodogram

MuSCAT Multi-color Simultaneous Camera for studying Atmospheres of Transiting planets

MuSCAT2 Multi-color Simultaneous Camera for studying Atmospheres of Transiting planets 2

MuSCAT3 Multi-color Simultaneous Camera for studying Atmospheres of Transiting planets 3

N$_2$O Nitrous Oxide

NEB near-by eclipsing binary

NH$_3$ Ammonia

NIR near-infrared

NIRC2/Keck/NIRC2 Keck Near-Infrared Camera 2

NIRI/Gemini/NIRI Gemini Near-Infrared Imager

NO$_2$ Nitrogen dioxide

O$_2$ Oxigen

O$_3$ Oxigen

PDCSAP systematics-corrected simple aperture photometry

pEW$'$ pseudo-equivalent width

ppm parts per million

ppt parts per thousand

PSF point spread function

rms root mean square

RUWE re-normalised unit weight error

RV radial velocity

S/N signal-to-noise ratio

SAINT-EX Searching and characterising transiting exoplanets

SAP simple aperture photometry

SDE signal detection efficiency

SPOC Science Processing Operations Center

TESS Transiting Exoplanet Survey Satellite

TFOP TESS Follow-Up Observing Program

Th-Ar Thorium-Argon

Th-Ne Thorium-Neon

TiO Titanium oxide (used indice lines located at $705\,\mathrm{nm}$, $843\,\mathrm{nm}$ and $886\,\mathrm{nm}$)

TJO Joan Oró telescope

TLS Transit-Least-Squares

TOI TESS object of interest

TSM transmission spectroscopy metric

TTV transit timing variation

U-Ar Uranium-Argon

U-Ne Uranium-Neon

USAFA United States Air Force Academy

USP ultra-short-period

VIS visual

VO Vanadium oxide (used indice lines located at $743.6\,\mathrm{nm}$, and $794.2\,\mathrm{nm}$)

wrms weighted rms

Symbols

[**Fe/H**] metallicity

α right ascension

δ declination

$\Delta\lambda$ wavelength shift

$\Delta\lambda$ wavelength range

$\Delta\ln\mathcal{Z}$ difference in the logarithm of the Bayesian evidence for two models

δ_θ rms of guiding error

ΔF stellar flux difference or transit depth

Δm contrast in magnitudes

Δt time difference (timespan, or exposure time)

γ systemic velocity

λ wavelength

$\ln\mathcal{Z}$ logarithm of the Bayesian evidence

$\log g$ surface gravity

μ `juliet` parametrisation for the RV instrument offset

μ_δ proper motion in declination

$\mu_\alpha\cos\delta$ proper motion in right ascension

$\nu(t)$ true anomaly

ω argument of periastron

π parallax

$\rho_\star$ stellar density

$\rho_{\mathbf{p}}$ planetary density

σ `juliet` parametrisation for the RV or photometric instrument jitter

$\sigma_{\mathbf{meas}}$ uncertainty of the measurements

$\sqrt{e_b}\sin\omega_b$, $\sqrt{e_b}\cos\omega_b$ `juliet` parametrisation for the eccentricity, e, and the argument of periastron, ω

θ projected fiber size

$\theta_{1,2,\ldots,\textbf{etc.}}$ `juliet` parametrisation for linear detrending coefficients

a semi-major axis

$a_\star$ stellar semi-major axis

$a_{\textbf{p}}$ planet semi-major axis

c speed of light

d distance to Earth

E Epoch with respect to t_0

e orbital eccentricity

F stellar flux

i inclination

$I_\star$ stellar light intensity

K RV semi-amplitude

$L_\star$ stellar luminosity

$M_\star$ stellar mass

$M_{\textbf{p}}$ planetary mass

N number of observations

$N_{\textbf{obs}}$ number of observations

p planet-to-star radius ratio

P orbital period

$P_{\textbf{GP, rv}}$, $\sigma_{\textbf{GP, rv}}$, $f_{\textbf{GP, rv}}$, $Q_{0,\textbf{GP, rv}}$, $dQ_{\textbf{GP, rv}}$ `juliet` parametrisation for the dSHO-GP kernel.

$P_{\textbf{rot}}$ stellar rotation period

$Pr(\textbf{transit})$ transit probability

q_1, q_2 juliet parametrisation for linear or quadratic limb-darkening

R spectrograph resolution

r_1, r_2 juliet parametrisation for the impact parameter, b and the planet-to-star radius ratio p

$R_\star$ stellar radius

$R_\mathbf{p}$ planetary radius

S insolation flux

t_0 time of transit centre at epoch 0

$T_\mathbf{eff}$ effective stellar temperature

$T_\mathbf{eq}$ planetary equilibrium temperature

$t_\mathbf{exp}$ exposure time

$t_\mathbf{p}$ periastron time

t_E time of transit centre at epoch E

t_f time of full transit

t_t total transit duration

U, V, W Galactocentric space velocities

$v \sin i$ stellar rotation velocity

$v_\mathbf{r}$ radial velocity

au astronomical unit ($1.495\,978\,71 \times 10^{11}$ m)

G gravitational constant ($6.6743 \times 10^{-11}\,\mathrm{m^3\,kg^{-1}\,s^{-2}}$)

GP$_\sigma$, GP$_\Gamma$, GP$_\alpha$, GP$_{P,\mathbf{rot}}$, GP$_\sigma$ juliet parametrisation for the quasi-periodic GP kernel.

M$_\odot$ Solar mass ($1.988\,409\,87 \times 10^{30}$ kg)

M$_\oplus$ Earth mass ($5.972\,167\,87 \times 10^{24}$ kg)

mdilution juliet parametrisation for the dilution of the light curve from neabry sources

mflux juliet parametrisation for the photometric instrument offset

R$_\odot$ nominal Solar radius ($695\,700\,000$ m)

$\mathbf{R}_{\oplus}$ nominal Earth equatorial radius ($6\,378\,100\,\mathrm{m}$)

$\mathbf{S}_{\oplus}$ insolation in Earth units ($1361\,\mathrm{W\,m^{-2}}$)

Appendix to chapter 3

Known transiting planets with precise mass measurements around M dwarfs

Tab. A.1.: Small transiting planets with precise masses around M dwarfs.

Name	Alternative name	Radius [$R_\oplus$]	Mass [$M_\oplus$]	Reference
GJ 3473 b[a,b]	G 50–16 b	1.264 ± 0.050	1.86 ± 0.30	This work
LP 729–54 b[a,b]	LTT 3780 b	1.35 ± 0.06	2.34 ± 0.24	Nowak et al. (2020); Cloutier et al. (2020b)
TOI-1235 b[a,b]	TYC 4384–1735–1 b	1.69 ± 0.08	5.9 ± 0.6	Bluhm et al. (2020); Cloutier et al. (2020a)
GJ 357 b[a,b]	LHS 2157 b	1.217 ± 0.084	1.84 ± 0.31	Luque et al. (2019); Jenkins et al. (2019)
GJ 1252 b[a]	L 210–70 b	1.193 ± 0.074	2.10 ± 0.58	Shporer et al. (2020)
L 98–59 c[a]	TOI-175.01	1.35 ± 0.07	2.42 ± 0.35	Cloutier et al. (2019); Kostov et al. (2019)
L 98–59 d[a]	TOI-175.01	1.57 ± 0.14	2.31 ± 0.46	Cloutier et al. (2019); Kostov et al. (2019)
L 168–9 b[a]	CD–60 8051 b	1.39 ± 0.09	4.60 ± 0.58	Astudillo-Defru et al. (2020)
Kepler-138 c	KOI-314.2	1.67 ± 0.15	5.2 ± 1.3	Almenara et al. (2018); Kipping et al. (2014); Mann et al. (2017)
Kepler-138 d	KOI-314.3	1.68 ± 0.15	1.17 ± 0.30	Almenara et al. (2018); Kipping et al. (2014); Mann et al. (2017)
GJ 1132 b	LTT 3758 b	1.130 ± 0.057	1.66 ± 0.23	Bonfils et al. (2018); Berta-Thompson et al. (2015)
LHS 1140 b	GJ 3053 b	1.727 ± 0.033	6.99 ± 0.89	Ment et al. (2019); Dittmann et al. (2017)
LHS 1140 c	GJ 3053 c	1.282 ± 0.024	1.81 ± 0.39	Ment et al. (2019)
TRAPPIST-1 b	2MUCD 12171 b	1.121 ± 0.033	1.017 ± 0.16	Grimm et al. (2018); Delrez et al. (2018); Gillon et al. (2016)
TRAPPIST-1 c	2MUCD 12171 c	1.095 ± 0.031	1.156 ± 0.15	Grimm et al. (2018); Delrez et al. (2018); Gillon et al. (2016)
TRAPPIST-1 d	2MUCD 12171 d	0.784 ± 0.023	0.297 ± 0.039	Grimm et al. (2018); Delrez et al. (2018); Gillon et al. (2017)
TRAPPIST-1 e	2MUCD 12171 e	0.910 ± 0.027	0.772 ± 0.079	Grimm et al. (2018); Delrez et al. (2018); Gillon et al. (2017)
TRAPPIST-1 f	2MUCD 12171 f	1.046 ± 0.030	0.934 ± 0.095	Grimm et al. (2018); Delrez et al. (2018); Gillon et al. (2017)
TRAPPIST-1 g	2MUCD 12171 g	1.148 ± 0.033	1.148 ± 0.098	Grimm et al. (2018); Delrez et al. (2018); Gillon et al. (2017)
TRAPPIST-1 h	2MUCD 12171 h	0.773 ± 0.027	0.331 ± 0.056	Grimm et al. (2018); Delrez et al. (2018); Luger et al. (2017)

[a] Planets discovered by TESS.
[b] Target stars in the CARMENES guaranteed time observations survey (Quirrenbach et al., 2014; Reiners et al., 2018a).
The table is based on TEPCat (Southworth, 2011, visited on 15 July 2020) and shows the known transiting planets with radii smaller than $2\,R_\oplus$ and mass determinations to a precision better than $30\,\%$ in orbits around stars with temperatures lower than $4000\,K$. The first reference always denotes the source of the properties.

Priors for `juliet`

Tab. A.2.: Priors used for `juliet` in the joint fit of transits and RV.

Parameter	Prior	Units	Description
		Stellar parameters	
$\rho_\star$	$\mathcal{N}(10520.0, 836.2)$	$\mathrm{kg\,m^{-3}}$	Stellar density
		Planetary parameters	
P_b	$\mathcal{N}(1.1980004, 0.000009)$	d	Period of the transiting planet
$t_{0,b}$	$\mathcal{N}(2458492.2041, 0.0015)$	d	Time of transit centre of the transiting planet
$r_{1,b}$	$\mathcal{N}(0.55, 0.15)$	...	Parametrisation for p and b
$r_{2,b}$	$\mathcal{N}(0.0318, 0.0021)$	...	Parametrisation for p and b
K_b	$\mathcal{N}(2.4, 1.5)$	$\mathrm{m\,s^{-1}}$	Radial-velocity semi-amplitude of the transiting planet
$\sqrt{e_b}\sin\omega_b$	fixed(0)	...	Parametrisation for e and ω.
$\sqrt{e_b}\cos\omega_b$	fixed(0)	...	Parametrisation for e and ω.
P_c	$\mathcal{N}(15.51, 0.16)$	d	Period of the second RV signal
$t_{0,c}$	$\mathcal{N}(2458575.7, 1.5)$	d	Time of transit centre of the second RV signal
K_c	$\mathcal{N}(3.7, 1.5)$	$\mathrm{m\,s^{-1}}$	Radial-velocity semi-amplitude of the second RV signal
$\sqrt{e_c}\sin\omega_c$	fixed(0)	...	Parametrisation for e and ω.
$\sqrt{e_c}\cos\omega_c$	fixed(0)	...	Parametrisation for e and ω.
		Instrument parameters CARMENES, HARPS, IRD	
μ	$\mathcal{U}(-10, 10)$	$\mathrm{m\,s^{-1}}$	Instrumental offset
σ	$\mathcal{U}(0, 10)$	$\mathrm{m\,s^{-1}}$	Jitter term
		Instrument parameters TESS	
q_1	$\mathcal{U}(0, 1)$	...	Quadratic limb-darkening parametrisation
q_2	$\mathcal{U}(0, 1)$	...	Quadratic limb-darkening parametrisation
mdilution	fixed(1)	...	Dilution factor
mflux	$\mathcal{N}(0.0, .01)$	ppm	Instrumental offset
σ	$\mathcal{U}(1, 500)$	ppm	Jitter term
		Instrument parameters MuSCAT2	
q_1	$\mathcal{U}(0, 1)$	...	Linear limb-darkening parametrisation
mdilution	fixed(1)	...	Dilution factor
mflux	$\mathcal{N}(0.0, .01)$	ppm	Instrumental offset
σ	$\mathcal{U}(1, 500)$	ppm	Jitter term
		Instrument parameters MuSCAT, LCOGT	
q_1	$\mathcal{U}(0, 1)$	...	Linear limb-darkening parametrisation
mdilution	fixed(1)	...	Dilution factor
mflux	$\mathcal{N}(0.0, .01)$	ppm	Instrumental offset
σ	$\mathcal{U}(1, 500)$	ppm	Jitter term
θ_0	$\mathcal{U}(-100, 100)$	...	Linear airmass detrending coefficient

The prior labels $\mathcal{U}$ and $\mathcal{N}$ represent uniform and normal distributions, respectively.

Tab. A.3.: Priors used with `juliet` for the determination of the rotation period.

Parameter	Prior	Units	Description
	Instrument parameters Mearth, TJO		
mdilution	fixed(1)	...	Dilution factor
mflux	$\mathcal{N}(0.0, 1e5)$	ppm	Instrumental offset
σ	$\mathcal{J}(1e-5, 1e5)$	ppm	Jitter term
	GP parameters (individual) Mearth, TJO		
GP-σ	$\mathcal{J}(1e-8, 1e8)$	ppm	GP amplitude
GP-Γ	$\mathcal{J}(1e-2, 1e2)$	...	GP amplitude of the sine-squared component
	GP parameters (shared) Mearth, TJO		
GP-α	$\mathcal{J}(1e-10, 1)$	d^{-2}	GP inverse length scale of the exponential component
GP-$P_{\rm rot}$	$\mathcal{U}(2, 200)$	d	GP rotation period of the quasi-periodic component

The prior labels $\mathcal{U}$ and $\mathcal{N}$ represent uniform, and normal distributions. $\mathcal{J}$ is the log-uniform Jeffrey's distribution (Jeffreys, 1946).

Continuation of the posteriors

Tab. A.4.: Posteriors of the joint fit for the different instrumental parameters.

Parameter	Posterior[a]	Units	Parameter	Posterior	Units
	TESS			*MuSCAT$_r$ 18 Jan. 2020*	
q_1	$0.17^{+0.25}_{-0.12}$	...	q_1	$0.867^{+0.09}_{-0.172}$	...
q_2	$0.35^{+0.33}_{-0.24}$	...	σ	385^{+76}_{-143}	ppm
σ	34^{+31}_{-22}	ppm	θ_0	$0.0054^{+0.0011}_{-0.0011}$	...
	LCO McD$_{z_s}$ 19 Mar. 2019			*MuSCAT$_z$s 18 Jan. 2020*	
q_1	$0.49^{+0.29}_{-0.30}$	...	q_1	$0.147^{+0.150}_{-0.098}$	...
σ	437^{+42}_{-78}	ppm	σ	$440.0^{+38.0}_{-55.0}$	ppm
θ_0	$-0.00302^{+0.00058}_{-0.00058}$	...	θ_0	$0.00346^{+0.00067}_{-0.00069}$	...
	MuSCAT2$_i$ 21 Dec. 2019			*LCO CTIO$_{ip}$ 21 Feb. 2020*	
q_1	$0.77^{+0.16}_{-0.26}$	...	q_1	$0.873^{+0.085}_{-0.158}$	...
σ	113^{+104}_{-72}	ppm	σ	$492.9^{+4.9}_{-9.2}$	ppm
	MuSCAT2$_{zs}$ 21 Dec. 2019		θ_0	$0.0015^{+0.00017}_{-0.00017}$	...
q_1	$0.57^{+0.26}_{-0.31}$	...		*LCO CTIO$_{ip}$ 27 Feb. 2020*	
σ	155^{+136}_{-100}	ppm	q_1	$0.52^{+0.28}_{-0.30}$	...
	MuSCAT2$_i$ 2 Jan. 2020		σ	482^{+12}_{-22}	ppm
q_1	$0.57^{+0.27}_{-0.31}$	...	θ_0	$0.00243^{+0.00017}_{-0.00018}$	...
σ	114^{+99}_{-72}	ppm		*LCO SAAO$_{zs}$ 13 Mar. 2020*	
	MuSCAT2$_r$ 2 Jan. 2020		q_1	$0.60^{+0.26}_{-0.33}$	...
q_1	$0.54^{+0.28}_{-0.31}$	...	σ	413^{+56}_{-98}	ppm
σ	121^{+109}_{-77}	ppm	θ_0	$-0.00086^{+0.0007}_{-0.00071}$	...
	MuSCAT2$_{zs}$ 2 Jan. 2020				
q_1	$0.78^{+0.15}_{-0.23}$	...			
σ	109^{+90}_{-69}	ppm			

[a] Error bars denote the 68% posterior credibility intervals.

Appendix to chapter 4

<div style="text-align: right; font-size: xx-large; color: #2b7bba;">B</div>

Differentiating aliases using posterior samples

The `AliasFinder` is based on creating synthetic data from the periods, amplitudes and phases retrieved from an observed periodogram. One advantage of this approach is that it allows to perform an alias analysis solely from a given set of RV measurements. However, in the presence of additional signals unrelated to the aliases in question (e.g. additional planets or stellar activity), those have to be taken into account by pre-whitening the data to mitigate their influence on the observed periodogram and make it comparable to the synthetic data. Yet, stellar activity, which often produces only quasi-periodic signals, poses a problem in this respect: the GPs that are commonly used to model such signals are not static model components, but parametrise the covariance between the data points. This makes the pre-whitening impossible because if the signal in question is omitted during pre-whitening, the GP model will be influenced by it and may absorb it from the residuals. Conversely, if the signal in question is taken into account in the pre-whitening (and later reinserted into the data), the GP model implies its presence in the residuals. In both cases, the signals recovered from the residual data do not resemble those of the original data and thus break the concept of `AliasFinder`.

Bayesian modelling approaches, such as the nested sampling used in our analysis, however, offer a direct solution to this issue: the results from the posterior can also be adopted to generate the synthetic RV models used to create the comparison periodograms. In this way each model can include all required components of the fit and thus make the resulting periodograms directly comparable with the observed periodogram. Pre-whitening is no longer necessary in this case.

The procedure is as follows: For each possible alias period that is going to be investigated, a fit has to be performed. Thereby, the period of the fitted alias signal needs to be reasonably constrained, such that other aliases are excluded. Further, the fit should consider all other signals of interest. Then the synthetic RVs can be created using the solutions from the individual posterior samples of the fit results. For each sample that is drawn, the RV model is calculated on the timestamps of the observations and the uncertainties of the original measurements are adopted — analogous to the method of the `AliasFinder` and Dawson & Fabrycky (2010). These model RVs however do not include any noise and would therefore result in highly significant peaks in the periodogram for each considered period. A good measure of the noise is the rms of the residuals
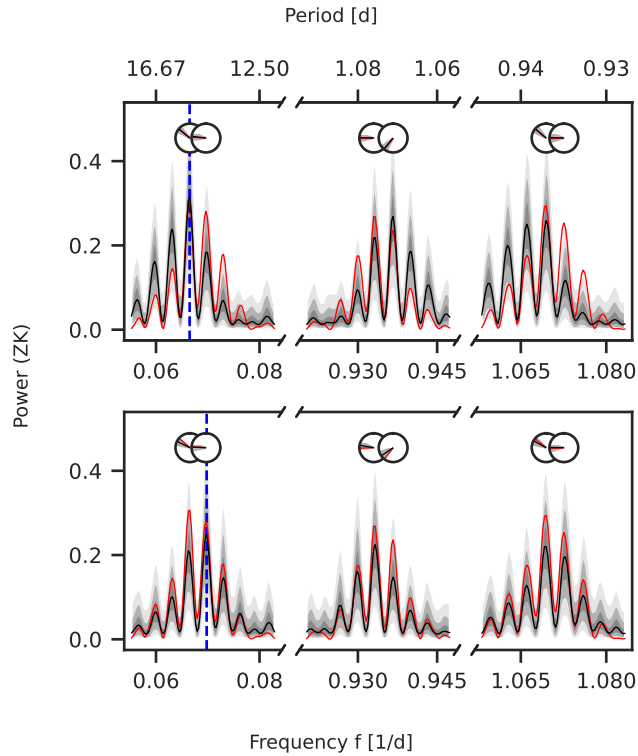
Fig. B.1.: Alias test for the $\sim15\,\mathrm{d}$ and $\sim14.3\,\mathrm{d}$ periods using the posterior samples from the RV only fits. We took 5000 posterior samples of the second component from the **2P+dSHO-GP$_{120\,\mathrm{d}}$** models to produce synthetic periodograms (black lines) which can be compared with the periodogram of the observed data (red lines). The results for the model considering $\sim15\,\mathrm{d}$ signal is shown in the first row and the results for the $\sim14.3\,\mathrm{d}$ signal in the second row, each period indicated by a vertical blue dashed line, respectively. Black lines depict the median of the samples for each simulation, and the grey shaded areas are the 50, 90 and $99\,\%$ confidence intervals. Further, the phases of the peaks as measured from the GLS are displayed in the circles, following the same colour scheme (the grey shades denote the standard deviations of the simulated peaks).

after subtracting it from the observed data. In analogy to the jitter determination in the `AliasFinder`, one can therefore add white noise to the synthetic models that is drawn from a normal distribution and follows the residual rms. The evaluation is then analogous to the `AliasFinder`. After calculating the GLS periodogram for all synthetic RV datasets, the median GLS and its confidence intervals, as well as the phases of the peaks can be determined and compared to the observed GLS and its phases.

In Figure B.1, we present the results from the **2P+dSHO-GP$_{120\,\mathrm{d}}$** models as described in subsection 4.4.5, were the second period was either constrained to the 14.3-day or 15.0-day period. The resulting synthetic periodograms are consistent with the results using the `AliasFinder` and confirm also that considering the 14.3-day period results in a better match to the observed periodogram.

Additional figures
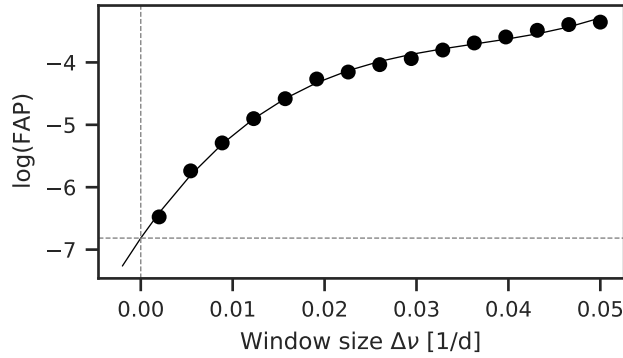
Fig. B.2.: Determining the FAP for the signal of the transiting planet in the RVs. For each window size, the FAP was calculated from comparing the combined power of the highest peaks appearing around the 2.62-day period of the transiting planet candidate and the 1.62-day alias from $50\,000$ permutations with the combined power of the signals in the original GLS. The black line shows a third order polynomial fit to the data, which is extrapolated to zero to determine the FAP.
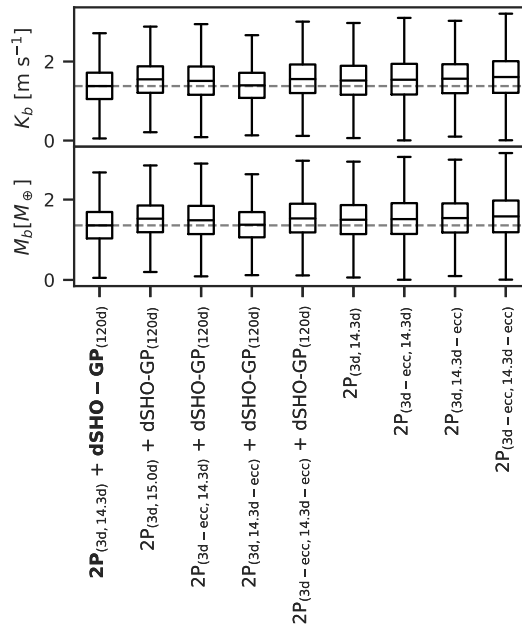
Fig. B.3.: Comparison of the amplitudes and resulting minimum masses for the different models considered. The box plots show the posterior distribution from the model comparison presented in the RV-only analysis (subsection 4.4.5). The width of each box corresponds to the interquartile range (IQR) and the whiskers mark the first quartile minus $1.5\times$ the IQR and the third quartile plus $1.5\times$ the IQR, respectively.
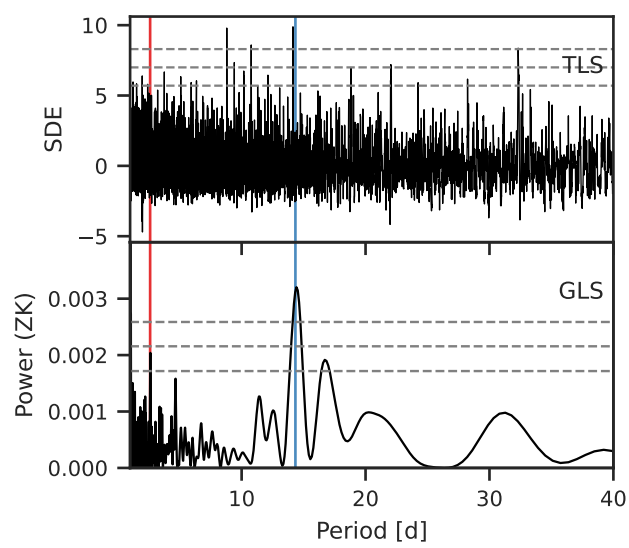
Fig. B.4.: TLS and GLS periodograms of the unbinned HATNet data. The periods of GJ 3929 b and the candidate GJ 3929 [c] are marked by the vertical red and blue lines, respectively

Priors for `juliet`

Parameter	Prior	Units	Description
		Stellar parameters	
$\rho_\star$	$\mathcal{N}(13.880, 2)$	$\mathrm{g\,cm^{-3}}$	Stellar density
		Stable components	
P_{b}	$\mathcal{U}(2.0, 3.0)$	d	Period of the transiting planet
$t_{0,\mathrm{b}}$	$\mathcal{U}(2459319.0, 2459322.0)$	d	Time of transit centre of the transiting planet
$r_{1,\mathrm{b}}$	$\mathcal{U}(0, 1)$	...	Parameterisation for p and b
$r_{2,\mathrm{b}}$	$\mathcal{U}(0, 1)$	...	Parameterisation for p and b
K_{b}	$\mathcal{U}(0, 50)$	$\mathrm{m\,s^{-1}}$	Radial-velocity semi-amplitude of the transiting planet
$\sqrt{e_{\mathrm{b}}}\sin\omega_{\mathrm{b}}$	fixed (0)	...	Parameterisation for e and ω.
$\sqrt{e_{\mathrm{b}}}\cos\omega_{\mathrm{b}}$	fixed (0)	...	Parameterisation for e and ω.
$P_{(14.3\,\mathrm{d})}$	$\mathcal{U}(13.98, 14.71)$	d	Period of the second RV signal
$t_{0,\,(14.3\,\mathrm{d})}$	$\mathcal{U}(2459061.0, 2459081.0)$	d	Time of transit centre of the second RV signal
$K_{(14.3\,\mathrm{d})}$	$\mathcal{U}(0, 50)$	$\mathrm{m\,s^{-1}}$	Radial-velocity semi-amplitude of the second RV signal
$\sqrt{e_{(14.3\,\mathrm{d})}}\sin\omega_{(14.3\,\mathrm{d})}$	fixed (0)	...	Parameterisation for e and ω.
$\sqrt{e_{(14.3\,\mathrm{d})}}\cos\omega_{(14.3\,\mathrm{d})}$	fixed (0)	...	Parameterisation for e and ω.
		RV GP component	
$P_{\mathrm{GP,\,rv}}$	$\mathcal{U}(100, 150)$	d	Rotation period of the primary mode
$\sigma_{\mathrm{GP,\,rv}}$	$\mathcal{U}(0, 10)$	$\mathrm{m\,s^{-1}}$	The standard deviation of the GP
$Q_{0,\mathrm{GP,\,rv}}$	$\mathcal{J}(0.1, 10000)$	...	Quality factor of the secondary mode
$dQ_{\mathrm{GP,\,rv}}$	$\mathcal{J}(0.1, 10000)$	...	Difference between the quality factors of the primary and secondary modes
$f_{\mathrm{GP,\,rv}}$	$\mathcal{U}(0.1, 1.0)$	...	Fractional amplitude of the secondary mode
		Instrument parameters CARMENES	
μ	$\mathcal{U}(-100, 100)$	$\mathrm{m\,s^{-1}}$	Instrumental offset
σ	$\mathcal{U}(0, 100)$	$\mathrm{m\,s^{-1}}$	Jitter term
		Instrument parameters TESS	
q_1	$\mathcal{U}(0.0, 1.0)$	...	Quadratic limb-darkening parameterisation, shared between Sectors 24 and 25
q_2	$\mathcal{U}(0.0, 1.0)$	...	Quadratic limb-darkening parameterisation, shared between Sectors 24 and 25
mdilution	fixed (1)	...	Dilution factor
mflux	$\mathcal{N}(0.0, 0.01)$	...	Instrumental offset
σ	$\mathcal{U}(1, 500)$	ppm	Jitter term

Parameter	Prior	Units	Description
	Instrument parameters SAINT-EX, LCOGT		
q_1	$\mathcal{U}(0,1)$	...	Linear limb-darkening parameterisation
mdilution	fixed (1)	...	Dilution factor
mflux	$\mathcal{N}(0,0.1)$	...	Instrumental offset
σ	$\mathcal{U}(1,5000)$	ppm	Jitter term
	Detrending parameters LCOGT CTIO$_{z'_s}$		
θ_0	$\mathcal{N}(0,1\times10^{-8})$	...	Linear detrending with the comparison ensemble counts
θ_1	$\mathcal{N}(0,0.001)$	...	Linear detrending with target FWHM
	Detrending parameters LCOGT McD$_{z'_s}$		
θ_0	$\mathcal{N}(0,1\times10^{-8})$	...	Linear detrending with the comparison ensemble counts
θ_1	$\mathcal{N}(0,0.001)$	...	Linear detrending with target FWHM
	Detrending parameters LCOGT HAL$_{g'}$		
θ_0	$\mathcal{N}(0,1\times10^{-8})$	...	Linear detrending with the comparison ensemble counts
θ_1	$\mathcal{N}(0,0.1)$	...	Linear detrending with the BJD timestamps
	Detrending parameters LCOGT HAL$_{r'}$		
θ_0	$\mathcal{N}(0,1\times10^{-8})$	...	Linear detrending with comparison ensemble counts
θ_1	$\mathcal{N}(0,0.1)$	...	Linear detrending with the BJD timestamps
	Detrending parameters LCOGT HAL$_{i'}$		
θ_0	$\mathcal{N}(0,0.0001)$	...	Linear detrending with the sky background
θ_1	$\mathcal{N}(0,0.1)$	...	Linear detrending with the BJD timestamps
	Detrending parameters LCOGT HAL$_{z'_s}$		
θ_0	$\mathcal{N}(0,0.001)$	...	Linear detrending with the target FWHM
θ_1	$\mathcal{N}(0,0.1)$	...	Linear detrending with the BJD timestamps

The prior labels $\mathcal{U}$, $\mathcal{J}$, $\mathcal{N}$ represent uniform, log-uniform and normal distributions, respectively.

Continuation of the instrumental posteriors

Tab. B.2.: Posteriors of the joint fit for the different instrumental parameters.

Parameter	Posterior[a]	Units	Parameter	Posterior	Units
CARMENES			**LCOGT HAL$_{g'}$ 15 Apr. 2021**		
μ	$1.26^{+0.4}_{-0.41}$	$\mathrm{m\,s^{-1}}$	q_1	$0.868^{+0.086}_{-0.115}$	...
σ	$2.24^{+0.31}_{-0.28}$	$\mathrm{m\,s^{-1}}$	mflux	$-0.001^{+0.0052}_{-0.0043}$	...
TESS Sector 24			σ	$28.0^{+234.0}_{-25.0}$	ppm
mflux	$-0.000\,119^{+3.2\times10^{-5}}_{-3.2\times10^{-5}}$	...	θ_0	$5.2e-09^{+1.4e-09}_{-1.1e-09}$	...
σ	$48.0^{+78.0}_{-35.0}$	ppm	θ_1	$-0.0174^{+0.002}_{-0.0019}$	...
TESS Sector 25			**LCOGT HAL$_{i'}$ 15 Apr. 2021**		
q_1	$0.63^{+0.22}_{-0.27}$	...	q_1	$0.63^{+0.16}_{-0.18}$	...
q_2	$0.34^{+0.35}_{-0.23}$	...	mflux	$0.0033^{+0.0012}_{-0.0012}$	...
mflux	$-8.4\times10^{-5}{}^{+3.4\times10^{-5}}_{-3.3\times10^{-5}}$	...	σ	$526.0^{+35.0}_{-33.0}$	ppm
σ	$69.0^{+47.0}_{-33.0}$	ppm	θ_0	$4.74e-05^{+7.2e-06}_{-7.2e-06}$	...
SAINT-EX$_{I+z}$ 19 Mar. 2021			θ_1	$-0.001^{+0.0016}_{-0.0016}$	...
q_1	$0.854^{+0.096}_{-0.145}$	...	**LCOGT HAL$_{r'}$ 15 Apr. 2021**		
mflux	$-9\times10^{-5}{}^{+0.000\,14}_{-0.000\,14}$	...	q_1	$0.71^{+0.13}_{-0.14}$	...
σ	$350.0^{+300.0}_{-200.0}$	ppm	mflux	$-0.02^{+0.005}_{-0.0037}$	...
LCOGT CTIO$_{z'_s}$ 10 Apr. 2021			σ	$299.0^{+38.0}_{-38.0}$	ppm
q_1	$0.84^{+0.11}_{-0.16}$	...	θ_0	$-1.26e-09^{+2.3e-10}_{-1.8e-10}$	...
mflux	$0.0004^{+0.0035}_{-0.0034}$	...	θ_1	$0.00548^{+0.00078}_{-0.0007}$	...
σ	$3040.0^{+180.0}_{-170.0}$	ppm	**LCOGT HAL$_{z'_s}$ 15 Apr. 2021**		
θ_0	$1.3\times10^{-9}{}^{+1.5\times10^{-9}}_{-1.6\times10^{-9}}$	...	q_1	$0.66^{+0.16}_{-0.19}$	...
θ_1	$-0.000\,14^{+0.000\,33}_{-0.000\,38}$	...	mflux	$0.0045^{+0.0011}_{-0.0011}$	...
LCOGT McD$_{z'_s}$ 10 Apr. 2021			σ	$422.0^{+37.0}_{-35.0}$	ppm
q_1	$0.856^{+0.093}_{-0.129}$	...	θ_0	$-0.000466^{+6.9e-05}_{-6.5e-05}$	...
mflux	$-0.0143^{+0.005}_{-0.0055}$	...	θ_1	$0.011^{+0.00074}_{-0.00073}$	...
σ	$1850.0^{+130.0}_{-130.0}$	ppm			
θ_0	$-6.8\times10^{-9}{}^{+2.2\times10^{-9}}_{-2.5\times10^{-9}}$	...			
θ_1	$-0.0001^{+0.000\,23}_{-0.000\,22}$	...			

Error bars denote the 68% posterior credibility intervals.

Alternative joint fit considering $P_2 \sim 15\,\mathrm{d}$

In this section, we present an alternative joint fit, in which we consider the $15.0\,\mathrm{d}$ period to be the signal underlying the aliases discussed in subsubsection 4.4.5. The priors are identical to the joint fit in subsection 4.4.6, except the prior for the period of the second component, which was set uniform between $14.71\,\mathrm{d}$ and $15.48\,\mathrm{d}$ according to its peak width in the GLS periodogram. The posterior for the transiting planet, the $15.0\,\mathrm{d}$ signal and the GP for this fit are shown in Table B.3 and the resulting planetary parameters for GJ 3929 b in Table B.4. We found no significant deviation and almost identical uncertainties compared to the values obtained from considering the $14.34\,\mathrm{d}$ period. However, the higher planetary mass of GJ 3929 b derived from the $15.0\,\mathrm{d}$ fit, which was already evident in the RV only fit, in combination with the consistent uncertainties lead to a significant ($> 3\sigma$) mass measurement.

Tab. B.3.: Median posterior parameters from the alternative joint fit for the transiting planet, the $\sim 15.0\,$d signal and the GP.

Parameter	Posterior[a]	Units
	Stellar density	
$\rho_\star$	$12.89^{+0.73}_{-0.920}$	$\mathrm{g\,cm^{-3}}$
	GJ 3929 b	
P_b	$2.616\,271\,5^{+3.3\times 10^{-6}}_{-3.5\times 10^{-6}}$	d
$t_{0,\mathrm{b}}$[b]	$2\,459\,320.057\,86^{+0.000\,22}_{-0.000\,25}$	d
$r_{1,\mathrm{b}}$	$0.553^{+0.046}_{-0.047}$	...
$r_{2,\mathrm{b}}$	$0.033\,69^{+0.000\,54}_{-0.000\,55}$	...
K_b	$1.49^{+0.45}_{-0.43}$	$\mathrm{m\,s^{-1}}$
	15.0 d signal	
$P_{(15.0\,\mathrm{d})}$	$15.036^{+0.04}_{-0.037}$	d
$t_{0,(15.0\,\mathrm{d})}$[b]	$2\,459\,071.01^{+0.41}_{-0.42}$	d
$K_{(15.0\,\mathrm{d})}$	$3.17^{+0.46}_{-0.46}$	$\mathrm{m\,s^{-1}}$
	GP parameters	
$P_\mathrm{GP,\,rv}$	$132.7^{+8.1}_{-7.8}$	d
$\sigma_\mathrm{GP,\,rv}$	$1.32^{+0.62}_{-0.47}$	$\mathrm{m\,s^{-1}}$
$f_\mathrm{GP,\,rv}$	$0.55^{+0.19}_{-0.21}$	...
$Q_{0,\mathrm{GP,\,rv}}$	$0.6^{+2.27}_{-0.42}$	...
$dQ_\mathrm{GP,\,rv}$	210^{+1730}_{-200}	...

[a] Error bars denote the 68% posterior credibility intervals.

[b] Barycentric Julian Date in the Barycentric Dynamical Time standard.

Tab. B.4.: Alternative derived planet parameters for GJ 3929 b and the planet candidate considering the $15.0\,\mathrm{d}$ period.

Parameter	Posterior $\mathrm{P_b}^{(a)}$	Posterior $\mathrm{P_{(15.0\,d)}}^{(a)}$	Units
Derived transit parameters			
$p = R_\mathrm{p}/R_\star$	$0.033\,69^{+0.000\,54}_{-0.000\,55}$	...	...
$b = (a_\mathrm{p}/R_\star)\cos i_\mathrm{p}$	$0.33^{+0.069}_{-0.07}$	...	...
$a_\mathrm{p}/R_\star$	$16.71^{+0.31}_{-0.41}$	...	...
i_p	$88.87^{+0.26}_{-0.27}$	...	deg
Derived physical parameters[b]			
M_p	$1.47^{+0.44}_{-0.43}$	...	$M_\oplus$
$M_\mathrm{p}\sin i$	$1.47^{+0.44}_{-0.43}$	$5.6^{+0.83}_{-0.82}$	$M_\oplus$
R_p	$1.158^{+0.041}_{-0.041}$	...	$R_\oplus$
ρ_p	$5.2^{+1.7}_{-1.6}$	...	$\mathrm{g\,cm^{-3}}$
g_p	$10.7^{+3.4}_{-3.2}$	...	$\mathrm{m\,s^{-2}}$
a_p	$0.024\,43^{+0.000\,92}_{-0.000\,97}$	$0.0806^{+0.0012}_{-0.0012}$	au
$T_\mathrm{eq,\,p}$[c]	583^{+12}_{-11}	$321.1^{+7.5}_{-7.4}$	K
S	$19.4^{+1.7}_{-1.4}$	$1.778^{+0.055}_{-0.052}$	$S_\oplus$
ESM[d]	$5.27^{+0.35}_{-0.3}$	...	...
TSM[d]	$21.6^{+9.0}_{-5.1}$	...	...

[a] Error bars denote the 68% posterior credibility intervals.

[b] We sample from a normal distribution for the stellar mass, stellar radius and stellar luminosity that is based on the results from section 4.3.

[c] Assuming a zero Bond albedo.

[d] Emission/transmission spectroscopy metric (Kempton et al., 2018).

Declaration

I hereby declare that this thesis is my own work and that I have used no other than the stated sources and aids.

Ich versichere, dass ich diese Arbeit selbstständig verfasst habe und keine anderen als die angegebenen Quellen und Hilfsmittel benutzt habe.

_____   _____
Ort, Datum   Jonas Kemmer